

**MAGNETO-TRANSPORT, MAGNETO-OPTICAL AND
DYNAMIC PROPERTIES OF FERROMAGNETIC
NANOSTRUCTURES**

LIU XINMING

NATIONAL UNIVERSITY OF SINGAPORE

2013

**MAGNETO-TRANSPORT, MAGNETO-OPTICAL AND
DYNAMIC PROPERTIES OF FERROMAGNETIC
NANOSTRUCTURES**

LIU XINMING

(M.Eng, HUAZHONG UNIVERSITY OF SCIENCE AND TECHNOLOGY)

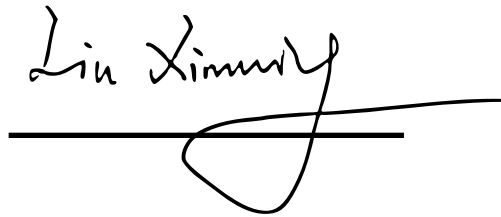
**A THESIS SUBMITTED
FOR THE DEGREE OF DOCTOR OF PHILOSOPHY
DEPARTMENT OF ELECTRICAL AND COMPUTER
ENGINEERING
NATIONAL UNIVERSITY OF SINGAPORE**

2013

DECLARATION

I hereby declare that the thesis is my original work and it has been written by me in its entirety. I have duly acknowledged all the sources of information which have been used in the thesis.

This thesis has also not been submitted for any degree in my university previously

A handwritten signature in black ink, reading "Liu Xinming". The signature is written in a cursive style and is positioned above a solid horizontal line.

Liu Xinming

29th November 2013

Acknowledgements

I feel grateful to meet these people who have contributed in different ways to the work presented in this thesis. Firstly, I would like to express my sincerest thanks to my supervisor, Prof. Adekunle Olusola Adeyeye for giving me the opportunity to join his group and work on this topic. His constant encouragement, patient guidance, scientific thinking and great passion all have greatly affected me and motivated me to move forwards. It is my honor to meet such a nice professor.

I would like to thank Dr. Navab Singh for providing the templates of nanostructures using deep ultraviolet lithography. I would also like to express my appreciation towards Assoc. Prof. Vivian Ng, Assoc. Prof. Chen Jingsheng and Prof. Mikhail Kostylev for the useful suggestions in the research work. Also, I would like to acknowledge Dr. Ren Yang, Dr. Shikha Jain and Dr. Tripathy Debashish for the helpful discussion and guidance at the beginning of the PhD study. I would like to specially thank Mr. Ding Junjia and Mr. Shimon for the useful discussion in research work and kindhearted help in personal life. I would like to thank Miss Ho Pin for the XRD and XRR measurements in this study. I would also like to thank the lab officers, Ms. Loh Fong Leong and Ms. Xiao Yun for the support during my candidature. Thanks to all the friends for the pleasant time we have shared in ISML and in Singapore.

I would like to thank my parents and little brother, who have given selfless support without reservation in the past 4 years. Finally, I would like to send the special thanks to my wife Du Zhijun for the understanding and the encouragement during the candidature study. Thank you so much, my families.

Table of Contents

Acknowledgements	i
Table of Contents	ii
Summary	vi
List of Tables	viii
List of Figures	ix
List of Symbols and Abbreviations	xvi
Statement of Originality	xviii
Chapter 1 Introduction	1
1.1 Background	1
1.2 Motivation	3
1.3 Focus of Thesis	5
1.4 Organization of Thesis	5
Chapter 2 Theoretical Background	7
2.1 Introduction	7
2.2 Co/X (=Pd, Pt, Ni...) Multilayers	7
2.2.1 Origin of Perpendicular Magnetic Anisotropy	7
2.2.2 Co/Pd Multilayer Systems	9
2.3 Spin Dependent Transport Phenomenon	11
2.3.1 Anisotropic Magnetoresistance	11
2.3.2 Giant Magnetoresistance	12
2.3.3 Magnon Magnetoresistance	14
2.4 Coupling Mechanism in Multilayer Films	16
2.4.1 Pinhole Coupling	16
2.4.2 Ruderman-Kittel-Kasuya-Yosida (RKKY) Coupling	17
2.4.3 Néel Coupling	18

Table of Contents

2.4.4 Interlayer Magnetostatic Coupling	19
2.5 Magnetization Dynamics	20
2.5.1 Fundamental of Magnetization Dynamics	21
2.5.2 Ferromagnetic Resonance	22
2.5.3 Magnonic Crystals	23
2.6 Summary	24
Chapter 3 Experimental Techniques	25
3.1 Introduction	25
3.2 Fabrication Techniques	25
3.2.1 Photolithography	26
3.2.1.1 KrF Deep Ultraviolet (DUV) Lithography	26
3.2.1.2 Ultraviolet (UV) Lithography	29
3.2.2 Deposition Techniques	30
3.2.2.1 Magnetron Sputtering	30
3.2.2.2 E-beam Evaporation	31
3.2.3 Lift-off, BARC Removal and Wire Bonding	31
3.3 Structural and Magnetic Characterization Techniques	33
3.3.1 X-Ray Diffractometer and X-Ray Reflectometry	33
3.3.2 Scanning Electron Microscopy	35
3.3.3 Scanning Probe Microscopy	37
3.3.4 Magneto-Optical Kerr Effect	38
3.3.5 Vibrating Sample Magnetometer	43
3.3.6 Magnetotransport Measurement	44
3.3.6.1 Room Temperature Setup	44
3.3.6.2 Low Temperature Setup	46
3.3.7 Ferromagnetic Resonance Spectroscopy	47
Chapter 4 Magnetization Reversal of Circular Co/Pd Nanomagnets	49
4.1 Introduction	49

Table of Contents

4.2 Experimental Details	49
4.3 Magnetic Properties of Pre-patterned Co/Pd Dots	52
4.3.1 Effects of Bi-layer Repeat	52
4.3.1.1 Continuous Films	52
4.3.1.2 Pre-patterned Dots	55
4.3.2 Effects of Dot Diameter	57
4.4 Magnetic Properties of Co/Pd Dot Clusters	60
4.4.1 Effects of Dipolar Coupling	60
4.4.2 Implementation of Logic ‘NOT’ Using Coupled Co/Pd Dots	62
4.4.2.1 Logical Schematic	62
4.4.2.2 Experimental Verification	64
4.5 Magnetic Properties of [Co/Pd] ₄ /Au/[Co/Pd] ₂ Rings	66
4.5.1 Structure Analysis of [Co/Pd] ₄ /Au/[Co/Pd] ₂ Films	67
4.5.2 Effects of Interlayer Coupling	68
4.5.3 Effects of Inter-ring Dipolar Coupling	70
4.6 Summary	72
Chapter 5 Magnetic and Transport Behaviors of Co/Pd Nanowires	73
5.1 Introduction	73
5.2 Experimental Details	73
5.3 Magnetic Behaviors of Co/Pd Nanowires	75
5.3.1 Room Temperature	75
5.3.2 Temperature Dependence	78
5.3.2.1 Perpendicular MR Response	78
5.3.2.2 Longitudinal and Transverse MR Responses	83
5.3.3 Effects of Cu Buffer Layer Thickness	86
5.3.3.1 Continuous Film	86
5.3.3.2 Nanowires	89
5.4 Interlayer Coupling and MR Behaviors of [Co/Pd] ₄ /Au/[Co/Pd] ₂ Nanowires	91

Table of Contents

5.4.1 Effects of Au Spacer Layer Thickness	91
5.4.2 Effects of Temperature	99
5.4.3 Effects of Co and Pd Insertion Layers	106
5.5 Interlayer Coupling in [Co/Pd] ₄ /Co/Ru/[Co/Pd] ₂ Multilayers	111
5.6 Summary	115
Chapter 6 Two-dimensional (2-D) Magnonic Crystals	116
6.1 Introduction	116
6.2 Modulated Ni ₈₀ Fe ₂₀ Film	116
6.2.1 Experimental Details	117
6.2.2 Ni ₈₀ Fe ₂₀ Film on Top of Periodic Arrays of Co/Pd Dots	120
6.2.3 Ni ₈₀ Fe ₂₀ Film on Top of Periodic Arrays of Ni ₈₀ Fe ₂₀ Dots	122
6.3 Fe Filled Ni ₈₀ Fe ₂₀ Antidot Nanostructures	128
6.3.1 Experimental Details	128
6.3.2 Magnetization Reversal Mechanism	131
6.3.3 Ferromagnetic Resonance Behavior	135
6.3.4 Magnetoresistance Behaviors	141
6.3.4.1 Angular Dependence	141
6.3.4.2 Temperature Dependence	146
6.3.4.3 Effects of Antidot Diameter	147
6.4 Summary	148
Chapter 7 Conclusion and Outlook	150
7.1 Overview	150
7.2 Summary of Results	150
7.3 Future Work	153
References	155
List of Publications	166

Summary

Ferromagnetic nanostructures have received much interest over the past decades due to their great importance in fundamental research and their potential in a wide range of emerging applications. In this thesis, a systematic investigation of magneto-transport, magneto-optical and dynamic properties of Co/Pd multilayer based nanostructures and bi-component magnonic crystals (MCs) is presented.

Firstly, the magnetization reversal mechanism of circular Co/Pd nanomagnets including nanodots and nanorings has been investigated. It was observed that the reversal process of the Co/Pd dots is dependent on both the number of Co/Pd bi-layer repeat and the dots diameter. For closely packed Co/Pd dots, dipolar coupling plays a crucial role in affecting the switching behaviors, with potential for magnetic logic applications. Further investigation of interlayer coupling was performed in $[\text{Co/Pd}]_4/\text{Au}(t_{\text{Au}})/[\text{Co/Pd}]_2$ pseudo-spin-valve (PSV) rings by varying the Au spacer layer thickness t_{Au} .

Secondly, magnetoresistance (MR) behaviors of $[\text{Co/Pd}]_n$ nanowires (NWs) have been systematically probed as a function of temperature T . A linear non-saturating MR response was observed in the NWs up to a maximum field as large as 40 kOe due to magnon magnetoresistance (MMR) effect. The MMR effect is strongly dependent on both the bi-layer repeat n and the temperature T .

Thirdly, the effects of interlayer coupling on the magnetization reversal and MR behaviors of $[\text{Co/Pd}]_4/\text{Au}(t_{\text{Au}})/[\text{Co/Pd}]_2$ PSV NWs have been studied. The interlayer coupling field (H_{coup}) was extracted using minor MR loop measurements. The H_{coup} of the PSV NWs is much larger than the corresponding continuous PSV films due to stray field interactions and it is markedly sensitive to both t_{Au} and T . At low T , the competition between the

Summary

interlayer coupling strength and the margin of switching field difference among the soft and hard Co/Pd stacks determines the overall magnetization reversal process and MR behavior of the PSV NWs. It is further shown that either ferromagnetic or antiferromagnetic type of interlayer coupling can be achieved in the $[\text{Co/Pd}]_4/\text{Co/Ru}(t_{Ru})/[\text{Co/Pd}]_2$ PSVs by varying t_{Ru} .

Finally, a novel process for fabricating high quality 2-D MCs has been developed. The MCs includes a continuous $\text{Ni}_{80}\text{Fe}_{20}$ film on top of periodic 2-D arrays of perpendicularly magnetized Co/Pd dots (or $\text{Ni}_{80}\text{Fe}_{20}$ dots with in-plane anisotropy) and Fe filled $\text{Ni}_{80}\text{Fe}_{20}$ antidot nanostructures in which the “holes” of $\text{Ni}_{80}\text{Fe}_{20}$ antidot are filled with Fe dots. The presence of Co/Pd dots (or $\text{Ni}_{80}\text{Fe}_{20}$ dots) array significantly modifies the static and dynamic behaviors of the top $\text{Ni}_{80}\text{Fe}_{20}$ film when compared with the reference $\text{Ni}_{80}\text{Fe}_{20}$ film without the dot array underneath. In the Fe filled $\text{Ni}_{80}\text{Fe}_{20}$ antidot nanostructures, although the Fe dots are not in direct contact with the $\text{Ni}_{80}\text{Fe}_{20}$ antidot, their stray fields strongly influence the magnetization reversal, the ferromagnetic resonance and the MR behaviors of the host $\text{Ni}_{80}\text{Fe}_{20}$ antidot. The experimental results are in good agreement with micromagnetic simulations.

List of Tables

Table 4.1 Favorable energy states based on dipolar energy calculation of all the possible input and output combinations in a [Co(0.5 nm)/Pd(3 nm)] ₆ two-dot cluster with s=100 nm.	64
---	----

List of Figures

Fig. 2.1	Schematics of various energy terms contributing to K_u in Co/X multilayers.	8
Fig. 2.2	Schematics of magnetization reversal for (a) large Co/Pd dots; and (b) single domain Co/Pd dots.	11
Fig. 2.3	Schematics of AMR effect in a ferromagnetic metal.	11
Fig. 2.4	Schematics of two-current model for GMR effect in (a) parallel; and (b) antiparallel spin configurations.	14
Fig. 2.5	Typical MR curve for MMR effect ^[91] .	15
Fig. 2.6	Configuration of magnetization for direct exchange coupled FM layers.	17
Fig. 2.7	Schematics of RKKY coupling strength as a function of spacer layer thickness.	18
Fig. 2.8	Schematics of the layer geometry giving rise to Néel coupling.	19
Fig. 2.9	Magnetostatic energy levels for PSVs with (a) in-plane anisotropy; and (b) out-of-plane anisotropy.	20
Fig. 2.10	Schematics of dynamic response of a magnetic spin (a) without; and (b) with the damping term.	22
Fig. 2.11	Schematics of typical single-component 1-D (a); 2-D (b); and bi-component 1-D (c); 2-D (d) MCs.	23
Fig. 3.1	Schematics of typical fabrication process flow for the nanostructure arrays.	26
Fig. 3.2	Schematics of DUV lithography process using (a) Binary mask; and (b) Phase shift mask.	28
Fig. 3.3	Schematics of the fabrication process flow for Si nanopillars ^[117] .	29
Fig. 3.4	Schematics of thin film deposition using AJA.	31
Fig. 3.5	Electrical bond pads for MR measurements.	32
Fig. 3.6	Schematics of constructive interface of X-ray.	33
Fig. 3.7	Schematics of an X-ray diffractometer.	34
Fig. 3.8	Schematics of total reflection of X-ray.	35
Fig. 3.9	Schematics of the SEM.	36

List of Figures

Fig. 3.10	Schematics of atomic force microscopy measurements ^[125] .	37
Fig. 3.11	Schematics of MFM measurements.	38
Fig. 3.12	Schematics of MOKE with (a) polar; (b) longitudinal; and (c) transverse configurations.	39
Fig. 3.13	(a)Schematics; and (b)Experimental demonstrations of a longitudinal MOKE setup.	41
Fig. 3.14	(a) Schematics; and (b) Experimental demonstrations of a polar MOKE setup.	43
Fig. 3.15	Schematics of VSM setup.	44
Fig. 3.16	Schematics of room temperature MR measurement setup.	45
Fig. 3.17	Schematics of Janis SVT research cryostat.	47
Fig. 3.18	Schematics of FMR measurements ^[128]	48
Fig. 4.1	(a) Schematics of Co/Pd multilayers on top of pre-patterned Si nanopillars; and (b) SEM image of arrays of [Co(0.5 nm)/Pd(3 nm)] ₁₂ dots with d=185 nm. Schematics and SEM images of the Co/Pd two-dot cluster fabricated using method B are shown in (c) and (d) respectively.	50
Fig. 4.2	(a) Schematics of the deposited Co/Pd PSV structure; and (b) representative SEM images of the PSV nanorings with s=200 nm and s=650 nm.	52
Fig. 4.3	(a) M-H loops; and (b) XRD patterns for continuous [Co(0.5 nm)/Pd(3 nm)] _n films as a function of n. The atomic force microscopy and MFM images taken after AC demagnetization are shown in (c) and (d).	53
Fig. 4.4	Out-of-plane and in-plane M-H loops measured using VSM for the [Co/Pd] _n multilayer films with (a) n=4; and (b) n=18. A plot of K _u extracted from the M-H loops as a function of n is shown in (c).	55
Fig. 4.5	(a) Hysteresis loops of pre-patterned Co/Pd dots with d=185 nm as a function of n; and (b) A plot of H _{s1} , H _{s2} (defined in (a)) and the switching field of continuous films as a function of n.	56
Fig. 4.6	(a) Hysteresis loops of pre-patterned [Co(0.5 nm)/Pd(3 nm)] ₁₂ structures as a function of d (A plot of H _{s1} and H _{s2} as a function of d is shown as an inset); and (b) MFM images of the Co/Pd dots with varied d taken at remanence after the samples were first saturated in a field of -3.5 kOe followed by a reversal field of +2.11 kOe.	58
Fig. 4.7	(a) M-H loops of [Co(0.5 nm)/Pd(3 nm)] ₂ two-dot clusters as a function of s; and (b) A plot of measured H _{sw} (rectangular symbols)	

List of Figures

- and calculated H_{dip} (circular symbols) as a function of s . The corresponding results for the $[\text{Co}/\text{Pd}]_n$ dot cluster with $n=6$ are shown in (c) and (d) respectively. 60
- Fig. 4.8 Schematics of the input and output for a Co/Pd two-dot cluster. 62
- Fig. 4.9 (a) MFM images of the two-dot cluster with states of (01) and (10) taken at remanence after the sample was first saturated by external fields of ∓ 3 kOe followed by a clock-field of amplitude ± 1.96 kOe respectively. MFM image of a 5×5 dot cluster array taken after a saturation field of -3 kOe followed by a reversal field of (b)+1.78 kOe; (c)+1.96 kOe; and (d)+2.04 kOe respectively. 65
- Fig. 4.10 XRD patterns of $[\text{Co}/\text{Pd}]_4/\text{Au}(t_{\text{Au}})/[\text{Co}/\text{Pd}]_2$ PSV films as a function of t_{Au} . 67
- Fig. 4.11 M-H loops for $[\text{Co}/\text{Pd}]_4/\text{Au}(t_{\text{Au}})/[\text{Co}/\text{Pd}]_2$ PSV rings with (a) $t_{\text{Au}} = 1$ nm, compared with the hysteresis loop of $[\text{Co}/\text{Pd}]_4$ multilayer rings; (b) $t_{\text{Au}} = 2$ nm; (c) $t_{\text{Au}} = 5$ nm (d) $t_{\text{Au}} = 8$ nm; and (e) a plot of H_{s1} , H_{s2} , H_{AP} (defined in (c)) as a function of t_{Au} . 69
- Fig. 4.12 Polar MOKE M-H loops of $[\text{Co}/\text{Pd}]_4/\text{Au}(t_{\text{Au}})/[\text{Co}/\text{Pd}]_2$ PSV rings as a function of edge-to-edge spacing s for (a) $t_{\text{Au}} = 1$ nm; and (b) $t_{\text{Au}} = 5$ nm (A plot of H_{s1} , H_{s2} and H_{AP} as a function of s is shown as an inset). 71
- Fig. 5.1 (a) Representative SEM micrograph of arrays of $[\text{Co}(0.5 \text{ nm})/\text{Pd}(3 \text{ nm})]_{18}$ NWs; and (b) Schematics of the Co/Pd NWs including Al bond pads for MR measurements. 74
- Fig. 5.2 (a) Schematics of deposited film structure for $[\text{Co}(0.5 \text{ nm})/\text{Pd}(3 \text{ nm})]_n$ NWs. M-H loops and perpendicular MR responses of the NWs for (b) $n=4$; (c) $n=8$; and (d) $n=18$. 76
- Fig. 5.3 Perpendicular MR response of the $[\text{Co}/\text{Pd}]_4$ NWs at $T=5$ K. 78
- Fig. 5.4 Perpendicular MR responses as a function of T for the $[\text{Co}/\text{Pd}]_n$ NWs with (a) $n=4$ (Experimental MR slope (solid symbol) with fitted MMR curve (solid line) is shown as an inset); (b) $n=8$; and (c) $n=18$ (A plot of H_{sw} Vs T extracted from the MR responses as a function of n is shown as an inset). The perpendicular MR responses for the corresponding continuous $[\text{Co}/\text{Pd}]_n$ films with $n=4$, 8 and 18 are shown in (d), (e) and (f) respectively. 79
- Fig. 5.5 A plot of MR, LFMR and HFMR (defined in Fig. 5.4(b)) as a function of T for the Co/Pd NWs with (a) $n=4$; (b) $n=8$; and (c) $n=18$. Results for the corresponding Co/Pd continuous films are shown in (d)-(f) respectively. 82
- Fig. 5.6 Longitudinal MR responses as a function of T for the $[\text{Co}(0.5$

List of Figures

-
- nm)/Pd(3 nm)]₄ (a) NWs; and (b) continuous film (The H_{sat} Vs T for both the structures is shown as an inset). 84
- Fig. 5.7 Transverse MR responses for the [Co(0.5 nm)/Pd(3 nm)]₄ (a) NWs; and (b) continuous film taken at T=5 K. 85
- Fig. 5.8 (a) Schematics of deposited Cu(t_{Cu})/Pd(5 nm)/[Co(0.5 nm)/Pd(3 nm)]₄ multilayer structure; and (b) hysteresis loops of the multilayer films as a function of t_{Cu} . 86
- Fig. 5.9 (a) XRD patterns as a function of t_{Cu} ; and (b) Rocking curve XRD; (c) Atomic force micrographs for $t_{\text{Cu}}=0$ nm and $t_{\text{Cu}}=15$ nm. (d) A plot of the mean grain size and RMS roughness of the Cu(t_{Cu})/Pd/[Co/Pd]₄ multilayer films as a function of t_{Cu} . 87
- Fig. 5.10 Representative XRR spectra and best fits for the Cu(t_{Cu})/Pd/[Co/Pd]₄ multilayer films with $t_{\text{Cu}}=0$ nm and $t_{\text{Cu}}=15$ nm (the extracted interface roughness as a function of t_{Cu} is shown as an inset). 88
- Fig. 5.11 (a) Hysteresis loops of arrays of Cu(t_{Cu})/Pd(5 nm)/[Co(0.5 nm)/Pd(3 nm)]₄ NWs as a function of t_{Cu} ; and (b) A plot of H_{sw} Vs t_{Cu} for both the [Co/Pd]₄ NWs and continuous films (The line is used to guide the eyes). Hysteresis loops of the [Co/Pd]₂ NWs and film with $t_{\text{Cu}}=15$ nm are shown as an inset in (b). 90
- Fig. 5.12 (a) Schematics of deposited Cu/Pd/[Co/Pd]₄/Au(t_{Au})/[Co/Pd]₂ PSV structure; (b) Hysteresis loops (minor loop shift represents the interlayer coupling field H_{coup}); and (c) MR responses of the PSV NWs with $t_{\text{Au}}=1.5$ nm. Results of corresponding continuous PSV film with $t_{\text{Au}}=1.5$ nm are shown in (d) and (e) respectively (VSM result for the PSV film is shown as an inset in (d)). 92
- Fig. 5.13 M-H loops of the Cu/Pd/[Co/Pd]₄/Au(t_{Au})/[Co/Pd]₂ PSV NWs with (a) $t_{\text{Au}}=1$ nm (M-H loops of corresponding continuous film are shown as an inset); (b) $t_{\text{Au}}=1.5$ nm; (c) $t_{\text{Au}}=2$ nm; (d) $t_{\text{Au}}=2.5$ nm; and (e) $t_{\text{Au}}=3.5$ nm. The corresponding MR loops are shown in (f)-(j) respectively. The dashed lines indicate the reduced interlayer coupling with t_{Au} . 95
- Fig. 5.14 (a) Schematics for stray field calculation of the [Co/Pd]₄ NWs; and (b) A plot of calculated stray fields (empty circle), interlayer coupling field H_{coup} extracted experimentally from minor M-H loop shift of Cu/Pd/[Co/Pd]₄/Au(t_{Au})/[Co/Pd]₂ PSV NWs (solid circle) and corresponding continuous films (solid triangle) as a function of t_{Au} . 97
- Fig. 5.15 A plot of H_{s1} , H_{s2} and H_{AP} (defined in Fig. 5.13(e)) of the PSV NWs as a function of t_{Au} . 99
-

List of Figures

- Fig. 5.16 Major (black rectangular) and minor (red circular) MR loops as a function of T for the Cu/Pd/[Co/Pd]₄/Au(t_{Au})/[Co/Pd]₂ PSV (a) NWs (the dash line indicates interlayer coupling field H_{coup}); and (b) corresponding continuous film with t_{Au}=1.5 nm. The enlarged half-loop MR curves are shown as insets. 101
- Fig. 5.17 MR loops as a function of T for the PSV (a) NWs; and (b) corresponding continuous film with t_{Au}=2.5 nm. 103
- Fig. 5.18 A plot of (a) H_{coup} Vs T extracted from the minor loop MR measurements; and (b) MR ratio Vs T for the Cu/Pd/[Co/Pd]₄/Au(t_{Au})/[Co/Pd]₂ PSV NWs and films as a function of t_{Au}. 104
- Fig. 5.19 (a) Schematics; and M-H loops of the PSV NWs (b); continuous film (c) with structure I where the Au spacer is sandwiched by two Co layers. Results for the PSVs with structure II (Au spacer sandwiched by two Pd layers) are shown in (d)-(f) respectively. 107
- Fig. 5.20 MR responses as a function of T for the PSV NWs (a); and corresponding continuous film (b) with structure I. A plot of MR ratio Vs T is shown in (c). 108
- Fig. 5.21 MR responses as a function of T for the PSV NWs (a); and corresponding continuous film (b) with structure II. A plot of MR ratio Vs T is shown in (c). 109
- Fig. 5.22 (a) Schematics of the deposited Pd/[Co/Pd]₄/Co/Ru(t_{Ru})/[Co/Pd]₂ PSV structures with a Ru spacer; and (b-g) M-H loops of the PSV films as a function of t_{Ru}. 111
- Fig. 5.23 (a) Experimental H_{coup} (solid symbol) extracted from minor M-H loop measurements and RKKY fitting results (solid line) as a function of t_{Ru}; and (b) a plot of H_{s1}, H_{s2} and H_{AP} (defined in Fig. 5.20(c)) as a function of t_{Ru}. 113
- Fig. 5.24 Perpendicular MR responses of the Pd/[Co/Pd]₄/Co/Ru(t_{Ru})/[Co/Pd]₂ PSV films as a function of t_{Ru}. 114
- Fig. 6.1 (a) Schematic illustration of fabrication process flow for dot modulated Ni₈₀Fe₂₀ film; (b) SEM image of Co/Pd dots embedded in BARC matrix; and (c) Schematics of cross section for the modulated Ni₈₀Fe₂₀ film with Co/Pt dots underneath. 117
- Fig. 6.2 (a) Schematics of cross-section for modulated Ni₈₀Fe₂₀ film with Ni₈₀Fe₂₀ dots underneath; (b) Atomic force micrograph of the Ni₈₀Fe₂₀ dots embeded in BARC matrix and a cross-section across the dashed line; and (c) Schematics of coplanar waveguide deposited on top of the modulated Ni₈₀Fe₂₀ film for FMR

List of Figures

-
- measurements. 118
- Fig. 6.3 (a) 2-D FMR absorption spectra (An FMR trace for $H_{app}=-1000$ Oe is shown at right-hand side); (b) Hysteresis loop; and (c) An MFM image taken at remanence after saturation for the reference $Ni_{80}Fe_{20}$ film. The results for the modulated $Ni_{80}Fe_{20}$ film with Co/Pd dots underneath are shown in (d)-(f). 121
- Fig. 6.4 (a) Experimental; and (b) simulated hysteresis loops for the modulated $Ni_{80}Fe_{20}$ films (Structure B) with different values of film thickness t varied from 0 to 60 nm. Inserts to the simulated hysteresis loops are the simulated magnetization configurations for middle sections of the dot and film parts of the given modulated film at remanence. 123
- Fig. 6.5 (a) Experimental FMR spectra at -1400 Oe for modulated $Ni_{80}Fe_{20}$ films (Structure B) as a function of the film thickness t and for a 60 nm-thick continuous film. (b-e) Profiles (obtained from micromagnetic simulations) of mode A; and (f-i) mode B for middle sections of the dot and film part of modulated $Ni_{80}Fe_{20}$ films as a function of t . Blue color represents large precession amplitudes. 125
- Fig. 6.6 (a) Experimental 2-D FMR spectra of the modulated $Ni_{80}Fe_{20}$ film with $t=15$ nm, reference $Ni_{80}Fe_{20}$ dots and reference 15 nm thick $Ni_{80}Fe_{20}$ film. (b) Spatial distributions of demagnetization field H_{d-x} in the top $Ni_{80}Fe_{20}$ film for $H = -1400$ Oe (The H_{d-x} profile along dashed line is shown below). 127
- Fig. 6.7 Schematics of typical fabrication process flow for the $Ni_{80}Fe_{20}/Fe$ structure. 129
- Fig. 6.8 SEM micrographs of (a) reference Fe dots; (b) reference $Ni_{80}Fe_{20}$ antidot; and (c) the $Fe/Ni_{80}Fe_{20}$ structure. Schematics of coplanar waveguide deposited on top of the fabricated nanostructures for FMR measurements and Au bond pads for MR measurements are shown (d) and (e), respectively. 130
- Fig. 6.9 Hysteresis loops for (a) Fe dots; (b) $Ni_{80}Fe_{20}$ antidot (hysteresis loop for correspond -ing $Ni_{80}Fe_{20}$ film is shown as an inset); and (c) $Ni_{80}Fe_{20}/Fe$ structure (The interpolate loop assuming no coupling between the Fe dots and $Ni_{80}Fe_{20}$ antidot is shown as an inset). The simulated hysteresis loops are shown in (d)-(f) respectively. 132
- Fig. 6.10 MFM images taken at remanence after negative saturation for the (a) Fe dots; (b) $Ni_{80}Fe_{20}$ antidot; and (c) $Ni_{80}Fe_{20}/Fe$ structure. The corresponding simulated magnetization states are shown in (d)-(f) respectively. 134
- Fig. 6.11 Experimental M-H loops of $Ni_{80}Fe_{20}$ antidot with (a) $d=300$ nm; (b)
-

List of Figures

- d=430 nm; and (c) d=550 nm. The corresponding results of the Ni₈₀Fe₂₀/Fe structures are shown in (d)-(f) respectively. 135
- Fig. 6.12 (a) FMR traces of the Ni₈₀Fe₂₀/Fe structure with varying H_{app} for $\theta = 0^\circ$; (b) Experimental 2-D absorption spectra. Results for reference Fe dots (solid line), Ni₈₀Fe₂₀ antidot (dashed line) and Ni₈₀Fe₂₀ film (dot-dash line) are also shown. (c) Simulated FMR spectra for H_{app} = -1000 Oe. (d) The spatial distributions of spin precession amplitudes for respective modes. 136
- Fig. 6.13 (a) FMR traces of the Ni₈₀Fe₂₀/Fe structure with varying θ for H_{app}=-1000 Oe. (b) Experimental 2-D angular dependence absorption spectra. (c) Simulated FMR spectra for $\theta=-45^\circ$. (d) The spatial distributions of spin precession amplitudes for respective modes. 140
- Fig. 6.14 3-D current density distribution of the Ni₈₀Fe₂₀ antidot obtained from LLG simulation at H_{app}=-10 kOe. 141
- Fig. 6.15 (a) Experimental; (b) simulated longitudinal MR curves; and (c) simulated magnetization states at various applied fields for the Ni₈₀Fe₂₀ antidot with d=430 nm. The corresponding results for the Ni₈₀Fe₂₀/Fe structure are shown in (d)-(f) respectively. 143
- Fig. 6.16 MR responses as a function of θ for (a-d) Ni₈₀Fe₂₀ antidot; and (e-h) Ni₈₀Fe₂₀/Fe structure with d=430 nm. The measured M-H loop of Ni₈₀Fe₂₀ antidot at $\theta = 45^\circ$ is shown as an inset in (c). 146
- Fig. 6.17 LMR responses as a function of temperature T for (a) Ni₈₀Fe₂₀ antidot and (b) the Ni₈₀Fe₂₀/Fe structure with d=430 nm. The extracted H_{sw} (defined in (a)) as a function of T for the two structures are shown in (c). 147
- Fig. 6.18 (a) Experimental; and (b) Simulated LMR curves for the Ni₈₀Fe₂₀/Fe structure as a function of the antidot diameter d. 148
- Fig. 7.1 (a) Optical photo; and (b) SEM micrograph of a Si₃N₄ membrane mask. 153
- Fig. 7.2 Schematics of fabrication process flow for the modulated Co/Pd film. 154

List of Symbols and Abbreviations

2-D	Two-Dimensional
AFM	Antiferromagnetic
Al	Aluminum
Al ₂ O ₃	Alumina
AMR	Anisotropic Magnetoresistance
Au	Gold
BARC	Bottom Anti-Reflection Coating
BPM	Bit Patterned Media
CPW	Coplanar Waveguide
Co	Cobalt
DUV	Deep Ultraviolet
DWR	Domain Wall Resistance
E-beam	Electron Beam
Fe	Iron
FM	Ferromagnetic
FMR	Ferromagnetic Resonance
GMR	Giant Magnetoresistance
H _{app}	Applied Magnetic Field
H _{coup}	Interlayer Coupling Field
H _{sw}	Switching Field
HFMR	High Field Magnetoresistance
LCP	Left-hand Circularly Polarized
LFMR	Low Field Magnetoresistance
LLG	Landau-Lifshitz-Gilbert
LMR	Longitudinal Magnetoresistance
MCs	Magnonic Crystals

List of Symbols and Abbreviations

MFM	Magnetic Force Microscopy
MMR	Magnon Magnetoresistance
MOKE	Magneto-Optical Kerr Effect
MR	Magnetoresistance
MRAM	Magnetic Random Access Memory
NA	Numerical Aperture
Ni ₈₀ Fe ₂₀	Permalloy
NM	Non-magnetic
NW	Nanowire
Pd	Palladium
PEM	Photoelastic Modulator
PMA	Perpendicular Magnetic Anisotropy
PSM	Phase Shift Mask
PSV	Pseudo-Spin-Valve
RCP	Right-hand Circularly Polarized
RKKY	Ruderman-Kittel-Kasuya-Yosida
RMS	Root Mean Square
SEM	Scanning Electron Microscopy
SPM	Scanning Probe Microscopy
T	Temperature
Ti	Titanium
UV	Ultraviolet
VNA	Vector Network Analyzer
VSM	Vibrating Sample Magnetometer
XRD	X-ray Diffractometer
XRR	X-ray Reflectometry

Statement of Originality

The author claims the following aspects of this thesis to be original contributions to scientific knowledge.

- A systematic study of magnetization reversal process in $[\text{Co/Pd}]_n$ multilayer nanorings and $[\text{Co/Pd}]_4/\text{Au}(t_{\text{Au}})/[\text{Co/Pd}]_2$ pseudo-spin-valve (PSV) rings.
[1] “Magnetic Properties of Perpendicularly Magnetized $[\text{Co/Pd}]/\text{Au}/[\text{Co/Pd}]$ Pseudo-Spin-Valve Nanoring Structures”, X. M. Liu, S. Jain, and A. O. Adeyeye, *IEEE Trans. Magn.* **47**, 2628 (2011).
[2] “Influence of magnetostatic interaction on the magnetization reversal of patterned Co/Pd multilayers nanorings”, Y. Ren, X. M. Liu, N. Singh, and A. O. Adeyeye, *IEEE Trans. Magn.* **49**, 3620 (2013).
- A systematic investigation on the effects of interlayer coupling on the magnetization reversal mechanism and magnetoresistance behaviors of $[\text{Co/Pd}]_4/\text{Au}(t_{\text{Au}})/[\text{Co/Pd}]_2$ PSV nanowires as a function of the Au spacer layer thickness and temperature.
[3] “Magnetization reversal and magnetoresistance behavior of perpendicularly magnetized $[\text{Co/Pd}]_4/\text{Au}/[\text{Co/Pd}]_2$ nanowires”, X. M. Liu, P. Ho, J. S. Chen, and A. O. Adeyeye, *J. Appl. Phys.* **112**, 073902 (2012).
- Development of a multi-level process based on deep ultraviolet lithography for fabrication of a new type of magnonic crystals (MCs): $\text{Ni}_{80}\text{Fe}_{20}$ films deposited on top of periodic 2-D arrays of $\text{Ni}_{80}\text{Fe}_{20}$ dots.
[4] “Magnonic crystals composed of $\text{Ni}_{80}\text{Fe}_{20}$ film on top of $\text{Ni}_{80}\text{Fe}_{20}$ two-dimensional dot array”, X. M. Liu, J. Ding, G.N. Kakazei, and A.O. Adeyeye, *Appl. Phys. Lett.* **103**, 062401 (2013).

List of Symbols and Abbreviations

- Development of a novel process for fabrication of high quality bi-component MCs: Fe filled Ni₈₀Fe₂₀ antidot nanostructures.
- [5] “Magnetization dynamics and reversal mechanism of Fe filled Ni₈₀Fe₂₀ antidot nanostructures”, X. M. Liu, J. Ding, and A. O. Adeyeye, *Appl. Phys. Lett.* **100**, 242411 (2012).
- [6] “Magnetoresistance Behavior of Bi-component Antidot Nanostructures”, X. M. Liu, J. Ding, N. Singh, M. Kostylev, and A. O. Adeyeye, *Europhys. Lett.* **103** 67002 (2013).

Chapter 1

Introduction

1.1 Background

Ferromagnetic nanostructures have attracted tremendous interest in the past decades due to their great importance in fundamental research and the potential in a wide range of emerging applications^[1, 2]. From a fundamental viewpoint, due to the extremely small dimensions, both the static and dynamic properties of these nanomagnets are usually quite different from those of bulk materials or thin films^[3]. Magnetization reversal behavior^[4], transport properties^[5, 6] as well as dynamic responses^[7, 8] can therefore be drastically modified in nanostructures due to lateral confinement. These modifications become extremely prominent when the lateral size is comparable to or smaller than certain characteristic length scales, such as spin diffusion length, carrier mean free path and magnetic domain wall width^[9, 10].

Magnetic nanostructures are also the basic building blocks for future spintronic devices such as magnetic logic devices^[11, 12], magnetic random access memory (MRAM)^[13-15] and magnonic devices^[7, 8]. For successful implementation of logic devices, single-domain ferromagnetic nanomagnets are required due to their well-defined logical values (“0” and “1”) by magnetization states (spin “up” and “down”). Perpendicularly magnetized nanostructures show advantages in logic implementation due to their inherent logic states (i.e. up and down magnetization), given by the uniaxial nature of perpendicular anisotropy. Realization of logical “NOT” function has been reported using coupled Co/Pt nanowires (NWs) with perpendicular magnetic anisotropy (PMA)^[12]. The idea was using the dipolar field interaction created by the input wire to control the magnetic switching of the output wire.

Magnetic nanostructures have also attracted much attention in MRAM design due to their non-volatile characteristic: when switched off, the magnetic state is preserved. In MRAM, the information is stored based on the spin dependent transport phenomena. For a viable MRAM cell design, a device configuration consisting of at least two ferromagnetic (FM) layers separated by a nonmagnetic (NM) spacer layer would be desirable. Depending on the relative orientation of magnetization of the two FM layers, the resistance can be high or low, which represent the states “1” and “0” respectively. The writing of an MRAM cell can be achieved by applying a current induced magnetic field or via spin transfer torque (STT)^[16]. Compared to nanostructures with in-plane magnetic anisotropy, perpendicularly magnetized nanostructures are predicted to be more beneficial from their improved thermal stability, lower critical current density for spin transfer switching and lower cell geometry dependence, implying higher packing density for future MRAM design^[17-19].

Among the material choices for fabricating nanostructures with PMA are CoCrX (X=Pt, Ta, Nb....) alloys, L1₀ alloys (e.g. FePt) and [Co/X(=Pd, Pt, Ni...)]_n based magnetic multilayers^[20]. CoCrX alloys are commonly used for conventional continuous film recording, and they are advantageous due to the widely available information on fabrication and characterization. However, the achievable PMA in CoCrX alloys is very limited, which raises question on their future technology extension. The L1₀ alloys possess large PMA when the as-deposited fcc texture is transformed into fct texture upon high temperature annealing^[20]. In contrast, [Co/X(=Pd, Pt, Ni...)]_n multilayers do not need high temperature to form perpendicular anisotropy. It exhibits high inter-granular exchange coupling, high and easily controllable PMA, high coercivity and large squareness^[21, 22] as deposited at room temperature, making it suitable for future spintronic applications. Compared with other [Co/X(=Pt, Ni...)]_n systems, [Co/Pd]_n multilayer structures are more attractive for

magneto-transport applications due to their higher magnetoresistance ratio and larger PMA resulting from smaller Pd layer thickness^[15]. This work will focus on [Co/Pd]_n multilayer based nanostructures with perpendicular anisotropy.

Another emerging application of magnetic nanostructures is in the area of magnonic devices. The artificial magnetic nanostructures with periodic lateral variations in their magnetic properties are called magnonic crystals (MCs). MCs can be conceived as the magnetic analog of photonic crystals because of the possibility to manipulate spin-wave propagation. Since spin waves in microwave frequency range (GHz-THz) have shorter wavelengths (ranging from nanometer to micrometer) as compared to electromagnetic waves (in millimeter range), magnonic devices based on MCs offer better prospects for device miniaturization^[7, 8, 23] at these frequencies.

1.2 Motivation

One of the major challenges for technological applications utilizing perpendicularly magnetized nanostructures is to precisely control the magnetic switching process. This is linked directly to the understanding of the reversal mechanism with geometrical variation such as shape, size and element spacing. However, most of the works done so far have been focused on the magnetic switching of Co/Pd (or Co/Pt, FePt) islands with perpendicular anisotropy^[24-27]. There have been limited studies on other type of nanostructure geometries with PMA, such as antidot^[28-31], nanorings^[32] and nanowires^[33-35].

Since the MRAM exploits the ‘spin’ of electrons to store information, it is important to understand the spin dependent transport phenomena in magnetic nanostructures. The magneto-transport technique provides an efficient way to electrically sense the magnetization states during the reversal process, and hence it has been widely used to probe the magnetoresistance (MR) behavior of various magnetic nanostructures with in-plane anisotropy^[36-38]. However, the investigation on the magneto-transport properties of perpendicularly

magnetized nanostructures is still lacking.

Furthermore, when the ferromagnetic layers are arranged in a pseudo-spin-valve (PSV) stack (typical film structure for an MRAM cell), interlayer coupling plays an important role in determining the magnetic switching behaviors. The interlayer coupling of patterned nanostructures is significantly different from that of continuous PSV films due to the contribution from stray field interactions, which becomes extremely prominent as the magnetic elements are scaled down^[39, 40]. Moreover, depending on the material and thickness of the spacer layer, either ferromagnetic or antiferromagnetic type of interlayer coupling can be achieved in the PSVs^[41, 42]. In this regard, the understanding of interlayer coupling of patterned nanostructures with perpendicular anisotropy is of significant importance for future MRAM design. However, earlier studies have focused on the interlayer coupling of PSVs with in-plane anisotropy^[39, 43, 44] and on the continuous PSV films with perpendicular anisotropy^[45-51]. There have been limited number of reports on the investigation of interlayer coupling in patterned PSV nanostructures with PMA^[15, 52] and even fewer about temperature dependent study.

Apart from the static properties, the dynamic response of magnetic nanostructures have also received a lot of attention recently due to their potential in a wide range of magnonic applications such as microwave resonators, filters and spin logic devices^[8, 53-55]. These artificial magnetic nanostructures are called magnonic crystals (MCs). In contrast to single component MCs^[56, 57], one can introduce bi-component MCs which consist of arrays of one FM material in the matrix of another FM material. This allows for an additional degree of freedom in tailoring spin wave properties^[23, 58]. However, because of the difficulty in fabricating high quality bi-component MCs, only several experimental studies of such structures have been reported^[59-61].

1.3 Focus of Thesis

In this thesis, a comprehensive study of magneto-transport, magneto-optical and dynamic properties of ferromagnetic nanostructures is presented. The discussion in this thesis is divided into two parts. The first part focuses on the magnetization reversal and MR behaviors of Co/Pd multilayer based nanostructures as a function of various geometrical parameters. The second part discusses the static and dynamic properties of bi-component 2-D MCs including continuous $\text{Ni}_{80}\text{Fe}_{20}$ films which was placed on top of arrays of Co/Pd dots (or $\text{Ni}_{80}\text{Fe}_{20}$ dots) and Fe filled $\text{Ni}_{80}\text{Fe}_{20}$ antidot nanostructures.

The main objectives of this thesis are listed as follows:

- (a) Developing a large area process for fabricating magnetic nanostructures with perpendicular anisotropy by leveraging on what has been done with in-plane nanostructures.
- (b) Probing the magnetization reversal and MR behavior of $[\text{Co/Pd}]_n$ multilayer based nanostructures as a function of geometrical parameters.
- (c) Investigating the influence of interlayer coupling on the magnetization reversal and MR behavior of $[\text{Co/Pd}]_4/\text{Au}/[\text{Co/Pd}]_2$ PSV nanostructures as a function of Au spacer layer thickness and temperature.
- (d) Developing novel processes for fabricating high quality bi-component 2-D MCs and mapping their static and dynamic behaviors.

1.4 Organization of Thesis

The thesis is organized as follows: in chapter 1, the background and motivation for this research work are discussed. In chapter 2, a theoretical background for a better understanding of the experimental work is described. This is followed by chapter 3 where the fabrication process and various characterization techniques utilized in this thesis are introduced. In chapter 4, the magnetization reversal of circular Co/Pd nanomagnets including nanodots,

Chapter I Introduction

antidots and nanorings is investigated with emphasis on coupled Co/Pd dots which shows potential for magnetic logic applications. In chapter 5, the magnetization reversal and MR behaviors of Co/Pd NWs and [Co/Pd]₄/Au(*t*_{Au})/[Co/Pd]₂ PSV NWs are systematically investigated as a function of *t*_{Au} and temperature *T*. In chapter 6, the static and dynamic properties of 2-D MCs including continuous Ni₈₀Fe₂₀ films on top of arrays of Co/Pd dots (or Ni₈₀Fe₂₀ dots) and Fe filled Ni₈₀Fe₂₀ antidot nanostructures are investigated. Finally in chapter 7, a summary of the main points of this thesis together with suggestions for future work is presented.

Chapter 2

Theoretical Background

2.1 Introduction

This chapter provides the basic theoretical concepts and reviews of earlier work relevant to the main research topics of this thesis. § 2.2 discusses the origin of perpendicular magnetic anisotropy and magnetization reversal mechanism of Co/X (=Pd, Pt, Ni...) multilayer systems. § 2.3 introduces the typical spin dependent transport phenomena associated with the Co/Pd multilayer nanostructures. This is followed by § 2.4 which provides a brief overview of various interlayer coupling mechanisms for a typical multilayer system. Finally, § 2.5 describes the basic concepts of spin dynamics with emphasis on ferromagnetic resonance (FMR) and magnonic crystals (MCs).

2.2 Co/X (=Pd, Pt, Ni...) Multilayers

2.2.1 Origin of Perpendicular Magnetic Anisotropy

In Co/X (=Pd, Pt, Ni...) multilayers, the magnetic anisotropy can shift from in-plane to out-of-plane as the thickness of Co layer reduces below a critical value. The determination of anisotropy axis depends on the combination of the anisotropy from the ferromagnetic Co layers and those contributions from induced magnetization in the nonmagnetic X (=Pd, Pt, Ni...) layers^[62]. The total anisotropy energy K_u is defined as the difference in between the perpendicular and parallel magnetization energy density as given by^[62-65]:

$$K_u = \frac{2K_s}{t_{Co}} + K_v - 2\pi M_0^2 \quad (2.1)$$

where K_s is the interface anisotropy energy at each of the two interfaces in one bi-layer period which also includes the shape and volume anisotropy contributions from the induced magnetization in the X layers^[66, 67]. K_v is the volume anisotropy of the Co layers which includes magnetoelastic contributions arising from lattice mismatch between the Co and X layers^[68, 69]. $-2\pi M_0^2$ and t_{Co} represent the shape anisotropy and thickness of the Co layers respectively. Schematics of the various anisotropy energy terms contributing to K_u are shown in Fig. 2.1. When K_u is positive, the easy axis of magnetization is normal to the film surface, whereas for negative K_u , the magnetic easy axis is in-plane. Experimentally, K_u is obtained from the estimated areas between the perpendicular and parallel magnetization curves, approximated by the horizontal bisectors of the hysteresis loops^[62].

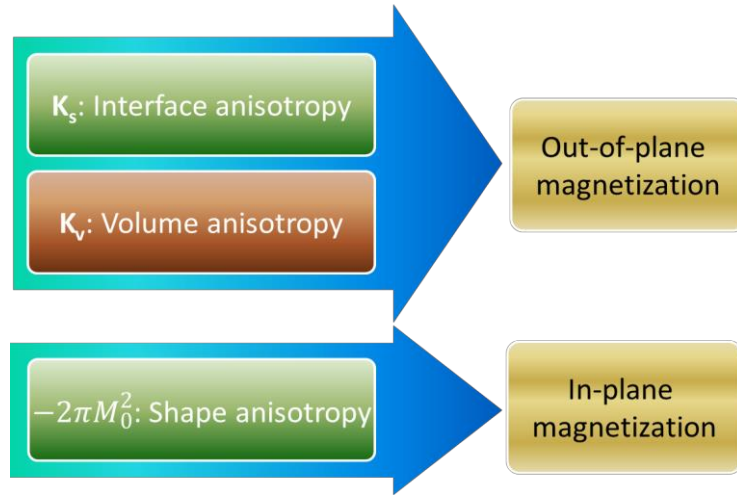


Fig. 2.1 Schematics of various energy terms contributing to K_u in Co/X multilayers.

Positive K_s and K_v favor out-of-plane magnetization while the negative shape anisotropy $-2\pi M_s^2$ tends to drag the magnetization to in-plane. The interface anisotropy K_s , also known as Néel anisotropy^[68, 70], is the main source of perpendicular magnetic anisotropy in the Co/X multilayer structures, which arises from $d-d$ orbital hybridization of the Co and X layers^[67]. Interface anisotropy not only occurs in Co/Pd multilayers, but also exists in

other metallic multilayer structures, i.e. Co/X (=Pt, Ni, Au, Ag, Cu, Ir...)^[66, 67, 71-76]. Compared with Co/Au (or Ag, Cu, Ir), Co/Pd (or Pt, Ni) multilayers show much larger PMA due to the stronger *d-d* orbital hybridization^[73]. The PMA is markedly dependent on the Co layer thickness t_{Co} . For Co/X (=Pd, Pt, Ni...) multilayers with large t_{Co} , shape anisotropy dominates K_u . However, as the Co layer becomes thinner than a certain critical value, large Co/X interface anisotropy dominates the effective anisotropy, leading to a transition of magnetic easy axis from in-plane to out-of-plane.

2.2.2 Co/Pd Multilayer Systems

The magnetic properties of Co/Pd multilayers are largely dependent on the individual layer thickness of both Co and Pd^[77, 78]. The Co layer should be thin enough (≤ 8 Å) to maintain the perpendicular anisotropy^[77] while the Pd layer should be thick enough (≥ 5 Å) to achieve a good squareness^[79]. In this work, we will use a multilayer film structure of [Co(0.5 nm)/Pd(3 nm)]_n, which gives both large perpendicular anisotropy and good squareness of M-H loops. Film continuity is expected to be achieved at these thicknesses for both the Co layer and the Pd layer^[80]. The saturation magnetization M_s of the Co/Pd multilayers is significantly dependent on the individual layer thickness of the Co and Pd given by^[67]:

$$M_s t_{total} = M_s^{Co} t_{Co} + M_s^{Pd} t_{Pd} \quad (2.2)$$

where t_{total} , M_s^{Co} , t_{Co} , M_s^{Pd} , t_{Pd} represent the total thickness of the Co/Pd bi-layer, the saturation magnetization and individual layer thickness for Co and Pd respectively. In the Co/Pd multilayers, the Pd layer is magnetically polarized in such a way that the induced polarization reaches maximum at the Co/Pd interface and becomes weaker as the Pd atoms are far away from the interface^[78]. Therefore, M_s^{Pd} is an effective saturation magnetization for the Pd layers. Typical value of M_s^{Pd} is 148 kA/m^[78] for a [Co(0.2 nm)/Pd(1nm)]₂₀

multilayer.

The perpendicular anisotropy K_u of $[\text{Co/Pd}]_n$ multilayers is a function of the bi-layer repeat n , showing a maximum at a certain critical value ($\sim n=20$). Below this critical value, the perpendicular anisotropy shows a monotonic increase with n . However, as n goes beyond this critical value, the anisotropy energy reduces due to the loss of conformality of the interface roughness in the Co/Pd multilayers^[81, 82]. For $[\text{Co}(0.5 \text{ nm})/\text{Pd}(3 \text{ nm})]_n$ multilayers, the K_u normally ranges from $\sim 0.3 \times 10^6 \text{ erg/cm}^3$ to $\sim 3.5 \times 10^6 \text{ erg/cm}^3$ ^[81].

Magnetization reversal of Co/Pd multilayer structures depends on the competition of the reverse domain nucleation field H_n and the domain wall depinning field H_p ^[83]. For Co/Pd multilayered films, H_n is usually smaller than H_p and the magnetization reversal occurs via rapid domain wall motion from a few very low anisotropy nucleation sites. However, when the Co/Pd multilayers are patterned into micrometer or sub-micrometer sized structures, the nucleation sites of the films are sampled and the probability to find such nucleation sites is reduced due to decreased film area of the magnetic structures^[26]. Therefore, H_n becomes higher than H_p . No magnetization reversal can occur until the applied field reaches H_n because there is no domain wall. Once the reversed domain is nucleated, the domain wall propagates rapidly until the whole nanomagnet is reversed. The magnetic switching of the large Co/Pd nanostructures (diameter $d \geq 200 \text{ nm}$) is thus governed by the nucleation event and the observed switching behavior is that of the small nucleation site^[25, 26], as illustrated in Fig. 2.2(a). As the size of Co/Pd nanostructures is shrunk down ($d < 200 \text{ nm}$)^[26, 83], single domain ground state is favored due to the high exchange coupling in the Co/Pd multilayers. Magnetization reversal in such small Co/Pd nanostructures is therefore mediated by coherent spin rotation, as illustrated in Fig. 2.2(b).

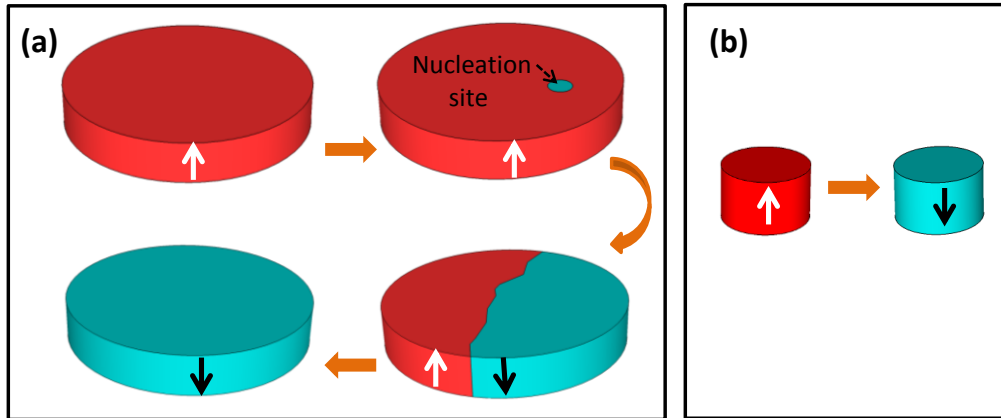


Fig. 2.2 Schematics of magnetization reversal for (a) large Co/Pd dots; and (b) single domain Co/Pd dots.

2.3 Spin Dependent Transport Phenomenon

2.3.1 Anisotropic Magnetoresistance

The anisotropic magnetoresistance (AMR) effect was first discovered by William Thomson^[84] in 1857, when it was found that the resistance of a ferromagnetic material is strongly dependent on the angle between the current and the magnetization direction. The AMR effect is attributed to the spin-orbit coupling and can be described by a simple model as illustrated in Fig. 2.3.

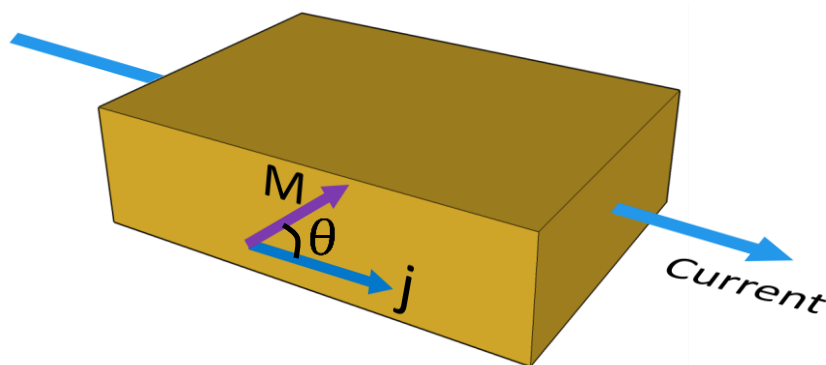


Fig. 2.3 Schematics of AMR effect in a ferromagnetic metal.

When a constant current with density \vec{j} is passed through a uniform ferromagnetic material, the electric field \vec{E} is given by^[85]:

$$\vec{E} = \vec{\rho} \cdot \vec{j} = \rho_{\perp} \vec{j} + (\rho_{\parallel} - \rho_{\perp}) \frac{\vec{j} \cdot \vec{M}}{M^2} \vec{M} + \rho_H \frac{\vec{M} \times \vec{j}}{M} \quad (2.3)$$

where \vec{M} is the magnetization of the sample, ρ_{\perp} , ρ_{\parallel} and ρ_H represent the resistivities perpendicular, parallel to \vec{M} and the Hall resistivity respectively. From Eq. (2.3), it is evident that the total resistance is dependent on the angle (θ) of current density with respect to the magnetization. The AMR resistivity can be deduced from Eq. (2.3) as^[10]:

$$\begin{aligned} \rho_{AMR} &= \frac{\vec{E} \cdot \vec{j}}{j^2} = \frac{(\vec{E}_{\perp} + \vec{E}_{\parallel}) \cdot \vec{j}}{j^2} = \frac{(E_{\perp} \sin \theta + E_{\parallel} \cos \theta) j}{j^2} \\ &= \frac{(\rho_{\perp} j \sin \theta) \sin \theta + (\rho_{\parallel} j \cos \theta) \cos \theta}{j} = \rho_{\perp} \sin^2 \theta + \rho_{\parallel} \cos^2 \theta \quad (2.4) \\ &= \rho_{\perp} + (\rho_{\parallel} - \rho_{\perp}) \cos^2 \theta = \rho_{\perp} + \Delta \rho \cos^2 \theta \end{aligned}$$

Clearly, the resistivity of the ferromagnet reaches a maximum when the magnetization and the current are either parallel ($\theta=0^\circ$) or antiparallel ($\theta=180^\circ$), and reaches a minimum when they are perpendicular with each other ($\theta=90^\circ$). In multi-domain structures, the AMR depends on the relative orientation of the magnetization in each domain with respect to the current density distribution as a whole.

2.3.2 Giant Magnetoresistance

The giant magnetoresistance (GMR) effect was first discovered independently in 1988 by A.Fert in the (Fe/Cr)₆₀ multilayer^[86] and P. Grünberg in the Fe/Cr/Fe tri-layer^[87]. This effect presents a resistance variation much larger than the normal MR caused by Lorentz forces or AMR caused by spin orbit coupling, thus was termed as giant MR. GMR effects have also been observed in PSV structures consisted of two ferromagnetic (FM) layers separated by a nonmagnetic (NM) spacer layer^[39, 44]. When the two FM layers are in parallel alignment, conduction electrons are able to move through both layers with minimal scattering and the overall resistance of the PSV structure

is low. By changing the relative magnetization of the FM layers from parallel to antiparallel, a large increase in resistance can be observed.

The GMR effect can be understood using the two-current model based on the fact that electron spin is conserved over a distance up to tens of nanometers, which is normally larger than the typical thickness of a FM layer. The essential mechanism is that electrons with spin parallel and antiparallel to the magnetization of the ferromagnetic layers are scattered at different rates when they enter the FM layers. Electrons with spin parallel to the magnetization are scattered weakly while electrons with spin antiparallel to the magnetization direction are scattered strongly. The current in the tri-layer flows through two channels, corresponding to electrons with spin up (\uparrow) and spin down (\downarrow) respectively. The two channels experience different scattering rate in the two FM layers which can be equivalent to two parallel resistors^[88, 89], as illustrated in Fig. 2.4. Equation (2.5) and (2.6) show the resistivity formulae for the parallel (ρ_P) and antiparallel (ρ_{AP}) configurations:

$$\rho_P = \frac{2\rho_{\uparrow}\rho_{\downarrow}}{\rho_{\uparrow} + \rho_{\downarrow}} \quad (2.5)$$

$$\rho_{AP} = \frac{\rho_{\uparrow} + \rho_{\downarrow}}{2} \quad (2.6)$$

When the two FM layers are in parallel state, the spin \uparrow electrons will experience low scattering while the spin \downarrow electrons will experience large scattering. Since the spin \uparrow and spin \downarrow channels are connected in parallel, the total resistivity of the tri-layer will be limited by the low resistance of the spin \uparrow channel (Eq.(2.5)). The total resistivity is low. On the other hand, the spin \uparrow electrons in the antiparallel configuration are weakly scattered in the first FM layer but strongly scattered in the second layer, while the spin \downarrow electrons are strongly scattered in the first FM layer and weakly scattered in the second layer. It is then easy to deduce that the total resistivity in antiparallel configuration becomes higher than the parallel configuration (Eq.(2.6)).

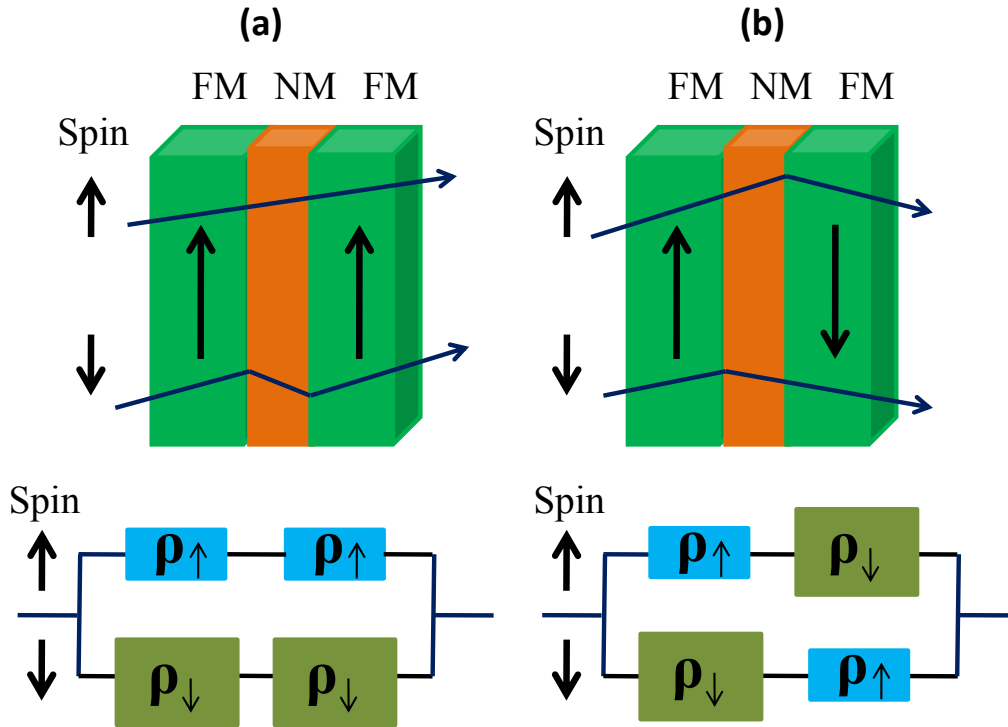


Fig. 2.4 Schematics of two-current model for GMR effect in (a) parallel; and (b) antiparallel spin configurations.

2.3.3 Magnon Magnetoresistance

A magnon is a quasi-particle of spin waves in magnetically ordered materials. It can be considered as a quantized spin wave from the quantum mechanics point of view. The concept of magnon was first introduced by Felix Bloch^[90] in 1930 in order to explain the reduction of the spontaneous magnetization in a ferromagnet. At absolute zero temperature, a ferromagnet reaches the state of lowest energy, in which all of the atomic spins (and hence magnetic moments) point in the same direction. As the temperature increases, more and more spins deviate randomly from the common direction, thus increasing the internal energy and reducing the net magnetization.

Magnons usually give rise to a linear non-saturating decrease of MR via magnon-electron scattering at high field, which is the so-called magnon magnetoresistance (MMR) effect. Shown in Fig. 2.5 is a typical MMR curve^[91]. When we consider the magnon as a particle, the non-saturating

resistance value at high field can be explained by the reduction of the electron-magnon scattering. In other words, by considering the magnon as a travelling spin wave, we can view this behavior as a result of spin-wave damping at high fields^[92]. The MMR effect has been previously observed in 3d ferromagnets (Fe, Co, Ni) with high applied field up to 40 tesla^[92, 93], FePt films^[94], patterned FePt nanowires^[91] with strong magnetocrystalline anisotropy and narrow Ni₈₄Fe₁₆ nanowires with large shape anisotropy^[37, 95].

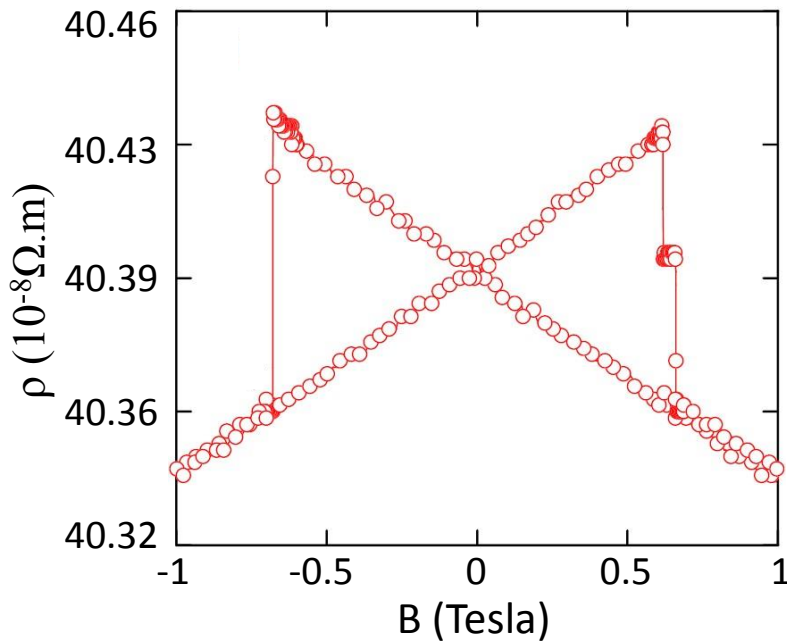


Fig. 2.5 Typical MR curve for MMR effect^[91].

The MMR contribution to magnetoresistance is given as follows^[92, 94]:

$$\Delta\rho(T, B) \approx \rho(T, B) - \rho(T, 0) \propto \frac{B+B_A}{D(T)^2} T \ln\left(\frac{g\mu_B(B+B_A)}{kT}\right) \quad (2.7)$$

where B , B_A , D and T represent the external field, anisotropy field, exchange stiffness constant and temperature respectively. Clearly, the MMR effect is significantly dependent on B , B_A and T . High-field resistivity driven by the magnon-electron scattering roughly follows a $(B+B_A)\ln(B+B_A)$ dependence. $\Delta\rho$ is quasi-linear with B when B is extremely large. In the case of 3d ferromagnets, the linearity of resistance with B above magnetic saturation

comes from the large amplitude of the external fields ($B=10-40$ tesla). In materials with strong magnetocrystalline anisotropy (FePt) and narrow $\text{Ni}_{84}\text{Fe}_{16}$ nanowires with large shape anisotropy, the role of the large applied field is replaced by the anisotropy field ($B_A \gg B$). Therefore, even for low fields, there is a linear dependence of resistance with field. The MMR effect is also predicted to be a useful tool to detect magnetization reversal and domain wall motion in patterned nanowires based on the fact that the MR is proportional to the magnetization of the nanowires^[37, 91, 94].

2.4 Coupling Mechanism in Multilayer Films

In PSV structures consisting of two ferromagnetic (FM) layers separated by a nonmagnetic (NM) spacer layer, interlayer coupling between the two FM layers determines the magnetic switching behaviors of the PSVs. The interlayer coupling have four different origins: direct ferromagnetic coupling through pinholes in the thin metallic spacer^[96], indirect exchange coupling through Ruderman-Kittel-Kasuya-Yosida (RKKY) interactions^[97], orange peel (Néel) coupling due to interfacial roughness^[51], and magnetostatic coupling via the stray fields^[98, 99].

2.4.1 Pinhole Coupling

Pinhole coupling is a direct exchange coupling which occurs when the NM spacer layer is too thin to form a continuous film. The discontinuity of the spacer layer results in a direct contact between the two FM layers, leading to a direct ferromagnetic coupling between the two layers^[96, 100]. For spacer layer thickness below a critical value (~ 1 nm), the two FM layers may present a collective magnetic switching with a coercive field in between the two respective FM layers. Shown in Fig. 2.6 is a schematic illustration of magnetization reversal for two direct exchange coupled FM layers. The

ferromagnetic coupling strength spatially distributes in the soft layer in such a way that it is the strongest at the interface and becomes weaker as it is away from the interface. Therefore, the two FM layers perform like an exchange spring, in which magnetization reversal in upper surface of the soft FM layer drags the hard FM layer to form a collective magnetic switching.

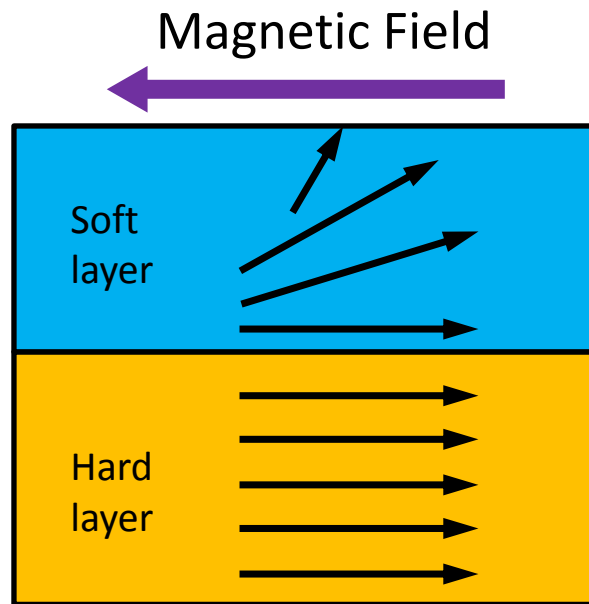


Fig. 2.6 Configuration of magnetization for direct exchange coupled FM layers.

2.4.2 Ruderman-Kittel-Kasuya-Yosida (RKKY) Coupling

The RKKY coupling is an indirect exchange interaction between two localized spins via a hyperfine interaction within a sea of conduction electrons^[101]. For PSVs, magnetic spins in the two FM layers interact with each other through the NM metallic spacer layer. Both the interaction strength and the interaction sign oscillate with the distance of the two localized spins, leading to an alternating FM and antiferromagnetic (AFM) coupling depending on the thickness of NM spacer layer^[41, 42, 102], as illustrated in Fig. 2.7. RKKY coupling usually occurs in multilayers with good film quality and the coupling strength is only dominant in the range below a few nanometers.

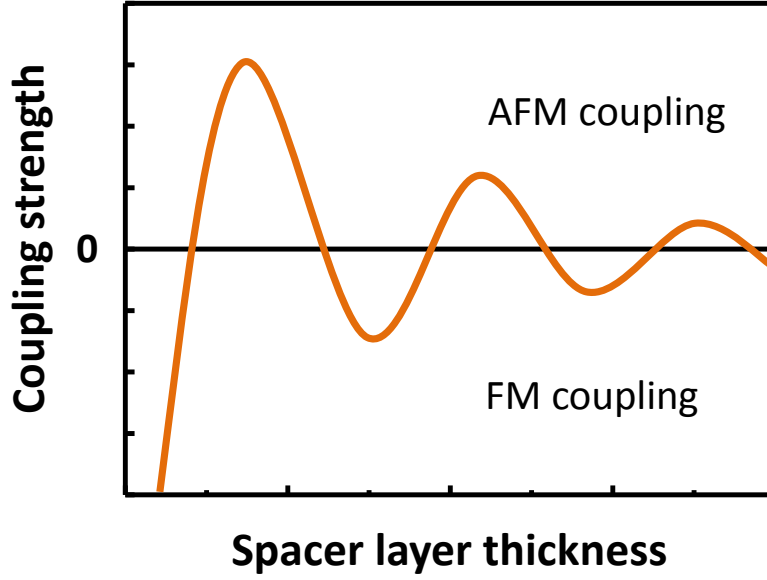


Fig. 2.7 Schematics of RKKY coupling strength as a function of spacer layer thickness.

2.4.3 Néel Coupling

The Néel coupling, also known as the “orange peel” coupling, is an indirect exchange coupling resulted from interface roughness of neighboring FM layers^[103]. This consequently gives rise to magnetic poles along the film surface, leading to the formation of fringing fields which favor parallel alignment of the magnetizations of the two FM layers, as illustrated in Fig. 2.8. By assuming the NM layer with thickness t following a two-dimensional sinusoidal behavior with an amplitude h and a wavelength w , the Néel coupling energy density in the limit of rigid in-plane magnetization is given as^[101]:

$$J = \frac{\pi^2 h^2}{\sqrt{2}w} (\mu_0 M_1 M_2) e^{-\frac{2\sqrt{2}\pi t}{w}} \quad (2.8)$$

where M_1 and M_2 represent the magnetization of two neighboring FM layers. It is clear from eq.(2.8) that the Néel coupling strength decays exponentially with increase in spacer layer thickness.

Néel’s theory can also be extended to the case of multilayers with perpendicular anisotropy. It has been shown that the magnetostatic interaction

between two perpendicularly magnetized layers in the presence of a interfacial roughness can favor either a parallel or an antiparallel alignment of magnetization in the two FM layers^[51]. The sign of the coupling depends on the interplay among magnetostatic, exchange and anisotropy energy terms. For low values of anisotropy constant, FM coupling is favored. However, when the anisotropy is larger than a certain critical value, AFM type of coupling is favored.

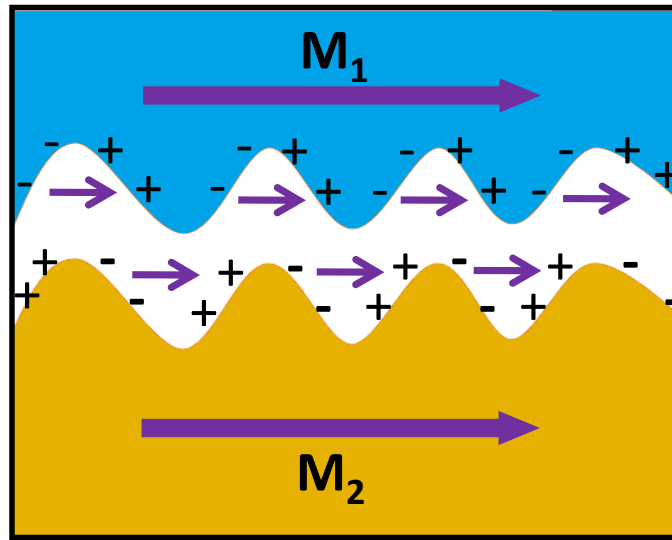


Fig. 2.8 Schematics of the layer geometry giving rise to Néel coupling.

2.4.4 Interlayer Magnetostatic Coupling

The interlayer magnetostatic coupling is a long-range magnetostatic interaction arising from stray fields at the edge of two FM layers. In multilayer systems with in-plane anisotropy, the coupling tends to form an antiparallel alignment of magnetization to reduce the magnetostatic energy of the system. However, for multilayers with perpendicular magnetic anisotropy, parallel alignment of magnetization is energetically more favorable than the antiparallel state^[104], as illustrated in Fig. 2.9.

In magnetic multilayer films with multi-domain configurations^[99, 105] magnetostatic interactions are notably prominent. Non-uniform magnetization

distribution in one FM layer induces local stray fields around the domain walls (DWs), which directly affect magnetic switching of the other FM layer and hence the behavior of the PSV films. The stray fields show a fast decay with increase in distance from the DW border and film surface^[98, 106, 107]. It has been reported that local stray fields from DWs are efficient to induce domain replication from a hard FM layer to a neighboring soft FM layer in ferromagnetically coupled Co/Pd^[108] and Co/Pt^[99] based PSV films. Interlayer magnetostatic coupling can also be significantly enhanced in patterned nanostructures due to the accumulation of magnetic poles at the pattern edge [52, 109, 110]

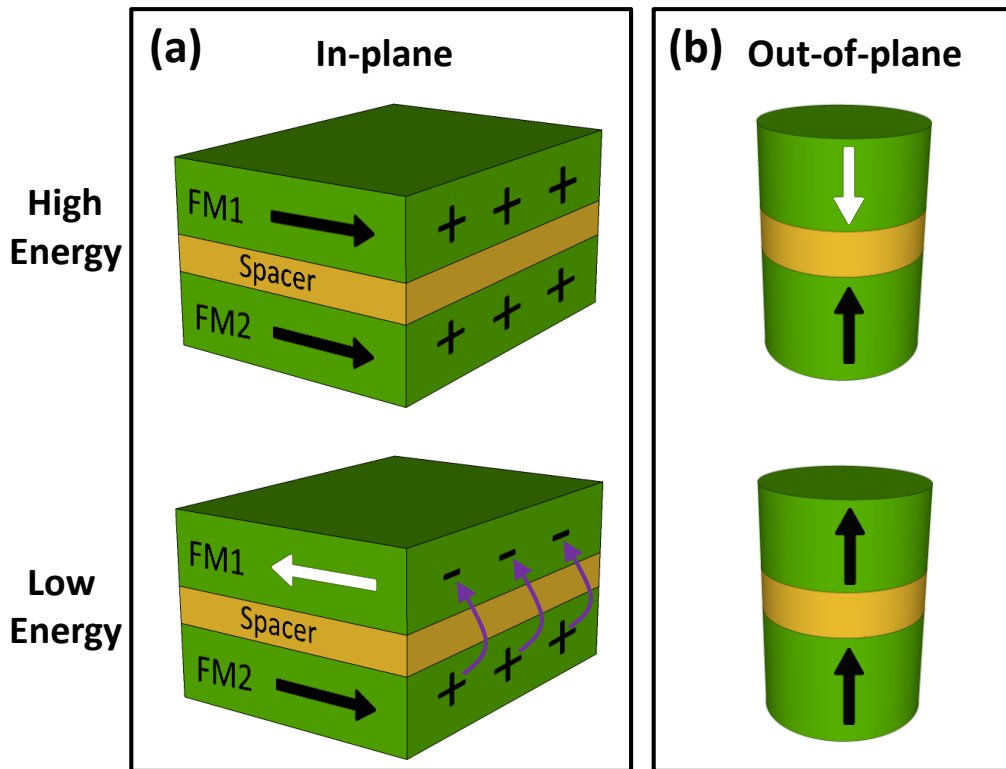


Fig. 2.9 Magnetostatic energy levels for PSVs with (a) in-plane anisotropy; and (b) out-of-plane anisotropy.

2.5 Magnetization Dynamics

Compared with static magnetic phenomena, the crucial difference of magnetization dynamics is the time scale on which the magnetic system is

disturbed by an external stimulus and its response. When applying quasi static fields to a magnetic system, the magnetization appears to be always in equilibrium since the dynamic process happens on the nanosecond timescale or faster. However, when an alternating magnetic field is applied with a frequency equal to the resonance frequency of the system, the magnetization configuration is resonantly disturbed from its equilibrium position. In this section, the basic underlying physical concepts of the magnetization dynamics and the commonly used characterizing method will be introduced.

2.5.1 Fundamental of Magnetization Dynamics

By applying an external magnetic field H_0 to a single magnetic spin, the moment will undergo an effective magnetic field H_{eff} consisting of both H_0 and local exchange, anisotropy and dipolar fields. Magnetization of the spin therefore tends to align parallel to H_{eff} for energy minimization, leading to a precession of magnetization at an angle of $\varphi \neq 0$ relative to H_{eff} , as illustrated in Fig. 2.10(a). Due to a damping term, the amplitude of the spin precession will decrease until reaching an equilibrium position. The dynamic response of a magnetic moment can thus be described using the Landau-Lifshitz-Gilbert (LLG) equation given as follows^[111, 112]:

$$\frac{dM}{dt} = \underbrace{-\gamma\mu_0 M \times H_{eff}}_{\text{precessional term}} + \underbrace{\frac{\alpha}{M_s} \left(M \times \frac{dM}{dt} \right)}_{\text{damping term}} \quad (2.9)$$

where γ , M and α represent the gyromagnetic ratio, magnetization of the spin and dimensionless damping parameter respectively. The first term on the right hand side of Eq. (2.9) is the precessional term while the second part represents the damping term. As a result of the damping term, the motion of the magnetization follows a helical trajectory as illustrated in Fig. 2.10(b).

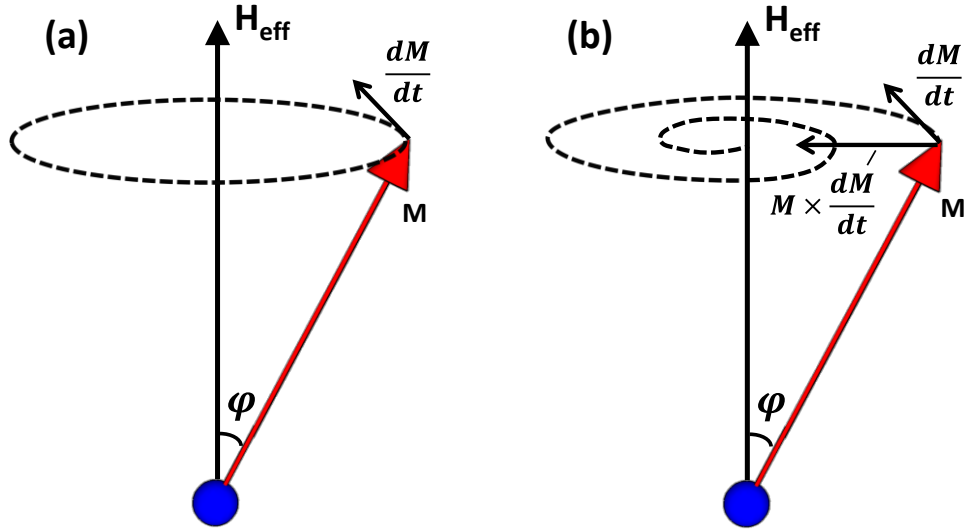


Fig. 2.10 Schematics of dynamic response of a magnetic spin (a) without; and (b) with the damping term.

2.5.2 Ferromagnetic Resonance

One of the most established techniques to study and characterize the dynamic responses of a magnetic system is ferromagnetic resonance (FMR) spectroscopy. The FMR measurement is based on the fact that strong energy absorption occurs when the frequency of an applied RF microwave is equal to the precessional frequency of a magnetic spin. The FMR absorption was first reported by Griffiths^[113] in 1946 while a complete theory was first given by C. Kittel^[114] in 1948. According to Kittel's theory, the resonance condition is expected to depend on the shape of the ferromagnetic specimen, and in the case of a single crystal on the orientation of the crystal. By applying an external magnetic field H_x along X-axis direction, the resonance frequency of a polycrystalline specimen is given by:

$$\omega_0 = \gamma \{ [H_x + (N_z - N_x)4\pi M_x] \times [H_x + (N_y - N_x)4\pi M_x] \}^{1/2} \quad (2.10)$$

where N_x , N_y , and N_z are the demagnetizing factors of the sample along the X, Y direction and the thickness of the specimen respectively, γ is the gyromagnetic ratio of the material (17.6 MHz/Oe), and $4\pi M_x$ is the magnetization of the sample along H_x .

2.5.3 Magnonic Crystals

Magnonic crystals (MCs), a magnetic analog of photonic crystals, are artificial magnetic nanostructures with periodic lateral variations in their magnetic properties which can be used to manipulate magnetostatic spin wave propagation^[8]. Depending on the lateral confinement, artificial MCs can be divided into one-dimensional (1-D), two-dimensional (2-D) and three-dimensional (3-D) MCs.

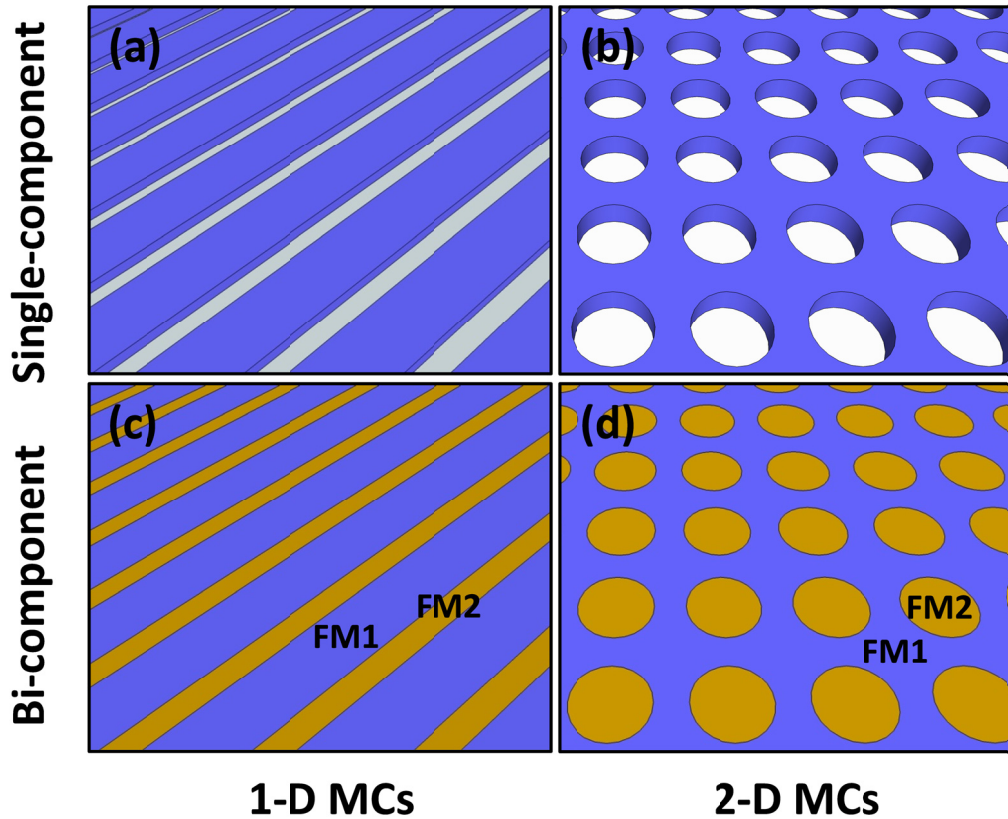


Fig. 2.11 Schematics of typical single-component 1-D (a); 2-D (b); and bi-component 1-D (c); 2-D (d) MCs.

1-D MCs are wirelike structures consisting of arrays of nanowires separated by an air gap^[115] (Fig. 2.11(a)), whereas periodic arrays of ferromagnetic antidot^[56] (Fig. 2.11(b)) represent the typical 2-D MCs. Besides the above mentioned single-component MCs, bi-component MCs consisted of

arrays of one FM material in the matrix of another FM material (Fig. 2.11(c & d)) have also attracted much research interest^[58, 60, 61] in recent years due to the additional degree of freedom in engineering the spin wave properties. Complicated magnetic structures with periodic lateral variations along three coordinate axes can be considered as 3-D MCs. The band spectrum of MCs which consists of allowed states (magnonic bands) and forbidden states (magnonic gaps) can be tuned by magnetic fields and geometrical parameters^[61, 116].

2.6 Summary

This chapter introduces a basic theoretical framework and literature review to better understand the experimental observations which will be presented in subsequent chapters. First, the origin of perpendicular magnetic anisotropy and reversal mechanism of Co/Pd multilayers were discussed. The various spin dependent transport phenomena related with the main research topics were then introduced. This was followed by an overview of the different interlayer coupling mechanisms which may exist in typical Co/Pd multilayer based systems. Finally, the basic concepts of spin dynamics with emphasis on FMR were presented.

Chapter 3

Experimental Techniques

3.1 Introduction

This chapter provides a detailed description of the fabrication and characterization techniques for the study of magnetic nanostructures presented in this thesis. The nanostructures were fabricated using deep ultraviolet lithography followed by ferromagnetic material deposition and the lift-off process. Details of the processing steps are introduced in § 3.2. This is followed in § 3.3 by a discussion of the various techniques employed for the structural analysis and mapping of magnetic properties of the fabricated nanostructures.

3.2 Fabrication Techniques

In this thesis, large area arrays of nanostructures were patterned using KrF deep ultraviolet (DUV) lithography at 248 nm exposure wavelength followed by the lift-off process. Shown in Fig. 3.1 is a typical fabrication process flow for the fabrication of nanostructures investigated in this thesis which consist of nanodots, nanorings and nanowires arrays. The fabrication process can be divided into five steps, namely, (i) bottom anti-reflection coating (BARC) and photoresist coating; (ii) DUV lithography, development and BARC etch; (iii) ferromagnetic material deposition; (iv) lift-off; and (v) BARC removal.

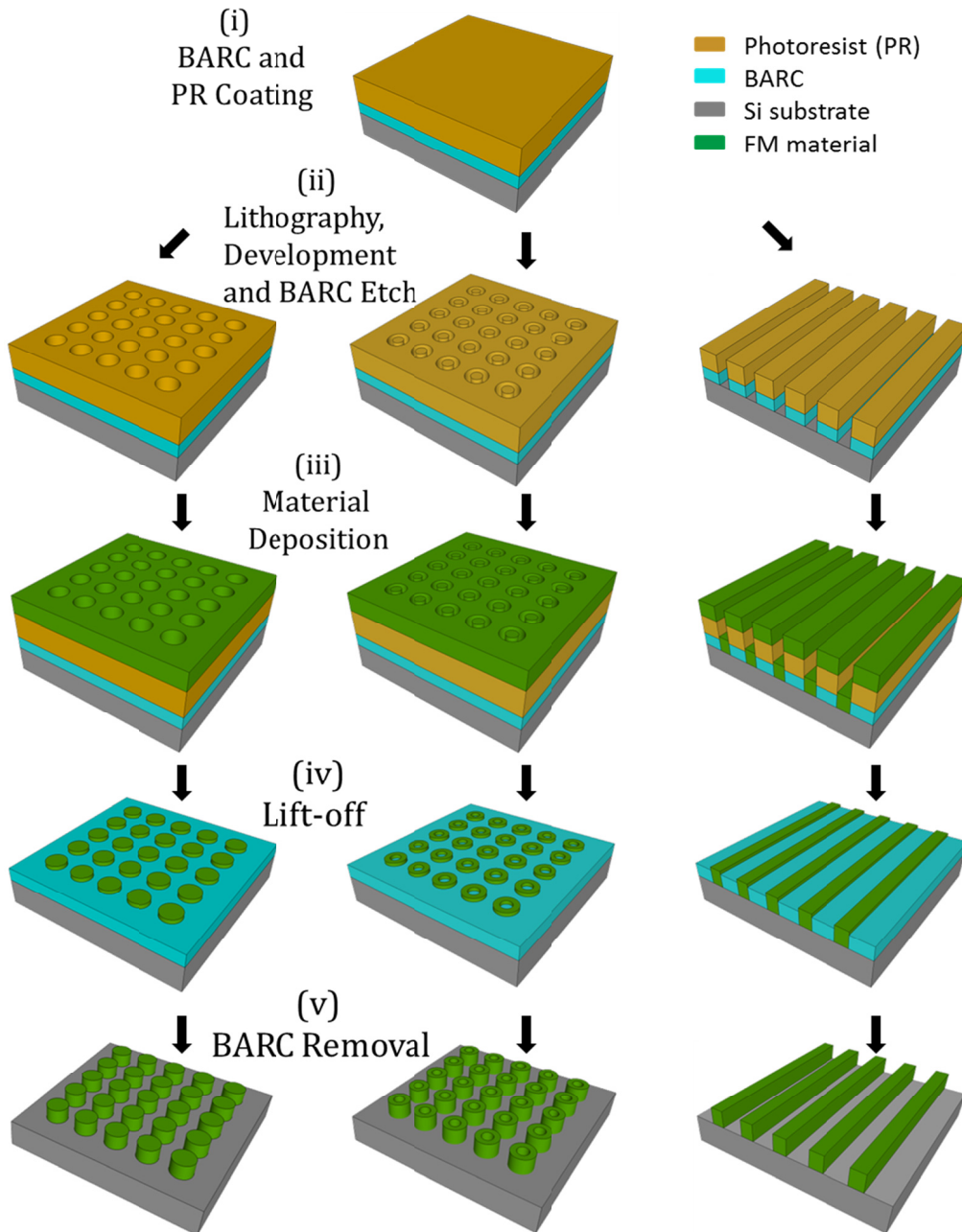


Fig. 3.1 Schematics of typical fabrication process flow for the nanostructure arrays.

3.2.1 Photolithography

3.2.1.1 KrF Deep Ultraviolet (DUV) Lithography

The minimum feature size that can be patterned in an optical lithography system is given by:

$$R = k_1 \cdot \frac{\lambda}{NA} \quad (3.1)$$

where k_1 is the process constant which is affected by numerous parameters, resist contrast, etch quality and photomask enhancements. λ is the wavelength of the light source used in the lithography. To improve the resolution, there is a need for light with shorter wavelength, thus the shift toward the DUV regime. NA is the numerical aperture which needs to be as large as possible and is constrained by the depth of focus. NA can be increased by increasing the refraction index of the focus lens. It is a fixed parameter for a particular lithographic system.

In this work, the improvement of lithography resolution was attained by using a KrF DUV source with 248 nm exposure wavelength, together with a phase-shift mask (PSM) which allows for the fabrication of large area arrays of nanostructures with good edge definition and uniformity. The PSM helps to bring down the k_1 factor. The PSM was designed to sharpen the resist profile and to enable the patterning of smaller features, as opposed to binary masks. In a binary mask, constructive interference of light due to diffraction may occur, resulting in an unexpected elevated exposure dose in the unintended region of photoresist which consequently enlarges the feature of the patterns, as illustrated in Fig. 3.2(a).

In order to resolve this problem, an alternating phase shift mask (ALT PSM) was used. The ALT PSM consisted of alternating areas of Cr and 180°-shifted quartz to pattern features on the wafer as illustrated in Fig. 3.2(b). The Cr region on the mask was bordered on one side by quartz of phase 0° and on the other side by quartz of phase 180°. Destructive interference of light therefore occurred in the Cr region, leading to the vanishing of the electric field. The intensity of DUV light, which is proportional to the square of the electric field, thus goes through zero, enabling very sharp edges to be patterned on the photoresist. By exploiting this technique, printing of lines smaller than the wavelength of light is possible. The DUV lithography technique used in this thesis was developed by N. Singh^[117].

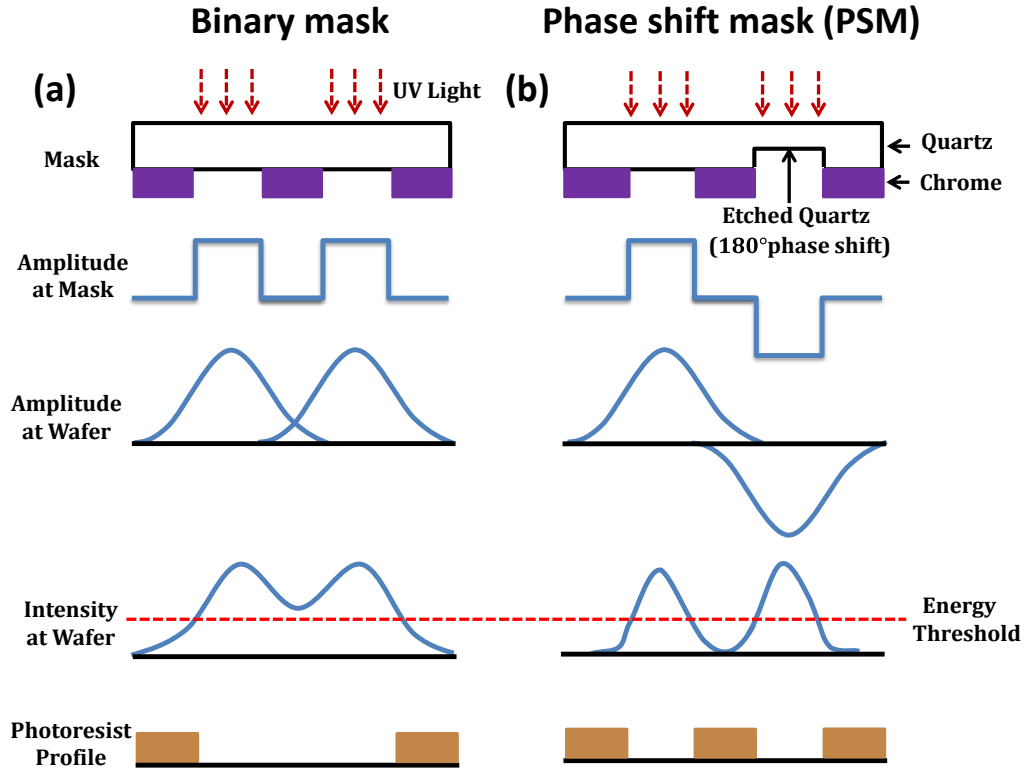


Fig. 3.2 Schematics of DUV lithography process using (a) Binary mask; and (b) Phase shift mask.

In our lithography process, the Si substrate was first coated with a 60 nm thick BARC layer, which was used to suppress reflectivity of exposure energy from the substrate in order to improve the critical dimensionality^[3]. This was followed by coating of a 280 nm thick positive DUV resist, UV210 from Shipley. Nikon lithographic scanner S203 with KrF excimer laser radiation at a wavelength of 248 nm was used for exposing the resist. The NA was kept at the maximum available of 0.68 to achieve the highest resolution possible. In the KrF photolithography process, two consecutive exposures were conducted to enhance pattern uniformity using opposite foci^[3, 118]. The double exposure with mask shift technique also enabled us to fabricate sub-resolution structure from wide patterns to reduce the feature size^[3, 117]. After the exposure and development, the BARC layer was etched at a rate of 7Å/sec in O₂ (5 sccm) plasma heavily diluted with Argon (45 sccm), leaving arrays of patterned photoresist on the Si substrate.

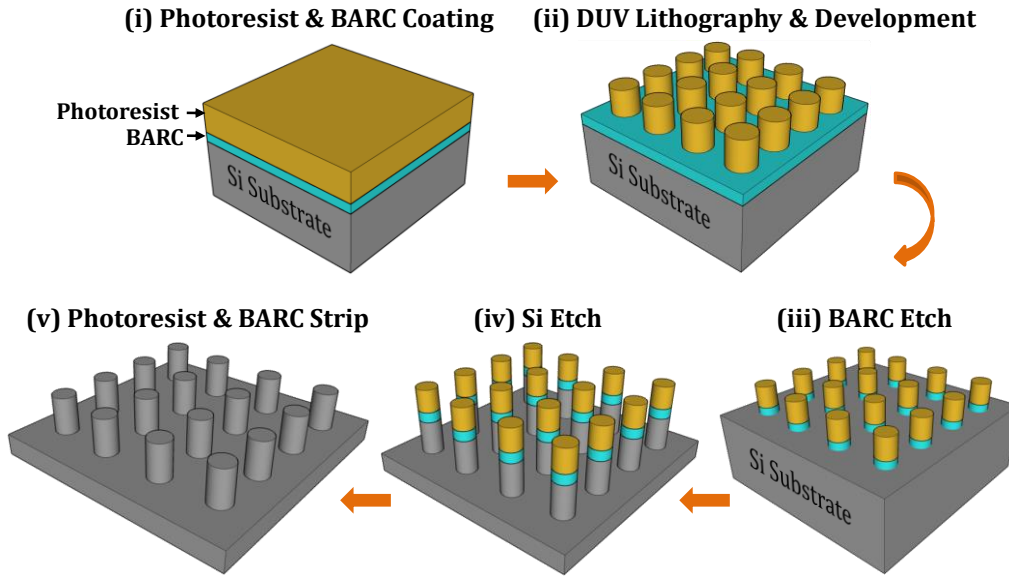


Fig. 3.3 Schematics of the fabrication process flow for Si nanopillars^[117].

The DUV lithography technique also allowed for the fabrication of large area ($4\text{ mm} \times 4\text{ mm}$) pre-patterned Si nanopillars^[117], as illustrated in Fig. 3.3. After DUV exposure, development and BARC layer etching, arrays of resist pillar structures were formed. The pattern was then transferred into silicon using a mixture of C_4F_8 (10 sccm) and SF_6 (40 sccm) gases with an etch rate of $22\text{ \AA}/\text{sec}$. The remaining photoresist and BARC materials on top of pillars were removed in a mixture of O_2 (3000 sccm) and forming gas (250 sccm) plasma at $250\text{ }^\circ\text{C}$. At the same time, amount of CF_4 (30 sccm) was added into this mixture to trim the pillars from the sides.

3.2.1.2 Ultraviolet (UV) Lithography

For magneto-transport and ferromagnetic resonance measurements, electrical contacts were fabricated on top of the ferromagnetic nanostructures using UV lithography followed by the lift-off process. Prior to lithography, the substrates were first cleaned thoroughly to remove any contaminations which may affect the quality of lithography and deposition. A positive photoresist PFI was then coated on the substrates at $\sim 6000\text{ rpm}$ in a spin coater, which gives a thickness of $\sim 2\text{ }\mu\text{m}$. After spin coating, the samples were

oven baked at 90° C for 20 mins to remove any remaining solvent and to improve the adhesion between the photoresist and the substrate. The exposure was carried out using a Karl Suss MA6 system with a UV source of wavelength 365 nm from a mercury (Hg) lamp. The exposure energy was set at 140 mJ/cm². After exposure, the samples were developed for 20 seconds in an AZ-300 MIF developer solution. The developed samples were then rinsed in DI water and blow dried using N₂ gas.

3.2.2 Deposition Techniques

3.2.2.1 Magnetron Sputtering

For the deposition of Co/Pd multilayers and other films, a hybrid deposition system ATC 2200-HY UHV from AJA International, Inc. was used. This system is capable of both magnetron sputtering and electron beam (e-beam) deposition processes. The hybrid system is equipped with six magnetron sputtering targets and five e-beam deposition crucibles, which allows the deposition of a wide range of materials without breaking the vacuum. The six targets were arranged in a specific circular pattern at the bottom of the chamber aiming at a common focal point on top. The samples were pasted onto a sample holder which was placed in the vicinity of the focal point and rotated around a central axis at 100 rad/min to ensure uniformity in the film deposition, as illustrated in Fig. 3.4.

The base pressure of the chamber was better than 2×10^{-8} Torr. The sputtering system is capable of both DC and RF magnetron sputtering. DC sputtering was used to deposit cobalt (Co) and palladium (Pd) while RF sputtering was used to deposit gold (Au) and copper (Cu). Alternating deposition of Co and Pd multilayers were controlled using a build-in LabVIEW program from AJA to ensure consistent repeatable layer thickness in all depositions. The pressure was fixed at 3 mTorr for all the depositions.

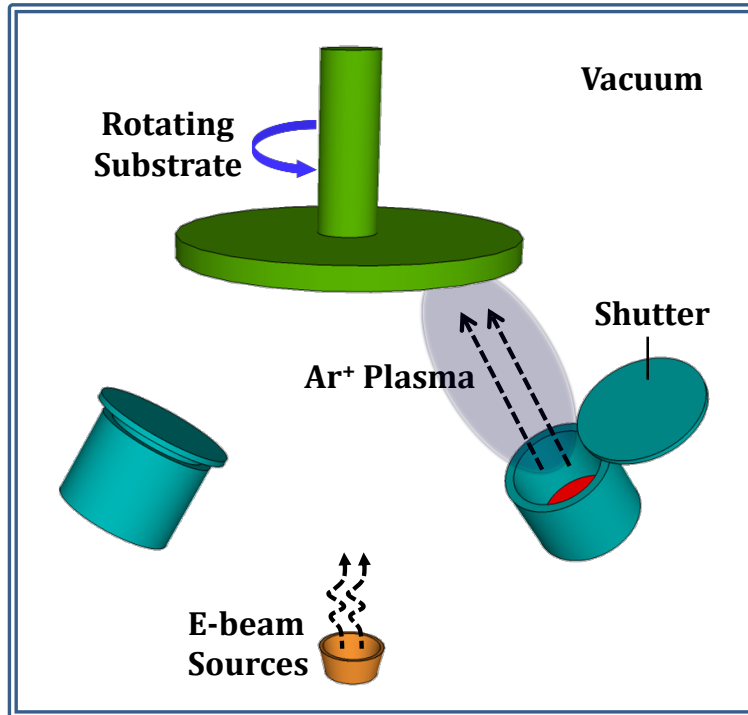


Fig. 3.4 Schematics of thin film deposition using AJA.

3.2.2.2 E-beam Evaporation

The e-beam source was placed directly under the sample holder at the bottom of the chamber to ensure a perpendicular incidence angle of the flux at the sample position. This significantly reduces the side-wall coating of photoresist during the deposition, which is helpful for lift-off process. The e-beam sources are indexed and arranged in a linear configuration. Different materials can be deposited by positioning the crucible of material at the center directly below the substrate. Various materials including $\text{Ni}_{80}\text{Fe}_{20}$, Fe and Al_2O_3 were deposited using this technique. The deposition rate was monitored using a quartz crystal microbalance.

3.2.3 Lift-off, BARC Removal and Wire Bonding

For patterned samples, the deposition was followed by the lift-off process in order to remove the excess material on top of the photoresist layer. This was achieved by soaking the samples in OK73 resist stripper for the DUV

resist patterns and in acetone for the UV resist patterns. The lift-off process was assisted using an ultrasonic bath. Thereafter, the samples were rinsed by isopropyl alcohol (IPA) followed by DI water rinsing. Completion of the lift-off process was determined by the color contrast of the patterned area and confirmed by inspection under a scanning electron microscope.

For the DUV patterns, the lift-off process yields arrays of nanostructures embedded in BARC matrix, as illustrated in Fig. 3.1. The remaining BARC layer was then stripped using a RIE-4 Samco UV Ozone Stripper at an oxygen flow rate of 0.5 L/min at room temperature, which gives an etching rate of 2 Å/s. Complete removal of the BARC layer is helpful for wire bonding.

For magnetotransport measurements, electrical contacts were deposited on top of the fabricated ferromagnetic nanostructures using UV lithography. The samples were then mounted on a 24-pin leadless chip carrier (LCC) package using a silver adhesive. This was followed by wire bonding using a Kulicke and Soffa Wire Bonder 4524AD system. Gold wire was ball bonded (thermosonic) to the device bond pad, and wedge-bonded to the Au pin bond pads of the LCC package. Gold wire and pins were used in the wire bonding process to ensure good conduction during measurements. An example of the bonded device is shown in Fig. 3.5.

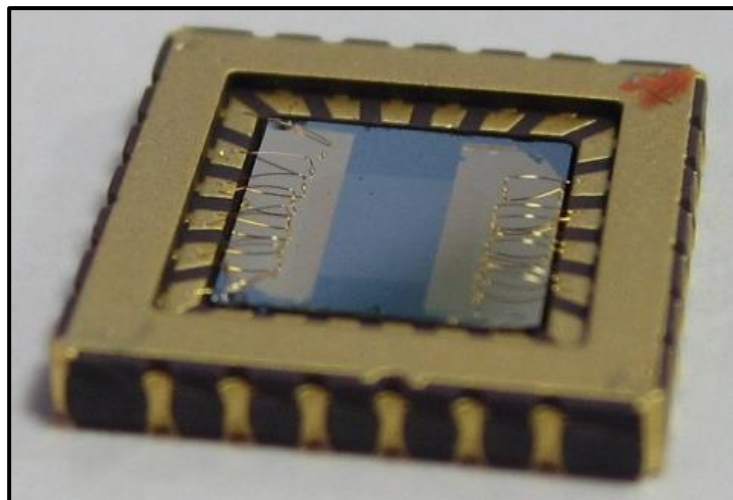


Fig. 3.5 Electrical bond pads for MR measurements.

3.3 Structural and Magnetic Characterization Techniques

3.3.1 X-Ray Diffractometer and X-Ray Reflectometry

When a beam of X-rays with a wavelength λ comes at an incident angle θ relative to the lattice planes, constructive interference of X-ray will take place if the Bragg condition is fulfilled. The condition follows Bragg's law^[119] as given by:

$$2d \sin \theta = n\lambda (n = 1, 2, 3, \dots) \quad (3.2)$$

where $2d\sin\theta$ is the path difference between two parallel X-rays reflected by adjacent Bragg planes, as illustrated in Fig. 3.6. This phenomenon is known as X-ray diffraction.

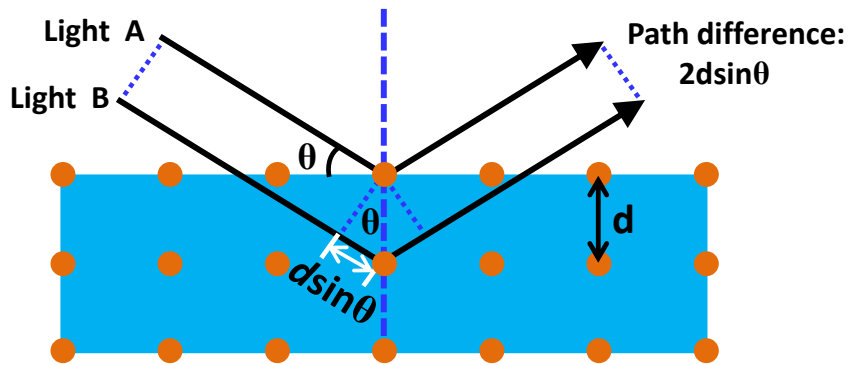


Fig. 3.6 Schematics of constructive interface of X-ray.

In this thesis, X-ray diffraction measurements were conducted using a Bruker D8 Advanced Thin Film X-ray Diffractometer (XRD) to characterize the preferred crystalline orientation of Co/Pd multilayer films. Shown in Fig. 3.7 are schematics of an XRD based on Bragg's law. The X-ray source generated by an X-ray tube was first narrowed by collimators to increase resolution. These beams were then collected by a detector after diffracted by the crystal. In the measurements, the sample was stationary, while the X-ray tube moved by the angle θ together with a simultaneous movement of the detector by an angle 2θ . As θ was varied, the detector recorded intensity peaks

corresponding to the orders predicted by equation (3.2). Each intensity peak is characteristic of a particular crystal orientation for a given material.

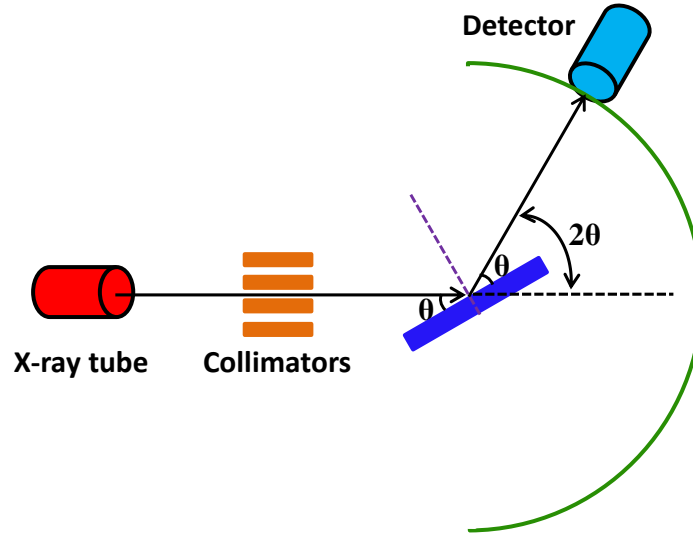


Fig. 3.7 Schematics of an X-ray diffractometer.

Low angle X-ray reflectometry (XRR) is another useful X-ray technique widely used to determine individual layer thicknesses, electron densities (ρ_e), interface roughness (σ) and surface roughness of multilayer films. The basic idea is to reflect a beam of X-rays from a flat surface at a small incident angle (θ_m) and then measure the intensity of X-rays reflected in the specular direction. If the interface is not perfectly sharp and smooth then the reflected intensity will deviate from that predicted by the law of Fresnel reflectivity. The deviations can then be analyzed to obtain various parameters of the multilayers.

When X-ray beam travels from air ($n = 1$) into a multilayer film ($n < 1$), the total external reflection will happen if θ_m is smaller than a critical angle θ_c , as illustrated in Fig. 3.8. At a certain incident angle $\theta_m (>\theta_c)$, the path difference between the adjacent planes is equal to the multiple of X-ray wavelength, and the constructive interference condition to generate a reflection peak is given by:

$$m\lambda = 2\Lambda \sin \theta_m \left(1 - \frac{4\bar{\delta}\Lambda^2}{m^2\lambda^2} \right) \quad (3.3)$$

where m , λ , $\bar{\delta}$, and Λ are the order of reflection, wavelength of X-ray, density average profile for a bi-layer pair and the bi-layer period respectively.

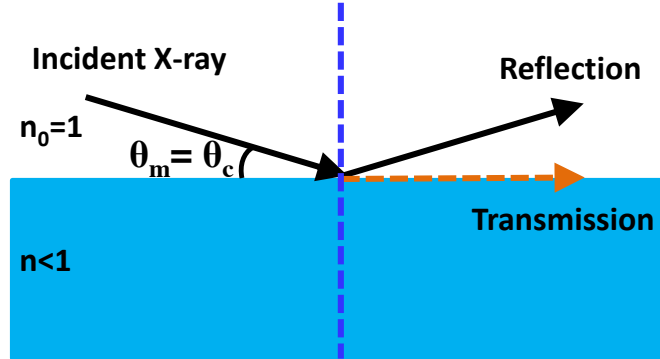


Fig. 3.8 Schematics of total reflection of X-ray.

By combining Snell's and Bragg's laws and through mathematical approximation, the modified Bragg's law can also be expressed as^[120, 121]:

$$\sin^2 \theta_m = (m\lambda / 2\Lambda)^2 + 2\delta \quad (3.4)$$

where δ is the real part of the average refractive index of the film. By plotting $\sin^2 \theta_m$ vs $m^2\lambda^2$ and fitting it to a straight line, Λ can be determined very accurately^[122]. However, to quantitatively determine the individual layer thicknesses and other parameters like interfacial roughness, simulations of the XRR patterns need to be performed^[123]. In this thesis, the XRR measurements were conducted using a Bruker D8 Discover Thin Film XRD and the simulation fittings were performed using a software package LEPTOS 4.02 (available from Bruker-AXS, Karlsruhe, Germany) to determine the individual layer thickness and interfacial roughness of the Co/Pd multilayers. The XRD and XRR measurements were performed by Miss. Ho Pin from Department of Material Science, National University of Singapore.

3.3.2 Scanning Electron Microscopy

Scanning electron microscopy (SEM) is a very important and powerful

analysis tool for imaging structures ranging from micrometer to nanometer scale. Due to the extremely small wavelength of the highly accelerated electrons ($\sim 0.12 \text{ \AA}$ at 10 kV), the SEM can resolve features down to nanometer regime. The schematic of a typical SEM setup is shown in Fig. 3.9.

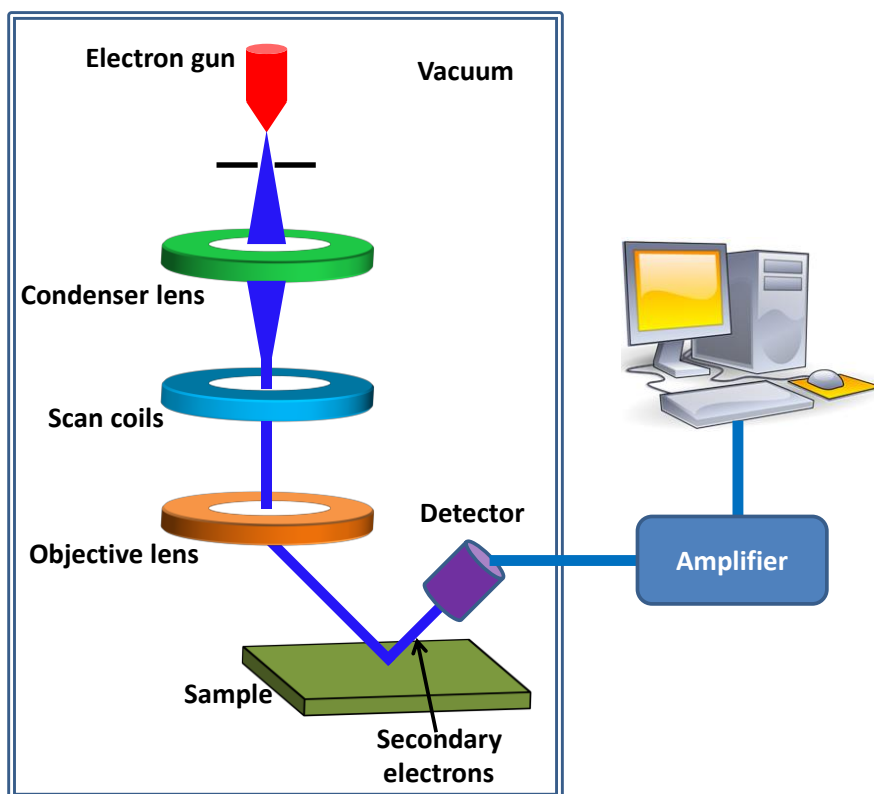


Fig. 3.9 Schematics of the SEM.

A beam of electrons was produced at the top of the microscope by an electron gun. The electron beam followed a vertical path through the microscope, which was held within a vacuum. The beam travelled through the focus lenses and scan coils, which focused the beam down towards the sample. Once the beam hit the sample, particles such as secondary electrons and backscattered electrons were ejected. Detectors collected these particles and converted them into a signal that was sent to a screen similar to a television screen, which produced the final image. In this thesis, a JSM 6700F SEM from JEOL was used to study the profile of the fabricated nanostructures through the detection of secondary electrons.

3.3.3 Scanning Probe Microscopy

Scanning probe microscopy (SPM) is a branch of microscopy that forms images of surface using a physical probe which scans the specimen. An image of the surface was obtained by mechanically moving the probe in a raster scan on the specimen, line by line, and recording the probe-surface interaction as a function of position. In this thesis, a Digital Instrument 3100 SPM system was used, which is capable of both atomic force microscopy and magnetic force microscopy (MFM) measurements.

The atomic force microscopy consisted of a cantilever with a sharp tip mounted at the end which was used to scan the specimen surface. The cantilever is typically made of silicon or silicon nitride with a tip's radius of curvature on the order of nanometers. When the tip was brought into proximity onto a sample surface, attractive or repulsive Van der Waals forces occurred between the tip and the sample which lead to a deflection of the cantilever according to Hooke's law^[124]. The magnitude of the deflection was monitored by a laser that is shining at an oblique angle from the end of the cantilever to a photo detector, as illustrated in Fig. 3.10. A feedback mechanism was used to adjust the tip-to-sample distance to maintain a constant force between the tip and the sample. Therefore, the resulting track of the tip movement represents the topography of the sample.

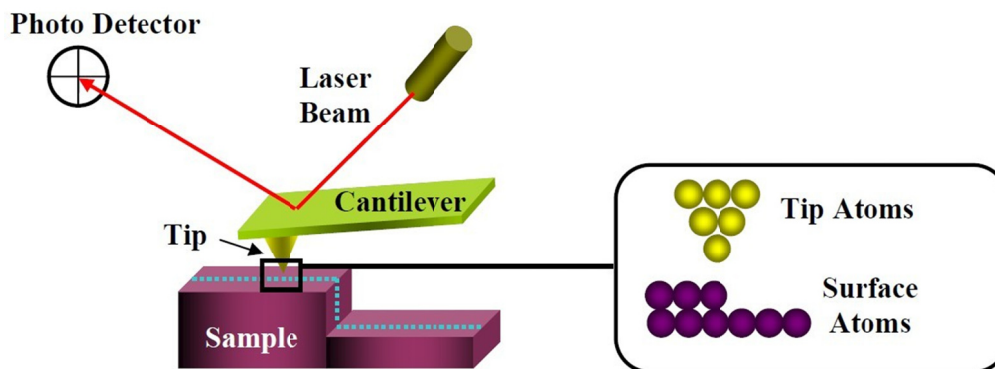


Fig. 3.10 Schematics of atomic force microscopy measurements^[125].

MFM is a variety of atomic force microscopy, where a sharp magnetized tip scans a magnetic sample. The tip-sample magnetic interactions were detected and used to reconstruct the magnetic contrast of the sample surface, as illustrated in Fig. 3.11. The MFM tip was coated with a ferromagnetic thin film, leading to a larger radius of curvature, which consequently lowered the spatial resolution in comparison with atomic force microscopy.

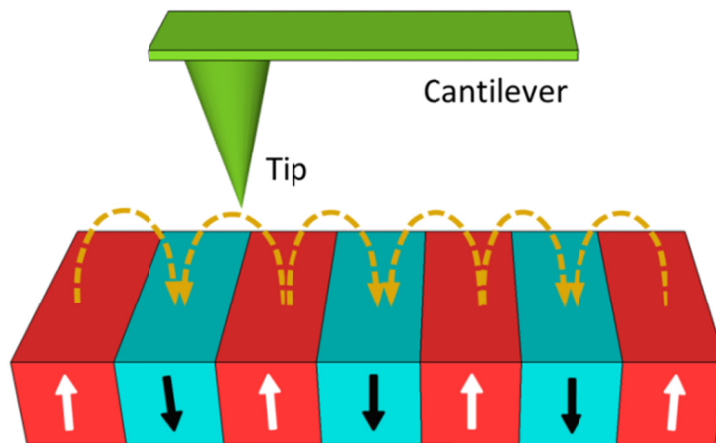


Fig. 3.11 Schematics of MFM measurements.

To separate the magnetic force from atomic force, MFM measurements were carried out using a two-pass technique, lift mode. In the first pass, the topography of the sample was recorded using tapping mode, while in the second pass the cantilever was lifted by a selected height, large enough to eliminate the atomic force. By subtracting the stored topography information, the spin configuration of a magnetic sample can be determined.

3.3.4 Magneto-Optical Kerr Effect

When a polarized light is reflected from a magnetic sample surface, both the Kerr rotation (θ_k) and ellipticity (ε_k) of the light will change depending on the magnetization of sample, which is the so-called Magneto-Optical Kerr Effect (MOKE). The effect is similar to the Faraday effect: the Faraday effect describes changes of light transmitted through a magnetic material, while the

Kerr effect describes changes of light reflected from a magnetic surface. Both effects are due to the difference in absorption coefficients for left-hand circularly polarized (LCP) and right-hand circularly polarized (RCP) light in a magnetic material. The MOKE is also known as surface MOKE because the penetration depth of the laser is only up to several tens of nanometers for most metals which means that MOKE is particularly surface sensitive^[10, 126]. The Kerr signals (ϵ_k and θ_k) are proportional to the magnetization and thickness of a magnetic thin film.

MOKE can be categorized by the direction of the magnetization vector with respect to the incidence plane of the laser, i.e. polar, longitudinal and transverse configurations. These configurations are schematically sketched in Fig. 3.12. The polar Kerr effect has the magnetic field H applied in the direction that is normal to the film plane, thus it is sensitive to the perpendicular component of the magnetization. To simplify the analysis, near normal incidence is usually used in the polar geometry. The longitudinal Kerr effect has H applied in the film plane and in the plane of the incident light, and thus is sensitive to the in-plane component of the magnetization. The transverse Kerr effect also has H applied in the film plane, but perpendicular to the incident plane of the light. The polar signal is typically an order of magnitude greater than the longitudinal and transverse signals^[126].

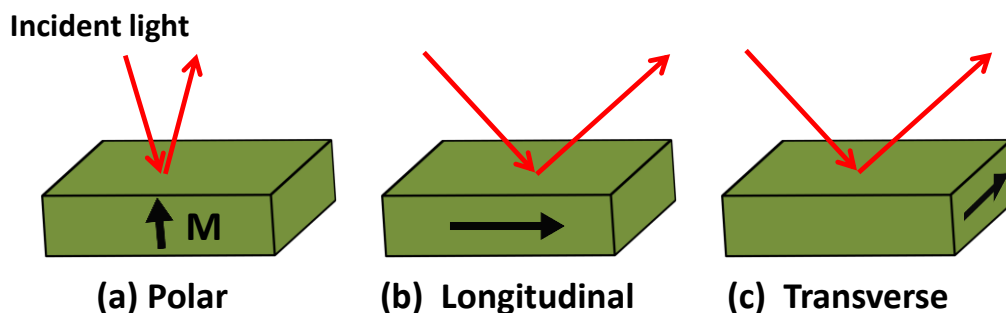


Fig. 3.12 Schematics of MOKE with (a) polar; (b) longitudinal; and (c) transverse configurations.

The MOKE system can be utilized for the measurement of hysteresis

loops of ferromagnetic materials. In this thesis, in-house developed longitudinal and polar MOKE setups were used to characterize samples with in-plane and out-of-plane magnetization respectively. Shown in Fig. 3.13(a) are schematics of a typical longitudinal MOKE setup. An ultra-low noise HeNe laser with a wavelength of 635 nm was used as the light source. This was followed by a beam expander which expanded the laser spot to about 1 cm to attain collimated light and by an aperture to define the spot shape. The collimated beam became linearly polarized after passing through a polarizer and was then focused on a magnetic sample by an achromatic doublet lens. The lens has a diameter of 20 mm, a focal length of 50 mm and an infinite conjugate ratio, which gives a spot size of $\sim 5 \mu\text{m}$. The magnetic sample changed the polarization of the incident light. The difference in polarization angle of the LCP and RCP lights resulted in the Kerr rotation (θ_k) while the change in major/minor axis ratio lead to the Kerr ellipticity (ε_k). Both θ_k and ε_k are proportional to the magnetization of the sample. The reflected light thus became elliptically polarized. The intensity of the reflected light was then modulated by a photoelastic modulator (PEM) resonating at a frequency of $f=50$ kHz. The Kerr rotation and ellipticity were modulated at different frequencies, i.e. $2f=100$ kHz for θ_k and $f=50$ kHz for ε_k ^[10, 127].

The modulated Kerr signal passed through an analyzer which was set at an angle ψ from the extinction and the intensity is given by^[126]:

$$I = |E_p \sin\psi + E_s \cos\psi|^2 \approx |E_p\psi + E_s|^2 \quad (3.5)$$

where E_p , and E_s are the p - and s -components of the electrical field of the laser. Since $E_s / E_p = \theta_k + i\varepsilon_k$ gives the Kerr rotation θ_k and Kerr ellipticity ε_k , Eq. (3.5) becomes:

$$I = |E_p|^2 |\psi + \theta_k + i\varepsilon_k|^2 \approx |E_p|^2 (\psi^2 + 2\psi\theta_k) = I_0 \left(1 + \frac{2\theta_k}{\psi} \right) \quad (3.6)$$

with $I_0 = |E_p|^2 \psi^2$ as the intensity at zero Kerr rotation. The signal was

focused using a lens and picked up by an AC photodiode detector. Thus, the measured intensity as a function of applied field yielded a magnetic hysteresis loop. The maximum Kerr rotation θ_{k-max} can be determined by the relative change of the Kerr intensity, $\Delta I/I_0$, between the two saturation magnetization directions:

$$\theta_{k-max} = \frac{\psi}{4} \frac{\Delta I}{I_0} \quad (3.7)$$

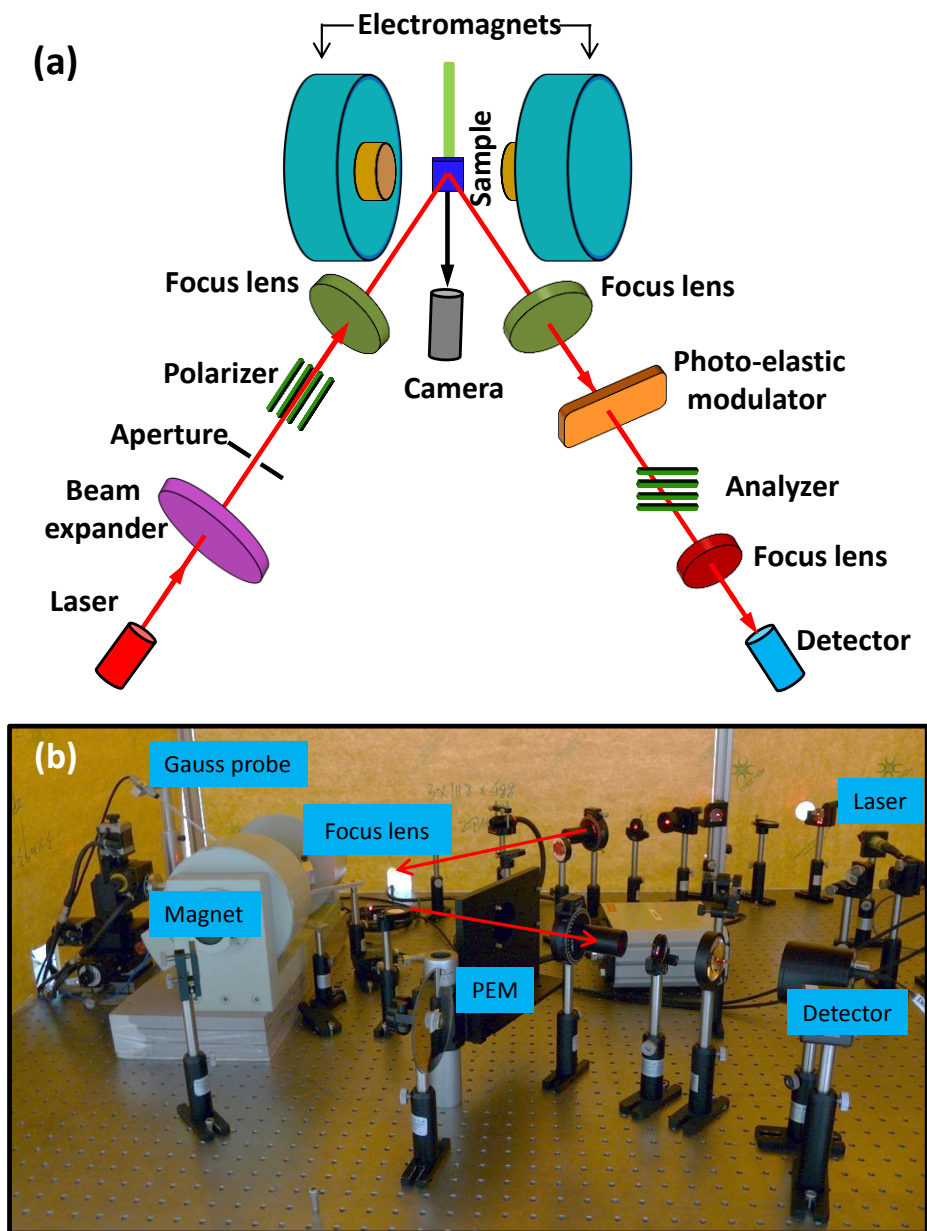


Fig. 3.13 (a)Schematics; and (b)Experimental demonstrations of a longitudinal MOKE setup.

It is also possible to measure the Kerr ellipticity by inserting a quarter waveplate in the MOKE setup, because the plate will produce a $\pi/2$ phase difference between the p - and s -components of the electrical fields. In this case, the analyzer ‘sees’ $i(\theta_k + i\varepsilon_k) = -\varepsilon_k + i\theta_k$ instead of $\theta_k + i\varepsilon_k$, and the measured Kerr intensity is given by:

$$I = |E_p|^2 (\psi^2 + 2\psi\varepsilon_k) = I_0 \left(1 + \frac{2\varepsilon_k}{\psi} \right) \quad (3.8)$$

The quarter waveplate thus exchanges the Kerr rotation and Kerr ellipticity. Another way to exchange θ_k with ε_k is to extract the modulated signal at a frequency of 50 kHz rather than at 100 kHz based on the fact that the Kerr ellipticity is modulated at $f=50$ kHz by the PEM. This can be achieved by sending the detector signal into a lock-in amplifier and providing a reference frequency of f from PEM. Fig. 3.13(b) shows the experimental setup of the longitudinal MOKE. The hysteresis loops of Fe filled $\text{Ni}_{80}\text{Fe}_{20}$ antidot nanostructures in § 6.3 were measured using this MOKE setup.

Shown in Fig. 3.14(a) are schematic illustrations of a typical polar MOKE setup. The linearly polarized light was focused on a magnetic sample through a small hole of one electromagnet. The magnetic field was applied along out-of-plane direction of the sample. The incident beam was normal to the sample surface and reflected back along the same path. This reflected light was split by a cubic lens, which is capable of both transmission and reflection, and collected by an AC detector after passing through the PEM and analyzer. The corresponding experimental setup of the polar MOKE is shown in Fig. 3.14(b). The hysteresis loops of Co/Pd multilayers investigated in this thesis were characterized using the polar MOKE setup.

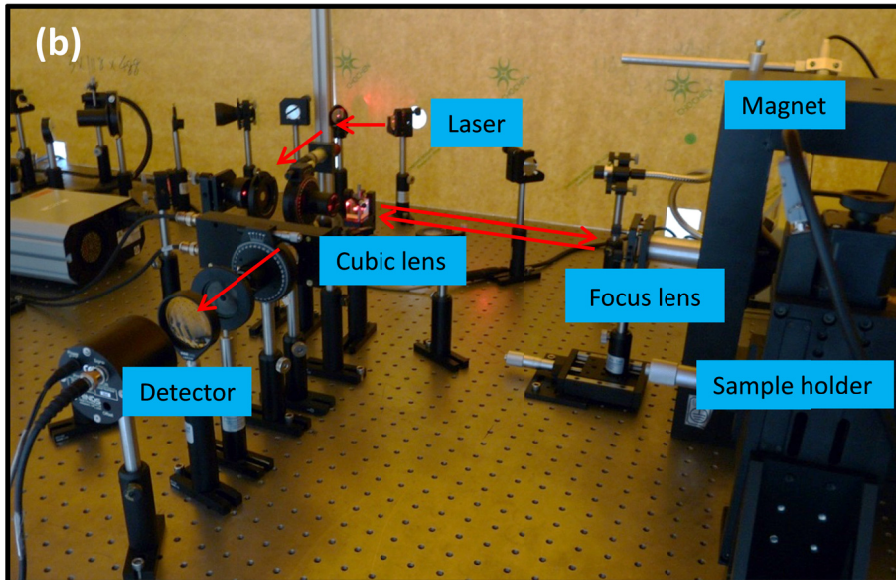
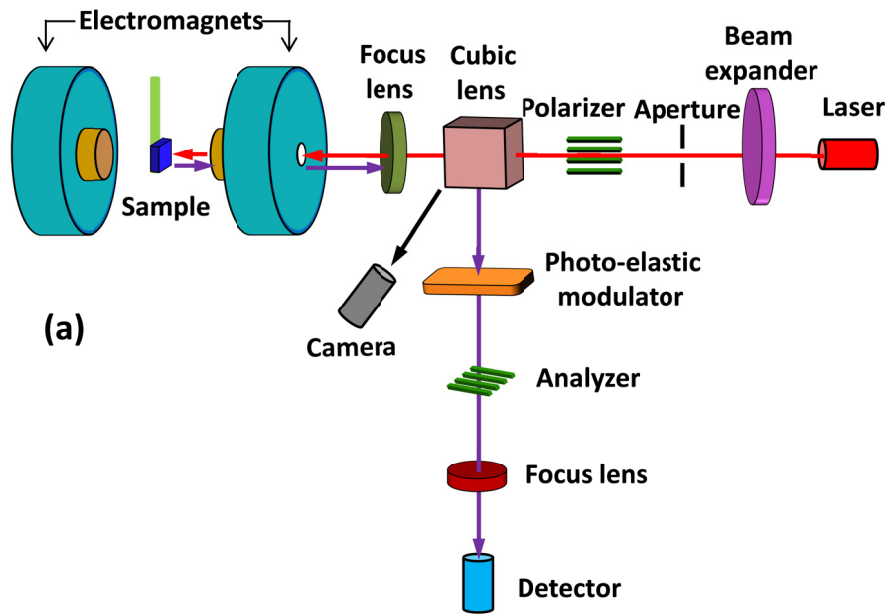


Fig. 3.14 (a) Schematics; and (b) Experimental demonstrations of a polar MOKE setup.

3.3.5 Vibrating Sample Magnetometer

The vibrating sample magnetometer (VSM) is widely used to characterize magnetic properties of samples using an induction technique based on Faraday's law. In this thesis, the hysteresis loops of $[\text{Co/Pd}]_4/\text{Co/Ru}/[\text{Co/Pd}]_2$ multilayers were measured using a mode 7404 VSM from LakeShore, which is capable of both out-of-plane and in-plane magnetic measurements with a

magnetic field up to 1.3 Tesla. The sensitivity of the VSM is in the order of 10^{-6} emu. Shown in Fig. 3.15 are schematics of the VSM setup.

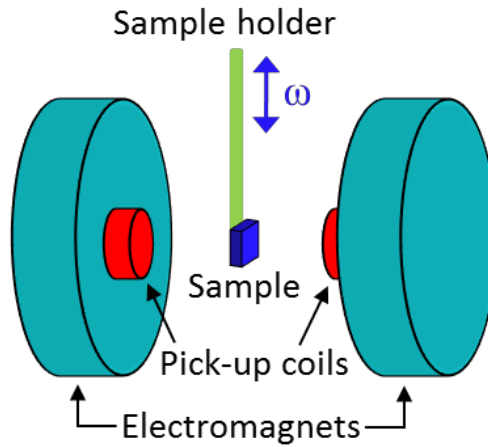


Fig. 3.15 Schematics of VSM setup.

The sample was mounted on a sample holder in between the electromagnetic poles and vibrated vertically at a constant frequency ω , leading to a change in magnetic flux of the pick-up coils. The changing flux in the pick-up coils changed the magnitude of the AC output voltage accordingly based on Faraday's law, as given by:

$$V = k\omega M \quad (3.9)$$

where k is a coefficient determined by the calibration of a nickel standard sample, and M is the magnetic moment of the sample. The induced AC voltage was detected and amplified by a lock-in amplifier, and was mapped into the magnetic moment of the sample using the experimental calibration parameters. Since the VSM is sensitive to the total moment, it is more suitable for the measurement of large area samples.

3.3.6 Magnetotransport Measurement

3.3.6.1 Room Temperature Setup

Magnetic materials have electrical properties which vary with their

magnetization. Therefore, their magnetic behavior can be investigated by the detection and analysis of electrical signal. In this thesis, a room temperature magnetoresistance (MR) measurement system was used to characterize the magnetotransport properties of the fabricated nanostructures. The schematic illustration of the MR measurement setup is shown in Fig. 3.16.

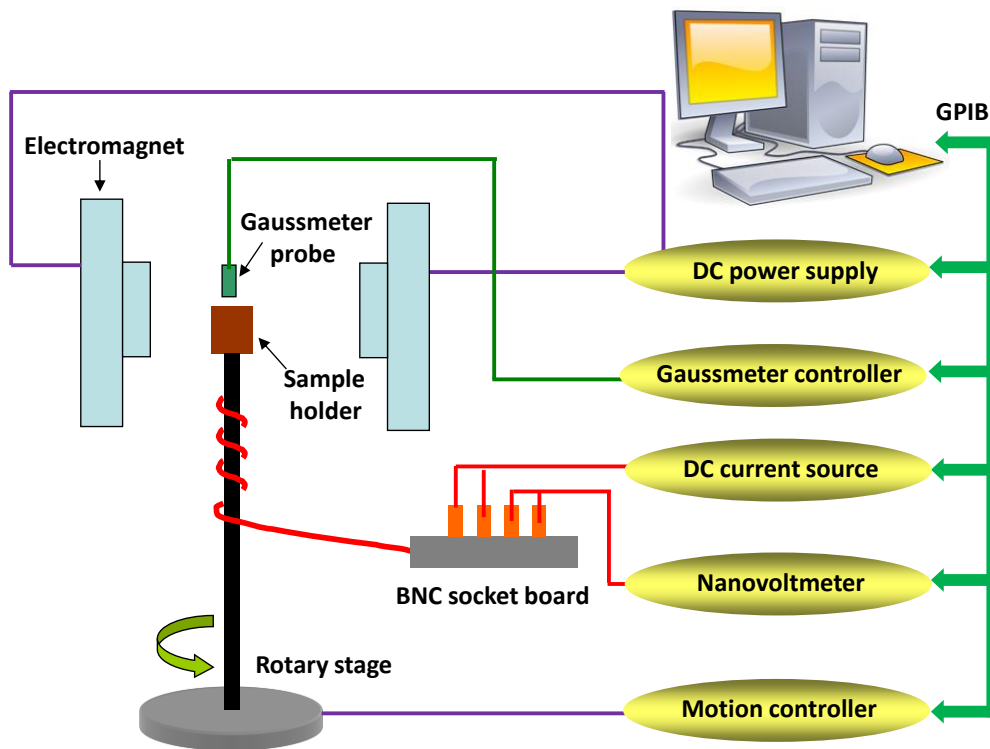


Fig. 3.16 Schematics of room temperature MR measurement setup.

The sample was first mounted onto a 24-pin chip carrier followed by Au wire bonding as described in § 3.2.3. The wire bonded samples were then clipped tightly onto a sample holder, placed between the poles of two electromagnets. The electromagnet was driven by a Kepco 36-12M bipolar DC power supply, and the magnetic field strength was monitored using a Lakeshore 450 gaussmeter. The sample holder was placed on a fully automated rotary stage which was controlled by a Newport ESP300 motion controller, so that the orientation of the samples can be accurately adjusted with respect to the magnetic field direction. Electrical connections from the 24-pin chip carrier were extended from the mechanical contact of the holder to

a Bayonet Neill Concelman (BNC) socket board, through which electrical connections were made to the instrument. For the electrical setup, a constant DC current from a Keithley 6221 programmable current source was passed through the device. The corresponding voltage signal levels were measured using a Keithley 2182 nanovoltmeter. Data acquisition was achieved through the general purpose interface bus (GPIB) communication channel.

3.3.6.2 Low Temperature Setup

The temperature dependent MR measurements were performed using a Janis Super-Vari-Temp (SVT) research cryostat which can be operated in the temperature range from 4.2 K to 350 K. Fig. 3.17 shows the schematic of the research cryostat. The system combines a variable temperature insert, model CNDT vacuum insulated dewar, sample holder assembly and a temperature controller. The sample bonded to the 24 pin chip carrier was loaded onto the sample holder and then placed inside the cryostat. The samples can be loaded in two different positions to obtain both in-plane and out-of-plane magnetic field orientations. The SVT system used helium gas flow, which was obtained by vaporizing liquid helium (LHe), to cool or warm the sample within the operating temperature range. LHe exited the main reservoir through a needle valve, and entered the vaporizer at the bottom of the sample tube. The vaporizer temperature was regulated by the automatic Lakeshore 340 temperature controller using a control heater and thermocouple. After entering the vaporizer, the LHe evaporated, warmed up to the desired temperature, and then entered the sample tube. The helium vapors flowing past the sample mount warm or cool the sample, and then exited through a vent port. The actual temperature of the sample can be monitored by the temperature controller sensor located on the sample holder. The magnetic field was generated by an electromagnet positioned inside the dewar. It was controlled by a Cryomagnetics Bipolar Superconducting Magnet Power Supply.

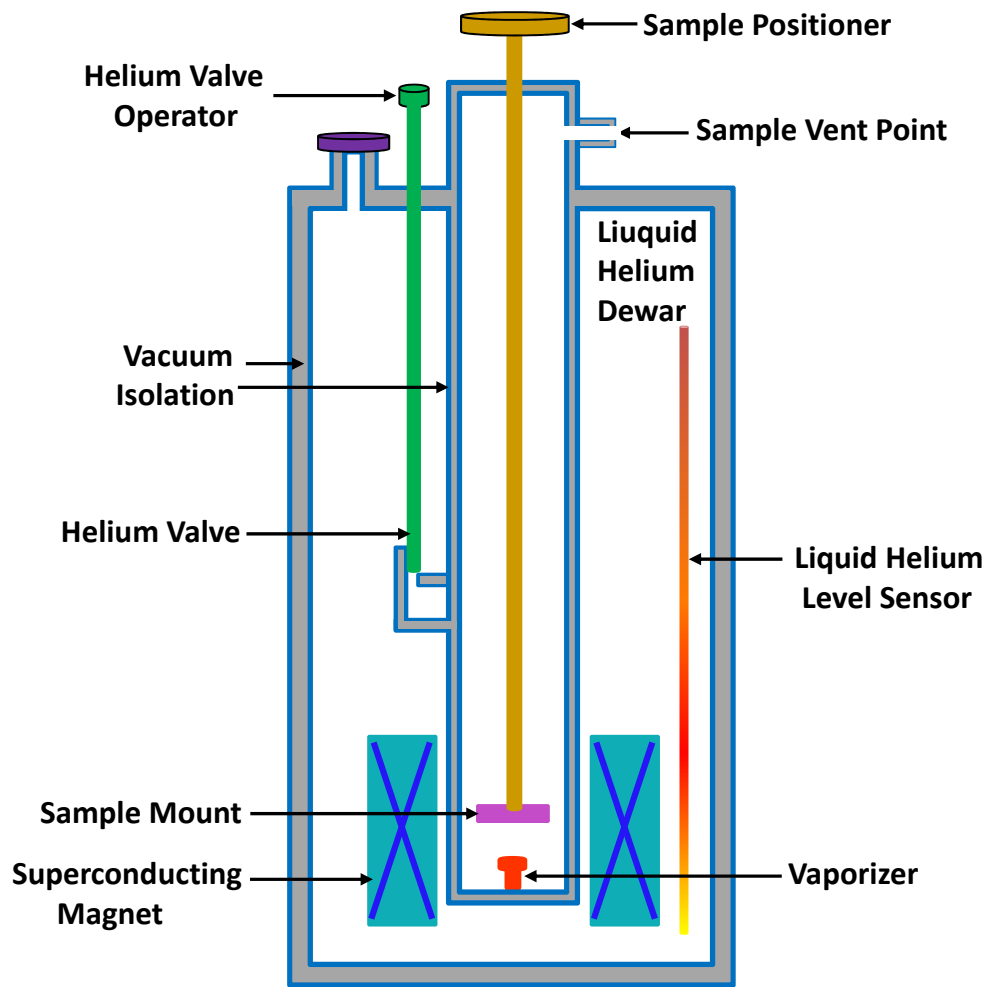


Fig. 3.17 Schematics of Janis SVT research cryostat.

3.3.7 Ferromagnetic Resonance Spectroscopy

The dynamic measurements were conducted using a broadband ferromagnetic resonance (FMR) spectroscopy. Shown in Fig. 3.18 is a schematic of a magnetic sample incorporating a coplanar waveguide (CPW) for FMR measurements. Typical CPW with signal line length of 300 μm , width of 20 μm were fabricated on top of magnetic nanostructures using photolithography followed by deposition of $\text{Al}_2\text{O}_3(50 \text{ nm})/\text{Ti}(5 \text{ nm})/\text{Au}(150 \text{ nm})$ and lift-off process.

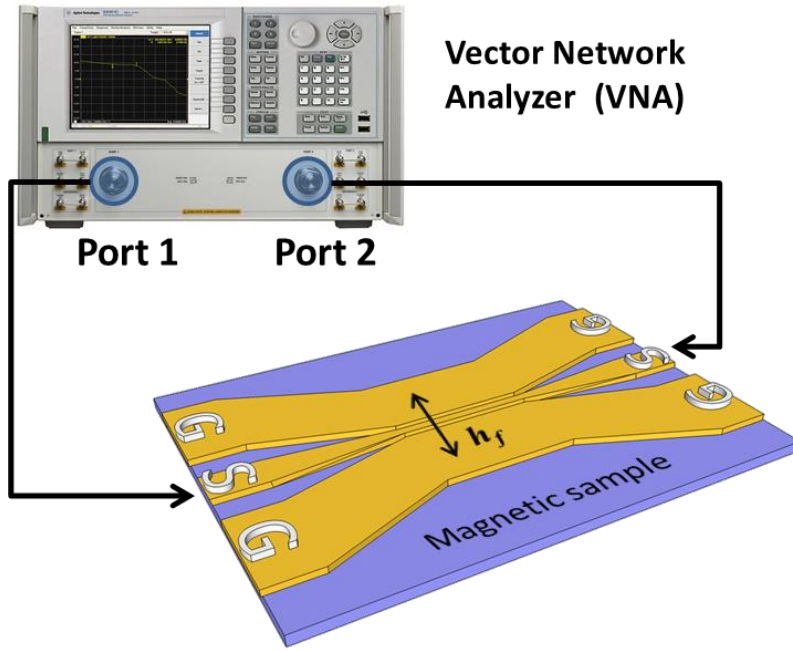


Fig. 3.18 Schematics of FMR measurements^[128]

The FMR responses were measured using a microwave vector network-analyzer (VNA). The ports of VNA were connected to the CPW using G-S-G-type microwave coplanar probes. The FMR responses were measured at room temperature by sweeping the frequency for fixed in-plane field (H_{app}) in the 1-20 GHz range. This process was repeated for a large number of H_{app} values starting from negative saturation field, passing through zero, and then gradually increasing to positive saturation field. The FMR setup used in this thesis was developed by Mr. Ding Junjia^[128]. The microwave magnetic field h_f produced by the signal line of CPWs is shown in Fig. 3.18. Compared with conventional FMR setup, where the measurements were performed by sweeping a static external field at fixed frequency, our setup is advantageous since it would not alter the magnetization configuration and thereby would not change the resonance condition of the magnetic sample during the measurement.

Chapter 4

Magnetization Reversal of Circular Co/Pd Nanomagnets

4.1 Introduction

This chapter presents a systematic investigation of magnetization reversal of circular Co/Pd nanomagnets including dots and rings. It was observed that the magnetic switching of the $[\text{Co/Pd}]_n$ dots is markedly dependent on both the bi-layer repeat n and the dot diameter d . When the Co/Pd dots are densely arranged in a cluster, dipolar coupling strongly affect the switching behavior, which shows potential for magnetic logic applications. Further investigation of interlayer coupling was carried out in $[\text{Co/Pd}]_4/\text{Au}/[\text{Co/Pd}]_2$ rings by varying the Au spacer layer thickness.

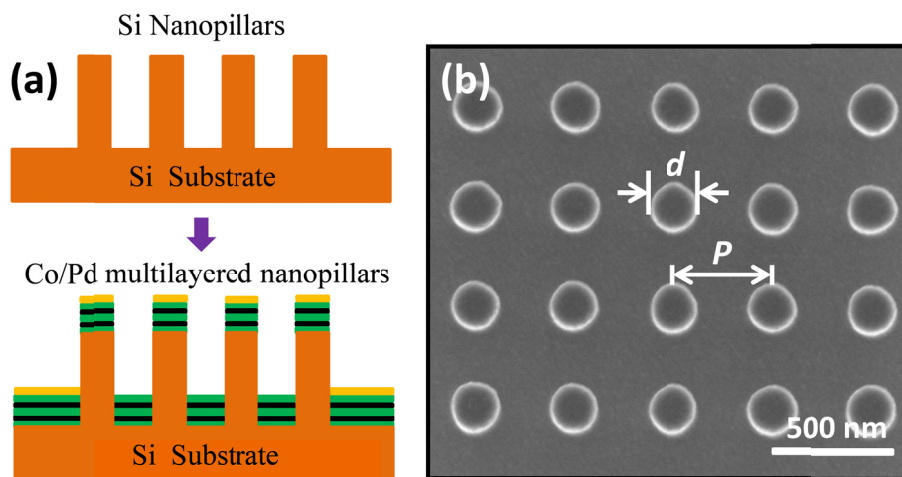
4.2 Experimental Details

In this chapter, two methods have been adopted for the fabrication of circular Co/Pd nanomagnets, namely, (i) method A by depositing Co/Pd multilayer on pre-patterned Si nanopillars and (ii) method B using lift-off process after Co/Pd multilayer film deposition on resist patterned template. One of the limitations of depositing thin film directly on pre-patterned Si nanopillars is that when characterizing the magnetic properties, in addition to the signal from the dots, there is also magnetic signal from the trenches. However, this method of fabrication is good because no resist is used during Co/Pd film deposition, therefore there is no contamination to the multilayers.

Shown in Fig. 4.1(a) are schematics of the deposited Co/Pd film on top of the pre-patterned Si nanopillars. Details of the fabrication process of the Si

nanopillars have been described in § 3.2.1.1. The diameter d of the pillar was varied in the range from 170 nm to 205 nm while the pitch p was fixed at 400 nm. Pd(5 nm)/[Co(0.5 nm)/Pd(3 nm)] $_n$ /Au(4 nm) multilayers with n varied from 1 to 12 were then deposited on the Si pillars using magnetron sputtering. The 5 nm Pd seed layer was deposited prior to the Co/Pd multilayer stack to obtain perpendicular anisotropy and the complete film structure was capped with 4 nm Au to prevent oxidation.

Method A



Method B

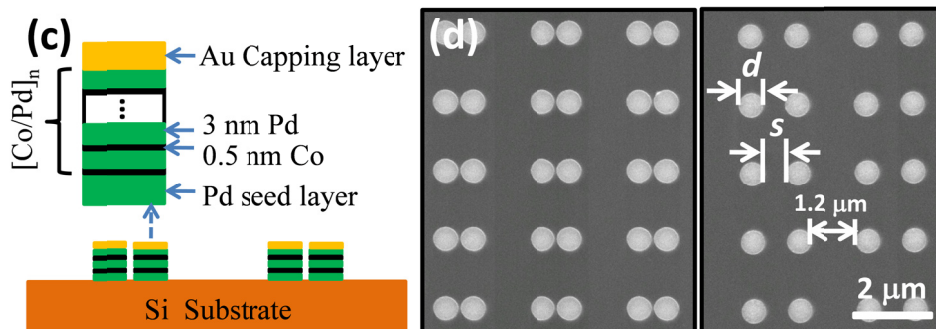


Fig. 4.1 (a) Schematics of Co/Pd multilayers on top of pre-patterned Si nanopillars; and (b) SEM image of arrays of [Co(0.5 nm)/Pd(3 nm)] $_{12}$ dots with $d=185$ nm. Schematics and SEM images of the Co/Pd two-dot cluster fabricated using method B are shown in (c) and (d) respectively.

The Co/Pd multilayer deposition resulted in arrays of Co/Pd dots on top of the pillars and antidot in the pillar trench. Shown in Fig. 4.1(b) is a

representative SEM micrograph of arrays of $[\text{Co}(0.5 \text{ nm})/\text{Pd}(3 \text{ nm})]_{12}$ dots with $d = 185 \text{ nm}$. The height of the nanopillars is 450 nm , which is large enough to ensure that the Co/Pd dots on top of the pillars and the antidot in the trench are magnetically decoupled.

In order to eliminate the influence of trench material, method B was used to fabricate Co/Pd dot clusters. Arrays of $\text{Pd}(5 \text{ nm})/[\text{Co}(0.5 \text{ nm})/\text{Pd}(3 \text{ nm})]_n/\text{Au}(4 \text{ nm})$ two-dot clusters (illustrated in Fig. 4.1(c)) with varied n from 2 to 6 were fabricated on silicon substrates using deep ultraviolet lithography at 248 nm wavelength followed by lift-off process. Details of the fabrication process has been described in § 3.2. Shown in Fig. 4.1(d) are representative SEM micrographs of the Co/Pd two-dot clusters. The diameter d of the Co/Pd dots was fixed at 600 nm while the edge-to-edge spacing s between the dots was varied from 100 nm to 600 nm . The distance between the dot clusters was kept at $1.2 \mu\text{m}$ which is large enough to ensure the clusters are magnetically decoupled.

Method B has also been used to fabricate $\text{Pd}(5 \text{ nm})/[\text{Co}(0.5 \text{ nm})/\text{Pd}(3 \text{ nm})]_4/\text{Au}(t_{\text{Au}})/[\text{Co}(0.5 \text{ nm})/\text{Pd}(3 \text{ nm})]_2$ pseudo-spin-valve (PSV) rings with inner diameter of 190 nm and outer diameter of 520 nm . Shown in Fig. 4.2 (a) and (b) are schematics of the PSV film structures and representative SEM images of the PSV rings respectively. The Au spacer thickness t_{Au} was varied from 1 nm to 8 nm while the edge-to-edge spacing s was changed from 200 nm to 650 nm .

The structural properties and surface topography of the Co/Pd multilayer films were characterized using X-ray Diffractometer (XRD) and atomic force microscopy respectively. The collective magnetic switching behavior of Co/Pd nanostructures was measured using a focused polar Magneto-Optical Kerr Effect (MOKE) setup with external magnetic field applied perpendicular to the plane of the sample. Magnetic force microscopy (MFM) was performed in the phase detection mode to probe the switching behavior of dots.

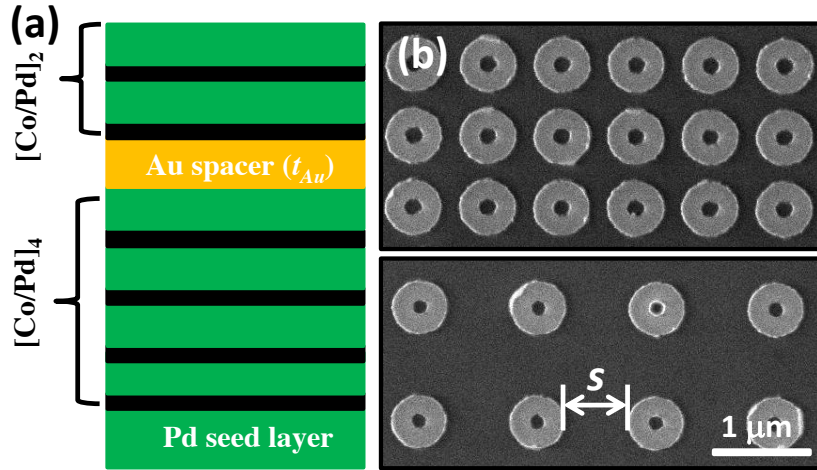


Fig. 4.2 (a) Schematics of the deposited Co/Pd PSV structure; and (b) representative SEM images of the PSV nanorings with $s=200$ nm and $s=650$ nm.

4.3 Magnetic Properties of Pre-patterned Co/Pd Dots

4.3.1 Effects of Bi-layer Repeat

4.3.1.1 Continuous Films

The magnetic properties of [Co/Pd]_n multilayer films were studied as a function of the bi-layer repeat n . Shown in Fig. 4.3(a) are the hysteresis loops for the Co/Pd continuous films as a function of n . Clearly, the switching field (H_{sw}) and detailed features of the hysteresis loops are strongly dependent on n . The squareness of all the loops with n up to 12 is equal to 1, indicating the good perpendicular magnetic anisotropy, even for the film with only one Co/Pd bi-layer. With increase in n from 1 to 6, the H_{sw} of the continuous film increases from 220 Oe to 370 Oe and further decrease to 265 Oe for $n=12$. Interestingly, for multilayers with $n \leq 6$, a sharp magnetization reversal was observed. This is in contrast to the multilayer with $n=12$ which shows a large tail in the hysteresis loop.

To explain this experimental observation, we have performed structure analysis of the Co/Pd multilayer films as a function of n , as shown in Fig. 4.3(b) the θ - 2θ curves. Only two main reflection peaks, namely, Au(111) and

CoPd(111) were observed in all the multilayer films, corresponding to $2\theta = 38.4^\circ$ and $2\theta = 40.6^\circ$, respectively. The Au(111) peak comes from the Au capping layer while the CoPd(111) peak is due to the Co/Pd multilayers. The CoPd(111) peak shifts upwards slightly by 0.2° in comparison with the fcc-Pd(111) peak ($2\theta = 40.4^\circ$) due to the compressive stress exerted by the neighboring Co layers, as Co has a smaller lattice constant ($a=3.54\text{\AA}$) than Pd ($a=3.89\text{\AA}$). The observation of the single CoPd peak is an indication of good growth of the fcc(111) phase of the Co/Pd multilayers which has close relationship with perpendicular anisotropy^[22, 129, 130]. With increase in n , there is no clear change in peak position for the Co/Pd(111) peak although the intensity increases significantly as expected, suggesting no microstructure change as n is increased.

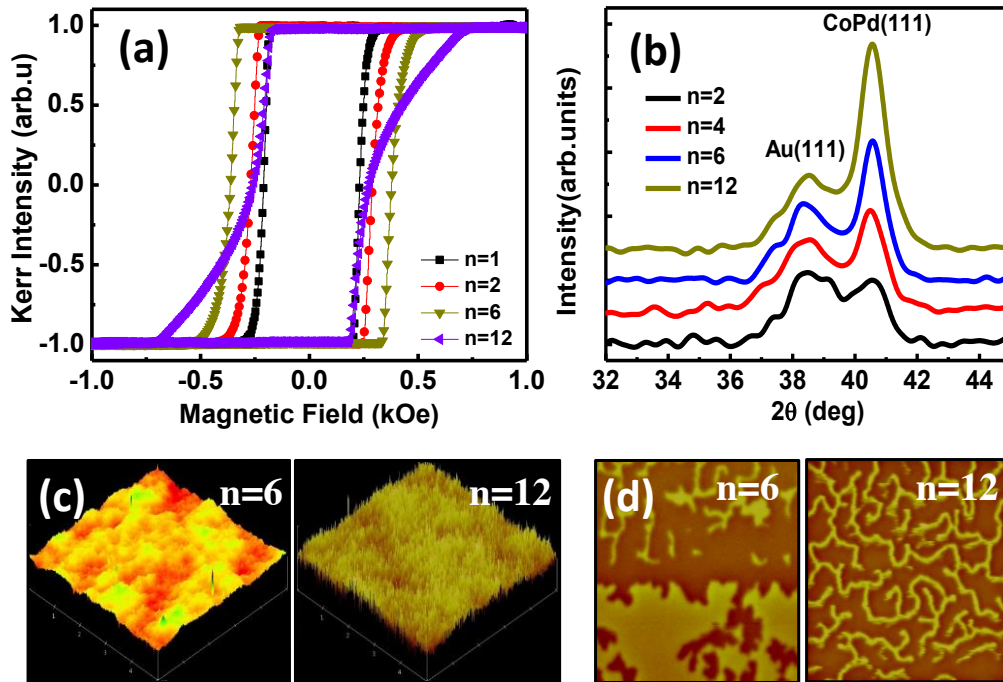


Fig. 4.3 (a) *M-H* loops; and (b) XRD patterns for continuous $[\text{Co}(0.5 \text{ nm})/\text{Pd}(3 \text{ nm})]_n$ films as a function of n . The atomic force microscopy and MFM images taken after AC demagnetization are shown in (c) and (d).

We have further investigated the surface roughness and domain configuration of the Co/Pd films as a function of n using atomic force microscopy and MFM respectively. Shown in Fig. 4.3(c) are atomic force

microscopy images of the Co/Pd multilayer films with $n=6$ and $n=12$ taken over an area of $5\ \mu\text{m} \times 5\ \mu\text{m}$. A significant increase of surface roughness from 0.431 nm to 1.235 nm is observed as n is increased from 6 to 12. The corresponding MFM images captured after AC demagnetization over an area of $10\ \mu\text{m} \times 10\ \mu\text{m}$ are shown in Fig. 4.3(d). Stripe domains are observed in both structures which are typical for a film with perpendicular anisotropy^[131]. Interestingly, there is a marked decrease of domain size from $\sim 1\ \mu\text{m}$ for $n=6$ to $\sim 200\ \text{nm}$ for $n=12$. This may suggest increased magnetostatic energy due to increased bi-layer repeat, which needs smaller domain size for energy minimization^[129, 131]. For samples with $n \leq 6$, no clear magnetic domains could be observed after AC demagnetization.

We believe that the combination of increased film roughness and interlayer magnetostatic interactions is responsible for the changes in magnetic properties of the Co/Pd multilayer films. Larger film roughness may constrain domain wall motion hence increase the saturation field of the multilayer films, whereas stronger interlayer magnetostatic coupling between neighboring Co layers increases the force for saturation^[132]. These effects consequently result in the large tail observed in the hysteresis loop for $n=12$ (Fig. 4.3 (a)). This observation is in good agreement with earlier work by R. Sbiaa et al.^[129]

We have also investigated the effects of bi-layer repeat n on the perpendicular anisotropy of the Co/Pd multilayer films. Shown in Fig. 4.4(a) and (b) are the out-of-plane and in-plane hysteresis loops measured using a vibrating sample magnetometer (VSM) for $n=4$ and $n=18$ respectively. Clearly, as n is increased from 4 to 18, the saturation field which is related to anisotropy field doubles from 5 kOe to 10 kOe, indicating a large increase in perpendicular anisotropy (K_u). We have further extracted K_u by calculating the area between the out-of-plane and in-plane magnetization curves^[62]. The results are plotted as a function of n , as shown in Fig. 4.4(c). We observed a monotonic increase of K_u from $0.83 \times 10^6\ \text{erg/cm}^3$ to $4.65 \times 10^6\ \text{erg/cm}^3$ as n is

increased from 2 to 18. Similar change trend has been previously observed by A. S. H. Rozatian et al.^[81] in Co/Pd multilayer films with identical film structure. The larger K_u value observed in our experiments might indicate better film quality benefitting from the high vacuum chamber for the multilayer film deposition.

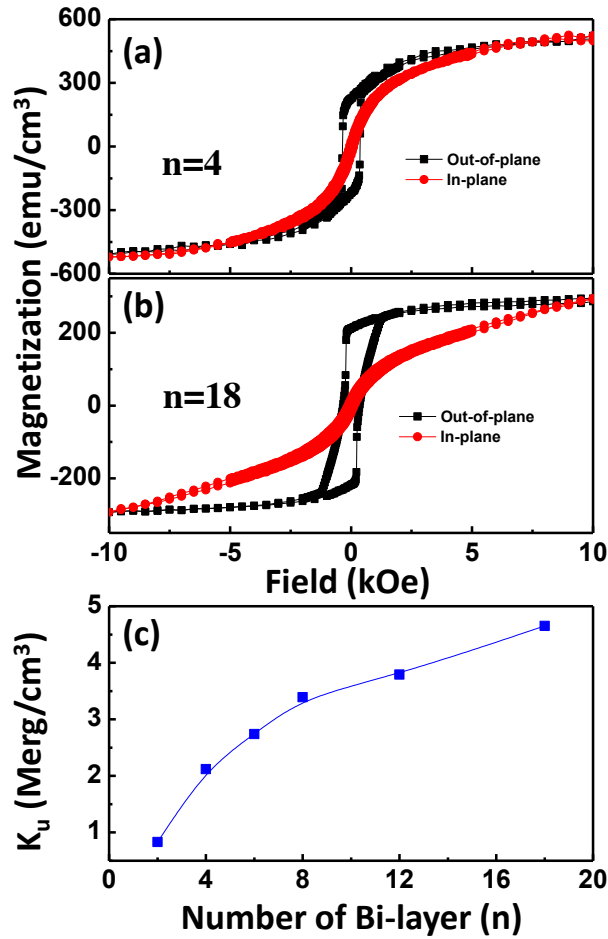


Fig. 4.4 Out-of-plane and in-plane M-H loops measured using VSM for the $[Co/Pd]_n$ multilayer films with (a) $n=4$; and (b) $n=18$. A plot of K_u extracted from the M-H loops as a function of n is shown in (c).

4.3.1.2 Pre-patterned Dots

Shown in Fig. 4.5(a) are hysteresis loops of the Co/Pd dots with diameter $d=185$ nm as a function of n . As expected, two prominent switching fields are observed in all the hysteresis loops, corresponding to the magnetic switching of Co/Pd antidot in the trench at lower switching field H_{s1} and Co/Pd dots on

top of the pillars at larger switching field H_{s2} respectively. H_{s1} and H_{s2} were determined by taking the derivative of the Kerr intensity plot in the ascending sweep direction in order to obtain the peak positions, as defined in Fig. 4.5(a). Interestingly, both the Co/Pd antidot and dots for $n=12$ shows a much larger switching field distribution than those with smaller bi-layer repeat ($n=2$ and $n=6$). This is a direct effect of increased interlayer magnetostatic interactions, in line with our earlier discussion of the continuous films.

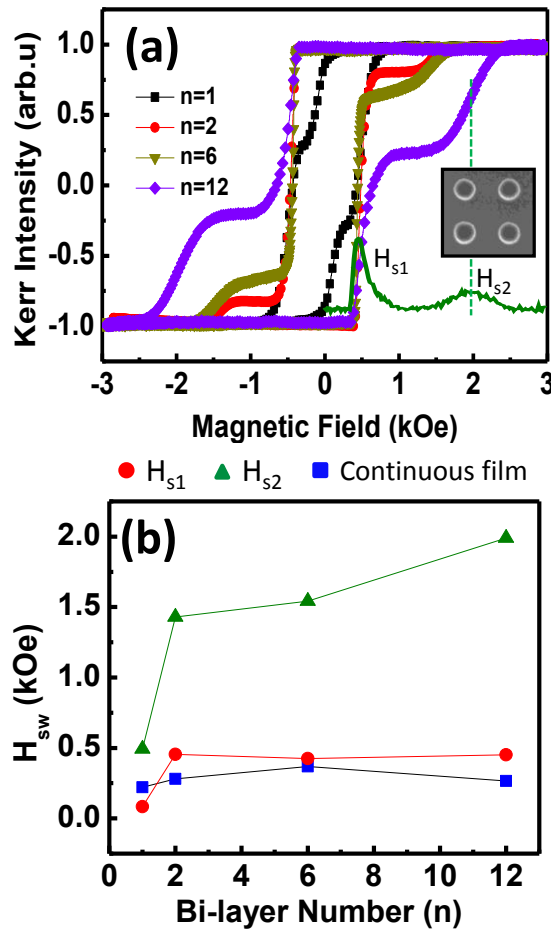


Fig. 4.5 (a) Hysteresis loops of pre-patterned Co/Pd dots with $d=185$ nm as a function of n ; and (b) A plot of H_{s1} , H_{s2} (defined in (a)) and the switching field of continuous films as a function of n .

Fig. 4.5(b) summarizes the H_{s1} and H_{s2} extracted from the M-H loops in Fig. 4.5(a). For direct comparison, the switching field of corresponding continuous films is also plotted as a function of n . The switching field H_{s1} of the Co/Pd antidot is slightly larger than the corresponding continuous films for

$n \geq 2$ due to domain wall pinning at the vicinity of the Si nanopillars. H_{s1} of the antidot stabilizes at ~ 450 Oe for $2 \leq n \leq 6$. For $n=1$, the extremely small H_{s1} (83 Oe) may come from the discrete nature of the Co film. Interestingly, H_{s2} of the Co/Pd dots is almost three times larger than H_{s1} of the antidot for all n . This is a direct effect of decreased number of domain nucleation sites. In the antidot region, the magnetization reversal process takes place by rapid domain wall propagation from a few nucleation sites which are usually the softest area with the lowest anisotropy. However, in the patterned dots, the probability of finding such nucleation sites decreases due to the reduction in the film area^[83]. We observed a significant increase of H_{s2} for the Co/Pd multilayer dots from 0.49 kOe to 1.99 kOe as n is increased from 1 to 12 due to increased intrinsic perpendicular anisotropy and reduced demagnetizing effects in thicker films^[133].

4.3.2 Effects of Dot Diameter

Shown in Fig. 4.6(a) are hysteresis loops of pre-patterned [Co(0.5 nm)/Pd(3 nm)]₁₂ structures as a function of pillar diameter d . Clearly, the Co/Pd dots on top of the pillars and the antidot in the pillar trench show different dependence on d . We have also plotted the extracted switching parameters (H_{s1} , H_{s2} , defined in Fig. 4.5 (a)) as a function of d for both the Co/Pd antidot and the dots, as shown in the inset of Fig. 4.6(a). While H_{s2} of the Co/Pd dots shows a significant decrease from 2.2 kOe to 1.36 kOe as d is increased from 170 nm to 205 nm, no clear dependence of H_{s1} is observed for the antidot due to the large defect size (i.e pillar diameter).

In antidots, magnetic switching is dependent on the ratio d/δ , where d is the antidot size and δ is the domain wall width^[28]. For $d/\delta < 1$, the coercivity increases linearly with d , reaching a maximum around $d/\delta \approx 1$. However, for large antidot defect sizes ($d/\delta > 1$), there are two possibilities which significantly depend on the magnetic parameters (i.e. magnetization,

magnetocrystalline anisotropy et al.) along the defect. If the magnetic parameters alter gradually, the switching field decreases with increasing defect size. However, if magnetic parameters vary abruptly, the switching field will be independent of the defect size^[28].

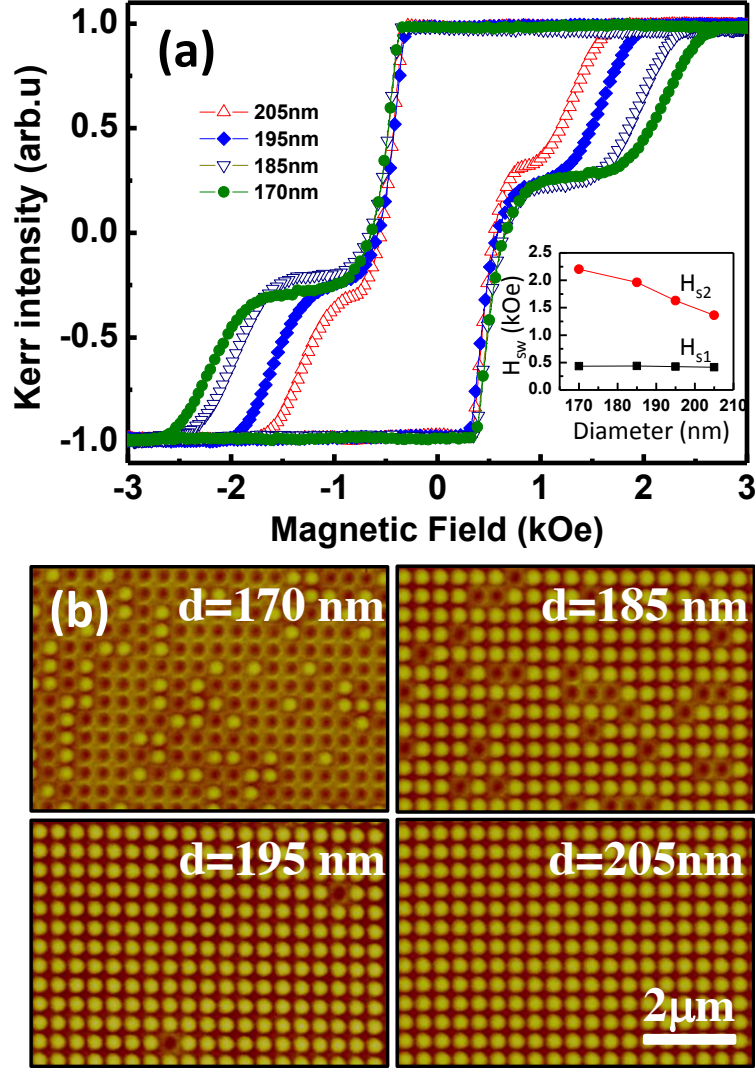


Fig. 4.6 (a) Hysteresis loops of pre-patterned $[\text{Co}(0.5 \text{ nm})/\text{Pd}(3 \text{ nm})]_{12}$ structures as a function of d (A plot of H_{s1} and H_{s2} as a function of d is shown as an inset); and (b) MFM images of the Co/Pd dots with varied d taken at remanence after the samples were first saturated in a field of -3.5 kOe followed by a reversal field of $+2.11 \text{ kOe}$.

In the antidot structure with perpendicular anisotropy, the domain walls are Bloch walls, and the wall width is given as^[25]:

$$\delta = \pi(A / K_u)^{1/2} \quad (4.1)$$

where A is the exchange stiffness constant and K_u is the intrinsic perpendicular anisotropy energy. Here, we calculated the Bloch wall width using the following parameters: $A=2 \times 10^{-6}$ erg/cm and $K_u=3.79 \times 10^6$ erg/cm³, which gives a domain wall width $\delta=22.8$ nm. K_u was extracted by VSM measurement of the corresponding Co/Pd continuous film with $n=12$. The calculation shows that the domain wall width of the Co/Pd antidot is much smaller than the pillar size (170~205 nm). The switching field thus should be independent of the defect size, which agrees well with our experimental observations.

The marked decrease of H_{s2} with increasing d might be due to the increase in demagnetizing effect and the presence of more nucleation sites. Larger dots have smaller length-to-diameter ratio and larger demagnetization factor^[133], resulting in stronger shape anisotropy given by^[134]:

$$K_{shape}^{dot} = N_{dot} (-2\pi M_s^2) \quad (4.2)$$

where $-2\pi M_s^2$ is the shape anisotropy of continuous film and N_{dot} is demagnetization factor of dots. The shape anisotropy favors in-plane magnetization^[62], which consequently reduces the perpendicular anisotropy in larger dots. In patterned Co/Pd dots, the magnetization reversal process is governed by a few domain nucleation sites which are usually the softest area with the lowest anisotropy. The probability of finding such nucleation sites increases in larger dots due to the increase in the film area^[83].

The $H_{s2}(d)$ dependence of the Co/Pd dots has been further verified using MFM imaging. Shown in Fig. 4.6(b) are the remanent MFM images captured at a fixed reversal field of +2.11 kOe after saturating the patterns in a field of -3.5 kOe for the Co/Pd dots with various d . Clearly, all the dots are in single domain state after DC magnetization. It can be observed that the reversal field of 2.11 kOe is large enough for bigger dots to be fully reversed (yellow contrast for $d = 205$ nm) in contrast to the smaller diameter dots ($d = 170$ nm) where only 28% of them have switched (yellow contrast corresponds to the reversed Co/Pd dots).

4.4 Magnetic Properties of Co/Pd Dot Clusters

4.4.1 Effects of Dipolar Coupling

When the Co/Pd dots are arranged in a closely packed pattern, magnetostatic interactions occur through dipolar coupling. In order to investigate the effects of dipolar coupling on the magnetic properties of Co/Pd dots, arrays of Co/Pd two-dot clusters with fixed dot diameter $d=600$ nm and varied edge-to-edge spacing s in the range from 100 nm to 600 nm were fabricated. Shown in Fig. 4.7(a) are hysteresis loops of the Pd(5 nm)/[Co(0.5 nm)/Pd(3 nm)]₂/Au(4 nm) two-dot cluster as a function s .

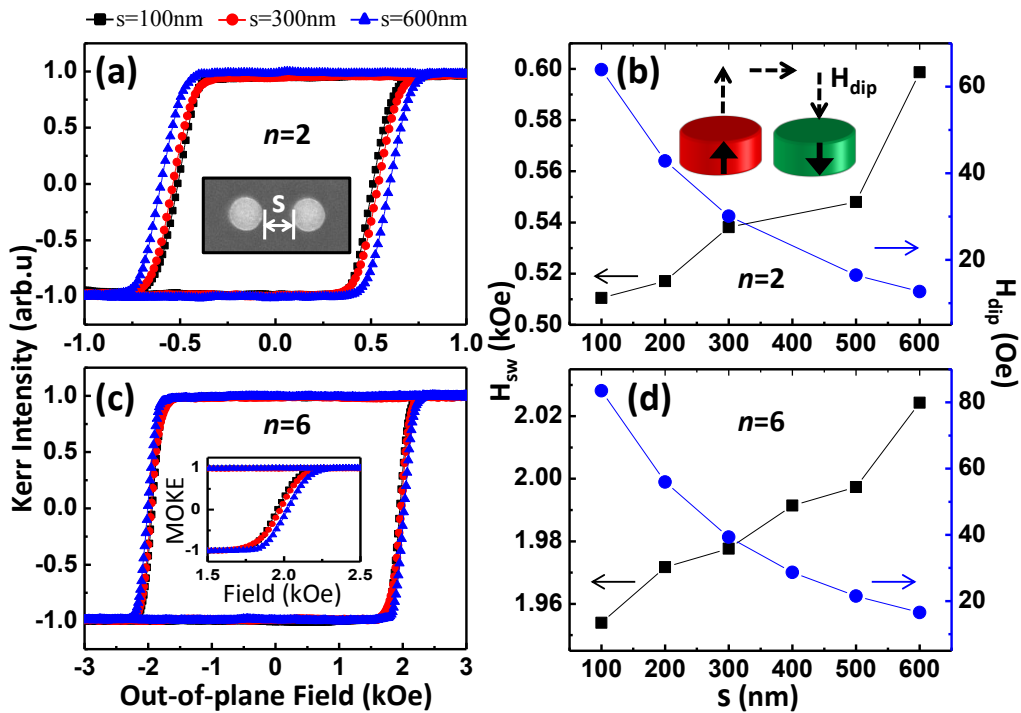


Fig. 4.7 (a) M - H loops of [Co(0.5 nm)/Pd(3 nm)]₂ two-dot clusters as a function of s ; and (b) A plot of measured H_{sw} (rectangular symbols) and calculated H_{dip} (circular symbols) as a function of s . The corresponding results for the [Co/Pd] _{n} dot cluster with $n=6$ are shown in (c) and (d) respectively.

Clearly, the switching field (H_{sw}) of the Co/Pd two-dot clusters is strongly dependent on s . Compared with the closely packed dot cluster ($s=100$

nm), the isolated one ($s=600$ nm) shows a much larger switching field due to reduced dipolar coupling (H_{dip}) between the Co/Pd dots. We have further extracted H_{sw} and plotted it as a function of s , as shown in Fig. 4.7(b) (rectangular symbols). There is a monotonic increase of H_{sw} from 510 Oe to 600 Oe as s is increased from 100 nm to 600 nm. This is a direct effect of reduced dipolar coupling strength between the two Co/Pd dots. Dipolar coupling tends to assist the magnetic switching of the two-dot cluster to form an antiparallel alignment of magnetization, as illustrated in the inset of Fig. 4.7(b).

We have also calculated the dipolar coupling field between the two Co/Pd dots by approximating the dot as a single microscopic spin. The calculation is based on the following equation^[135, 136]:

$$H_{dip} = M_s \cdot h_d \cdot \sum_{j \neq i} \frac{3(\hat{r}_{ij} \cdot \hat{m}_j) \cdot \hat{r}_{ij} - \hat{m}_j}{\tilde{r}_{ij}^3} \quad (4.3)$$

where h_d , \hat{r}_{ij} , \hat{m}_j and \tilde{r}_{ij} represent the ratio of dot volume to array cell volume, the unit distance vector, the unit moment vector of neighboring dots and the center-to-center distance in unit of dot pitch respectively. The saturation magnetization M_s used in the calculation was extracted from VSM measurements of the corresponding Co/Pd continuous film. The calculated H_{dip} as a function of s is shown in Fig. 4.7(b) (circular symbols). We observed a monotonic decrease of H_{dip} from 64 Oe to 13 Oe as s is increased from 100 nm to 600 nm. This calculated H_{dip} is of the same order of magnitude with the measured H_{sw} difference (90 Oe) for varied s . We do not expect to get the same value with the experiment because the above calculation can only provide rough estimation. Eq. (4.3) is valid for sufficiently small dot where single domain can be conserved. In our case, the single spin approximation was used which might not be as accurate in the large Co/Pd dot ($d=600$ nm).

Show in Fig. 4.7(c) are the measured hysteresis loops of the $[\text{Co/Pd}]_n$ dots

with $n=6$ as a function of s . We did not see clear H_{sw} difference in this field range because the H_{sw} is much larger than the H_{dip} . As the M-H loops are enlarged (inset of Fig. 4.7(c)), we again observed an increase of H_{sw} with s due to reduced dipolar coupling of neighboring Co/Pd dots. We have also plotted the extracted H_{sw} and the calculated H_{dip} for $n=6$, as shown in Fig. 4.7(d). There is a monotonic increase of H_{sw} from 1.955 kOe to 2.025 kOe as s is increased from 100 nm to 600 nm, which is related to the monotonic decrease of H_{dip} from 84 Oe to 17 Oe.

4.4.2 Implementation of Logic ‘NOT’ Using Coupled Co/Pd Dots

Based on the above discussion on dipolar coupling, in this section we further show that the dipolar coupling between neighboring two Co/Pd dots can be utilized for Boolean mapping, namely logical ‘NOT’ function.

4.4.2.1 Logical Schematic

The idea is based on the fact that the Co/Pd dots are in single domain state after DC demagnetization, therefore their spin “up” or “down” can be employed to represent logical “0” or “1”, respectively. Shown in Fig. 4.8 are schematics of the input and output for a two-dot cluster. The left dot “I” represents the input while the right dot “O” represents the output.

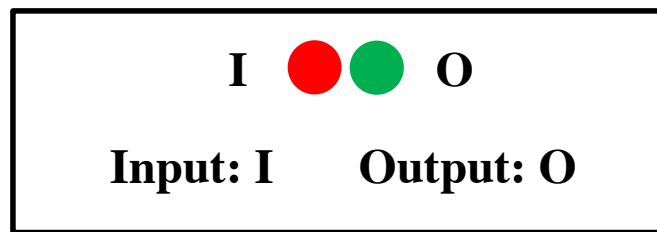


Fig. 4.8 Schematics of the input and output for a Co/Pd two-dot cluster.

Depending on the initial magnetization state of the input, the output attains the so called “favorable energy state” due to the magnetostatic

interactions. By accessing the favorable energy states of the elements, logical functions can be performed. To ensure large H_{dip} , the edge-to-edge spacing between the Co/Pd dots is fixed at $s=100$ nm.

In order to perform logical functions, it is important to first identify the available magnetic states and their equilibrium energies in each configuration. Therefore, to begin with, dipolar energy calculations of all the possible energy states were performed. Since the dots attain single domain configuration after DC demagnetization, they can be approximated by a single microscopic spin^[137, 138]. The total dipolar energy of the coupled dots with different configurations is then given by^[137]:

$$\sum_{i \neq j} E(\vec{r}_i, \vec{r}_j, \vec{m}_i, \vec{m}_j) = \sum_{i \neq j} \frac{1}{\|\vec{r}_{ij}\|^3} \left[\vec{m}_i \cdot \vec{m}_j - \frac{1}{\|\vec{r}_{ij}\|^2} (\vec{m}_i \cdot \vec{r}_{ij})(\vec{m}_j \cdot \vec{r}_{ij}) \right] \quad (4.4)$$

where \vec{m}_i and \vec{m}_j are the magnetic moments of two interacting dots i and j , and \vec{r}_{ij} is the distance vector between the centers of the two dots. The magnetic parameters used for calculations were extracted experimentally from VSM measurement of a [Co(0.5 nm)/Pd(3 nm)]₆ continuous film. The moment of each dot in our calculation is of the order of 10^8 Bohr magnetons which gives interaction energy between nearest neighbors of the order of 10^{-18} J. This energy is almost three orders larger than the thermal energy at room temperature which is large enough to overcome thermal fluctuations.

The calculated dipolar energies for the four possible energy states in the two-dot cluster are shown in Table 4.1. When the input I is “0”, output “1” causes the total dipolar energy to be negative which is lower than the case when output is “0”, thus (01) is more energetically favorable compared with (00). Similarly, state (10) is comparatively more favorable than (11). This shows that the dipolar coupling between the two dots results in antiferromagnetic type of coupling between them in which their magnetization tends to be antiparallel with each other. This configuration is indeed the lowest energy ground state for the two-dot cluster^[138], which is stable and can

therefore be employed to realize the ‘NOT’ function. We have also calculated the dipolar coupling field between the two Co/Pd dots based equation (4.3). The estimated dipolar field between the two Co/Pd dots is ~84 Oe which provides a comparatively large field tolerance to remain the favorable antiparallel spin configuration.

Input (I)	Output (O)	Energy (10 ⁻¹⁸ J)	Favored output	Boolean logic
0	1 (0)	-1.04 (1.04)	1	$O = \bar{I}$
1	0 (1)	-1.04 (1.04)	0	

Table 4.1 Favorable energy states based on dipolar energy calculation of all the possible input and output combinations in [Co(0.5nm)/Pd(3nm)]₆ two-dot cluster with s=100 nm.

The ‘NOT’ gate can be controlled by an external clock-field, which is an oscillating magnetic field consisting of a sequence of one up pulse followed by one down pulse. The input of the two-dot cluster can be set to “0” or “1” by an external negative or positive saturation field, respectively. The amplitude of the clock-field is high enough to attain antiparallel configuration but not large enough to achieve parallel configuration. Therefore, after one clock-field cycle, initial parallel magnetization state (00) or (11) can be switched to antiparallel state (01) or (10), while initial antiparallel magnetization state of (01) or (10) remains unchanged. Thus, a two-dot cluster can perform logical function ‘NOT’.

4.4.2.2 Experimental Verification

The above predicted logic functions have been experimentally verified using MFM imaging of a Pd(5 nm)/[Co(0.5 nm)/Pd(3 nm)]₆/Au(4 nm)

multilayer two-dot cluster with $s=100$ nm. Shown in Fig. 4.9(a) are MFM images taken at remanence after the two-dot cluster was first saturated in magnetic fields of ∓ 3 kOe followed by a clock-field cycle of amplitude ± 1.96 kOe, respectively. The ∓ 3 kOe fields were used to initialize the two-dot cluster to states (00) and (11), respectively. The uniform red (yellow) contrast shows the single domain state of the dots, indicating that the microscopic spin approximation used in the dipolar energy calculations is valid. The red and yellow colors correspond to spin “up” and “down”, representing logical “0” and “1” respectively. Depending on the direction of the saturation field, input was initially set at either “0” or “1” and the output always showed corresponding “1” or “0” after one clock-field cycle, which confirmed the logical function ‘NOT’.

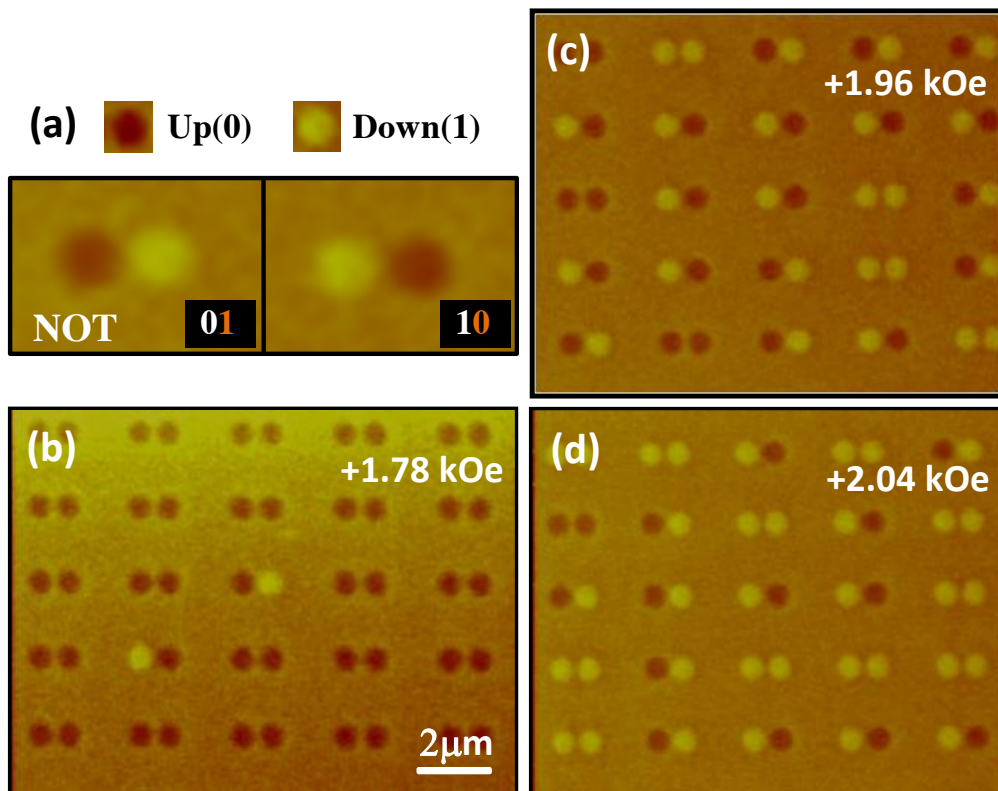


Fig. 4.9 (a) MFM images of the two-dot cluster with states of (01) and (10) taken at remanence after the sample was first saturated by external fields of ∓ 3 kOe followed by a clock-field of amplitude ± 1.96 kOe respectively. MFM image of a 5×5 dot cluster array taken after a saturation field of -3 kOe followed by a reversal field of (b)+1.78 kOe; (c)+1.96 kOe; and (d)+2.04 kOe respectively.

To verify the stability of the ‘NOT’ gate, MFM measurement was performed on an array of 5×5 gate cells. Shown in Figs. 4.9(b-d) are the MFM images of the gate array taken after applying a saturation field of -3 kOe followed by various reversal fields. All the gate cells were initialized to (00) state after the application of negative saturation field. Subsequent reversal field of +1.78 kOe switches 2 out of the 25 cells into antiparallel magnetization state. Further increase in the reversal field to +1.96 kOe results in 18 out of the 25 cells falling into antiparallel magnetization configuration, in which 10 cells are in state (10) while the other 8 cells are in state (01) resulting from slightly softer input, which can also perform logical ‘NOT’ function. The antiparallel state in 72% of the two-dot cluster cells indicates the implementation of ‘NOT’ function in majority gate cells. As the reversal field reaches +2.04 kOe, some gate cells were saturated to form (11) state, leaving 13 gate cells in antiparallel state. Our results are satisfactory since they agree well with our energy calculations and show promise for future magnetic logic applications using dipolar coupling of Co/Pd dots.

4.5 Magnetic Properties of $[\text{Co/Pd}]_4/\text{Au}/[\text{Co/Pd}]_2$ Rings

In this section, we investigate the effects of interlayer coupling and inter-ring dipolar coupling on the magnetization reversal of $\text{Pd}(5 \text{ nm})/[\text{Co}(0.5 \text{ nm})/\text{Pd}(3 \text{ nm})]_4/\text{Au}(t_{\text{Au}})/[\text{Co}(0.5 \text{ nm})/\text{Pd}(3 \text{ nm})]_2$ PSV rings by varying the Au spacer layer thickness t_{Au} and edge-to-edge spacing s . Schematics of the deposited film structure and representative SEM micrographs of the PSV rings have been shown in Fig. 4.2. The bottom four bi-layer ($n=4$) and the upper two bi-layer ($n=2$) Co/Pd stacks serve as the hard and the soft FM layers respectively due to the difference in switching field.

4.5.1 Structure Analysis of [Co/Pd]₄/Au/[Co/Pd]₂ Films

Shown in Fig. 4.10 are XRD patterns of continuous PSV films as a function of t_{Au} . We observed clear CoPd(111) peaks between $2\theta=40.4^\circ$ and $2\theta=40.5^\circ$ while individual Au peaks with incrementally increase in intensity were found at around 39.2° , 38.8° , and 38.6° for $t_{Au}=1, 2,$ and 8nm , respectively. The Au(111) peak shifts towards the Au bulk value (38.2°) as the thickness increases, indicating the reduced compressive stress placed by the Co/Pd stacks. As the lattice constant of Co/Pd stacks (3.54 \AA (for Co) $< a < 3.89\text{ \AA}$ (for Pd)) is smaller than that of Au ($a=4.078\text{ \AA}$), it will exert a compressive stress on the Au spacer layer, which is extremely strong for 1 nm and 2 nm thick Au films. However, as Au spacer layer becomes thicker, it will overcome some of the compressive stress, thus moving the XRD peak closer to the bulk value. Meanwhile, the Au spacer will cause an increased tensile stress on the Co/Pd multilayer stacks as Au layer become thicker, which is verified by the slight downwards shift of the CoPd(111) peak ($\sim 0.1^\circ$). A weak Co(002) peak was also observed at around 43.8° in the curve for $t_{Au}=8\text{ nm}$.

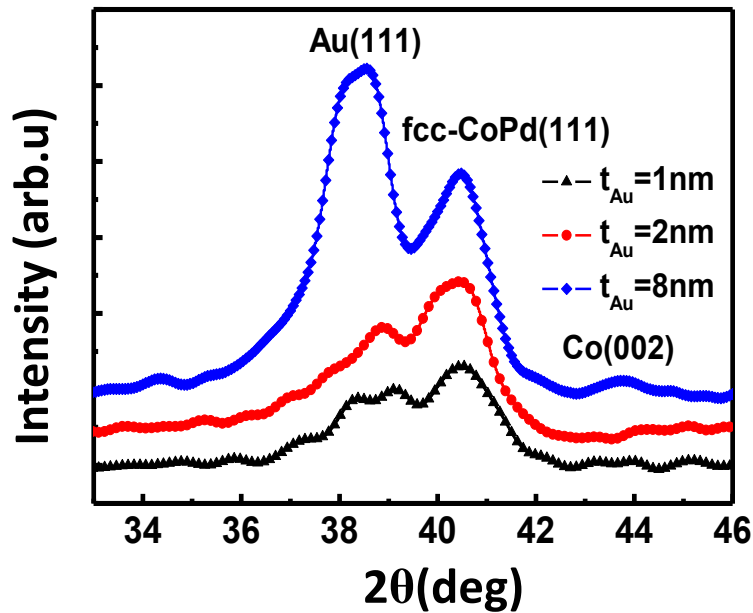


Fig. 4.10 XRD patterns of [Co/Pd]₄/Au(t_{Au})/[Co/Pd]₂ PSV films as a function of t_{Au} .

4.5.2 Effects of Interlayer Coupling

Shown in Fig. 4.11(a-d) are hysteresis loops of $[\text{Co/Pd}]_4/\text{Au}(t_{\text{Au}})/[\text{Co/Pd}]_2$ PSV nanorings with fixed $s=450$ nm as a function of t_{Au} . The hysteresis loop of the PSV nanorings with $t_{\text{Au}}=1$ nm shows a single-step switching due to direct interlayer exchange coupling between the two FM layers^[96, 100]. As a result, the two FM Co/Pd stacks are strongly coupled, resulting in a collective magnetization reversal of both the top and bottom Co/Pd multilayer stacks. As shown in Fig. 4.11(a), the switching behavior of the PSV nanorings with $t_{\text{Au}}=1$ nm is somewhat similar to that of individual four bi-layer rings ($n=4$), indicating that the hard bottom FM stack dominates the magnetization reversal of the structure. However, for the PSV nanorings with $t_{\text{Au}} \geq 2$ nm, two distinct steps are observed corresponding to the magnetic switching of the top Co/Pd bi-layer stack ($n=2$) at lower field H_{s1} and the bottom Co/Pd bi-layer stack ($n=4$) at higher field H_{s2} , respectively. The magnetization state of top FM stack reverses more easily due to the smaller number of Co/Pd elements.

In the PSV nanorings with $t_{\text{Au}}=2$ nm, the top Co/Pd stack shows a larger switching field, while the bottom stack shows a smaller switching field compared to that of individual Co/Pd stacks with $n=2$ (not shown here) and $n=4$ respectively. This is due to the interlayer coupling between the two FM stacks. The field offset of 81 Oe in the minor loop shown in Fig. 4.11(b) is a direct evidence of this interlayer coupling. As the Au spacer layer thickness increases, exchange coupling between the two FM stacks becomes weaker and magnetostatic coupling becomes more dominant, thus a two-step switching is clearly seen for the PSV nanorings with $t_{\text{Au}}=5$ nm and $t_{\text{Au}}=8$ nm. Interestingly, the bottom bi-layer stack ($n=4$) of the PSV rings with $t_{\text{Au}}=8$ nm shows a switching field (1.18 kOe) much larger than that of individual stacks with $n=4$ (0.67 kOe). This is due to the tensile stress mentioned before, which in turn enhances the perpendicular anisotropy of the bottom Co/Pd stack^[22].

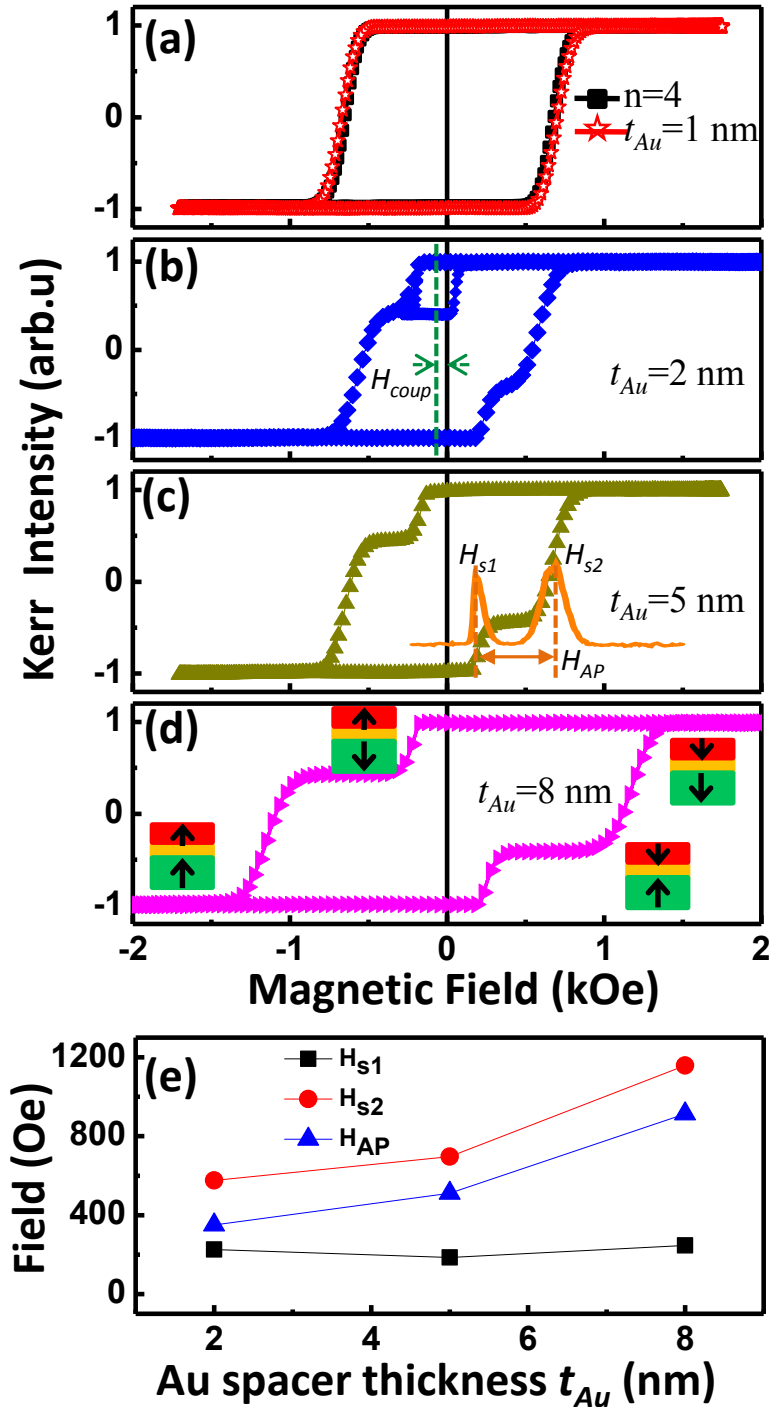


Fig. 4.11 M-H loops for $[Co/Pd]_4/Au(t_{Au})/[Co/Pd]_2$ PSV rings with (a) $t_{Au} = 1$ nm, compared with the hysteresis loop of $[Co/Pd]_4$ multilayer rings; (b) $t_{Au} = 2$ nm; (c) $t_{Au} = 5$ nm (d) $t_{Au} = 8$ nm; and (e) a plot of H_{s1} , H_{s2} , H_{AP} (defined in (c)) as a function of t_{Au} .

Shown in Fig. 4.11(e) is a summary of the switching parameters H_{s1} , H_{s2} and H_{AP} (defined in Fig. 4.11(c)) of the PSV rings as a function of t_{Au} . H_{AP} represents the stable field range over which the two FM stacks remain in

antiparallel state. Clearly, as t_{Au} is increased from 2 nm to 8 nm, H_{s1} of the soft bi-layer stack ($n=2$) changes slightly from 226 Oe to 246 Oe, whereas H_{s2} of the hard stack ($n=4$) increases drastically from 576 Oe to 1159 Oe. This consequently results in a significant increase of H_{AP} from 350 Oe to 913 Oe as the two FM stacks are exchange decoupled. The slight change of H_{s1} for the top Co/Pd stack ($n=2$) may be attributed to several factors. First, the lattice mismatch causes an increase in the tensile stress of the top Co/Pd stack as t_{Au} increases, which in turn enhances the perpendicular anisotropy. However, this enhancement may be weakened by reduced magnetostatic coupling. Magnetostatic coupling between the two FM stacks favors parallel alignment of magnetization of the stacks in PSV rings. Therefore, the bottom hard Co/Pd stack will constrain the magnetic switching of the top soft Co/Pd stack and plays a pinning effect. This pinning strength will become weaker in PSV rings with thicker Au spacer layer, leading to a reduction of H_{s1} .

4.5.3 Effects of Inter-ring Dipolar Coupling

We have also investigated the effects of dipolar coupling between the PSV nanorings on the magnetization reversal process by varying the rings edge-to-edge spacing s while keeping all the other geometrical parameters fixed. Shown in Fig. 4.12(a) are hysteresis loops of the PSV rings for $t_{Au}=1$ nm as a function of s . Only a single step switching is observed in all the loops due to the direct ferromagnetic coupling between the two FM stacks as mentioned before. The switching field of the loops is found to be markedly sensitive to s , showing a large increase from 670 Oe to 823 Oe as s is increased from 350 nm to 650 nm due to reduced dipolar interactions between neighboring nanorings^[139, 140]. Similar influence of dipolar coupling on switching field has been previously observed in Co/Pd multilayer dots in section § 4.4.1.

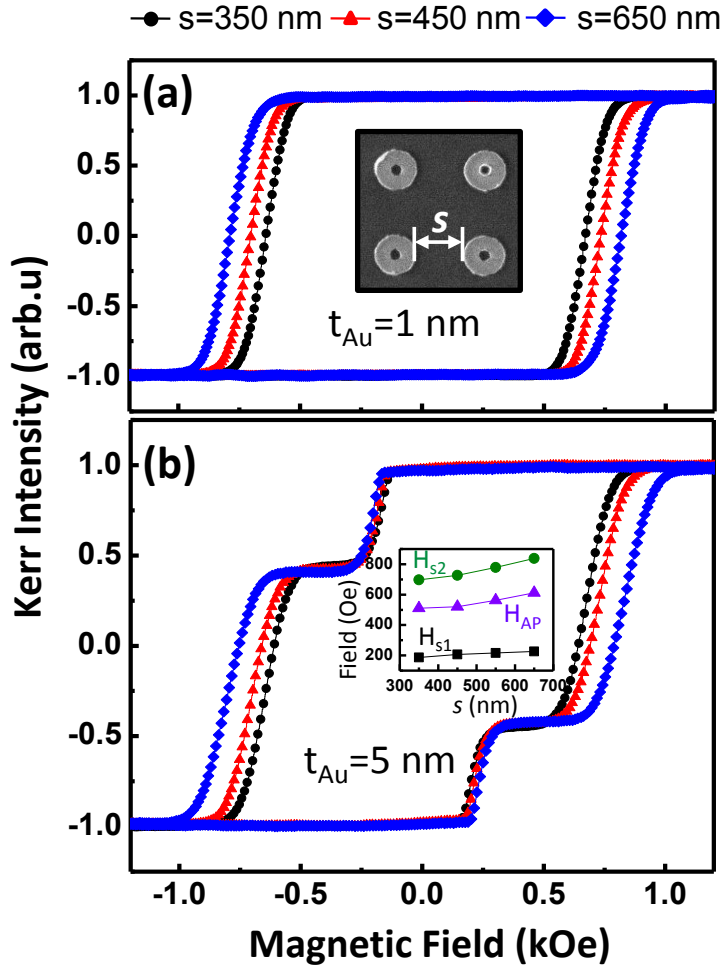


Fig. 4.12 Polar MOKE M-H loops of $[Co/Pd]_4/Au(t_{Au})/[Co/Pd]_2$ PSV rings as a function of edge-to-edge spacing s for (a) $t_{Au}=1$ nm; and (b) $t_{Au}=5$ nm (A plot of H_{s1} , H_{s2} and H_{AP} as a function of s is shown as an inset).

Shown in Fig. 4.12(b) are the polar MOKE hysteresis loops for PSV nanorings with $t_{Au}=5$ nm as a function of s . Two distinct switching steps are observed in all the loops, corresponding to the magnetic switching of top Co/Pd bi-layer stacks ($n=2$) at H_{s1} and bottom Co/Pd bi-layer stacks ($n=4$) at H_{s2} , respectively. H_{s1} of top Co/Pd stacks does not vary significantly with s . However, H_{s2} of the bottom Co/Pd stacks increases notably as s is increased. We have also extracted H_{s1} , H_{s2} and H_{AP} (defined in Fig. 4.11(c)) and plotted them as a function of s , as shown in the inset of Fig. 4.12(b). H_{s1} shows slight increase from 186 Oe to 226 Oe whereas H_{s2} increases prominently from 697 Oe to 838 Oe with as s is increased from 350 nm to 650 nm due to the reduced

dipolar coupling strength. Consequently, H_{AP} of the PSV rings increase monotonically from 511 Oe to 612 Oe. This huge dependence of switching field and H_{AP} on s provides a promising way to engineer the magnetic properties of PSV rings.

4.6 Summary

The magnetization reversal processes of circular Co/Pd nanodots and nanorings have been systematically investigated. For the $[\text{Co/Pd}]_n$ multilayer films deposited on pre-patterned high-aspect ratio Si nano-pillars, the switching field of Co/Pd antidot in the trench area shows no clear dependence on the bi-layer repeat n and the pillar diameter d due to the large defect size, while that of the Co/Pd dots on top of the pillars is significantly dependent on the two parameters. When the Co/Pd dots are densely arranged in a two-dot cluster, dipolar coupling strongly affect the switching behaviors, which might be employed for the application of magnetic logic ‘NOT’.

Further investigation of interlayer coupling was carried out in $[\text{Co/Pd}]_4/\text{Au}(t_{\text{Au}})/[\text{Co/Pd}]_2$ PSV rings by varying the Au spacer layer thickness t_{Au} . It was observed that exchange coupling dominates the magnetization reversal process in PSV rings with $t_{\text{Au}} = 1$ nm, while magnetostatic coupling plays a more significant role for thicker Au spacer layer. The magnetic switching behavior of the PSV nanorings was also found strongly dependent on the ring edge-to-edge spacing.

Chapter 5

Magnetic and Transport Behaviors of Co/Pd Nanowires

5.1 Introduction

This chapter presents a systematic investigation of magnetization reversal process and magnetoresistance (MR) behaviors of $[\text{Co/Pd}]_n$ multilayer nanowires (NWs) and $[\text{Co/Pd}]_4/\text{Au}/[\text{Co/Pd}]_2$ PSV NWs in the temperature range of $5 \text{ K} \leq T \leq 300 \text{ K}$. It was observed that MR responses of the Co/Pd NWs are markedly dependent on both the bi-layer repeat n and temperature T . The effects of interlayer coupling on magnetic switching and MR behaviors of the PSV NWs are also investigated. It will be shown that compared with continuous (un-patterned) films deposited at the same time, the PSV NWs display a much stronger temperature dependent interlayer coupling due to stray field interactions. The interlayer coupling has also been investigated in $[\text{Co/Pd}]_4/\text{Co}/\text{Ru}/[\text{Co/Pd}]_2$ PSV films with a Ru spacer, where RKKY type of interlayer coupling was observed.

5.2 Experimental Details

Arrays of $\text{Pd}(5 \text{ nm})/[\text{Co}(0.5 \text{ nm})/\text{Pd}(3 \text{ nm})]_n$ NWs of width $w=340 \text{ nm}$, length $l=4 \text{ mm}$ and edge-to-edge spacing $s=80 \text{ nm}$ were fabricated on silicon substrates using deep ultraviolet lithography at 248 nm wavelength followed by the lift-off process^[3]. Details of the fabrication process has been described in § 3.2. The bi-layer repeat n was varied from 4 to 18. Shown in Fig. 5.1(a) is a representative SEM micrograph of arrays of Co/Pd NWs with $n=18$.

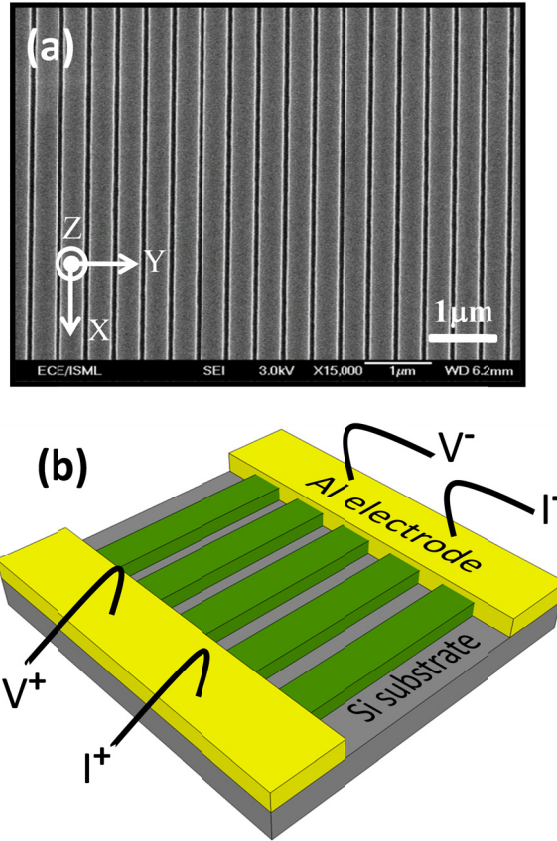


Fig. 5.1 (a) Representative SEM micrograph of arrays of $[\text{Co}(0.5 \text{ nm})/\text{Pd}(3 \text{ nm})]_{18}$ NWs; and (b) Schematics of the Co/Pd NWs including Al bond pads for MR measurements.

We have also fabricated $\text{Cu}(t_{\text{Cu}})/\text{Pd}(5 \text{ nm})/[\text{Co}(0.5 \text{ nm})/\text{Pd}(3 \text{ nm})]_4$ NWs by adding a Cu buffer layer prior to the Co/Pd multilayer stack to enhance perpendicular anisotropy. The Cu layer thickness t_{Cu} was varied in the range from 5 nm to 40 nm. Based on the switching field dependence on the $[\text{Co}/\text{Pd}]_n$ bi-layer repeat n , arrays of NWs with a PSV structure of $\text{Cu}(15 \text{ nm})/\text{Pd}(5 \text{ nm})/[\text{Co}(0.5 \text{ nm})/\text{Pd}(3 \text{ nm})]_4/\text{Au}(t_{\text{Au}})/[\text{Co}(0.5 \text{ nm})/\text{Pd}(3 \text{ nm})]_2$ were then fabricated. The upper $[\text{Co}/\text{Pd}]_2$ stack and the bottom $[\text{Co}/\text{Pd}]_4$ stack serve as the soft and hard FM layers respectively. The Au spacer layer thickness was varied from 1 nm to 8 nm while the Cu buffer layer was fixed at 15 nm. For direct comparison, the corresponding continuous Co/Pd PSV films were also deposited at the same time with the PSV NWs.

The structural properties and roughness of the Co/Pd multilayer films were characterized using X-Ray Diffractometer (XRD) and X-Ray

Reflectometry (XRR), atomic force microscopy respectively. The collective magnetic switching behaviors of the Co/Pd NWs were characterized using a focused polar Magneto-Optical Kerr Effect (MOKE) setup with external magnetic field applied perpendicular to the plane of the samples. In order to probe the MR behavior, electrical contacts were placed on top of the Co/Pd NWs using ultraviolet lithography followed by sputtering deposition of 200 nm Al and lift-off process. MR measurements were conducted using the standard four probe technique with a constant DC current of 1 mA (5 mA) for the NWs (corresponding continuous films) in the temperature range of $5 \text{ K} \leq T \leq 300 \text{ K}$. Shown in Fig. 5.1(b) are schematics of Co/Pd NWs including Al bond pads for MR measurements. The frame of reference used is shown in Fig. 5.1(a). We refer to the MR behaviors as longitudinal, transverse and perpendicular MR responses when the external field is applied along X, Y and Z axes respectively.

5.3 Magnetic Behaviors of Co/Pd Nanowires

In this section, The magnetization reversal and MR behaviors of Pd(5 nm)/[Co(0.5 nm)/Pd(3 nm)]_n multilayer NWs are investigated as a function of the bi-layer repeat n which was varied from 4 to 18 in the temperature range of $5 \text{ K} \leq T \leq 300 \text{ K}$. Schematics of the deposited film structure is shown in Fig. 5.2(a).

5.3.1 Room Temperature

Shown in Fig. 5.2(b-d) are the room temperature hysteresis loops combined with perpendicular MR curves of the [Co/Pd]_n NWs as a function of n . Clearly, magnetic switching of the [Co/Pd]_n NWs is markedly dependent on n . As n is increased from 4 to 18, a significant increase of switching field (H_{sw}) from 0.788 kOe to 1.16 kOe is observed due to increased intrinsic

perpendicular anisotropy and the reduced demagnetizing effects in thicker NWs. We also observe a good agreement between the MR peak position and H_{sw} of the hysteresis loops, corresponding to magnetization reversal of the NWs^[141]. The MR ratio is defined as:

$$MR = \frac{R(H) - R(H_{max})}{R(H_{max})} \times 100\% \quad (5.1)$$

where $R(H)$ and $R(H_{max})$ are the resistance of the sample at an applied magnetic field of H and the maximum field H_{max} respectively.

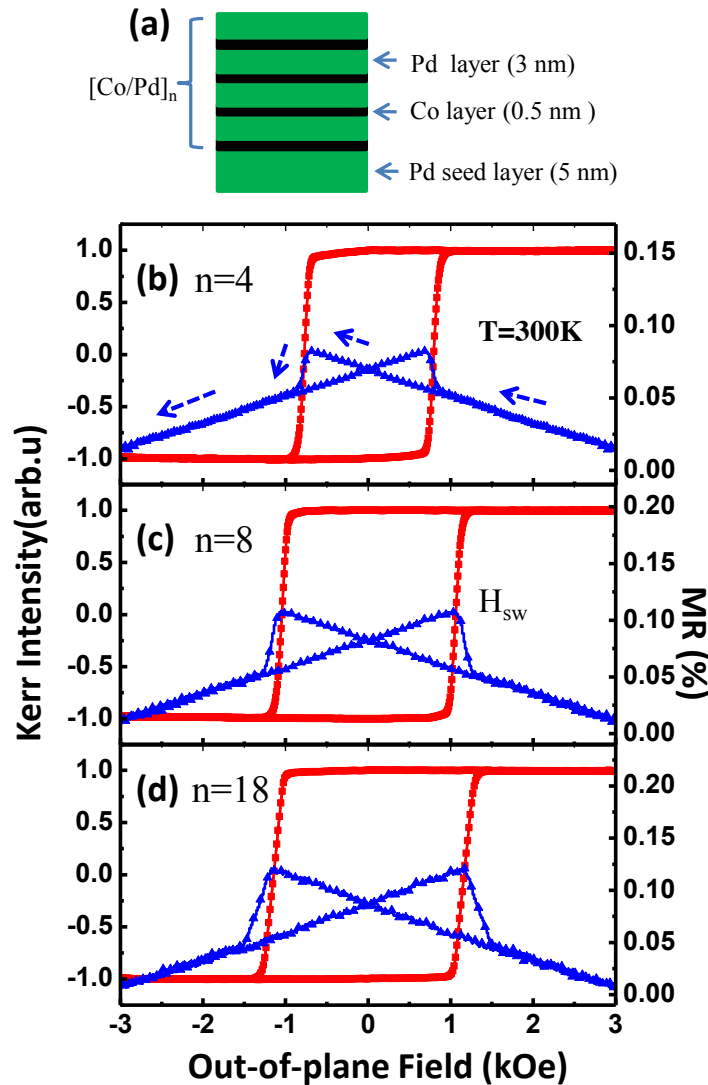


Fig. 5.2 (a) Schematics of deposited film structure for $[Co(0.5 \text{ nm})/Pd(3 \text{ nm})]_n$ NWs. M - H loops and perpendicular MR responses of the NWs for (b) $n=4$; (c) $n=8$; and (d) $n=18$.

As shown in the hysteresis loops, when the $[\text{Co/Pd}]_n$ NWs are magnetically saturated, a linear decrease in the resistivity with the applied field can be clearly seen for all n . This behavior, known as magnon magnetoresistance (MMR) effect, has been previously reported in continuous films of 3d ferromagnetic layers^[92, 93]. The linear variation in resistivity was attributed to the spin wave damping at high field corresponding to a decrease in the intrinsic spin disorder. At high field, there is a significant reduction in the electron-magnon scattering. The resistivity variation of a ferromagnetic material at a given temperature is mainly resulted from three contributions^[94], namely, anisotropic magnetoresistance (AMR), intrinsic domain wall resistance (DWR) and MMR. Since the magnetization of the Co/Pd NWs at high field is perpendicular to the applied sense current, and no domain wall exists at saturation states, the MR contributions from AMR and DWR are negligible at the high field region. Therefore, the linear variations of resistivity above saturation fields in Fig. 5.2(b-d) may simply correspond to the MMR effect. Interestingly, the linear MR behavior can also be observed in the low field and even negative field region where magnetization of the NWs and applied fields are anti-parallel. This is a direct effect of the strong perpendicular anisotropy of the Co/Pd multilayers, which is efficient to maintain the magnetization at low field and negative field. The linear MR behavior thus extends. Similar results have been observed in FePt films (and NWs) with strong magnetocrystalline anisotropy^[91, 94] and narrow $\text{Ni}_{80}\text{Fe}_{20}$ NWs with large shape anisotropy^[37, 95]. Interestingly, even though the Pd layers are non-magnetic, the Co/Pd multilayer structure shows similar MMR behavior with the FePt single layer films. In the Co/Pd multilayer structure, the Pd layers are magnetically polarized in such a way that the induced polarization reaches maximum at the Co/Pd interface and becomes weaker as the Pd atoms are far away from the interface^[78]. The Co/Pd multilayer thus performs as a non-uniformly magnetized ferromagnetic layer.

5.3.2 Temperature Dependence

5.3.2.1 Perpendicular MR Response

We have further investigated the temperature dependence of MR behavior of the $[\text{Co/Pd}]_n$ NWs as a function of n in the field range of ± 40 kOe. Shown in Fig. 5.3 is a typical full loop MR curve of the perpendicular MR response for the $[\text{Co/Pd}]_n$ NWs with $n=4$ taken at $T=5$ K. The rectangular symbols represent the descending half loop with field swept from positive saturation to negative saturation whereas the circular symbols indicate the reversed sweep. Since the two half loops are essentially symmetric, we will focus only on the descending half loop in the field range of ± 10 kOe for clarity in the following discussion.

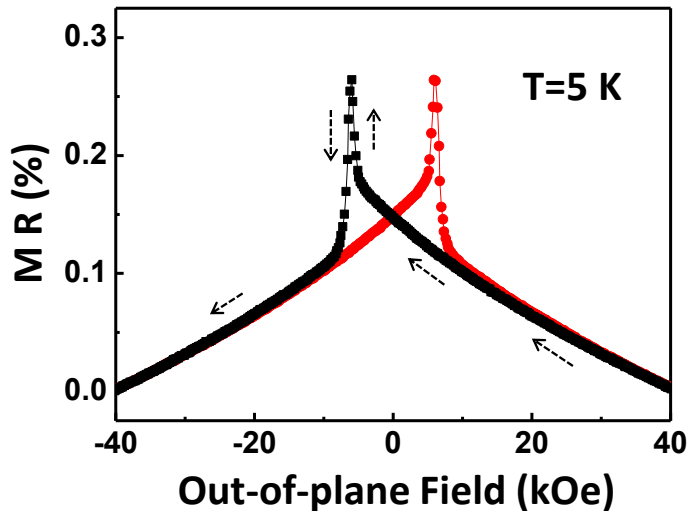


Fig. 5.3 Perpendicular MR response of the $[\text{Co/Pd}]_4$ NWs at $T=5$ K.

Shown in Fig. 5.4(a) are the descending half loop of the perpendicular MR response for the $[\text{Co/Pd}]_n$ NWs with $n=4$ as a function of T . The MR response can be broadly divided into two parts, namely: high field and the switching regions, both of which are temperature dependent. The linear MR response at high field up to the maximum applied field is attributed to the

MMR behavior as discussed before. As the temperature is decreased, the MMR effect is less obvious due to reduced magnon population^[94], as suggested by the decreased linear MR slope.

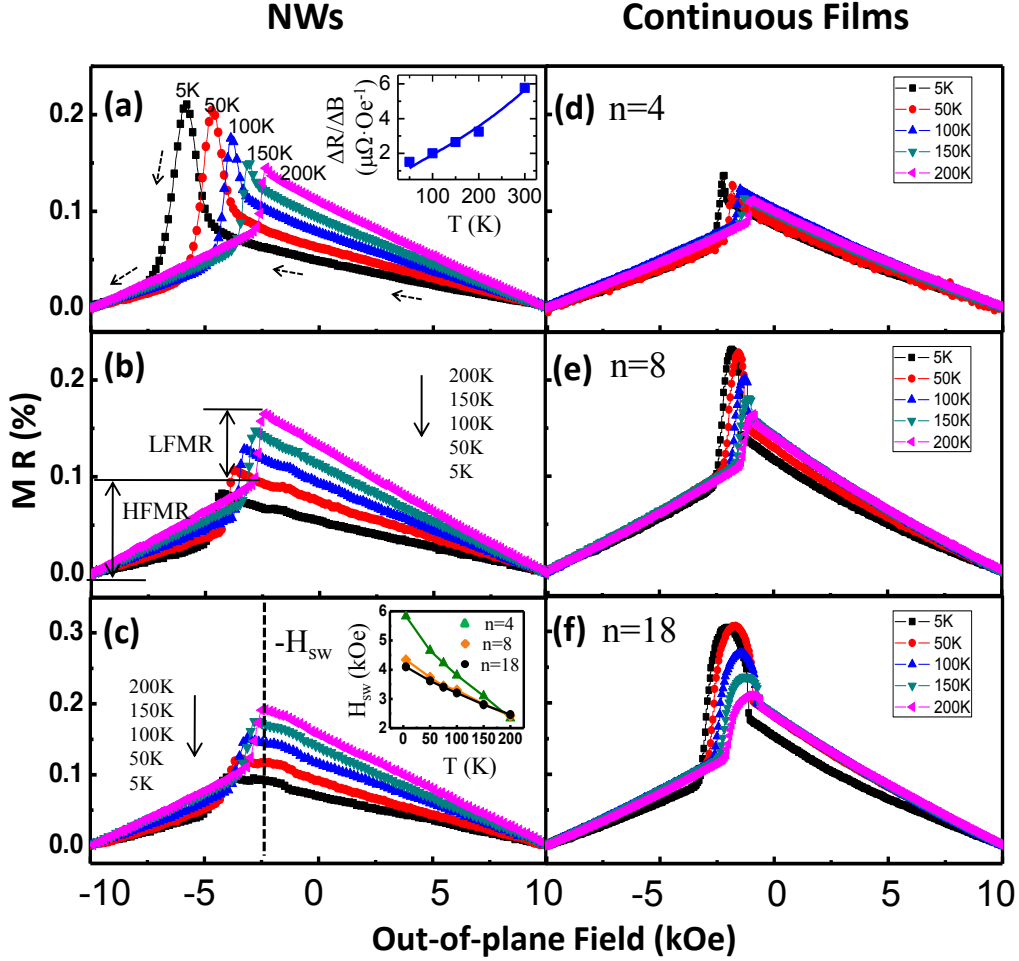


Fig. 5.4 Perpendicular MR responses as a function of T for the $[\text{Co/Pd}]_n$ NWs with (a) $n=4$ (Experimental MR slope (solid symbol) with fitted MMR curve (solid line) is shown as an inset); (b) $n=8$; and (c) $n=18$ (A plot of H_{sw} Vs T extracted from the MR responses as a function of n is shown as an inset). The perpendicular MR responses for the corresponding continuous $[\text{Co/Pd}]_n$ films with $n=4, 8$ and 18 are shown in (d), (e) and (f) respectively.

In order to further confirm that the linear variation in resistivity indeed comes from the MMR effect, we have plotted the extracted MR slope as a function of T and fitted to the MMR contributions using^[92, 94, 142]:

$$\frac{\partial \Delta R(T)}{\partial \Delta B} \propto T (1 + 2dT^2) [\ln(T) + C^{te}] \quad (5.2)$$

where d is a constant of the order of 10^{-6} K^{-2} and C^{te} is a temperature-independent term. The second term (i.e. $1+2dT^2$) in the right part of Eq. (5.2) indicates how the temperature affects the effective magnon mass. This has been shown as an inset in Fig. 5.4 (a). There is a good agreement between the extracted experimental data (solid symbol) and fitting results (solid line), suggesting that the MMR effect is actually the source of the linear MR. The fitting parameter $d=5.4 \times 10^{-6} \text{ K}^{-2}$ has similar order of magnitude with that obtained in FePt films with perpendicular anisotropy^[94].

The MR behavior in the switching region is also strongly dependent on T . At $T=200 \text{ K}$, there is a sharp switching from the anti-parallel states (between the magnetization of the NWs and the applied field) to the parallel state configurations. As T is decreased, the switching exhibits a gradual transformation (for example, see the MR curve for $T=5 \text{ K}$). Unlike the high field region, the contributions of both the AMR and DWR to the overall resistivity in this region are very significant. These contributions become more prominent at low T when the MMR effect is drastically reduced.

Shown in Fig. 5.4(b) are the perpendicular MR responses for the $[\text{Co/Pd}]_n$ NWs with $n=8$ as a function of T . The MR responses can also be divided into the high field and switching regions. While the high field linear MR response follows the same trend as discussed above for the NWs with $n=4$, the behavior in the switching regions is strikingly different. There is no transformation peak and the abrupt switching from the anti-parallel configuration to the parallel magnetic state in the MR curves is consistent for all T . The absence of gradual transformation may indicate a different magnetization reversal mechanism. As expected, when the bi-layer repeat n is increased from 4 to 8, there is a big reduction in magnetic domain size^[129] which may lead to a complex magnetic switching. We have indeed confirmed using magnetic force microscopy that the domain size is smaller for multilayers with larger n , as has been described in § 4.3.1.1.

For completeness, we show in Fig. 5.4(c) the MR responses of $[\text{Co/Pd}]_n$ NWs for $n=18$ as a function of T . The MR responses are very similar to that of $[\text{Co/Pd}]_n$ NWs with $n=8$. We have extracted the switching field (H_{sw}) corresponding to the transition regions from anti-parallel state to parallel configuration for the NWs and plotted it as a function of n for comparison, as shown in the inset of Fig. 5.4(c). We see clearly that the NWs with $n=8$ and 18 follow the same temperature dependence suggesting that the same reversal mechanism is involved in the magnetic switching process. For the NWs with $n=4$, a much stronger dependence of H_{sw} on T is observed.

Shown in Fig. 5.4(d-f) are the perpendicular MR responses of the corresponding continuous Co/Pd films deposited under identical conditions as the NWs. The MR behavior of the Co/Pd continuous films is markedly different from the NWs shown in Fig. 5.4(a-c). While there are also linear and switching field regions, the linear MR responses are not strongly dependent on T suggesting that magnetostatic energy plays a crucial role in determining the MR response. In the switching regions, the gradual transformation is observed at low T for all n .

In order to further understand the MR behaviors of the Co/Pd NWs at low T , we have extracted the MR ratio from Fig. 5.4 and plotted it as a function of T for both the Co/Pd NWs and corresponding continuous films, as shown in Fig. 5.5. The MR response is divided into two parts, namely, high field MR contribution (HFMR, defined in Fig. 5.4(b)) and low field MR contribution (LFMR). The HFMR mainly arises from MMR, while the LFMR is a combined effect of MMR and possibly AMR and DWR effects. Clearly, the MR ratios are markedly dependent on T . While the HFMR shows a similar monotonic increase with T for the NWs with all n , the contributions from LFMR are markedly different, as shown in Fig. 5.5(a-c).

For the NWs with $n=4$ (Fig. 5.5(a)), LFMR decreases significantly from 0.2% to 0.05% as the temperature is increased from $T=5$ K to $T=200$ K,

leading to the marked decrease of total MR ratio. This is in contrast to the NWs with $n=8$ and $n=18$ (Fig. 5.5(b & c)), where a large increase of total MR ratio with T is seen due to the small temperature independence of LFMR. The difference in temperature dependence of the LFMR may indicate a different MR mechanism involved in the switching region as n is varied. Based on the fact that the AMR and DWR decrease with increase in temperature^[91, 143-145] while the MMR is enhanced at higher T ^[91, 92], it is easy to deduce that AMR and DWR effects dominate the LFMR contribution for the NWs with $n=4$ whereas MMR may play a more important role in determining the MR behavior for $n=8$ and $n=18$. The MMR effect partially cancels the effects of AMR and DWR, leading to the almost constant temperature dependence of LFMR.

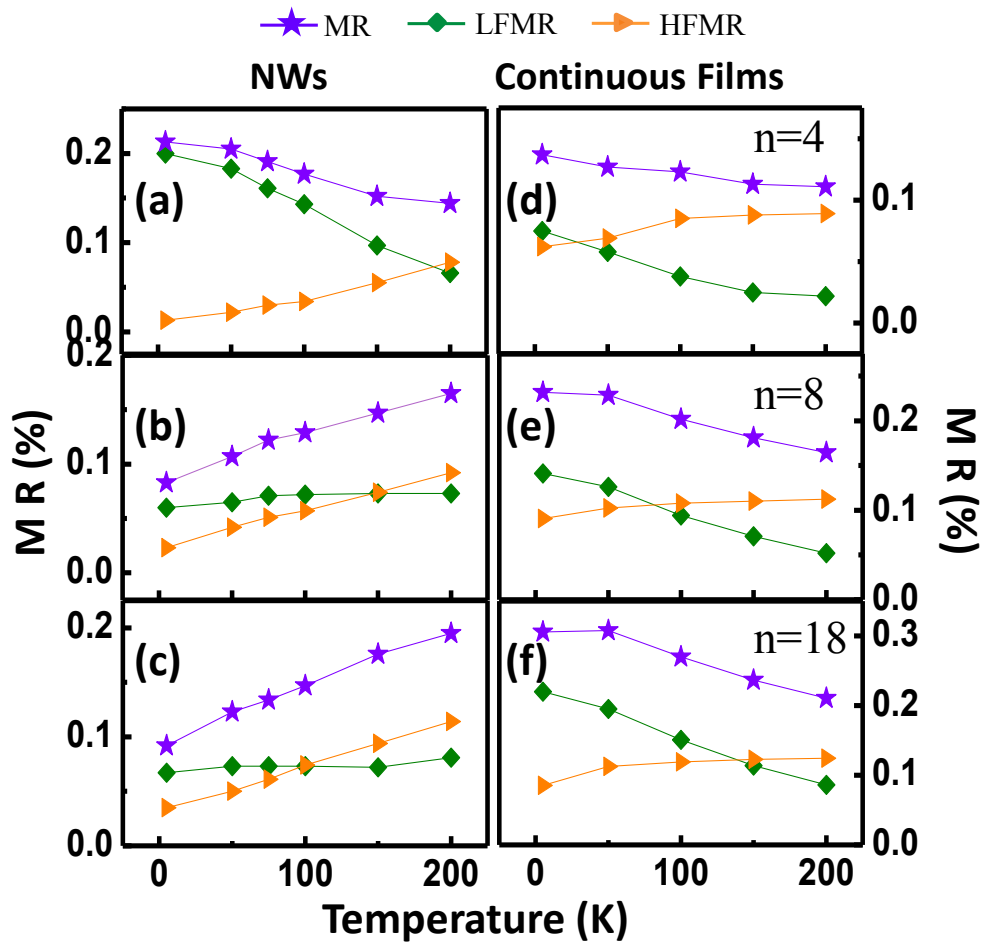


Fig. 5.5 A plot of MR, LFMR and HFMR (defined in Fig. 5.4(b)) as a function of T for the Co/Pd NWs with (a) $n=4$; (b) $n=8$; and (c) $n=18$. Results for the corresponding Co/Pd continuous films are shown in (d)-(f) respectively.

Shown in Fig. 5.5 (d-f) are the plotted MR ratios as a function of T for the corresponding Co/Pd continuous films. While the HFMR shows much weaker temperature dependence in comparison to the Co/Pd NWs, the LFMR shows a monotonic decrease with T for all n , suggesting a dominating AMR and DWR effects in the switching region. This consequently results in a monotonic decrease of total MR ratio as T is increased.

5.3.2.2 Longitudinal and Transverse MR Responses

We have also investigated the longitudinal and transverse MR behaviors of the Co/Pd NWs with field applied in-plane along (X-axis) and perpendicular (Y-axis) to the wire axis of the NWs respectively. Shown in Fig. 5.6 (a) is the longitudinal MR response of the [Co/Pd]₄ NWs as a function of temperature. The NWs show a quasi-parabolic MR behavior at low field region, which is a typical AMR response due to a coherent rotation of magnetization from in-plane along the wire axis to out-of-plane as the external field is reduced from negative saturation, as illustrated by the insets. As expected, the MR ratio increases with decrease in T . Above magnetic saturation, a linear decrease of resistance is observed due to the MMR effect. Again, the MMR slope is markedly dependent on temperature, showing a significant decrease with decrease in T .

Shown in Fig. 5.6 (b) is the longitudinal MR response for the corresponding Co/Pd continuous film. Similarly, we observe a quasi-parabolic MR behavior at low field region due to the AMR effect and a linear non-saturating MR behavior above magnetic saturation resulting from the MMR effect, both of which are markedly temperature dependent. Clear hysteresis behavior can be observed in the continuous film. Here, we have extracted the saturation field (H_{sat}) for both the Co/Pd NWs and the continuous film corresponding to the resistance maximum of the MR curves. H_{sat} can be considered as a direct measure of anisotropy field of the Co/Pd multilayers. A

plot of H_{sat} Vs T is shown as an inset in Fig. 5.6(b). Interestingly, we observed a significant decrease of H_{sat} from 29 kOe to 21 kOe for the Co/Pd NWs while only a slight change of H_{sat} from 10 kOe to 8.7 kOe is seen for the continuous film as the T is increased from 5 K to 200 K. H_{sat} of the NWs is almost twice larger than the corresponding continuous film due to reduced demagnetizing effects. The large difference in H_{sat} might be responsible for the significant difference in perpendicular MR response of the Co/Pd NWs and continuous films shown in Fig. 5.4.

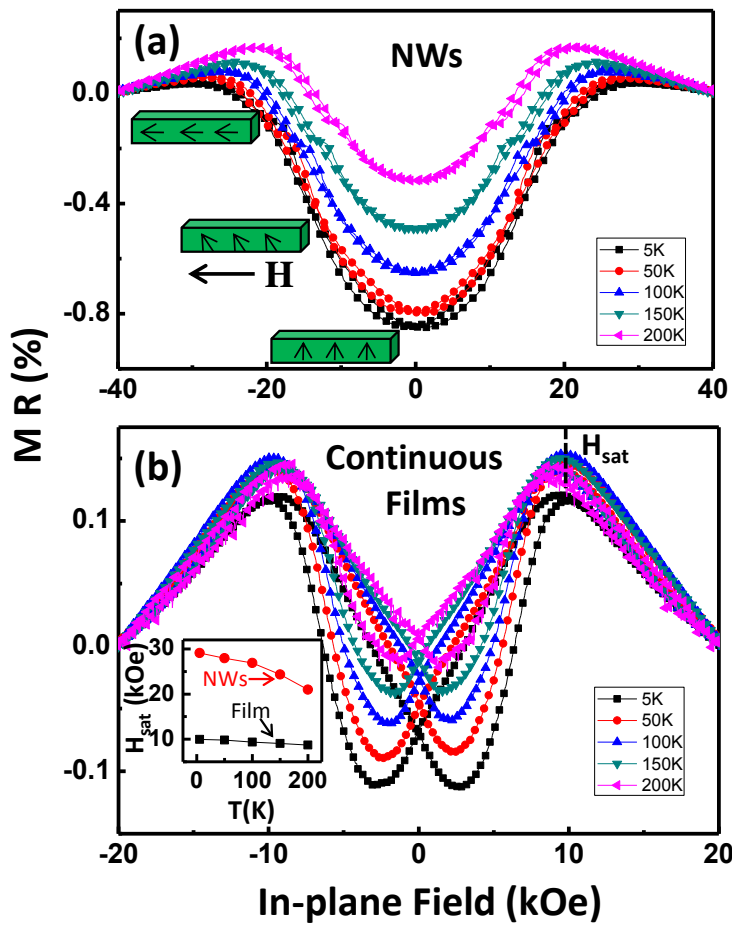


Fig. 5.6 Longitudinal MR responses as a function of T for the $[Co(0.5\text{ nm})/Pd(3\text{ nm})]_4$ (a) NWs; and (b) continuous film (The H_{sat} Vs T for both the structures is shown as an inset).

Shown in Fig. 5.7 (a) and (b) are transverse MR responses for the $[Co/Pd]_4$ NWs and continuous film taken at $T=5\text{ K}$. The red circular symbols represent the field sweep from positive saturation to negative saturation while

the black rectangular symbols represent the reversed field sweep. As the external field is reduced from positive saturation, we observe a monotonic increase of resistance until a reversal field is reached. Since the Co/Pd NWs and continuous film have out-of-plane anisotropy, spins aligned in the transversal direction will rotate coherently from in plane to out of plane forming spin-up and spin-down domains as the external field is reduced. Note that in this case the magnetization is always oriented perpendicular to the current direction, meaning that AMR contributions arising from the domains are negligible. The change in resistance may be due to domain wall resistance. Reducing the transverse field from saturation results in a decrease in domain wall width, leading to the monotonic increase of MR. Similar results have been observed in Co/Pt NWs^[33]. Interestingly, the MR ratio of the Co/Pd NWs (0.37%) is much smaller than the corresponding continuous film (0.9%) which might be due to the much stronger anisotropy field modifying the domain wall width.

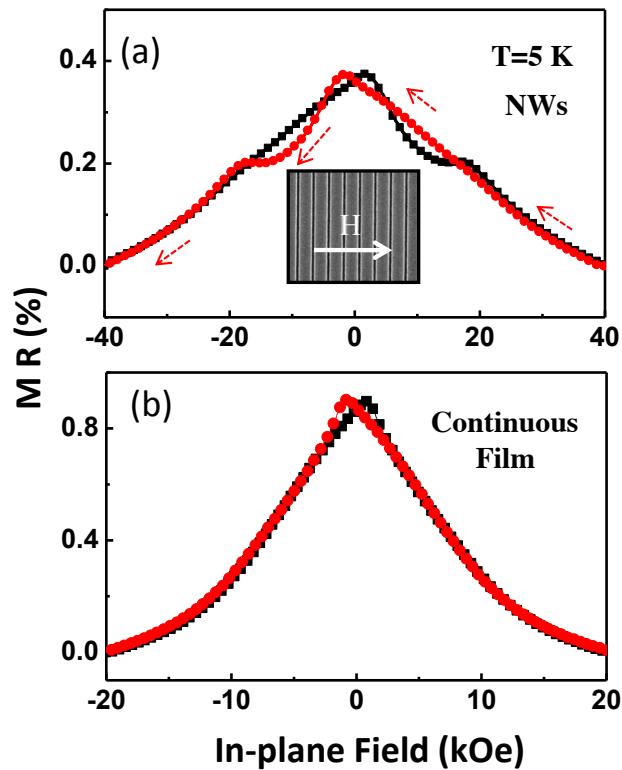


Fig. 5.7 Transverse MR responses for the $[Co(0.5 \text{ nm})/Pd(3 \text{ nm})]_4$ (a) NWs; and (b) continuous film taken at $T=5 \text{ K}$.

5.3.3 Effects of Cu Buffer Layer Thickness

In order to enhance the perpendicular magnetic anisotropy, a Cu buffer layer was deposited prior to the Co/Pd multilayer stack. In this section, the effects of Cu buffer layer thickness t_{Cu} on the magnetic properties of the Co/Pd multilayer films and NWs are investigated. The Co/Pd multilayers have a film structure of $Cu(t_{Cu})/Pd(5\text{ nm})/[Co(0.5\text{ nm})/Pd(3\text{ nm})]_4$ with t_{Cu} varied in the range from 0 nm to 40 nm.

5.3.3.1 Continuous Film

Shown in Fig. 5.8(a) and (b) are schematics of the deposited film structures and the representative hysteresis loops of the Co/Pd multilayer films as a function of t_{Cu} . Clearly, the switching field (H_{sw}) of the films is strongly dependent on the Cu buffer layer thickness, showing a marked increase from 445 Oe to 869 Oe as t_{Cu} is increased from 0 nm to 15 nm. Further increase in t_{Cu} does not result in significant enhancement of H_{sw} of the Co/Pd multilayer films. We observed that $t_{Cu}=15\text{ nm}$ is the optimum buffer layer thickness.

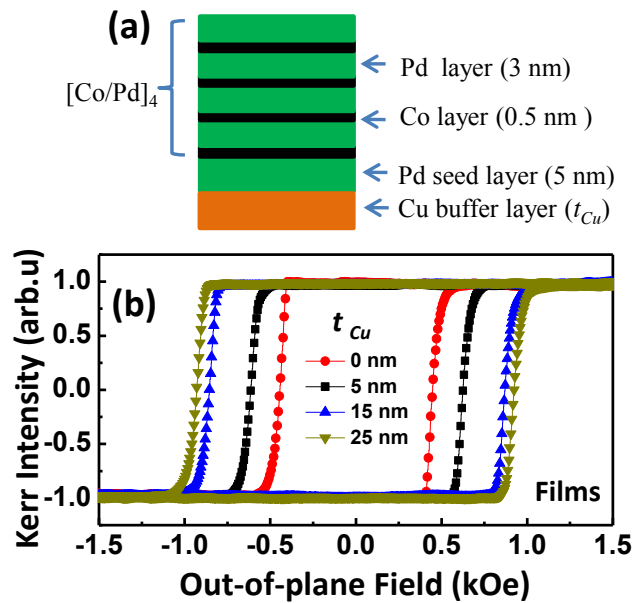


Fig. 5.8 (a) Schematics of deposited $Cu(t_{Cu})/Pd(5\text{ nm})/[Co(0.5\text{ nm})/Pd(3\text{ nm})]_4$ multilayer structure; and (b) hysteresis loops of the multilayer films as a function of t_{Cu} .

We have also measured the XRD patterns of the Co/Pd films as a function of t_{Cu} , as shown in Fig. 5.9(a). A clear CoPd(111) peak at around $2\theta=40.6^\circ$ is observed for all the Co/Pd multilayer films, which is an indication of the good growth of fcc(111) CoPd. No notable change in either the CoPd(111) peak position or the intensity is observed as t_{Cu} is increased. Furthermore, we did not see any clear difference in the rocking curve XRD measurements for the Co/Pd multilayers by comparing films with and without 15 nm thick Cu buffer layer (see Fig. 5.9(b)). These results suggest that there is no texture change in the Co/Pd multilayer films due to the Cu buffer layer. For films with $t_{Cu} \geq 15$ nm, we noticed an additional peak between $2\theta=43.4^\circ$ and $2\theta=43.5^\circ$, corresponding to a fcc(111) peak of the Cu buffer layer.

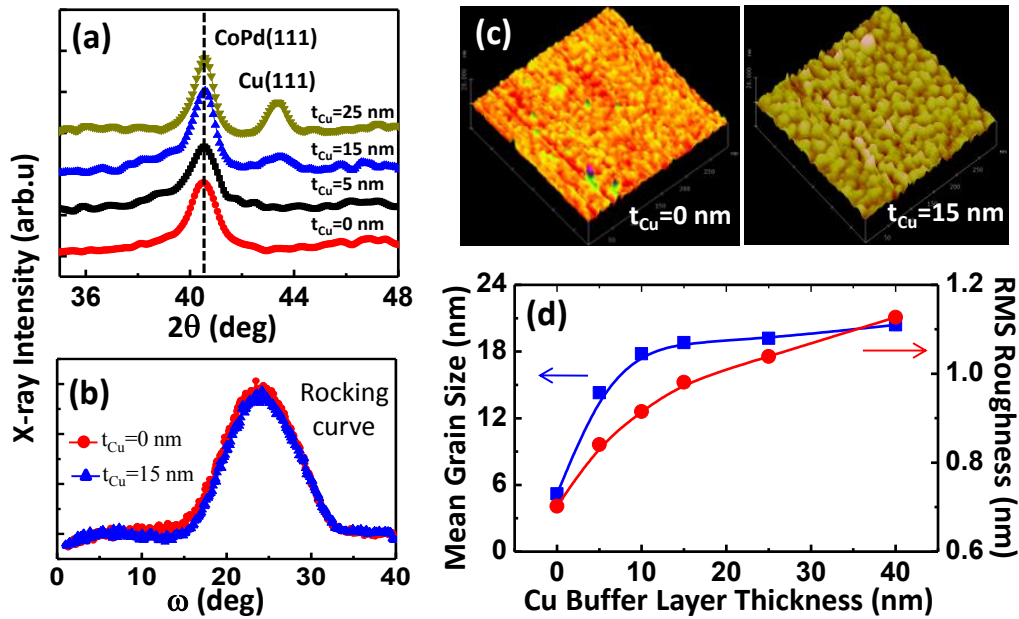


Fig. 5.9 (a) XRD patterns as a function of t_{Cu} ; and (b) Rocking curve XRD; (c) Atomic force micrographs for $t_{Cu}=0$ nm and $t_{Cu}=15$ nm. (d) A plot of the mean grain size and RMS roughness of the $Cu(t_{Cu})/Pd/[Co/Pd]_4$ multilayer films as a function of t_{Cu} .

We also studied the surface roughness of the Co/Pd films using atomic force microscopy. Shown in Fig. 5.9(c) are the representative atomic force micrographs for the Co/Pd multilayer films with $t_{Cu}=0$ nm and $t_{Cu}=15$ nm taken over an area of $300\text{ nm} \times 300\text{ nm}$. It is obvious that the mean grain size

of the Co/Pd multilayers is very sensitive to the Cu buffer layer thickness, similar to the previous observation in Cu buffered SmCo₅-film^[146]. We have plotted the mean grain size and surface roughness extracted from the atomic force micrographs of the continuous Co/Pd films as a function of t_{Cu} in Fig. 5.9(d). Both the mean grain size and root mean square (RMS) roughness show a rapid increase up to $t_{Cu}=15$ nm, after which they tend to be stabilized. It is worth mentioning that atomic force microscopy can only provide rough estimation of the mean grain size.

This roughness dependence on t_{Cu} has been further confirmed using XRR measurements. Fig. 5.10 shows the representative XRR spectra for the Co/Pd multilayer films with $t_{Cu}=0$ nm and $t_{Cu}=15$ nm. The simulation fits were performed using a software package LEPTOS 4.02 (available from Bruker-AXS, Karlsruhe, Germany), where the thickness and interface roughness of each layer were allowed to vary.

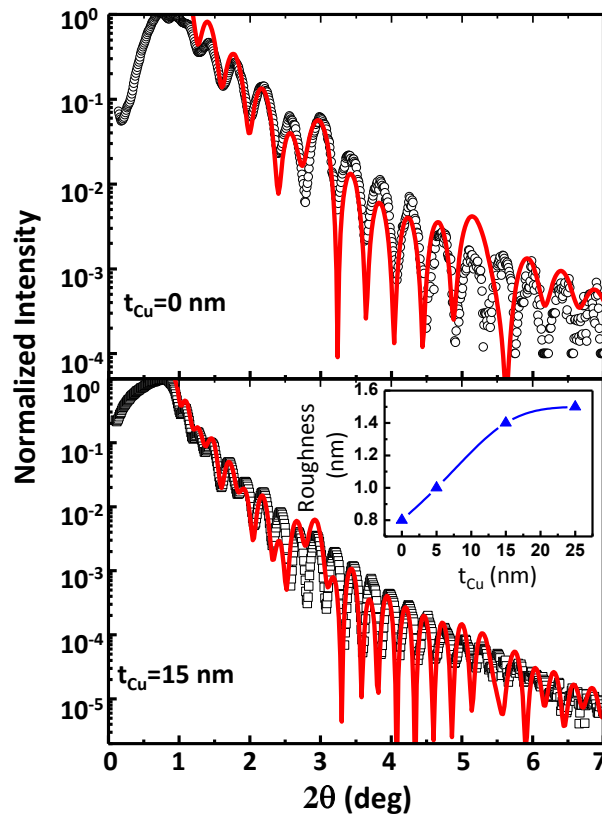


Fig. 5.10 Representative XRR spectra and best fits for the Cu(t_{Cu})/Pd/[Co/Pd]₄ multilayer films with $t_{Cu}=0$ nm and $t_{Cu}=15$ nm (the extracted interface roughness as a function of t_{Cu} is shown as an inset).

There is a comparatively good match between simulation and experimental results. The thickness of Co/Pd bi-layer was found to be approximately 6% smaller relative to the thickness determined from deposition rates calibrated using a surface profiler, which may be due to the use of bulk scattering and index of refraction constant in the fits. The plotted interface roughness $V_s t_{Cu}$ extracted from the XRR simulations is shown in the inset of Fig. 5.10. We observed a rapid increase of interface roughness from 0.8 nm to 1.4 nm as t_{Cu} is increased up to 15 nm, which follows similar trend with the RMS roughness measurements taken from the atomic force microscopy (see Fig. 5.9(d)). Again, the roughness value becomes almost stabilized for $t_{Cu} \geq 15$ nm. Interestingly, the interface roughness is larger than the RMS roughness, which has also been observed in Pd and Ta buffered Co/Pd multilayers^[147].

The combined effect of increased mean grain size and film roughness is responsible for the changes in magnetic properties of the Co/Pd multilayer films^[148, 149]. The magnetic properties of an assembly of small grains depend strongly on the counterplay of local magnetic anisotropy energy and ferromagnetic exchange energy. The effective anisotropy for the magnetic behaviors is an average over several grains. Larger grain size favors increased switching field due to enhanced effective anisotropy resulting from reduced lateral exchange interactions between grains^[150]. On the other hand, film roughness may constrain domain wall motion and hence retard the magnetic switching of the multilayer films. This claim is based on the fact that magnetization reversal of Co/Pd multilayer films occurs via reversed domain nucleation followed by rapid domain wall motion^[26].

5.3.3.2 Nanowires

Now, we focus on the magnetization reversal of $[\text{Co/Pd}]_n$ multilayer NWs with $n=4$ as a function of Cu buffer layer thickness. Shown in Fig. 5.11(a) are

the polar MOKE hysteresis loops for arrays of $[\text{Co/Pd}]_4$ NWs as a function of t_{Cu} . Again, we observed an increase in switching field H_{sw} for the NWs due to the effects of the Cu buffer layer. We have extracted the H_{sw} from the hysteresis loops and plotted it as a function of t_{Cu} for both the NWs and the continuous films in Fig. 5.11(b). A rapid increase of H_{sw} with t_{Cu} is observed when $t_{\text{Cu}} \leq 15$ nm. Further increase in t_{Cu} does not significantly affect the switching fields of both the NWs and the films. Interestingly, this H_{sw} dependence on t_{Cu} is in agreement with the earlier results on the mean grain size and film roughness (Fig. 5.9(d)), suggesting that mean the grain size and film roughness play an important role in determining the magnetization reversal of Co/Pd multilayer films and NWs.

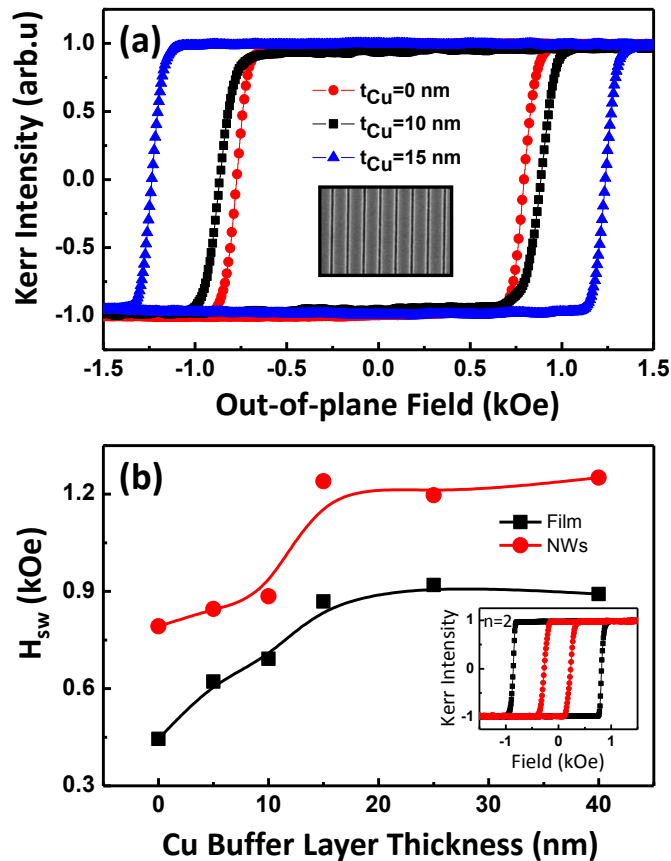


Fig. 5.11 (a) Hysteresis loops of arrays of $\text{Cu}(t_{\text{Cu}})/\text{Pd}(5 \text{ nm})/[\text{Co}(0.5 \text{ nm})/\text{Pd}(3 \text{ nm})]_4$ NWs as a function of t_{Cu} ; and (b) A plot of H_{sw} Vs t_{Cu} for both the $[\text{Co/Pd}]_4$ NWs and continuous films (The line is used to guide the eyes). Hysteresis loops of the $[\text{Co/Pd}]_2$ NWs and film with $t_{\text{Cu}} = 15$ nm are shown as an inset in (b).

We have also compared the hysteresis loops of the [Co/Pd]₂ NWs and corresponding continuous film with $t_{Cu}=15$ nm as shown in the inset of Fig. 5.11(b). Interestingly, in contrast to the [Co/Pd]₄ NWs where the switching field is much larger than the corresponding continuous film, H_{sw} of the [Co/Pd]₂ NWs is smaller than the continuous film. This could be due to a reduction in the perpendicular anisotropy or canted anisotropy axis at the edge of the NWs. It has been reported that variation in PMA or anisotropy axis of defects can cause a significant change in reversal field of patterned Co/Pd multilayer nanostructures^[151].

5.4 Interlayer Coupling and MR Behaviors of [Co/Pd]₄/Au /[Co/Pd]₂ Nanowires

Based on the switching field dependence on the bi-layer repeat n discussed in previous section, we have designed Co/Pd pseudo-spin-valve (PSV) structures consisting of Cu(15 nm)/Pd(5 nm)/[Co(0.5 nm)/Pd(3 nm)]₄/Au(t_{Au})/[Co(0.5 nm)/Pd(3 nm)]₂. Shown in Fig. 5.12(a) are schematics of the deposited film structure with t_{Au} varied in the range from 1 nm to 8 nm. The upper ($n=2$) and bottom ($n=4$) Co/Pd multilayer stacks serve as the soft and hard FM layers respectively. The interlayer coupling and MR behaviors of the PSV NWs are systematically investigated in this section.

5.4.1 Effects of Au Spacer Layer Thickness

Shown in Fig. 5.12(b-c) are the representative polar MOKE hysteresis loops and MR response taken at room temperature for the Co/Pd PSV NWs with $t_{Au}=1.5$ nm. For direct comparison, results of the corresponding continuous film are also shown in Fig. 5.12(d-e). For both the PSV NWs and the continuous film, we observed a distinct two-step switching, corresponding to the magnetization reversal of the soft Co/Pd multilayer stack ($n=2$) at low

field and the hard Co/Pd multilayer stack ($n=4$) at high field respectively. Schematics of the magnetization states are illustrated as insets in Fig. 5.12(b).

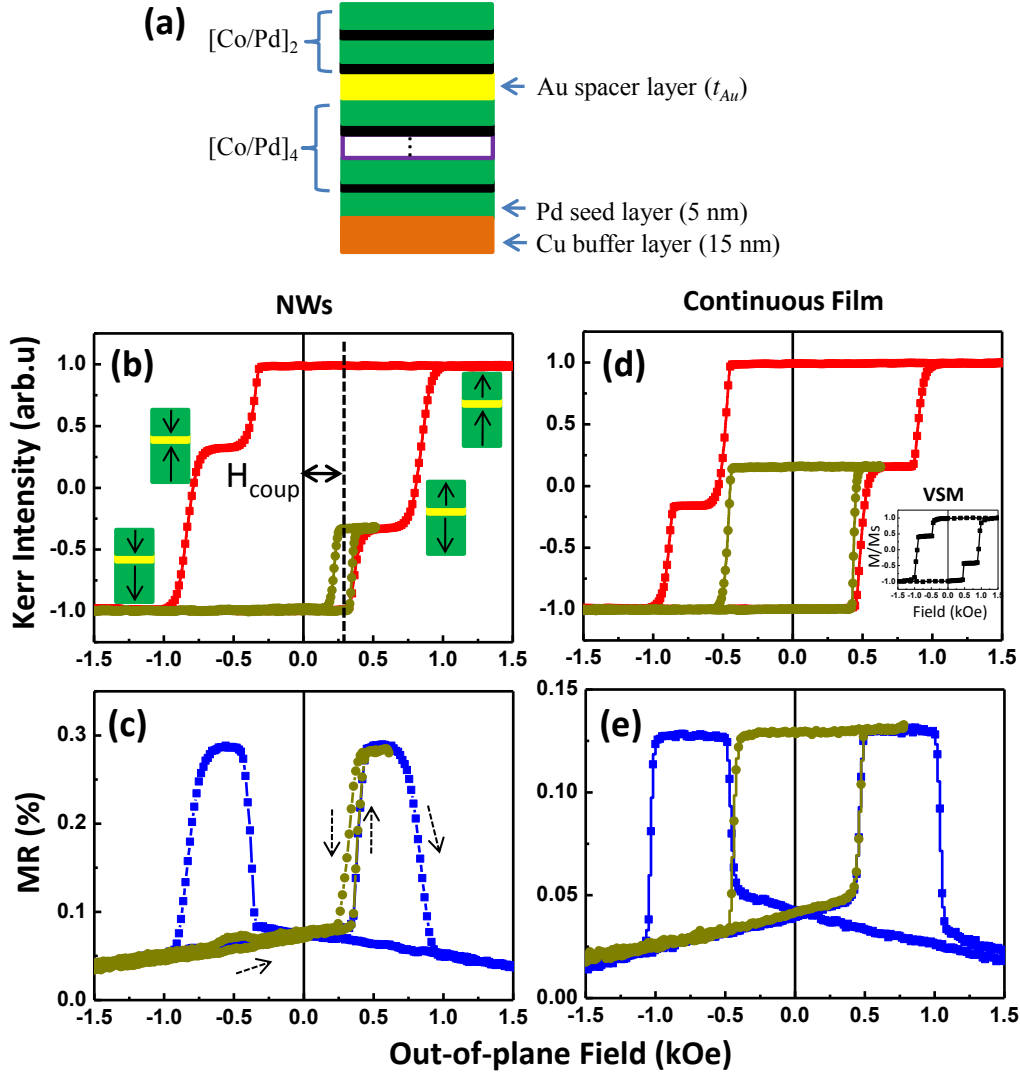


Fig. 5.12(a) Schematics of deposited Cu/Pd/[Co/Pd]₄/Au(t_{Au})/[Co/Pd]₂ PSV structure; (b) Hysteresis loops (minor loop shift represents the interlayer coupling field H_{coupl}); and (c) MR responses of the PSV NWs with $t_{Au}=1.5$ nm. Results of corresponding continuous PSV film with $t_{Au}=1.5$ nm are shown in (d) and (e) respectively (VSM result for the PSV film is shown as an inset in (d)).

Interestingly, the Kerr intensity drop of the two bi-layer stack at the top is larger than that of the four bi-layer stack at the bottom of the continuous PSV film because the MOKE setup is more sensitive to surface material. To confirm that the soft Co/Pd multilayer stack ($n=2$) indeed switches first, the

hysteresis loop measurement of the continuous film was repeated using a vibrating sample magnetometer (VSM) as shown in the inset of Fig. 5.12(d). As expected, the first switching step at low field occurs with smaller moment drop, implying that the soft Co/Pd multilayer stack ($n=2$) switches first.

There is also a good agreement between the hysteresis loops and the MR responses (Fig. 5.12 (b & c) and 5.12(d & e)). The MR plateau arises from the antiparallel relative alignment of magnetization of the two Co/Pd multilayer stacks. At saturation field, the two Co/Pd multilayer stacks are aligned parallel to the field direction resulting in the low MR ratio. Interestingly, the PSV NWs show much larger MR ratio (0.29%) compared to the corresponding continuous film (0.13%), which may be due to the enhanced spin scattering at the edge of the NWs. In the patterned nanostructures, electrons are physically confined by the edge boundaries, which may increase the possibility of spin reflection at the interfaces, leading to a higher MR ratio. Similar spin reflection induced MR enhancement has also been observed in nanostructures with current-confined-path nano-oxide layers^[152, 153].

Due to the different switching fields, the interlayer coupling (sign and strength) between the two Co/Pd multilayer stacks can be determined by conducting detailed minor loop measurements. To measure the minor loop, a large negative field is first applied to saturate both the soft and hard Co/Pd multilayer stacks, followed by application of a suitable positive field to switch only the upper soft Co/Pd stack, after which, the field is reversed until negative saturation to switch the soft stack again. If there is coupling between the soft and hard Co/Pd multilayer stacks, the minor M-H loop center will be shifted away from the zero-field axis, which is a measure of the inter-layer coupling field (H_{coup}). When the $H_{coup}>0$, there is a ferromagnetic (FM) coupling between the two layers. However, for $H_{coup}<0$, this is an indication that the coupling is antiferromagnetic (AFM). From the minor M-H loop shown in Fig. 5.12(b), a positive H_{coup} as large as 290 Oe is observed for the

PSV NWs, indicating that there is a strong FM coupling between the soft ($n=2$) and the hard ($n=4$) Co/Pd multilayer stacks. Again, there is a good agreement between the minor hysteresis loops of the MOKE signal and the MR response. Interestingly, the continuous film deposited at the same time as the PSV NWs shows a much weaker H_{coup} of 14 Oe originating from interlayer coupling due to possible pin holes, RKKY coupling or Néel type coupling. Since the NWs were fabricated under the same conditions as the continuous film, these three interlayer coupling mechanisms should have similar coupling strength in the PSV NWs. The only difference between the Co/Pd NWs and the continuous film is the interlayer magnetostatic interactions through stray fields in the NWs, which is negligible in the continuous Co/Pd PSV film.

We have systematically probed the influence of Au spacer layer thickness t_{Au} on the interlayer magnetostatic coupling and magnetization reversal of the Co/Pd PSV NWs. Shown in Fig. 5.13(a-e) are the major and minor M-H loops of the PSV NWs with t_{Au} varied in the range from 1 nm to 3.5 nm. For $t_{Au}=1$ nm, we observed only a single-step switching for the PSV NWs, compared to the two steps seen in the corresponding continuous film as shown in the inset of Fig. 5.13(a). This is a direct effect of the strong interlayer magnetostatic coupling and possible ferromagnetic coupling, which induces collective magnetization reversal of the soft and hard Co/Pd multilayer stacks. For the uniformly magnetized PSV film with $t_{Au}=1$ nm, however, the magnetostatic coupling via stray fields is very negligible. A much weaker positive H_{coup} of 20 Oe was measured. This interlayer coupling is considerably weak to overcome the switching field difference between the two FM stacks, thereby resulting in a clear two-step switching. For the PSV NWs with $1.5 \text{ nm} \leq t_{Au} \leq 3.5 \text{ nm}$, due to a reduction in the stray fields, two distinct switching steps are seen. As t_{Au} is increased, the minor loop center shifts towards zero field, which verifies the weakened magnetostatic coupling between the two Co/Pd multilayer stacks.

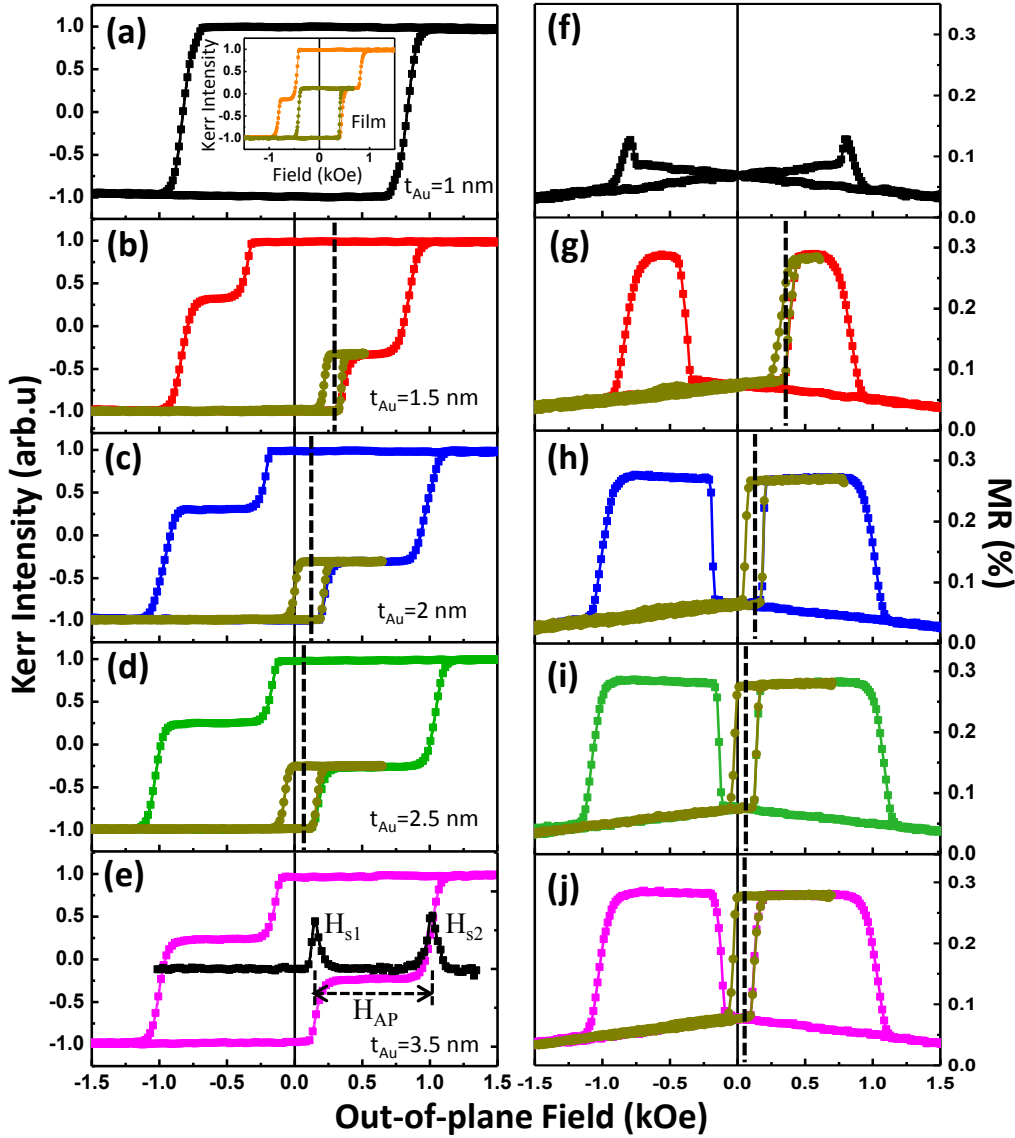


Fig. 5.13 M-H loops of the $Cu/Pd/[Co/Pd]_4/Au(t_{Au})/[Co/Pd]_2$ PSV NWs with (a) $t_{Au}=1$ nm (M-H loops of corresponding continuous film are shown as an inset); (b) $t_{Au}=1.5$ nm; (c) $t_{Au}=2$ nm; (d) $t_{Au}=2.5$ nm; and (e) $t_{Au}=3.5$ nm. The corresponding MR loops are shown in (f)-(j) respectively. The dashed lines indicate the reduced interlayer coupling with t_{Au} .

The corresponding MR responses for the PSV NWs with $1 \text{ nm} \leq t_{Au} \leq 3.5$ nm are shown in Fig. 5.13(f-j). In agreement with the M-H loop in Fig. 5.13(a), the MR curve for $t_{Au}=1$ nm displays a sharp peak with a small MR ratio of 0.13% due to the strong interlayer coupling between the soft and hard Co/Pd stacks. For the PSV NWs with $1.5 \text{ nm} \leq t_{Au} \leq 3.5$ nm, the MR curves display typical GMR behavior with distinct region of anti-parallel relative alignment of magnetization between the soft and hard Co/Pd stacks and a larger MR ratio

(~0.29%). Again, we observed a reduced interlayer coupling field based on the minor loop center shift as the Au spacer layer thickness is increased, as indicated by the dashed lines in Fig. 5.13(f-j). Interestingly, the MR ratio almost keeps constant with t_{Au} .

In order to further understand the influence of Au spacer layer thickness t_{Au} on the interlayer magnetostatic coupling strength of the Co/Pd PSV NWs, we have performed numerical calculations on the stray fields from the bottom hard Co/Pd multilayer stacks ($n=4$). We assume that the hard Co/Pd FM stacks are uniformly magnetized with a constant magnetization M_0 perpendicular to the film plane. Our assumption is reasonable since the [Co/Pd]₄ multilayer stacks possess high perpendicular anisotropy. Shown in Fig. 5.14(a) is a schematic of the modeled [Co/Pd]₄ multilayer NWs with a cuboid structure of length, width and thickness of $2L$, $2W$ and $2D$ respectively. The X and Y of Cartesian frame are along the length and width directions while the Z axis (out-of-plane) corresponds to the thickness of NWs. For uniform magnetization, the [Co/Pd]₄ multilayer NWs is equivalent to two rectangular sheets at a distance $2D$ with homogenous magnetic charge densities $\pm M_0$ distributed at the upper and lower surfaces. The charge configuration induces an expression for the stray fields^[154]:

$$H(\vec{r}) = \frac{M_0}{4\pi} \bullet \int_{-L}^{+L} dx' \int_{-W}^{+W} dy' \left[\frac{\vec{r} - (x', y', c)}{|\vec{r} - (x', y', c)|^3} - \frac{\vec{r} - (x', y', -c)}{|\vec{r} - (x', y', -c)|^3} \right] \quad (5.3)$$

By performing integral operation, the out-of-plane projection of the stray fields is give as follows^[154, 155]:

$$H_z(x, y, z) = -\frac{M_0}{4\pi} \bullet \sum_{m,n,k=1}^2 (-1)^{m+n+k} \frac{[z - (-1)^k D] \bullet [x - (-1)^m L]}{|z - (-1)^k D| \bullet |x - (-1)^m L|} \times \arctan \left\{ \frac{|x - (-1)^m L| \bullet [y - (-1)^n W]}{|z - (-1)^k D| \bullet \sqrt{[x - (-1)^m L]^2 + [y - (-1)^n W]^2 + [z - (-1)^k D]^2}} \right\} \quad (5.4)$$

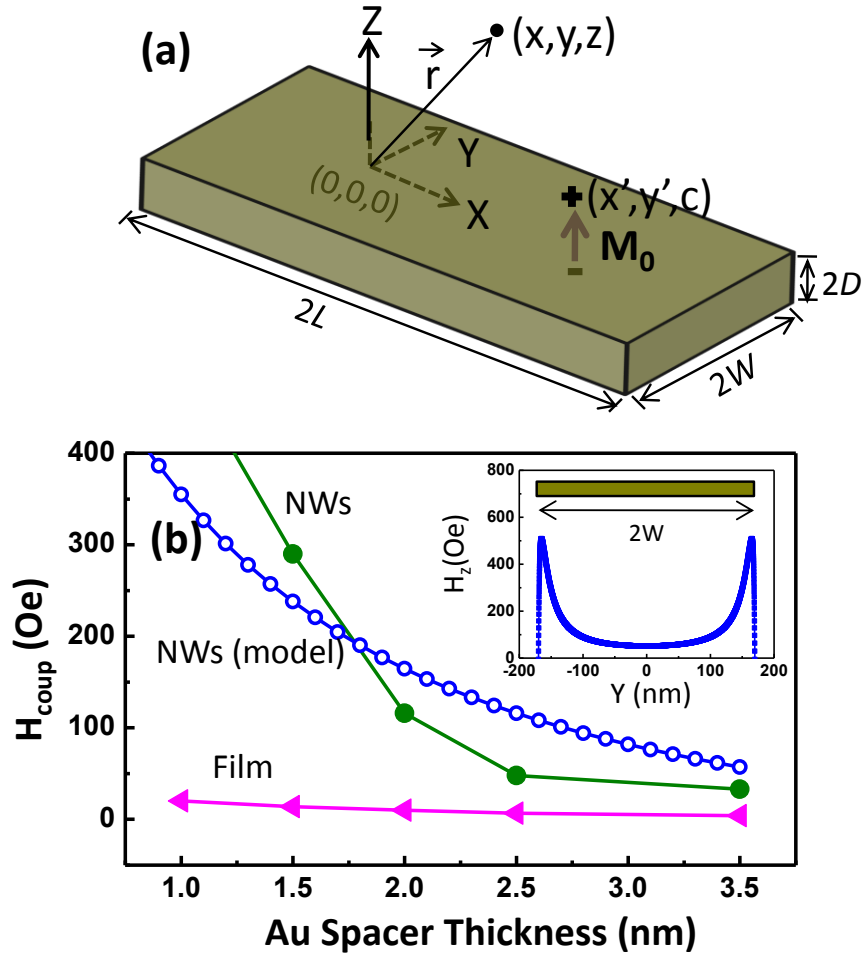


Fig. 5.14 (a) Schematics for stray field calculation of the $[\text{Co/Pd}]_4$ NWs; and (b) A plot of calculated stray fields (empty circle), interlayer coupling field H_{coup} extracted experimentally from minor M - H loop shift of $\text{Cu/Pd}/[\text{Co/Pd}]_4/\text{Au}(t_{\text{Au}})/[\text{Co/Pd}]_2$ PSV NWs (solid circle) and corresponding continuous films (solid triangle) as a function of t_{Au} .

Since the $[\text{Co/Pd}]_4$ NWs are infinitely long compared to the width and film thickness, the out-of-plane component of the stray fields can be simplified as follows:

$$H_z(x, y, z) = -\frac{M_0}{2\pi} \left[\arctan \frac{y-W}{t_{\text{Au}}} - \arctan \frac{y+W}{t_{\text{Au}}} - \arctan \frac{y-W}{t_{\text{Au}}+2D} + \arctan \frac{y+W}{t_{\text{Au}}+2D} \right] \quad (5.5)$$

where M_0 is the saturation magnetization of the $[\text{Co/Pd}]_4$ multilayer film which was extracted experimentally from the VSM measurement. Shown in the inset of Fig. 5.14(b) is the calculated out-of-plane component of the stray

field (H_z) generated by the hard Co/Pd FM stacks ($n=4$) in the soft Co/Pd stacks ($n=2$) with a spacer layer thickness $t_{Au}=1.5$ nm across the NW width. In our approximation, the magnetostatic interactions from the hard Co/Pd FM stacks of the nearest and second nearest neighboring PSV NWs were also taken into consideration in the calculation. H_z varies across the NW width in such a way that it is the weakest at the center and strongest at the edges in agree with the observation in Co/Ni multilayer constrictions^[109]. We have calculated H_z at the edge of the NWs ($y=169$ nm) as a function of t_{Au} , as shown in Fig. 5.14(b) (empty circle). H_z shows a fast decay from 238 Oe down to 57 Oe as t_{Au} is slightly increased from 1.5 nm to 3.5 nm.

The strong dependence of the stray fields on t_{Au} is further verified experimentally. We have extracted the interlayer coupling field (H_{coup}) from the minor M-H loops in Fig. 5.13 and plotted it as a function of t_{Au} in Fig. 5.14(b) (solid circle). We found a significant decrease of H_{coup} from 290 Oe for $t_{Au}=1.5$ nm to 48 Oe for $t_{Au}=2.5$ nm, after which only a slight decrease of H_{coup} is seen, implying that the two FM stacks are magnetically de-coupled. This is further confirmed by the PSV NWs with $t_{Au}=8$ nm (not shown), where only a small H_{coup} of 11 Oe is observed. There is only qualitative agreement between the experimental and calculation results. This is expected since the calculation only considers the stray field at one point ($y=169$ nm) while the interlayer magnetostatic coupling of the PSV NWs is the average effect of stray fields across the NW width, and the modeling does not take into account the defect distribution in the actual sample. For comparison, the H_{coup} of the corresponding continuous films is also shown in Fig. 5.14(b) (solid triangle). The PSV films show a much smaller H_{coup} due to the absence of interlayer magnetostatic coupling via the stray fields, with a monotonic decrease from 20 Oe to 4 Oe as t_{Au} is increased from 1 nm to 3.5 nm.

Interlayer coupling also plays an important role in engineering the magnetic switching of the PSV NWs. Here, we have defined three parameters

H_{s1} , H_{s2} and H_{AP} in Fig. 5.13(e), corresponding to the switching fields of the soft Co/Pd stack ($n=2$), the hard Co/Pd stack ($n=4$) and the stable field range over which the two FM stacks are in anti-parallel relative alignment of magnetization respectively. Shown in Fig. 5.15 is a plot of the three parameters extracted from the M-H loops in Fig. 5.13 as a function of t_{Au} . For $t_{Au} \leq 2.5$ nm, a marked decrease of H_{s1} and a notable increase of H_{s2} with t_{Au} are observed due to reduced interlayer coupling strength. Consequently, the stable field range H_{AP} shows a rapid increase from 0 for $t_{Au}=1$ nm to 610 Oe for $t_{Au}=2.5$ nm and becomes stabilized afterwards.

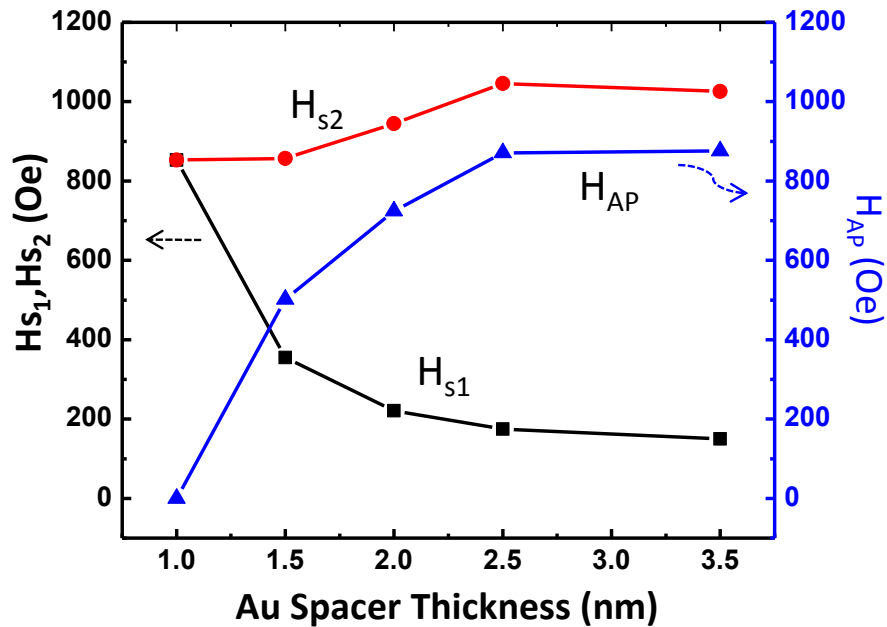


Fig. 5.15 A plot of H_{s1} , H_{s2} and H_{AP} (defined in Fig. 5.13(e)) of the PSV NWs as a function of t_{Au} .

5.4.2 Effects of Temperature

We have conducted a detailed investigation on the effects of temperature (T) on interlayer coupling and MR behavior of the Co/Pd PSV NWs and continuous films. Shown in Fig. 5.16(a) are major and minor MR loops of the PSV NWs with $t_{Au}=1.5$ nm as a function of T . At high temperature, the MR response is dominated by the GMR effect. However, as temperature is

decreased, a noticeable transition in the MR response to that dominated by MMR^[94] and possibly AMR, DWR is observed at $T=5$ K. The major loop of the MR response taken at $T=200$ K shows a typical GMR behavior with a clear plateau field range of 254 Oe, indicating a separate magnetic switching of the soft and the hard Co/Pd multilayer stacks. Interestingly, we observe a linear non-saturating MR response above saturation due to MMR effect, as shown an enlarged half loop MR curve in the inset of Fig. 5.16(a). However, the MMR contribution is almost one order of magnitude smaller than the GMR response.

As temperature is decreased to $T=150$ K, the MR plateau becomes rounded due to the combined effect of reduced switching field difference and enhanced interlayer coupling. In Co/Pd multilayer films, due to a Co 3d-Pd 4d hybridization at the Co/Pd interfaces, the Pd layers are polarized, thus becoming weakly ferromagnetic and favoring the FM interlayer coupling between the Co layers through the Pd layers. The Pd polarization can go into the Pd layer up to 0.7 nm at room temperature^[78]. It has been previously reported^[45, 156] that for Co/Pt multilayer, the Pt polarization goes deeply into the Pt layers with decrease in temperature, consequently strengthening the FM interlayer coupling and reinforcing the switching field of the Co/Pt multilayer stacks. This should also be valid for Co/Pd multilayers since both Pd and Pt have similar electronic configurations. The switching field of both the soft ($n=2$) and the hard ($n=4$) Co/Pd multilayer stacks increases with decrease in temperature. However, the soft Co/Pd stack shows a faster increase rate, leading to a reduction in the switching field difference at lower T . The temperature dependence of switching field on n has been indeed confirmed using MR measurements, as has been shown in the inset of Fig. 5.4 (c), where a stronger temperature dependence of H_{sw} is observed in the $[\text{Co/Pd}]_n$ NWs with smaller n . Similar temperature dependence have also been previously reported in Co/Ni^[157] and Co/Pt^[158, 159] multilayers.

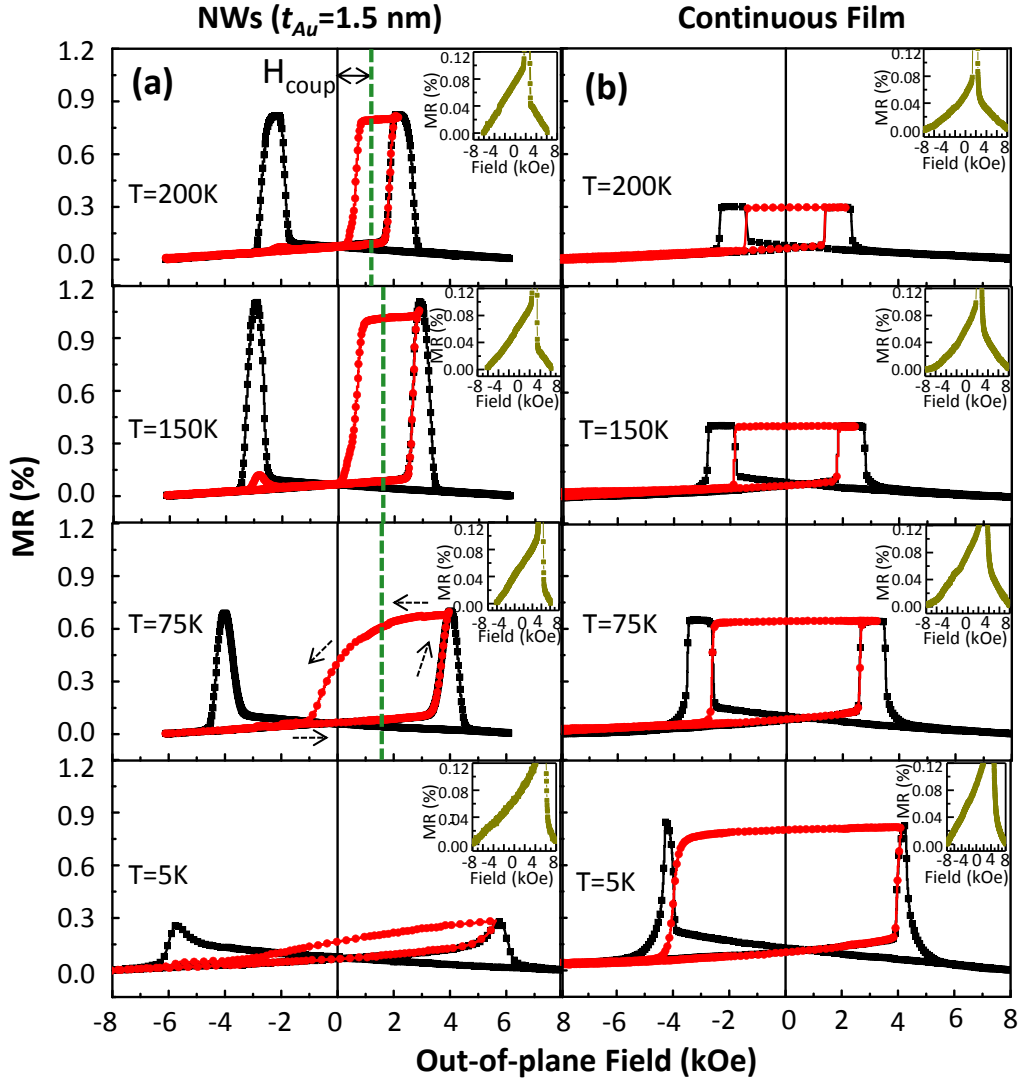


Fig. 5.16 Major (black rectangular) and minor (red circular) MR loops as a function of T for the Cu/Pd/[Co/Pd]₄/Au(t_{Au})/[Co/Pd]₂ PSV (a) NWs (the dash line indicates interlayer coupling field H_{coup}); and (b) corresponding continuous film with $t_{Au}=1.5$ nm. The enlarged half-loop MR curves are shown as insets.

We have also conducted minor loop measurements and extracted the interlayer coupling field H_{coup} between the two FM stacks from minor loop center shift of the MR curves. Compared with $T=200$ K, minor loop of the PSV NWs shows an upwards shift of H_{coup} to 1.65 kOe at $T=150$ K, indicating an enhanced interlayer coupling. As temperature is further decreased, there is a drastic reduction in the MR ratio from 1.1% for $T=150$ K to 0.27% for $T=5$ K. The MR response taken at $T=5$ K resembles that of a single Co/Pd multilayer stack with an MR peak mainly arising from MMR and possibly

AMR, DWR, as has been described in § 5.3.2. This suggests a collective magnetization reversal of the soft and hard Co/Pd multilayer stacks due to a strong interlayer coupling between the two FM stacks, which has been further verified by the gradual switching of the PSV NWs in the downwards branch of the minor loop. Again, we observed the linear non-saturating MMR response from the inset, which becomes more prominent due to the absence of GMR effect.

For comparison, the major and minor MR loops of the corresponding continuous Co/Pd PSV film with $t_{Au}=1.5$ nm are also shown in Fig. 5.16(b). We observed typical GMR responses at all temperatures. Again, the plateau field range over which the two Co/Pd multilayer stacks are in antiparallel magnetization state decreases with temperature and becomes rounded at $T=5$ K, which further confirms the reduced switching field difference between the two FM stacks at lower temperature. Interestingly, the MR ratio of the continuous film increases from 0.3% to 0.82% as the temperature is decreased from $T=200$ K to $T=5$ K. This is in direct opposite of the observation in the PSV NWs as shown in Fig. 5.16(a). The linear non-saturating MMR behavior is also observed at all T , as shown in the insets of Fig. 5.16(b).

Shown in Fig. 5.17 (a) and (b) are the temperature dependence of MR behaviors for the PSV NWs and corresponding continuous film with a thicker spacer $t_{Au}=2.5$ nm. Clear GMR response can be observed in the PSV NWs at all temperatures, even for $T=5$ K. The absence of MMR (and possibly AMR, DWR) dominated effects in the PSV NWs suggests no correlated magnetization reversal of the soft and hard Co/Pd stacks due to a much weaker interlayer coupling. This has been verified by the much smaller minor loop center shift, as indicated by the dashed lines in Fig. 5.17 (a). Again, the MR curves become rounded at $T=5$ K for both the PSV NWs and the continuous film due to a reduction in switching field difference of the two FM stacks.

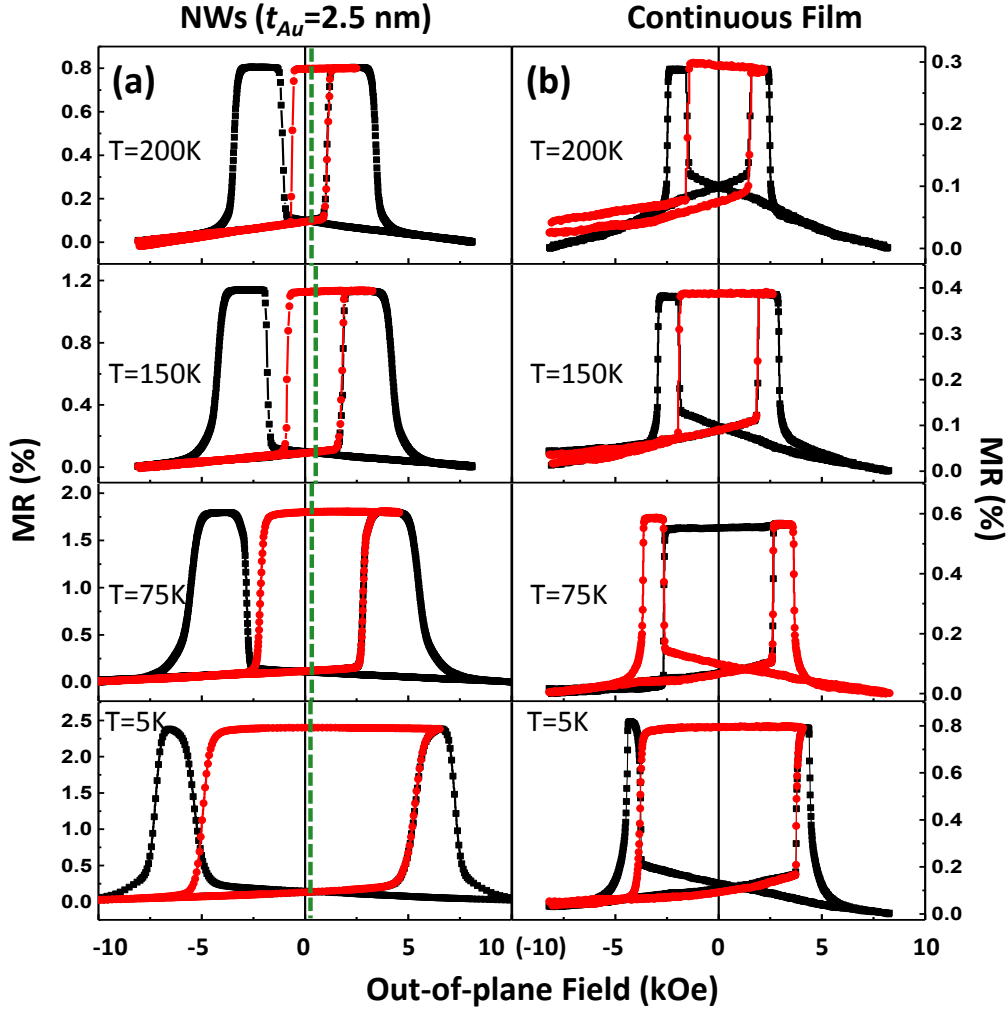


Fig. 5.17 MR loops as a function of T for the PSV (a) NWs; and (b) corresponding continuous film with $t_{Au}=2.5$ nm.

We have further extracted the interlayer coupling field H_{coup} Vs T from the minor loop MR measurements and plotted it as a function of t_{Au} for both the PSV NWs and the corresponding continuous films, as shown in Fig. 5.18(a). The solid and open symbols represent H_{coup} of the PSV NWs and continuous films respectively. For the continuous films, H_{coup} is small and almost independent on temperature, suggesting that the interlayer coupling originating from possible pin holes, RKKY coupling or Néel type coupling is negligible at low T . For the PSV NWs, however, the interlayer coupling is significantly larger and markedly dependent on both t_{Au} and T . There is a fast decay of H_{coup} with a slight increase of t_{Au} from 1.5 nm to 2.5 nm. Since the PSV NWs are deposited at the same time as the continuous films, the

interlayer coupling originating from possible pin holes, RKKY coupling or Néel type coupling should have similar temperature dependence in the NWs. It is then easy to deduce that the huge dependence of interlayer coupling on T in the PSV NWs mainly arise from the stray field interactions.

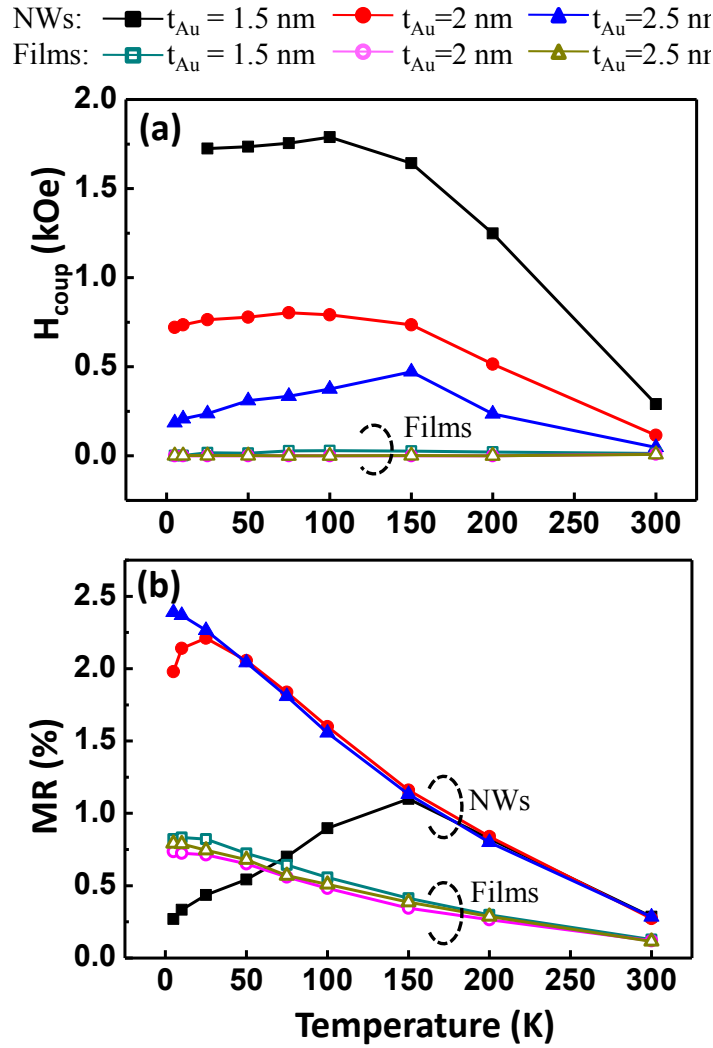


Fig. 5.18 A plot of (a) H_{coup} Vs T extracted from the minor loop MR measurements; and (b) MR ratio Vs T for the $Cu/Pd/[Co/Pd]_4/Au(t_{Au})/[Co/Pd]_2$ PSV NWs and films as a function of t_{Au} .

We observed a fast increase of H_{coup} for the PSV NWs with $t_{Au} = 1.5$ nm and $t_{Au} = 2$ nm as T is decreased from 300 K to 100 K, which is followed by a slight change of H_{coup} at $T \leq 100$ K. The reduced effective spacer layer thickness together with enhanced saturation magnetization of the hard Co/Pd multilayer stacks ($n=4$) may be responsible for the large increase of H_{coup} at

$T \geq 100$ K. In the PSV structure, the Au spacer layer is sandwiched by a 0.5 nm thick Co layer and a 3 nm thick Pd layer. Since only partial Pd layer is strongly polarized by the neighboring Co layer^[78], the effective spacer layer between the two FM stacks shall consist of both the Au layer and the weakly polarized part of the Pd layer. Although the Au layer thickness remains constant with temperature, the Pd polarization goes deeper into the Pd layer at low T , resulting in a reduced effective spacer layer thickness and hence enhanced interlayer magnetostatic coupling. On the other hand, the increased saturation magnetization with temperature^[45] may also contribute to the increased interlayer coupling according to Eq. (5.5). The slight change of H_{coup} at $T \leq 100$ K may indicate the almost constant saturation magnetization^[45] and effective spacer layer thickness at low T . Interestingly, for $t_{Au}=2.5$ nm, there is a slight decrease of H_{coup} at $T \leq 150$ K.

The effects of interlayer coupling on the MR ratio of the Co/Pd PSVs have also been analyzed as a function of T , as shown in Fig. 5.18 (b). Compared with the continuous PSV films, where typical GMR response with a monotonic increase of MR ratio with T are observed, the PSV NWs show more complicated MR dependence on T due to the presence of interlayer magnetostatic coupling. We observed a MR ratio peak for the PSV NWs with $t_{Au}=1.5$ nm at $T=150$ K corresponding to the transition between GMR and MMR dominated effects. At high T , GMR effect dominates the MR response of the PSV NWs. However, at low T , MMR and possibly AMR, DWR effects may begin to play a more important role in affecting the MR response, resulting in a reduction of MR ratio. As t_{Au} is increased, the MR peak shifts downwards to $T=25$ K for $t_{Au}=2$ nm and disappears for $t_{Au}=2.5$ nm due to reduced interlayer coupling strength. Interestingly, the PSV NWs show larger MR ratio at higher temperature ($T \geq 75$ K) compared to the corresponding continuous film due to the enhanced spin scattering at the edge of the NWs as discussed before.

5.4.3 Effects of Co and Pd Insertion Layers

In previous sections, the discussed PSV structure consists of an Au spacer layer sandwiched by a 3 nm thick Pd non-magnetic (NM) layer at the bottom and a 0.5 nm thick Co FM layer on the top. We have argued that the effective spacer should include not only the Au layer but also the weakly polarized part of the Pd layer. In order to confirm our assumption, another two PSV structures (structure *I* and *II*) have been designed by inserting either a 0.5 nm thick Co layer to the bottom side or a 3 nm thick Pd layer to the upper side of the Au layer, so that the Au spacer layer is always sandwiched symmetrically.

The complete film structures are as follows:

Structure *I*: Cu(15nm)/Pd(5nm)/[Co(0.5nm)/Pd(3nm)]₄/**Co(0.5nm)**/Au(1.5nm)
/[Co(0.5 nm) /Pd(3nm)]₂

Structure *II*: Cu(15nm)/Pd(5nm)/[Co(0.5nm)/Pd(3nm)]₄/Au(1.5nm)/**Pd(3nm)**
/[Co(0.5nm)/Pd(3nm)]₂

Shown in Fig. 5.19 (a) and (d) are schematics of the designed two PSV structures. If our assumption is correct, the Co insertion layer should give rise to an increase in interlayer coupling while the Pd layer will decrease the H_{coup} . Shown in Fig. 5.19(b) is the polar MOKE hysteresis loop of the PSV NWs with structure *I*. We observed a single step switching in the NWs, suggesting a collective magnetization reversal of the soft and the hard Co/Pd stacks due to a strong interlayer magnetostatic coupling. This is the direct opposite of the PSV NWs without the Co insertion layer, where a distinct two-step switching is seen (Fig. 5.12(b)). The strong interlayer coupling is further verified by the large minor loop center shift ($H_{coup}=119$ Oe) of the corresponding continuous PSV film, as shown in Fig. 5.19(c). The reduced effective spacer layer thickness is responsible for the large H_{coup} .

Shown in Fig. 5.19(d & e) are hysteresis loops of the PSV NWs and corresponding continuous film with structure *II*. As expected, a distinct

two-step switching is observed in the PSV NWs due to a much weaker interlayer magnetostatic coupling resulting from the increased effective spacer layer thickness. The minor loop measurement shows a much smaller H_{coup} (28 Oe) in comparison with the PSV NWs without the Pd insertion layer (290 Oe, see Fig. 5.12(b)). Interestingly, the corresponding continuous film shows a single step switching. This might indicate a negligible small difference of switching field between the two FM stacks resulting from enhanced perpendicular anisotropy of soft Co/Pd multilayer stack ($n=2$) at the additional Co/Pd interface. The above experimental observations confirm that the weakly polarized Pd layer indeed contributes largely to the effective spacer of the PSVs.

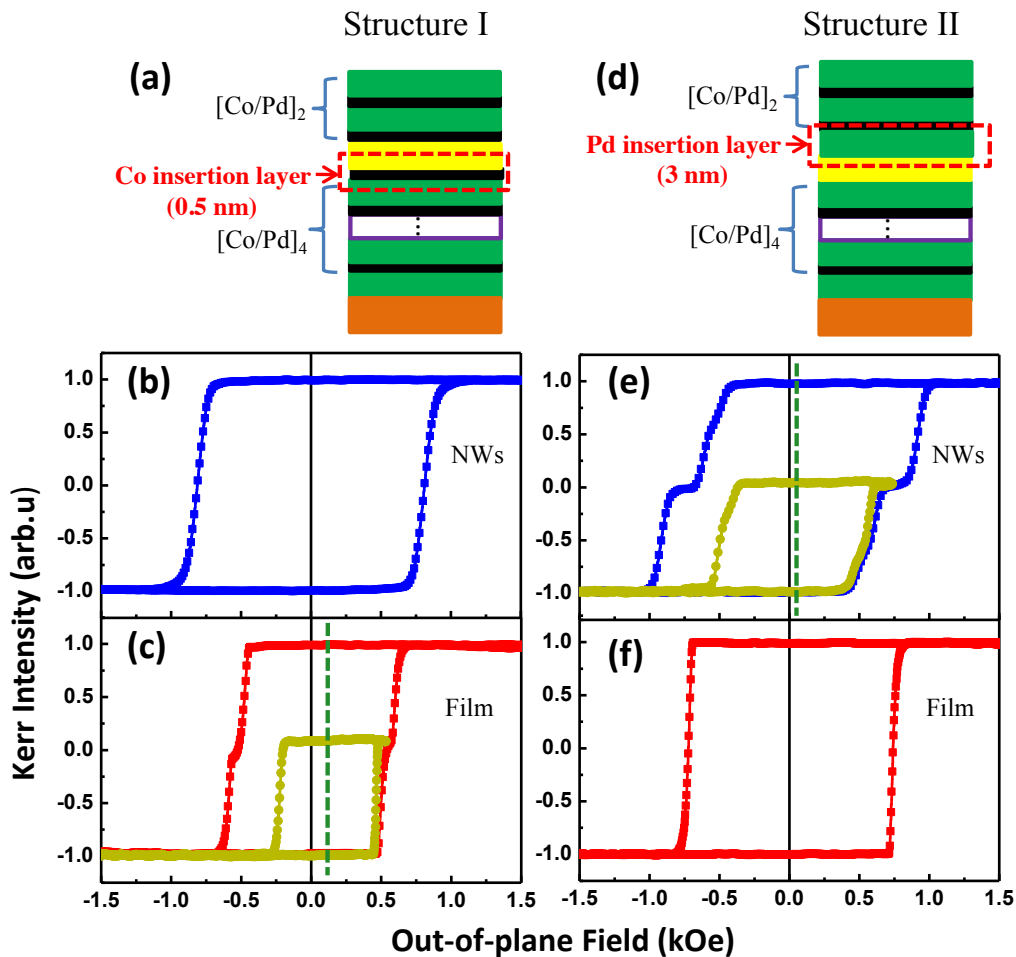


Fig. 5.19 (a) Schematics; and M-H loops of the PSV NWs (b); continuous film (c) with structure I where the Au spacer is sandwiched by two Co layers. Results for the PSVs with structure II (Au spacer sandwiched by two Pd layers) are shown in (d)-(f) respectively.

We have further investigated the temperature dependence of MR behaviors for the PSVs with structure *I* and *II*. Shown in Fig. 5.20 (a) are the perpendicular MR responses of the PSV NWs with structure *I* as a function of T . The MR curve performs like a single Co/Pd multilayer stack at all T , suggesting a collective magnetization reversal of the PSV NWs due to the strong interlayer magnetostatic coupling given by the Co insertion layer.

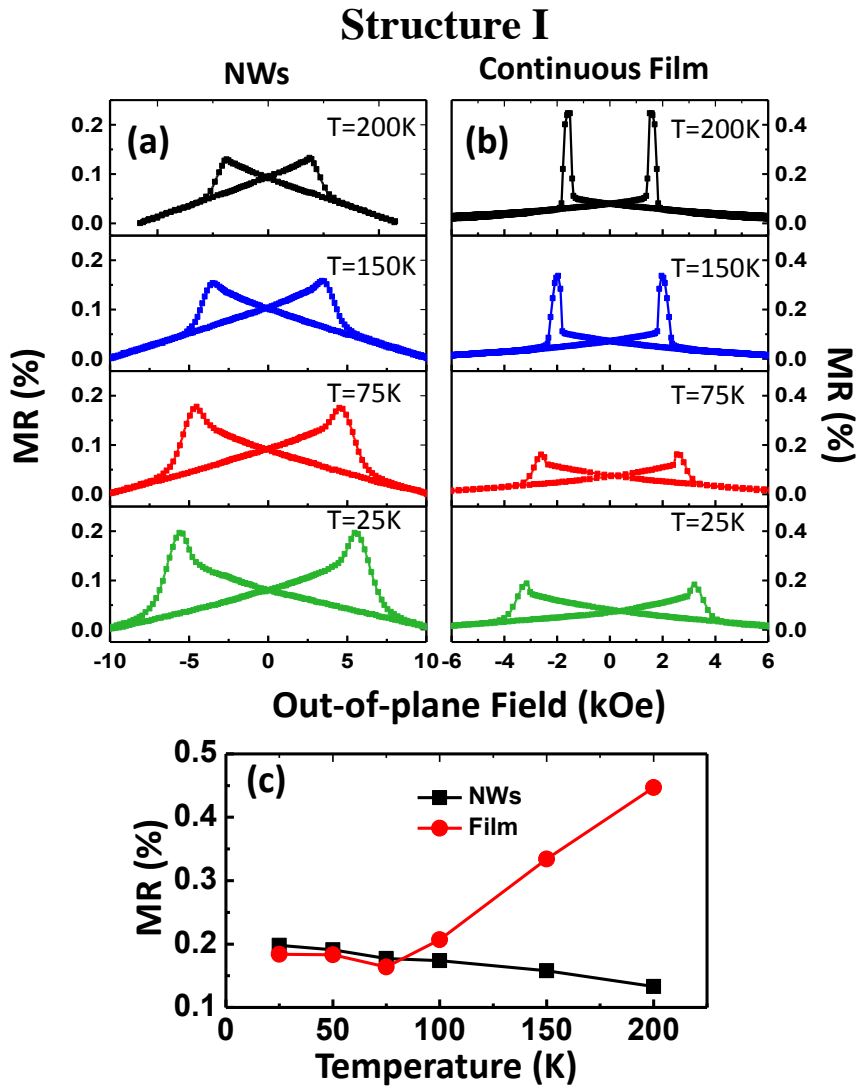


Fig. 5.20 MR responses as a function of T for the PSV NWs (a); and corresponding continuous film (b) with structure *I*. A plot of MR ratio Vs T is shown in (c).

For the continuous PSV film (Fig. 5.20(b)), however, a transition from GMR to MMR (and possibly AMR, DWR) dominated response is observed at $T \leq 75$ K due to enhanced interlayer coupling at low T . This consequently

results in a sharp decrease in MR ratio. Fig. 5.20(c) summarizes the MR ratio Vs T for the PSVs. While the NWs show a monotonic increase with decrease in T , the continuous film displays a MR ratio minimum at $T=75$ K, indicating the transition of different MR mechanisms.

Shown in Fig. 5.21 (a) are the MR responses for the PSV NWs with structure II. We observed a transition from GMR effect at higher T (≥ 150 K) to MMR (and possible AMR, DWR) dominated effects at intermediate T (~ 75 K) before it returned back to GMR effect at very low T (≤ 25 K).

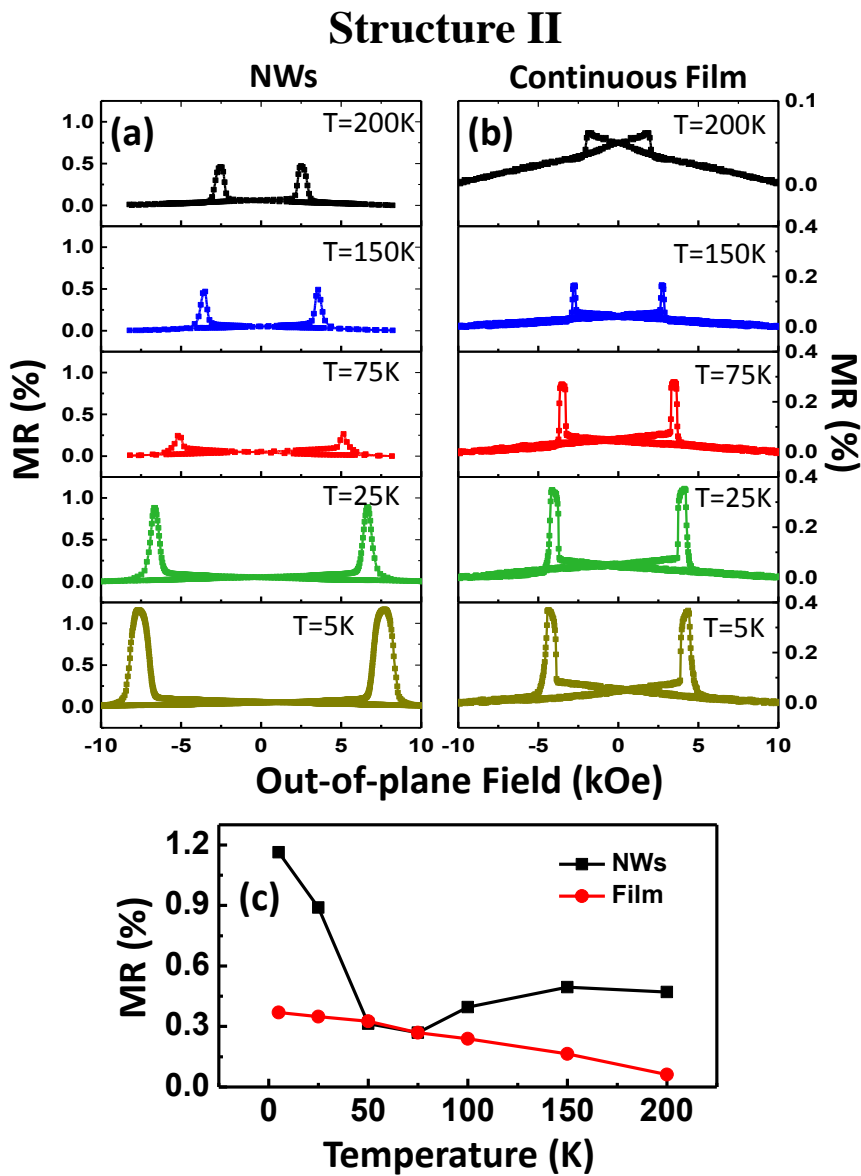


Fig. 5.21 MR responses as a function of T for the PSV NWs (a); and corresponding continuous film (b) with structure II. A plot of MR ratio Vs T is shown in (c).

Note that in this PSV structure the interlayer coupling is negligible small due to the additional Pd spacer. Therefore, the MR transition might simply indicate a crossover of switching field (H_{sw}) between the soft ($n=2$) and the hard ($n=4$) Co/Pd multilayer stacks. At $T=200$ K, H_{sw} of the two bi-layer stack is smaller than the four bi-layer stack, leading to the observed GMR response with clear MR plateau. However, as temperature is decreased, magnetic switching of the two FM stacks tends to overlap due to reduced H_{sw} difference at low T , resulting in a decrease in MR ratio and the MR minimum at $T=75$ K. Further decrease in T leads to a separated magnetic switching of the two FM stacks again because H_{sw} of the two bi-layer stack ($n=2$) is larger than the four bi-layer stack ($n=4$). This consequently gives rise to the clear MR plateau again with a large MR ration at $T=5$ K. The above claim is based on the fact that H_{sw} of the Co/Pd multilayers with smaller bi-layer repeat n show stronger temperature dependence^[157, 159].

The crossover of switching field is further confirmed in the continuous PSV film, where a transition from MMR (and possibly AMR, DWR) dominated behavior to typical GMR response is observed at low T due to the separation of magnetic switching of the two FM stacks, as shown in Fig. 5.21 (b). The temperature induced switching field crossover has also been previously observed in Co/Pt multilayer based magnetic tunnel junctions with perpendicular anisotropy^[158]. Shown in Fig. 5.21(c) is a summary of the MR ratio Vs T for the PSVs. Clearly, the MR minimum at $T=75$ K is a direct evidence of the switching field crossover for the PSV NWs whereas the transition from MMR to GMR dominated effects leads to the monotonic increase of MR ratio with decrease in T in the PSV film.

5.5 Interlayer Coupling in $[\text{Co}/\text{Pd}]_4/\text{Co}/\text{Ru}/[\text{Co}/\text{Pd}]_2$

Multilayers

We have shown in previous sections that strong FM coupling exists in the Co/Pd PSVs with a Au spacer. In this section, we further show that both FM and antiferromagnetic (AFM) type of coupling can be achieved in the Pd(5 nm)/ $[\text{Co}(0.5 \text{ nm})/\text{Pd}(3 \text{ nm})]_4/\text{Co}(0.5 \text{ nm})/\text{Ru}(t_{\text{Ru}})/[\text{Co}(0.5 \text{ nm})/\text{Pd}(3 \text{ nm})]_2$ PSV multilayers with a Ru spacer layer. Shown in Fig. 5.22 (a) and (b-g) are schematics of the deposited PSV structure and M-H loops of the PSV continuous films as a function of the Ru spacer layer thickness t_{Ru} . Clearly, magnetization reversal and detailed features of the M-H loops are markedly dependent on t_{Ru} .

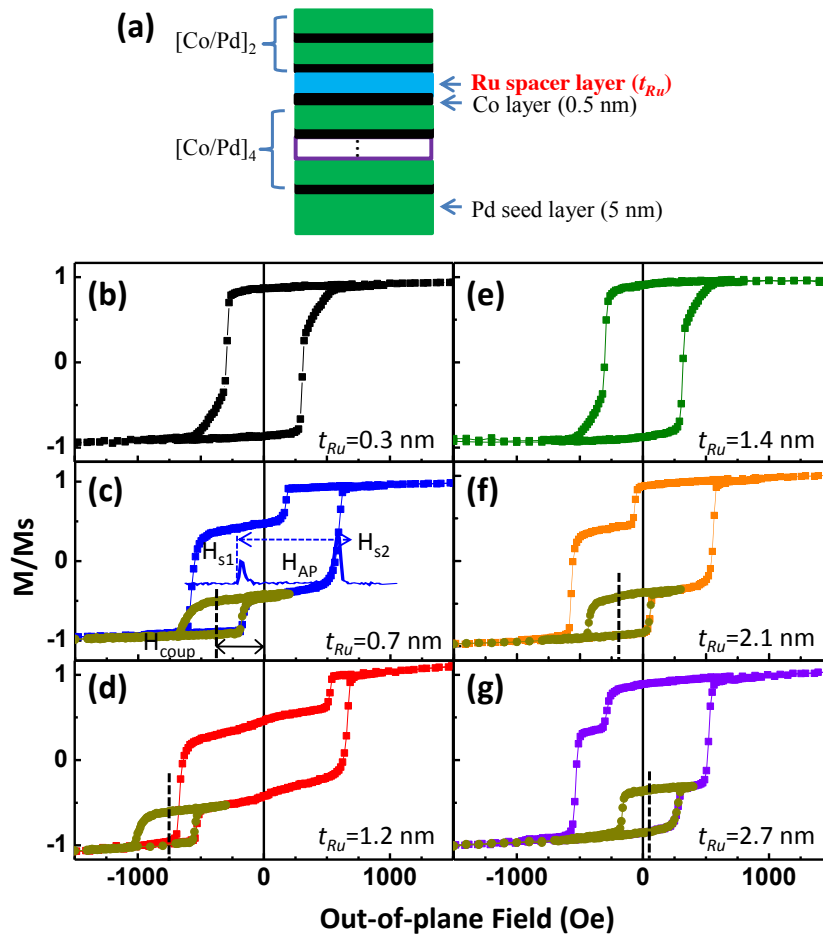


Fig. 5.22 (a) Schematics of the deposited Pd/ $[\text{Co}/\text{Pd}]_4/\text{Co}/\text{Ru}(t_{\text{Ru}})/[\text{Co}/\text{Pd}]_2$ PSV structures with a Ru spacer; and (b-g) M-H loops of the PSV films as a function of t_{Ru} .

We observed a single step switching for $t_{Ru} = 0.3$ nm, indicating a collective magnetization reversal of the soft ($n=2$) and the hard ($n=4$) Co/Pd multilayer stacks due to a strong FM coupling. However, for $t_{Ru} = 0.7$ nm, two distinct switching steps are seen, corresponding to the magnetization reversal of the soft Co/Pd stack at H_{s1} and the hard Co/Pd stack at H_{s2} respectively. The negative switching field $H_{s1} = -175$ Oe of the soft FM stack suggests the existence of a strong AFM coupling in the PSV structure, which has been further verified by the minor loop measurement, where a large negative coupling field $H_{coup} = -390$ Oe is observed. Further increase in t_{Ru} results in an oscillating change of H_{coup} in both amplitude and sign. The PSV structure with $t_{Ru} = 1.4$ nm shows a single step switching due to the strong FM coupling of the two Co/Pd stacks. This interlayer coupling changes to AFM type for $t_{Ru} = 2.1$ nm and changes back to FM type again for $t_{Ru} = 2.7$ nm, as indicated by the dashed lines in Fig. 5.22(f & g). The oscillation of H_{coup} is a typical behavior of RKKY coupling.

We have extracted the interlayer coupling field from the minor loop measurements and plotted it as a function of t_{Ru} , as shown in Fig. 5.23(a) (solid symbols). To confirm that the interlayer coupling indeed comes from RKKY, we have further fitted the experimental data using a RKKY type of expression given by^[41, 42]:

$$H_{coup} \propto \frac{\sin(\phi + 2\pi t_{Ru} / \lambda_F)}{t_{Ru}^p} \quad (5.6)$$

where λ_F represents the Fermi wavelength for Ru. There is a comparatively good agreement between the experimental data and the fitting results (solid line) for $\lambda_F = 1.43$ nm and $p = 1.8$, suggesting that the RKKY coupling is actually the source of the interlayer coupling in the PSV films. The fitting parameters have similar magnitude with those obtained by Parkin et al^[41].

Interlayer coupling also plays an important role in engineering the magnetic switching of the PSV films. Here, we have defined three parameters

H_{s1} , H_{s2} and H_{AP} in Fig. 5.22(c), corresponding to the switching field of the soft Co/Pd stack ($n=2$), the hard Co/Pd stack ($n=4$) and the stable field range over which the two FM stacks are in antiparallel state respectively. Shown in Fig. 5.23(b) is a plot of the three parameters as a function of t_{Ru} . Interestingly, all the three parameters show an oscillation behavior with a period identical to that of interlayer coupling. At $t_{Ru} \leq 1.16$ nm, the soft Co/Pd stack switches at negative field H_{s1} due to the strong AFM coupling. However, H_{s1} shifts to positive field as t_{Ru} is increased due to reduced interlayer coupling strength.

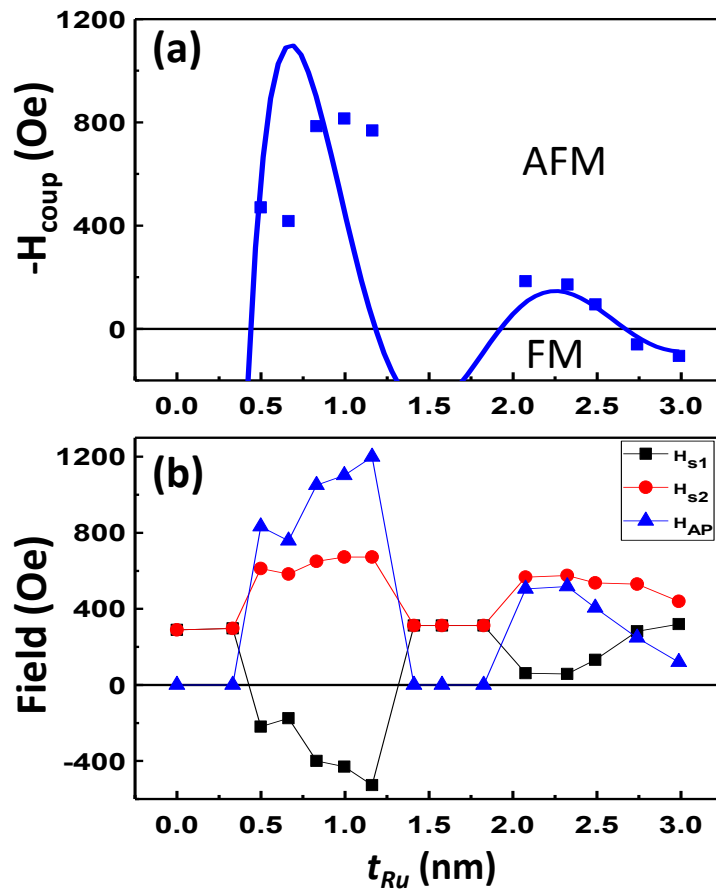


Fig. 5.23 (a) Experimental H_{coup} (solid symbol) extracted from minor M-H loop measurements and RKKY fitting results (solid line) as a function of t_{Ru} ; and (b) a plot of H_{s1} , H_{s2} and H_{AP} (defined in Fig. 5.20(c)) as a function of t_{Ru} .

Shown in Fig. 5.24 are the corresponding perpendicular MR responses of the PSV films taken at room temperature as a function of t_{Ru} . The blue rectangular symbols represent the ascending half loop with field swept from negative saturation to positive saturation while the red circular symbols

indicate the reversed field sweep. As expected, the two loops are symmetric, therefore we will focus only on the ascending half loop in our discussion below.

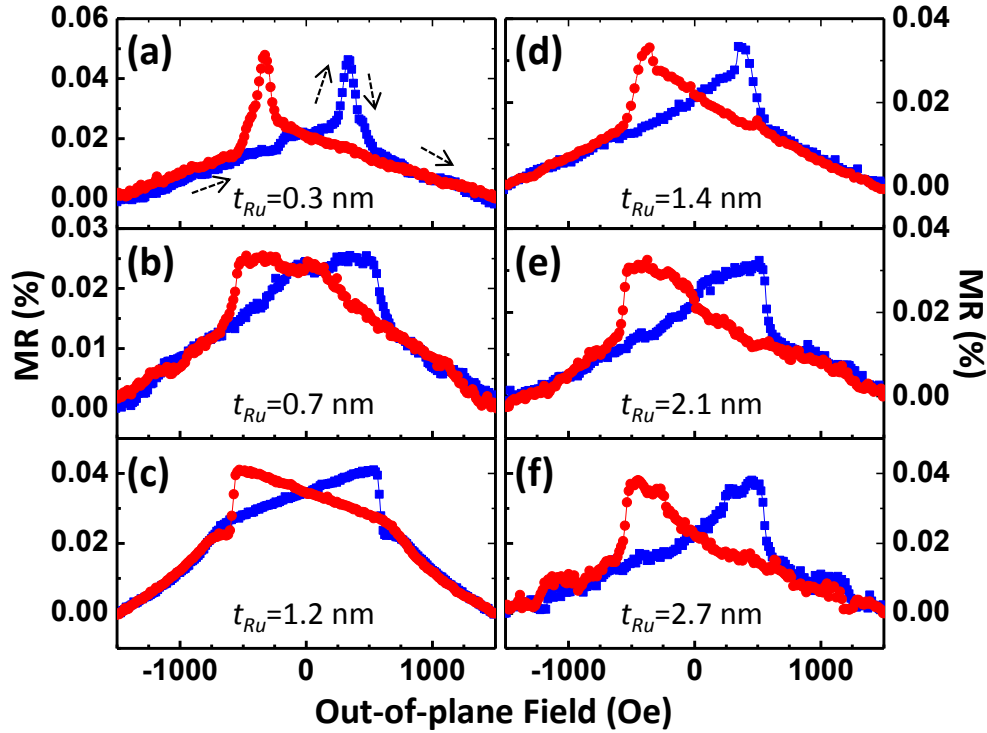


Fig. 5.24 Perpendicular MR responses of the Pd/[Co/Pd]₄/Co/Ru(*t_{Ru}*)/[Co/Pd]₂ PSV films as a function of *t_{Ru}*.

The MR curve for $t_{Ru}=0.3$ nm (Fig. 5.24(a)) performs like a single Co/Pd FM stack with a sharp MR peak appears in the switching region and a linear non-saturating behavior occurs above magnetic saturation due to the MMR effect. For $t_{Ru}=0.7$ nm (Fig. 5.24(b)) and $t_{Ru}=1.2$ nm (Fig. 5.24(c)) however, the sharp MR peak disappears. We observed a clear MR plateau around zero field, corresponding to the antiparallel alignment of the soft ($n=2$) and the hard ($n=4$) Co/Pd multilayer stacks. The onset of the plateau appears at large negative field, indicating the strong AFM coupling of the two Co/Pd stacks. As t_{Ru} is increased to 1.4 nm (Fig. 5.24(d)), the PSV film shows similar MR behavior as that in Fig. 5.24(a) because the two Co/Pd multilayer stacks ferromagnetically couple together again. Further increase in t_{Ru} (Fig. 5.24(e & f)) results in a shift of onset field of the MR plateau towards positive field

direction. All the above discussions are in good agreement with the M-H loops shown in Fig. 5.22 (b-g).

5.6 Summary

To conclude, a systematic investigation of magnetization reversal and MR behaviors of $[\text{Co/Pd}]_n$ NWs and $[\text{Co/Pd}]_4/\text{Au}(t_{\text{Au}})/[\text{Co/Pd}]_2$ PSV NWs are presented in this chapter. A linear non-saturating MR response up to a maximum field as large as 40 kOe was observed in the Co/Pd multilayer NWs, attributing to MMR effect, which are markedly dependent on both temperature T and the bi-layer repeat n . Switching field of the $[\text{Co/Pd}]_n$ NWs can be greatly enhanced by adding a Cu buffer layer due to the combined effect of increased mean grain size and film roughness.

The effects of interlayer coupling at various temperatures have been investigated by varying the Au spacer layer thickness t_{Au} in the PSV NWs. It was shown that for the continuous film deposited under the same condition, the interlayer coupling is almost independent of both t_{Au} and T . The interlayer coupling of the PSV NWs however is much larger and strongly sensitive to the two parameters due to stray field interactions. At low T , the competition between the interlayer coupling and switching field difference of the soft and hard Co/Pd stacks determines the overall magnetization reversal process and MR behavior of the PSV NWs. Interlayer coupling can be effectively manipulated by adding a Co or Pd insertion layer to change the effective spacer layer thickness of the PSV NWs. A transition between GMR and MMR dominated effects was observed in the PSV NWs with a 3 nm Pd insertion layer due to temperature induced switching field crossover of the soft and hard Co/Pd stacks. It was further shown that either ferromagnetic or antiferromagnetic type of coupling can be achieved by engineering the Ru spacer layer thickness in a $[\text{Co/Pd}]_4/\text{Co/Ru}/[\text{Co/Pd}]_2$ PSV film.

Chapter 6

Two-dimensional (2-D) Magnonic Crystals

6.1 Introduction

This chapter investigates the static and dynamic behaviors of 2-D magnonic crystals (MCs) with two different structures, namely, modulated $\text{Ni}_{80}\text{Fe}_{20}$ film and Fe filled $\text{Ni}_{80}\text{Fe}_{20}$ antidot structures. The modulated $\text{Ni}_{80}\text{Fe}_{20}$ film consists of a continuous $\text{Ni}_{80}\text{Fe}_{20}$ film on top of periodic 2-D arrays of perpendicularly magnetized Co/Pd dots (or $\text{Ni}_{80}\text{Fe}_{20}$ dots with in-plane anisotropy). The presence of dot arrays significantly modifies the magnetization reversal process and ferromagnetic resonance (FMR) mode profiles of the $\text{Ni}_{80}\text{Fe}_{20}$ film when compared with the $\text{Ni}_{80}\text{Fe}_{20}$ film without the dot array underneath. In the Fe filled $\text{Ni}_{80}\text{Fe}_{20}$ antidot nanostructures, the “holes” of the $\text{Ni}_{80}\text{Fe}_{20}$ antidot are filled with another ferromagnetic material Fe. It will be shown that although the Fe dots are not in direct contact with $\text{Ni}_{80}\text{Fe}_{20}$ antidot, their stray fields significantly modify the magnetization reversal, the FMR responses and the magnetoresistance behaviors of the host $\text{Ni}_{80}\text{Fe}_{20}$ antidot.

6.2 Modulated $\text{Ni}_{80}\text{Fe}_{20}$ Film

In this section, we present the study of static and dynamic properties of modulated $\text{Ni}_{80}\text{Fe}_{20}$ films deposited on top of periodic 2-D arrays of Co/Pd dots (or $\text{Ni}_{80}\text{Fe}_{20}$ dots). The continuous $\text{Ni}_{80}\text{Fe}_{20}$ film can be considered as a magnonic waveguide (particularly for magnetostatic surface spin waves) while the role of underneath dot array is to create periodic perturbations of

internal fields in the neighbor regions of the film. The advantage over antidot arrays is the absence of spin wave scattering on structural inhomogeneities, i.e. holes in the film. In conventional antidot arrays, scattering from the antidot boundary may cause unexpected influence of spin wave propagation because the wavelength of spin wave (ranging from nanometer to micrometer) is in similar order of magnitude with the dimension of the antidot nanostructure.

6.2.1 Experimental Details

Shown in Fig. 6.1(a) are schematics of the fabrication process flow for the modulated $\text{Ni}_{80}\text{Fe}_{20}$ film structure. Periodic arrays of circular holes with diameter $d = 400 \text{ nm}$ and pitch $p = 550 \text{ nm}$ were first patterned on Si substrate over a large area ($4 \text{ mm} \times 4 \text{ mm}$) using deep ultraviolet lithography at 248 nm exposure wavelength^[3]. The circular holes were defined on 280 nm thick positive photoresist on top of 60 nm thick bottom anti-reflective coating (BARC).

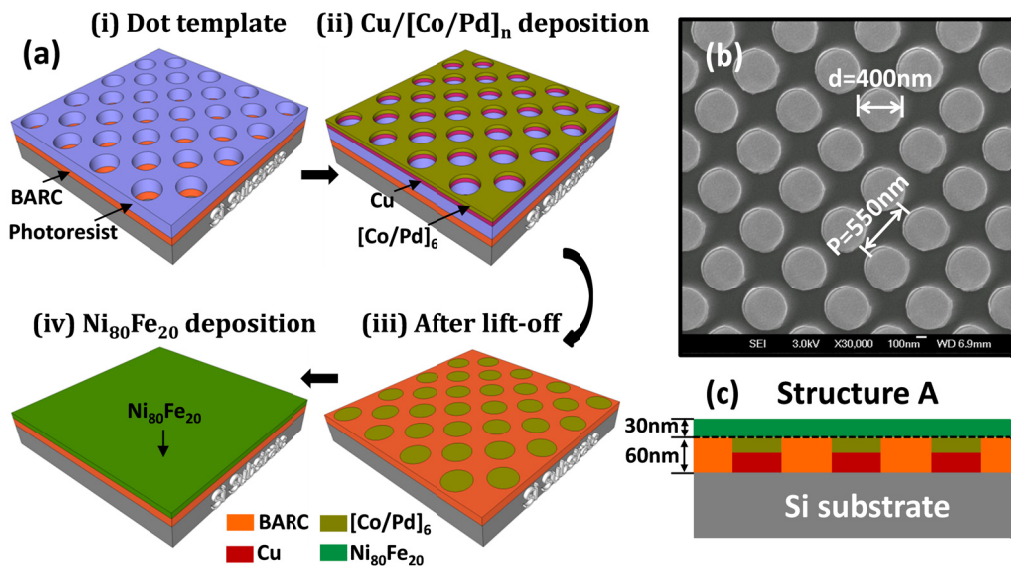


Fig. 6.1 (a) Schematic illustration of fabrication process flow for dot modulated $\text{Ni}_{80}\text{Fe}_{20}$ film; (b) SEM image of Co/Pd dots embedded in BARC matrix; and (c) Schematics of cross section for the modulated $\text{Ni}_{80}\text{Fe}_{20}$ film with Co/Pt dots underneath.

$\text{Cu}(34 \text{ nm})/\text{Pd}(5 \text{ nm})/[\text{Co}(0.5 \text{ nm})/\text{Pd}(3 \text{ nm})]_6$ multilayer film was then

deposited on the patterned substrate using magnetron sputtering deposition followed by the lift-off process, resulting in arrays of Co/Pd dots embedded in the BARC matrix. Shown in Fig. 6.1(b) is the representative SEM micrograph of the Co/Pd dots embedded in the BARC matrix. The thickness of the Cu/Pd/[Co/Pd]₆ multilayer stack is identical to the BARC layer (60 nm) to ensure a flat film surface. Subsequently, a 30 nm thick Ni₈₀Fe₂₀ layer was deposited on top of the structure using electron beam evaporation. The resulting final structure consists of Ni₈₀Fe₂₀ film (30 nm) on top of [Co/Pd]₆ dots embedded in BARC, as shown Fig. 6.1(c) the schematics of a cross-section. We refer to the final structure as “modulated Ni₈₀Fe₂₀ film (Structure A)”. For controlled experiment, the reference Ni₈₀Fe₂₀ film (30 nm) was also deposited during the same processing steps.

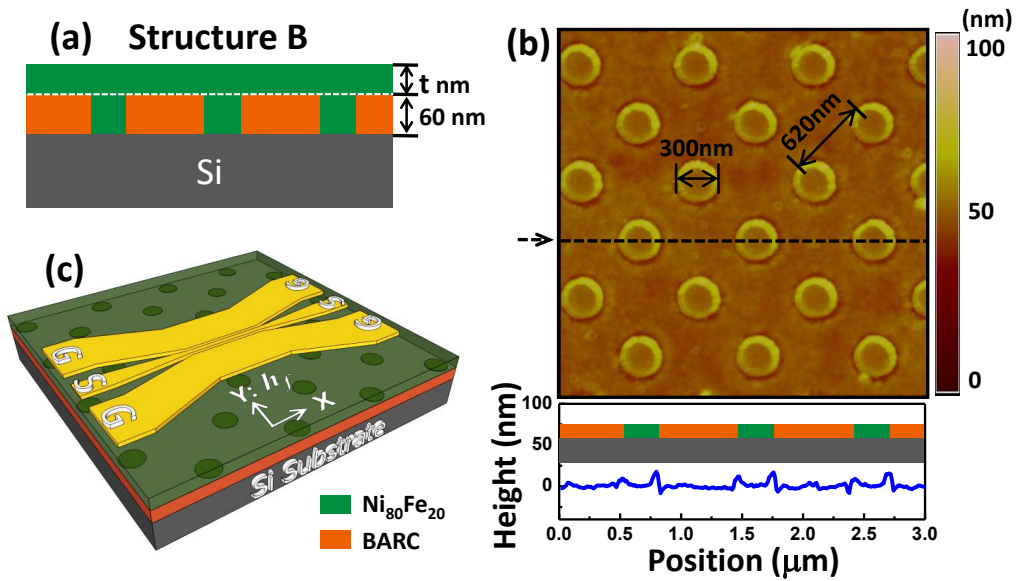


Fig. 6.2 (a) Schematics of cross-section for modulated Ni₈₀Fe₂₀ film with Ni₈₀Fe₂₀ dots underneath; (b) Atomic force micrograph of the Ni₈₀Fe₂₀ dots embedded in BARC matrix and a cross-section across the dashed line; and (c) Schematics of coplanar waveguide deposited on top of the modulated Ni₈₀Fe₂₀ film for FMR measurements.

We have also fabricated another type of 2-D MCs by replacing the perpendicularly magnetized Co/Pd dots with in-plane magnetized Ni₈₀Fe₂₀ dots. The final structure consists of Ni₈₀Fe₂₀ film (t nm) on top of Ni₈₀Fe₂₀

dots (60 nm) embedded in BARC, as shown in Fig. 6.2(a) the schematics of a cross-section. The $\text{Ni}_{80}\text{Fe}_{20}$ film thickness t was varied from 5 to 60 nm. We refer to this structure as “modulated $\text{Ni}_{80}\text{Fe}_{20}$ film (Structure B)”. Representative atomic force micrograph of the $\text{Ni}_{80}\text{Fe}_{20}$ dots with $d=300$ nm and $p=620$ nm embedded in BARC over an area of $3\ \mu\text{m} \times 3\ \mu\text{m}$ is shown in Fig. 6.2(b). A cross-section across the dashed line shows a horizontally flat surface profile of the $\text{Ni}_{80}\text{Fe}_{20}$ dots embedded in BARC matrix. Similarly, the reference $\text{Ni}_{80}\text{Fe}_{20}$ dots array (60 nm) and $\text{Ni}_{80}\text{Fe}_{20}$ continuous film (t nm) were fabricated at the same time with the modulated film.

The collective magnetic switching behaviors of the modulated $\text{Ni}_{80}\text{Fe}_{20}$ film with structure A and B were characterized using a focused longitudinal Magneto-Optical Kerr Effect (MOKE) setup and vibrating sample magnetometer (VSM) respectively with field applied in-plane along diagonal direction of the dot lattice (X-axis). For FMR measurements, typical coplanar waveguide (CPW) of $\text{Al}_2\text{O}_3(50\ \text{nm})/\text{Ti}(5\ \text{nm})/\text{Au}(150\ \text{nm})$ was placed on top of the fabricated magnetic structures using ultraviolet lithography followed by the lift-off process, as illustrated in Fig. 6.2(c). Details of the FMR measurement process has been described in § 3.3.7. The frame of reference used is shown in Fig. 6.2(c). The external field (H_{app}) is applied along the X-axis, while the microwave magnetic field h_f produced by the signal line of the CPW is applied along Y-axis.

Our understanding of the experimental results was further enhanced using the LLG micromagnetic simulator^[160]. Standard parameters for $\text{Ni}_{80}\text{Fe}_{20}$ (gyromagnetic ratio $\gamma = 2.8\ \text{GHz/kOe}$, saturation magnetization $M_s = 810\ \text{emu}\cdot\text{cm}^{-3}$, exchange constant $A = 1.05 \times 10^{-6}\ \text{erg}\cdot\text{cm}^{-1}$, damping parameter $\alpha = 0.01$, and anisotropy constant $K_U = 0$) were used in the simulation. The M_s and α were extracted using the least-squares-fit method from FMR data of the reference 30 nm thick $\text{Ni}_{80}\text{Fe}_{20}$ continuous film. The masks used in the simulations were derived from the SEM micrographs using 2-D periodic

boundary conditions with a cell size of $7 \text{ nm} \times 7 \text{ nm} \times 5 \text{ nm}$. The spatial characteristics of the different FMR modes were quantified by running time-dependent LLG simulations and analyzing the results using spatially and frequency-resolved fast Fourier transform imaging^[161-163].

6.2.2 $\text{Ni}_{80}\text{Fe}_{20}$ Film on Top of Periodic Arrays of Co/Pd Dots

Shown in Fig. 6.3(a & b) and (d & e) are the 2-D FMR absorption spectra and MOKE hysteresis loops for the $\text{Ni}_{80}\text{Fe}_{20}$ film (30 nm) without and with Co/Pd dots underneath respectively. There is a good agreement between the FMR responses and the hysteresis loops for both the $\text{Ni}_{80}\text{Fe}_{20}$ films. Clearly, FMR response and magnetization reversal of the modulated $\text{Ni}_{80}\text{Fe}_{20}$ film have been significantly modified due to the presence of Co/Pd dots when compared with the reference $\text{Ni}_{80}\text{Fe}_{20}$ film. Although only one resonance mode is observed in the modulated $\text{Ni}_{80}\text{Fe}_{20}$ film with Co/Pd dots underneath (Fig. 6.3(d)), which is similar to that observed in the reference $\text{Ni}_{80}\text{Fe}_{20}$ film (Fig. 6.3(a)), the linewidth becomes much wider. The combined effects of field-dragging and increased spatial magnetization distribution induced by the bottom Co/Pd dots might be responsible for this observation. The bottom perpendicularly magnetized Co/Pd dots tend to drag the neighboring $\text{Ni}_{80}\text{Fe}_{20}$ film to deviate from in-plane configuration, leading to an enhancement of Gilbert damping and hence the FMR linewidth^[164]. On the other hand, it is easy to understand that the region of the top $\text{Ni}_{80}\text{Fe}_{20}$ film that overlaps with the bottom Co/Pd dots (region α , defined in the inset of Fig. 6.3(d)) and the region of film without the Co/Pd dots underneath (region β) should have different magnetic parameters (like internal fields) due to the different exchange coupling strength of the two FM materials. This consequently results in a slight difference in resonance frequency of the two regions. The overall FMR signal will be a superposition of these local FMR lines yielding a broader linewidth.

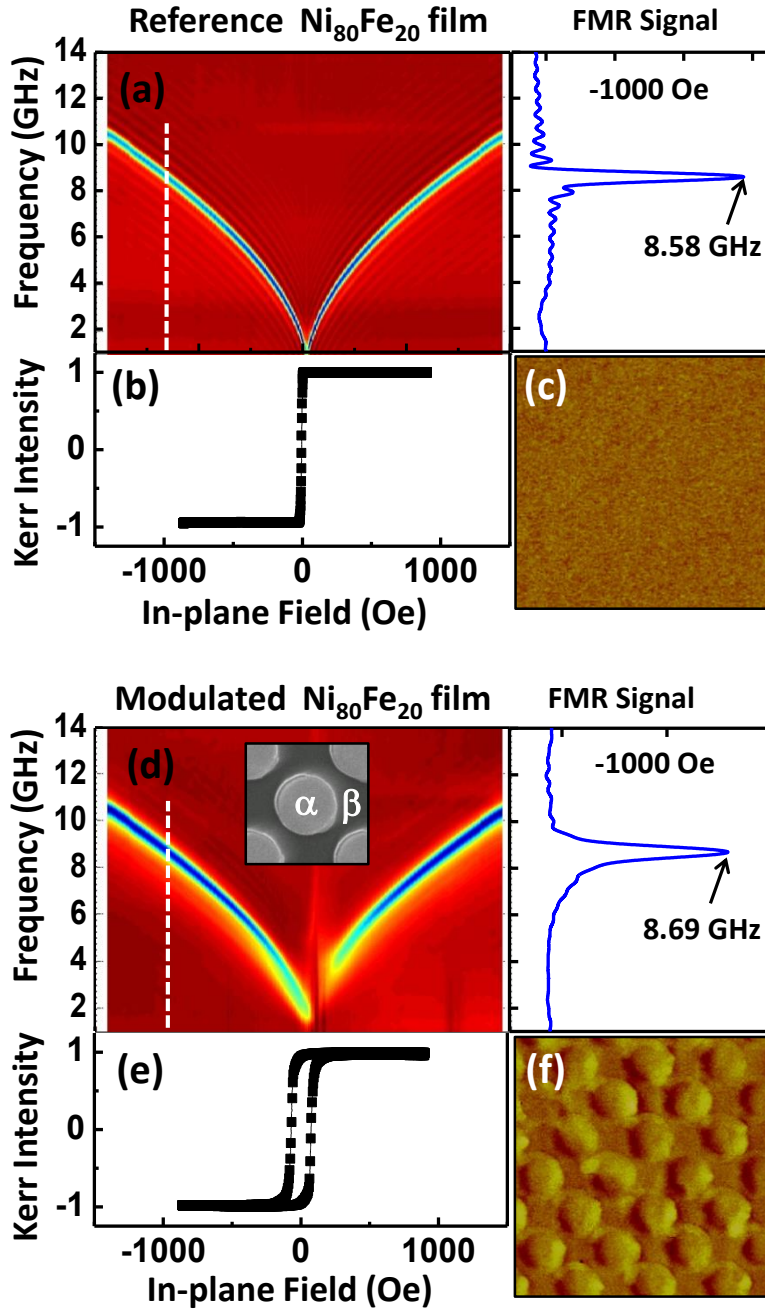


Fig. 6.3 (a) 2-D FMR absorption spectra (An FMR trace for $H_{app} = -1000$ Oe is shown at right-hand side); (b) Hysteresis loop; and (c) An MFM image taken at remanence after saturation for the reference $\text{Ni}_{80}\text{Fe}_{20}$ film. The results for the modulated $\text{Ni}_{80}\text{Fe}_{20}$ film with Co/Pd dots underneath are shown in (d)-(f).

Shown in the right-hand side of Fig. 6.3 (a & d) are FMR traces of the reference $\text{Ni}_{80}\text{Fe}_{20}$ film and modulated $\text{Ni}_{80}\text{Fe}_{20}$ film with Co/Pd dots underneath for $H_{app} = -1000$ Oe. Interestingly, there is an upwards shift of resonance frequency from 8.58 GHz to 8.69 GHz at the presence of the Co/Pd

dots. This is a direct effect of increased internal fields resulting from the additional anisotropy field of the Co/Pd dots.

The bottom Co/Pd dots also modify the magnetization reversal of the top Ni₈₀Fe₂₀ film. As expected, the switching field of the modulated Ni₈₀Fe₂₀ film is significantly increased from 6 Oe to 72 Oe due to the pinning effects of the bottom Co/Pd dots. This has been further verified using MFM imaging. Shown in Fig. 6.3(c) and (f) are MFM micrographs taken at remanence after negative saturation for the reference Ni₈₀Fe₂₀ film and the modulated Ni₈₀Fe₂₀ film respectively. We observed clear domain structures pinned at the Co/Pd dot boundary in the modulated Ni₈₀Fe₂₀ film. For the reference Ni₈₀Fe₂₀ film however, no clear domain structure can be observed.

6.2.3 Ni₈₀Fe₂₀ Film on Top of Periodic Arrays of Ni₈₀Fe₂₀ Dots

We have replaced the bottom perpendicularly magnetized Co/Pd dots with in-plane magnetized Ni₈₀Fe₂₀ dots and referred to this modulated film structure as “modulated Ni₈₀Fe₂₀ film (Structure B)”. Shown in Figs. 6.4(a) are the measured M-H loops of the modulated Ni₈₀Fe₂₀ films (Structure B) as a function of the Ni₈₀Fe₂₀ film thicknesses t . For $t = 0$ nm (i.e. the reference dot array), the M-H loop has a double triangle shape, typical for the circular dot with vortex ground state. Nucleation (H_n) and annihilation (H_a) fields are quite pronounced and can be easily extracted from the loop: $H_n = 750$ Oe and $H_a = 1150$ Oe.

For the modulated film with the smallest value $t = 5$ nm, the loop can be considered as a sum of loops from dot array and continuous film. With further increase of t the double triangle feature becomes more and more suppressed with H_n and H_a becoming less pronounced and gradually decreasing to 630 and 900 Oe respectively for $t = 30$ nm. This reduction is the direct effect of the strong exchange coupling between the dots and the continuous film. Nucleation and annihilation fields disappear completely for $t = 60$ nm,

however this structure still saturates only at around 1000 Oe (which is comparable with the H_a of pure dot array), indicating the existence of some vortex state remnants. It is also worth mentioning the significant dependence of the coercive field H_c on the film thickness (since the bottom dots serve as pinning sites for the upper film) with a clear maximum of 54 Oe for $t=15$ nm. The similar $H_c(t)$ dependence was observed previously in the $\text{Ni}_{80}\text{Fe}_{20}$ antidot arrays with fixed values of hole diameter and pitch^[165].

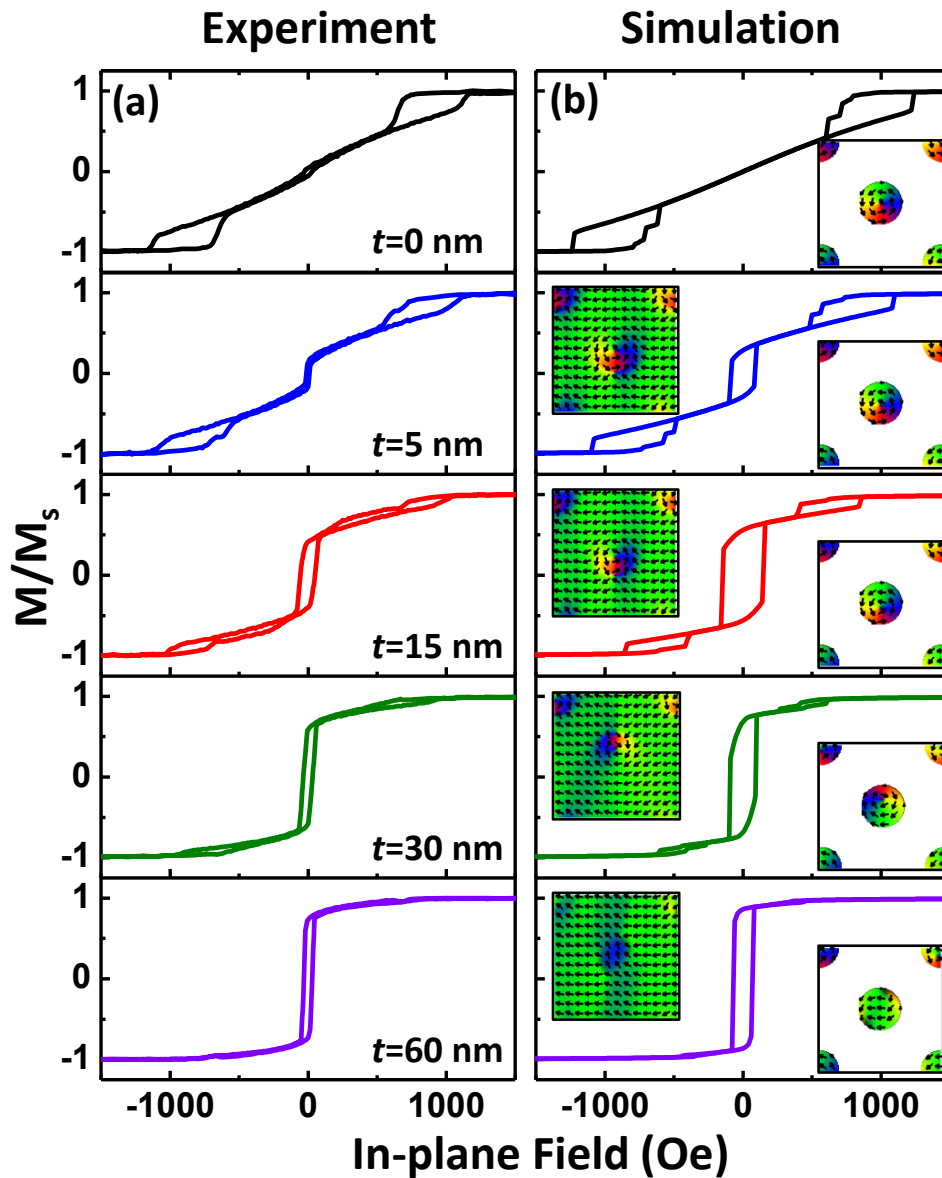


Fig. 6.4 (a) Experimental; and (b) simulated hysteresis loops for the modulated $\text{Ni}_{80}\text{Fe}_{20}$ films (Structure B) with different values of film thickness t varied from 0 to 60 nm. Inserts to the simulated hysteresis loops are the simulated magnetization configurations for middle sections of the dot and film parts of the given modulated film at remanence.

Shown in Fig. 6.4(b) are the corresponding simulated hysteresis loops for the reference $\text{Ni}_{80}\text{Fe}_{20}$ dots and the modulated $\text{Ni}_{80}\text{Fe}_{20}$ films (Structure B) of different thicknesses t . There is a good qualitative agreement between the experimental results and micromagnetic simulations, in particular disappearance of double triangle feature for the sample with $t = 60$ nm and maximum of H_c also corresponds to the sample with $t = 15$ nm. The difference in coercive fields may be attributed to the limited number of unit cells with periodic boundaries due to computation limitations.

Shown as insets in Fig. 6.4(b) are simulated magnetization states for middle sections of the dot (right inset) and film parts (left inset) of the corresponding modulated film at remanence. We would like to underline that each section is 5 nm thick due to the selection of unit cell size and that the magnetization configurations do not change significantly inside dot and film parts. As one may see, for the relatively thin films ($t = 5$ and 15 nm) the dots are still in the vortex state with a vortex positioned in the center of the dot. What is even more important, the vortex is propagated through the entire continuous film, creating some equivalent of antidots - i.e. areas with total zero in-plane magnetic moments. For the sample with $t = 30$ nm, the vortex becomes asymmetric (due to the strong interaction with saturated magnetic film), however it is still propagated through the continuous film without significant change of its profile. Finally, for the sample with $t = 60$ nm, the ground vortex state is replaced with a semi-saturated state. This change explains the disappearance of annihilation and nucleation fields from the hysteresis loop.

Fig. 6.5(a) presents the set of FMR spectra from modulated films with different values of t as well as from reference dot array and continuous film. The spectra were recorded at the external field of $H_{app} = -1400$ Oe that is well above both nucleation and annihilation fields for dot array. The marked shift of ~ 3 GHz of main FMR peaks for the dot array (case $t = 0$ nm) and 60 nm thick

continuous film can be attributed to the significant in-plane demagnetizing factors for dot with high aspect ratio^[166]. For most of the modulated films, two resonance modes were observed, namely “mode A” (at lower frequency, situates around 9 GHz, can be associated with resonance in dots) and “mode B” (at higher frequency, usually situates around 12 GHz, can be associated with resonance in continuous film). For the sample with $t = 5$ nm, the intensity of mode A is high and this mode situates at the same frequency as the main mode in reference dot array. However, the intensity of mode B is quite weak and the mode is shifted to lower frequencies comparing to the main mode of the continuous film. The linewidth of mode A is similar to the one from dot array. For the sample with $t = 15$ nm modes A and B have approximately the same amplitudes. The linewidth of mode A is much broader compared to mode A for $t = 5$ nm, while the linewidth of mode B is quite narrow. With further increase of t the relative amplitude of mode A decreases and both modes become broader, indicating the growth of internal inhomogeneities in the system.

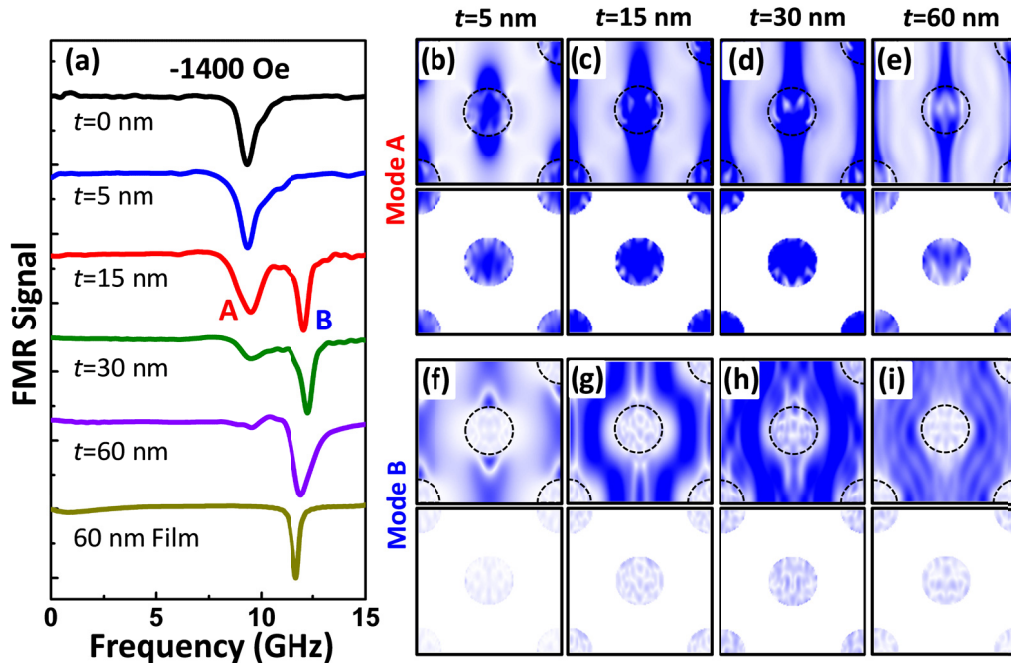


Fig. 6.5 (a) Experimental FMR spectra at -1400 Oe for modulated $Ni_{80}Fe_{20}$ films (Structure B) as a function of the film thickness t and for a 60 nm-thick continuous film. (b-e) Profiles (obtained from micromagnetic simulations) of mode A; and (f-i) mode B for middle sections of the dot and film part of modulated $Ni_{80}Fe_{20}$ films as a function of t . Blue color represents large precession amplitudes.

To better understand the FMR spectra, we have extracted different mode profiles for modulated films from micromagnetic simulations. Fig. 6.5 shows profiles of modes A (Fig. 6.5 (b-e)) and B (Fig. 6.5 (f-i)) for the middle section of the dot and film part of the modulated $\text{Ni}_{80}\text{Fe}_{20}$ film structures with different t for the external field $H_{app} = -1400$ Oe. Again we would like to underline that each section is 5 nm thick due to the selection of unit cell size and that the mode profiles do not change significantly inside the dots and film parts. It is not surprising that mode A is dominant in the dot part of the modulated film therefore it will be more interesting to discuss its localization in the film part of the sample. For $t = 5$ nm (Fig. 6.5(b)), it localizes in the areas above the dots and has a shape of ellipse in the direction perpendicularly to the direction of external magnetic field. With increase of t the ellipse became more and more elongated and for $t = 30$ nm (Fig. 6.5(d)), the mode profile transforms into an infinite stripe. With further increase of t to 60 nm (Fig. 6.5(e)), the width of the stripe becomes narrow. We also observed that the area above the dot is not at resonance anymore. For mode B, the situation is quite different. It is also not surprising that the dot part of the modulated film does not contribute to this mode, so we should focus again on the mode profile in the film part. For $t = 5$ nm (Fig. 6.5(f)) the mode seems to be dispersed over the film range and its intensity is very low compared to that of mode A. This result is in a good agreement with experiment and allows us to understand why this mode cannot be clearly detected. For the case $t = 15$ nm (Fig. 6.5(g)), mode B appears in the whole film in the areas outside the dots and has a shape of two unsymmetrical sinusoids oriented perpendicularly to the applied field. The mode profile is very sharp; therefore the mode resonance linewidth should be quite narrow, as was already observed in the experiment. With further increase of t the mode profile became less pronounced (Fig. 6.5(h & i)) - this explains the broadening of the mode resonance linewidth.

The evolution of resonance frequencies of modes A and B with the change of external field for the case $t = 15$ nm (since for this sample mode intensities are similar) is shown in Fig. 6.6(a). Experimentally obtained dependencies of resonance frequency f_r on resonance field H_r for the reference dot and film samples are also presented on the same graph for comparison.

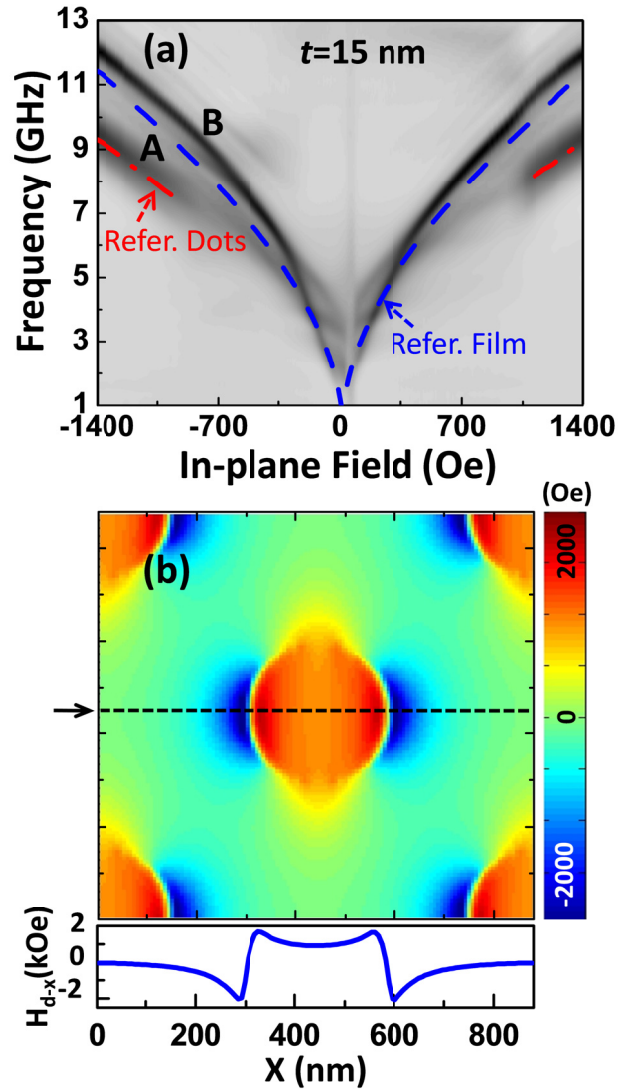


Fig. 6.6 (a) Experimental 2-D FMR spectra of the modulated $Ni_{80}Fe_{20}$ film with $t = 15$ nm, reference $Ni_{80}Fe_{20}$ dots and reference 15 nm thick $Ni_{80}Fe_{20}$ film. (b) Spatial distributions of demagnetization field H_{d-x} in the top $Ni_{80}Fe_{20}$ film for $H = -1400$ Oe (The H_{d-x} profile along dashed line is shown below).

We observed that mode A has the same resonance frequencies and exists in the same field range (above the dot nucleation field) as the main resonance mode of the dot array. Mode B however, exists in the whole range of fields. In

the low-field range, the frequency of mode B coincides with that of the reference film. Above 150 Oe, the resonance frequencies of the mode B for the given field became higher than the ones of continuous film. At ~400 Oe this difference reaches 600 MHz and keeps the same for the higher fields.

To better understand this difference, the spatial distributions of internal fields were extracted from simulations. Shown in Fig. 6.6(b) is the simulated spatial distribution of the X-component of the demagnetizing field H_{d-x} in the middle section of the film part of the sample with $t = 15$ nm for $H_{app} = -1400$ Oe. At the bottom of Fig. 6.6(b) the profile of H_{d-x} along the direction of the applied field (across the dashed line) is presented. Clearly, H_{d-x} is significantly modified due to the presence of $\text{Ni}_{80}\text{Fe}_{20}$ dots underneath. Due to the strong exchange coupling of the bottom $\text{Ni}_{80}\text{Fe}_{20}$ dots, the demagnetizing field directly above the dots is largely positive. On the contrary, a smaller negative H_{d-x} is observed in the regions that are not in direct contact with dots. Since mode B is localized in the second area, for the given field the f_r for mode B is higher than that for reference $\text{Ni}_{80}\text{Fe}_{20}$ film.

6.3 Fe Filled $\text{Ni}_{80}\text{Fe}_{20}$ Antidot Nanostructures

In this section, we investigate the magnetic properties of another type of 2-D MCs: Fe filled $\text{Ni}_{80}\text{Fe}_{20}$ antidot nanostructure in which the “holes” of $\text{Ni}_{80}\text{Fe}_{20}$ antidot are filled with Fe dots. We refer to this structure as “ $\text{Ni}_{80}\text{Fe}_{20}/\text{Fe}$ ”. It will be shown that both the static and dynamic behaviors of the $\text{Ni}_{80}\text{Fe}_{20}/\text{Fe}$ structure are significantly modified due to the presence of Fe dots when compared with the host $\text{Ni}_{80}\text{Fe}_{20}$ antidot.

6.3.1 Experimental Details

The fabrication of the $\text{Ni}_{80}\text{Fe}_{20}/\text{Fe}$ structure consists of a two-stage e-beam evaporation followed by the lift-off process^[167]. Shown in Fig. 6.7 is a

typical fabrication process flow. Periodic arrays of circular holes with varied diameter d in the range from 300 nm to 550 nm and fixed pitch $p=620$ nm were patterned onto Si substrate using deep ultraviolet lithography at 248 nm exposure wavelength. Fe(25 nm)/Au(5 nm)/Al₂O₃ (50 nm) films were then deposited on the patterned substrate using e-beam evaporation followed by lift-off process. Subsequently, the remaining BARC layer was stripped using an ozone stripper. This was followed by e-beam deposition of Ni₈₀Fe₂₀(25 nm)/Au(5 nm) on top of the Fe(25 nm)/Au(5 nm)/Al₂O₃ (50 nm) dots. In the final process, the sample was dipped in an AZ-300 MIF photoresist developer solution which is able to remove the Al₂O₃ layer and the Ni₈₀Fe₂₀/Au layer on top of the Fe/Au dots, resulting in the final Ni₈₀Fe₂₀/Fe nanostructure consisting of Ni₈₀Fe₂₀ antidot with holes filled by Fe dots. The thickness of Ni₈₀Fe₂₀ antidot is identical to that of the Fe dots in the final Ni₈₀Fe₂₀/Fe structure. The 5 nm Au film was used to protect the FM layers from oxidation during processing.

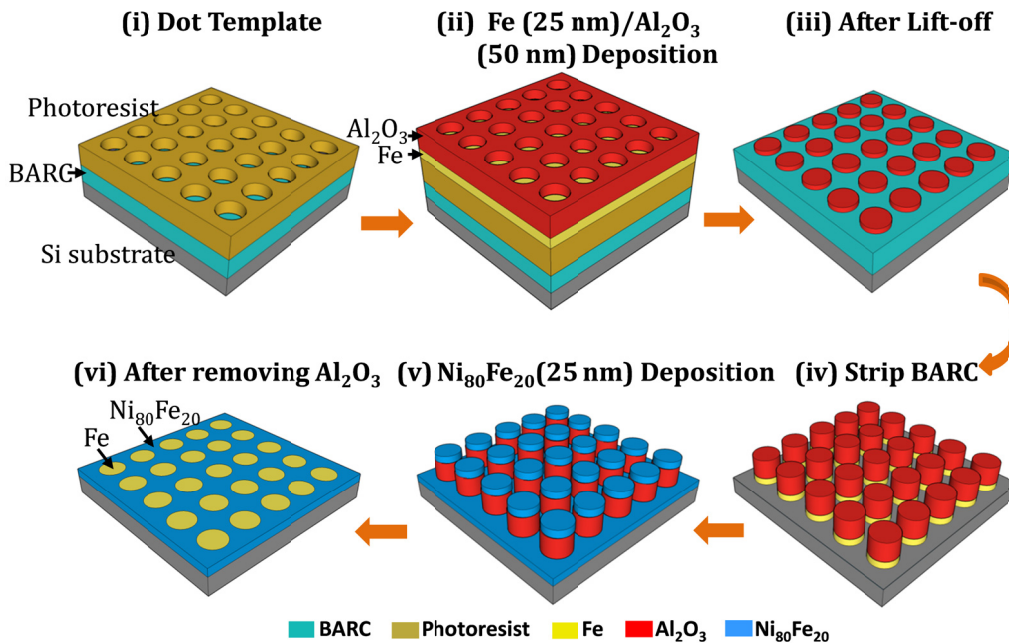


Fig. 6.7 Schematics of typical fabrication process flow for the Ni₈₀Fe₂₀/Fe structure.

For controlled experiment, reference Fe(25 nm)/Au(5 nm) dot array and Ni₈₀Fe₂₀(25 nm)/Au(5 nm) antidot array were also fabricated during the same

processing steps. In order to fabricate the Fe dots array, Fe(25 nm)/Au(5 nm)/Al₂O₃(50 nm) dots were prepared in the same process as the Ni₈₀Fe₂₀/Fe structure followed by a dip in the AZ photoresist developer solution to remove the Al₂O₃ layer. To fabricate the Ni₈₀Fe₂₀ antidot, 70 nm thick Al₂O₃ dot array was fabricated using the same templates as the Fe dots in the Ni₈₀Fe₂₀/Fe structure followed by the deposition of Ni₈₀Fe₂₀ (25 nm)/Au(5 nm) films at the same time as the Ni₈₀Fe₂₀/Fe sample. The Al₂O₃ dots were then dissolved in the AZ photoresist developer solution leaving behind array of holes in Ni₈₀Fe₂₀/Au film.

Shown in Fig. 6.8(a-c) are representative SEM micrographs of the Fe dots, Ni₈₀Fe₂₀ antidot and the Ni₈₀Fe₂₀/Fe structure with $d=550$ nm, respectively. As can be seen from Fig. 6.8(c), there is a small gap (~ 30 nm) between the Fe dots and the surrounding Ni₈₀Fe₂₀ antidot, implying that the two FM structures are not exchange coupled (only coupled magnetostatically).

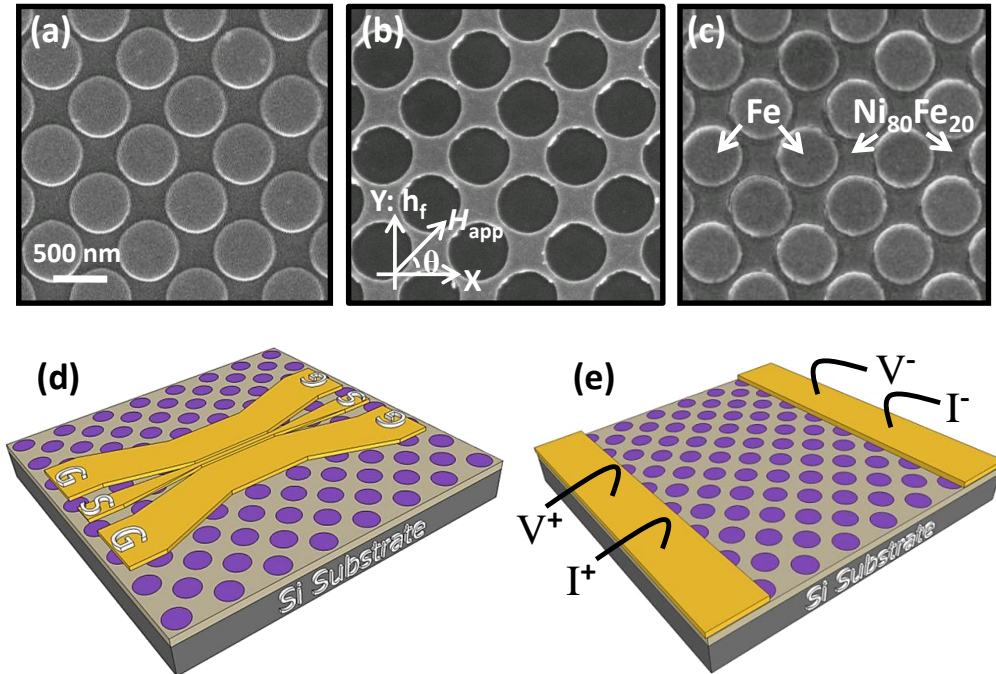


Fig. 6.8 SEM micrographs of (a) reference Fe dots; (b) reference Ni₈₀Fe₂₀ antidot; and (c) the Fe/Ni₈₀Fe₂₀ structure. Schematics of coplanar waveguide deposited on top of the fabricated nanostructures for FMR measurements and Au bond pads for MR measurements are shown (d) and (e), respectively.

The collective magnetic switching behaviors were characterized using a focused longitudinal Magneto-Optical Kerr Effect (MOKE) setup with field applied in-plane along diagonal direction of the dot lattice (X-axis). For FMR and magnetoresistance (MR) measurements, typical coplanar waveguide of $\text{Al}_2\text{O}_3(50 \text{ nm})/\text{Ti}(5 \text{ nm})/\text{Au}(150 \text{ nm})$ and electrical contacts of $\text{Ti}(5 \text{ nm})/\text{Au}(200 \text{ nm})$ were placed on top of the fabricated magnetic structures respectively using ultraviolet lithography followed by lift-off process, as illustrated in Fig. 6.8(d & e). Details of the FMR measurement process has been described in § 3.3.7. MR measurements were conducted using the standard four probe technique by applying a constant DC current of 1 mA along X-axis in the temperature range of $4.2 \text{ K} \leq T \leq 300 \text{ K}$. The frame of reference used is shown in Fig. 6.8(b) with H_{app} applied in-plane at an angle θ relative to the X-axis.

Understanding of the experimental results was facilitated using the LLG micromagnetic simulator^[160]. Standard parameters for $\text{Ni}_{80}\text{Fe}_{20}$ (gyromagnetic ratio $\gamma = 2.8 \text{ GHz/kOe}$, saturation magnetization $M_s = 810 \text{ emu}\cdot\text{cm}^{-3}$, exchange constant $A = 1.05 \times 10^{-6} \text{ erg}\cdot\text{cm}^{-1}$, and anisotropy constant $K_U = 0$) and Fe ($M_s = 1714 \text{ emu}\cdot\text{cm}^{-3}$, $A = 2.1 \times 10^{-6} \text{ erg}\cdot\text{cm}^{-1}$ and $K_C = 0$) were used in the simulation. Details of the simulation process has been described in § 6.2.1.

6.3.2 Magnetization Reversal Mechanism

Shown in Fig. 6.9(a) is the MOKE hysteresis loop for representative 25 nm thick Fe dot arrays with diameter $d=550 \text{ nm}$ for fields applied along the X-axis. The Fe dots show a typical dot reversal process, namely, vortex core nucleation followed by core propagation and annihilation^[168]. The corresponding hysteresis loop of the reference 25 nm $\text{Ni}_{80}\text{Fe}_{20}$ antidot is shown in Fig. 6.9(b). The $\text{Ni}_{80}\text{Fe}_{20}$ antidot show a sharp magnetic switching with a switching field (280 Oe) much larger than that of the corresponding continuous film (23 Oe, see the inset of Fig. 6.9(b)) due to pinning effects at the antidot edge and enhanced demagnetization fields.

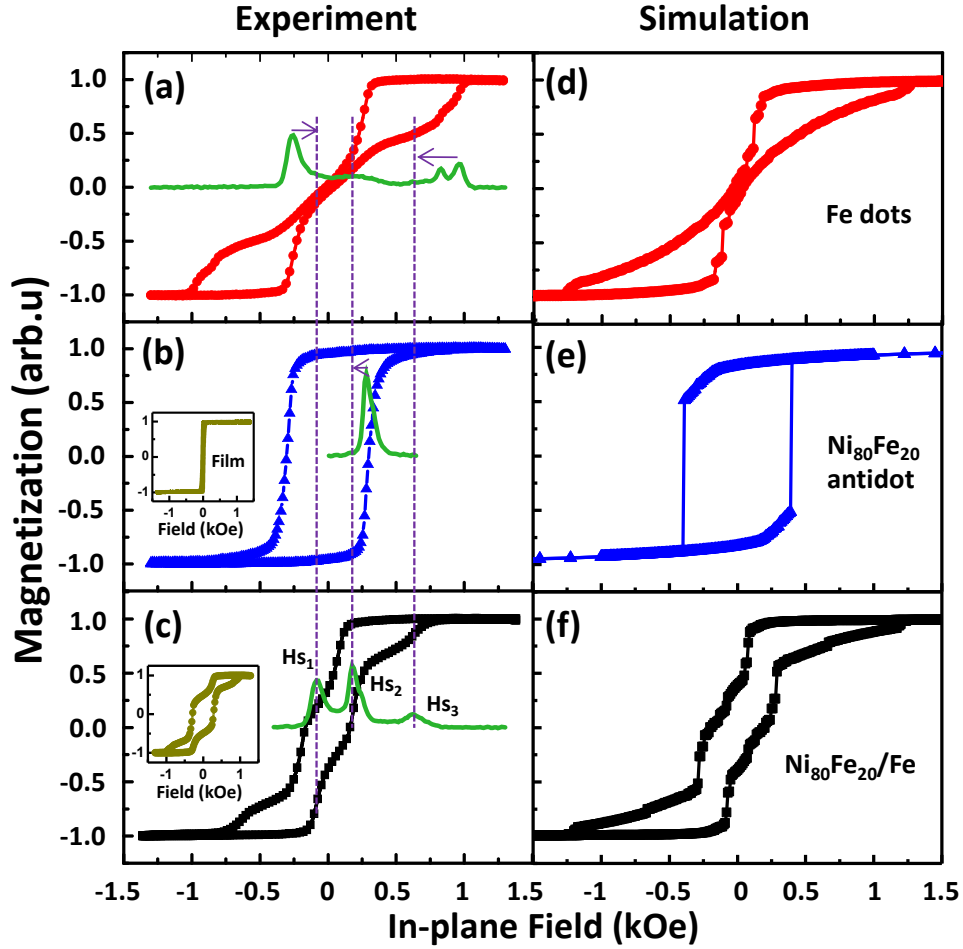


Fig. 6.9 Hysteresis loops for (a) Fe dots; (b) $\text{Ni}_{80}\text{Fe}_{20}$ antidot (hysteresis loop for corresponding $\text{Ni}_{80}\text{Fe}_{20}$ film is shown as an inset); and (c) $\text{Ni}_{80}\text{Fe}_{20}/\text{Fe}$ structure (The interpolate loop assuming no coupling between the Fe dots and $\text{Ni}_{80}\text{Fe}_{20}$ antidot is shown as an inset). The simulated hysteresis loops are shown in (d)-(f) respectively.

The corresponding M-H loop of the 25 nm thick $\text{Ni}_{80}\text{Fe}_{20}/\text{Fe}$ structure is shown in Fig. 6.9(c). Interestingly, we observed three distinct switching steps, corresponding to vortex core nucleation of Fe dots at H_{s1} , magnetization reversal of $\text{Ni}_{80}\text{Fe}_{20}$ antidot array at H_{s2} and vortex core annihilation of Fe dots at H_{s3} . As H_{app} is increased from negative saturation, the magnetization is maintained until $H_{s1} = -80$ Oe, when a rapid decrease of Kerr intensity occurs, indicating the nucleation process of vortex core in the Fe dots. This is followed by a comparatively slow decrease rate of Kerr intensity at around zero fields, attributed to the propagation of the vortex core in the Fe dots. Further increasing the field up to H_{s2} results in a sharp switching,

corresponding to the magnetization reversal of the $\text{Ni}_{80}\text{Fe}_{20}$ antidot. The last switching process is dominated by vortex core propagation of the Fe dots until the vortex core annihilates at the dot edge at a field $H_{s3}=630$ Oe.

We have compared the switching fields of the reference Fe dots (Fig. 6.9(a)) and $\text{Ni}_{80}\text{Fe}_{20}$ antidot (Fig. 6.9(b)) with the $\text{Ni}_{80}\text{Fe}_{20}/\text{Fe}$ structure (Fig. 6.9(c)). We observed that the Fe elements in the $\text{Ni}_{80}\text{Fe}_{20}/\text{Fe}$ structure show a significant decrease in both H_{s1} and H_{s3} from -257 Oe, 960 Oe down to -80 Oe and 630 Oe respectively, as marked by the solid arrows of Fig. 6.9(a). The reduction in the switching fields in the $\text{Ni}_{80}\text{Fe}_{20}/\text{Fe}$ structure is a direct effect of magnetostatic coupling between the Fe dots and $\text{Ni}_{80}\text{Fe}_{20}$ antidot. Similarly, the formation of vortex core in the Fe dots assists the magnetic switching of the $\text{Ni}_{80}\text{Fe}_{20}$ antidot, leading to a reduction of H_{s2} from 280 Oe to 177 Oe. In order to verify that the two FM elements are only coupled magnetostatically, an interpolated loop from Fig. 6.9(a & b) assuming no coupling between the Fe dots and $\text{Ni}_{80}\text{Fe}_{20}$ antidot is shown as left inset in Fig. 6.9(c). The loop resembles that of the $\text{Ni}_{80}\text{Fe}_{20}/\text{Fe}$ structure suggesting that the two FM structures are exchange decoupled. Shown in Fig. 6.9(d-f) are the corresponding LLG simulations for the results shown in Fig. 6.9(a-c). There is a good agreement between the experimental results and micromagnetic simulations. The difference in switching fields may be attributed to limited number of unit cells with periodic boundaries due to computation limitations, making it difficult to account for the actual roughness in shapes across the entire sample.

We have further characterized the static magnetic properties using MFM imaging at zero field after first applying a negative saturation field of -3 kOe. The corresponding MFM images taken at remanence for the Fe dots, $\text{Ni}_{80}\text{Fe}_{20}$ antidot and $\text{Ni}_{80}\text{Fe}_{20}/\text{Fe}$ structures are shown in Fig. 6.10(a-c) respectively. Interestingly, the Fe dots in the $\text{Ni}_{80}\text{Fe}_{20}/\text{Fe}$ structure adopt single vortex core (indicated by the dashed arrows in Fig. 6.10(c) while in the reference Fe dots,

two or more vortex cores are observed at remanence (indicated by the dashed arrows in Fig. 6.10(a)). This may be due to the modified demagnetization field resulting from surrounding $\text{Ni}_{80}\text{Fe}_{20}$ antidot array in the $\text{Ni}_{80}\text{Fe}_{20}/\text{Fe}$ structure. The domain configuration of the $\text{Ni}_{80}\text{Fe}_{20}$ antidot in the $\text{Ni}_{80}\text{Fe}_{20}/\text{Fe}$ structure is similar to that of the reference $\text{Ni}_{80}\text{Fe}_{20}$ antidot (Fig. 6.10(b)). The simulated magnetization states at remanence are shown in Fig. 6.10(d-f) respectively. Again, there is a good agreement between the experimental results and micromagnetic simulations.

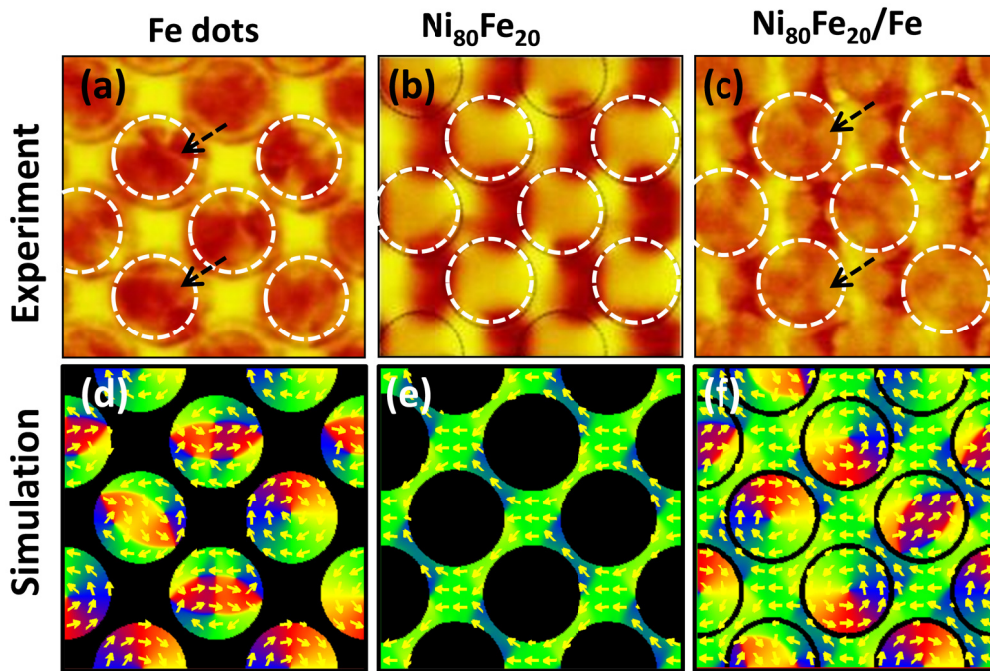


Fig. 6.10 MFM images taken at remanence after negative saturation for the (a) Fe dots; (b) $\text{Ni}_{80}\text{Fe}_{20}$ antidot; and (c) $\text{Ni}_{80}\text{Fe}_{20}/\text{Fe}$ structure. The corresponding simulated magnetization states are shown in (d)-(f) respectively.

We have also investigated the effects of dot diameter d on the switching behaviors of the $\text{Ni}_{80}\text{Fe}_{20}/\text{Fe}$ structures. Shown in Fig. 6.11(a-c) are the measured hysteresis loops for reference $\text{Ni}_{80}\text{Fe}_{20}$ antidot as a function of d for field applied along the X-axis. There is a significant increase of switching field H_{s2} from 145 Oe to 280 Oe as d is increased from 300 nm to 550 nm due to increased demagnetizing effects. The corresponding M-H loops for the $\text{Ni}_{80}\text{Fe}_{20}/\text{Fe}$ structures are shown in Fig. 6.11(d-f). Similar loop shapes are

observed as d is varied, suggesting that similar reversal mechanism is involved in the switching process. We observed an increase of H_{s2} from 135 Oe to 177 Oe for the $\text{Ni}_{80}\text{Fe}_{20}$ antidot element in the $\text{Ni}_{80}\text{Fe}_{20}/\text{Fe}$ structure as d is decreased from 300 nm to 550 nm, in agreement with that observed in reference $\text{Ni}_{80}\text{Fe}_{20}$ antidot. However, for the Fe element, a significant decrease of annihilation field (H_{s3}) from 960 Oe to 630 Oe is seen as d is increased due to reduced demagnetizing effects.

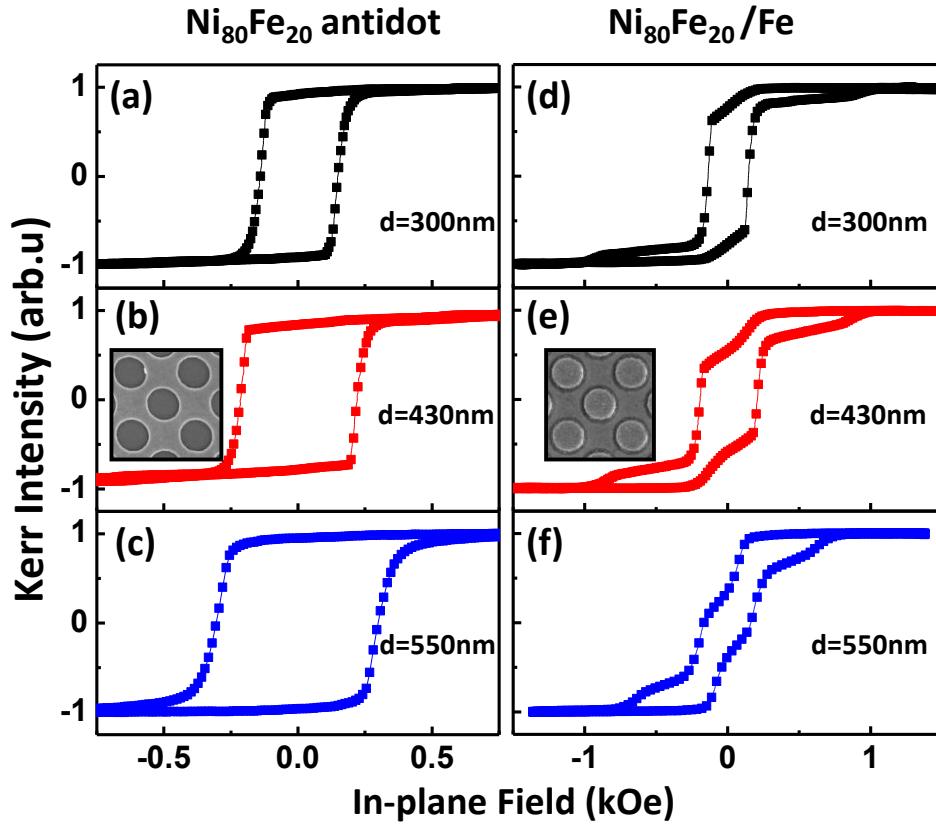


Fig. 6.11 Experimental M - H loops of $\text{Ni}_{80}\text{Fe}_{20}$ antidot with (a) $d=300$ nm; (b) $d=430$ nm; and (c) $d=550$ nm. The corresponding results of the $\text{Ni}_{80}\text{Fe}_{20}/\text{Fe}$ structures are shown in (d)-(f) respectively.

6.3.3 Ferromagnetic Resonance Behavior

The dynamic behaviors of the $\text{Ni}_{80}\text{Fe}_{20}/\text{Fe}$ structures have also been investigated. Shown in Fig. 6.12(a) are the FMR traces of the $\text{Ni}_{80}\text{Fe}_{20}/\text{Fe}$ structure with $d=550$ nm as a function of H_{app} for $\theta = 0^\circ$. We observed that the

number of modes and profiles are markedly different for various magnetic ground states set by the applied field amplitude. At $H_{app} = -1000$ Oe the $\text{Ni}_{80}\text{Fe}_{20}/\text{Fe}$ structure should be saturated based on the M-H loop shown in Fig. 6.9(c). The observed two main resonance peaks at 11.4 GHz and 13.5 GHz correspond to modes originating from the $\text{Ni}_{80}\text{Fe}_{20}$ antidot and Fe dots regions respectively. For the saturated state, it is easy to infer that the resonance peak A with highest frequency is localized in the Fe dots, while the resonance originating from $\text{Ni}_{80}\text{Fe}_{20}$ antidot structure gives rise to the lower frequency peak B due to the lower saturated magnetization ($4\pi M_s$) of $\text{Ni}_{80}\text{Fe}_{20}$ (800 Oe) compared to that of Fe (1714 Oe) based on the Kittel's equation^[114] for saturated film. In addition, a weak resonance mode C is also observed at around 10.4 GHz (as indicated by the dashed arrow). The lower absorption and resonance frequency of this peak suggests that the resonance may come from the edges of the Fe dots and $\text{Ni}_{80}\text{Fe}_{20}$ antidot due to the strong demagnetizing effect^[169].

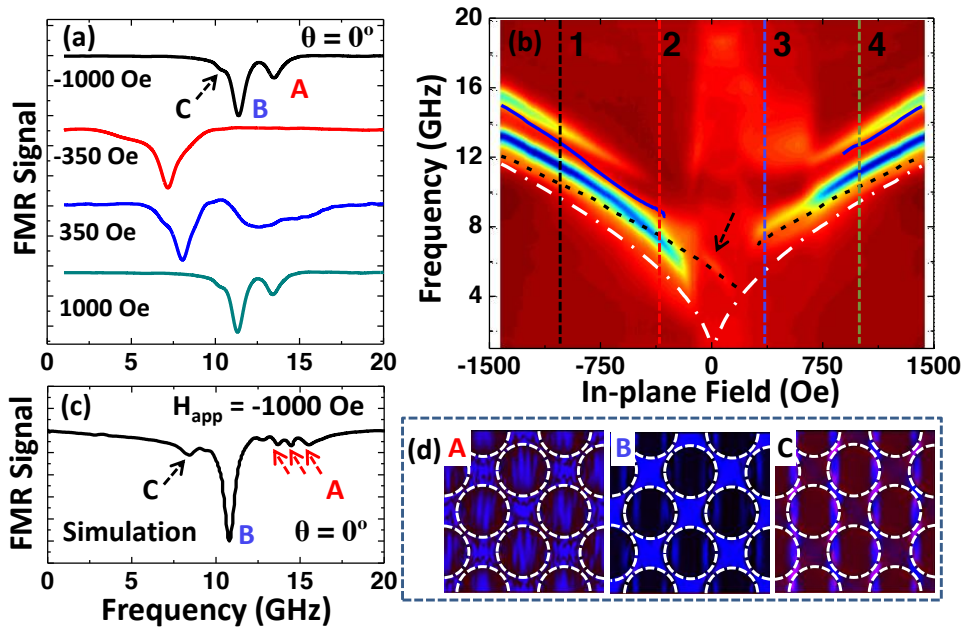


Fig. 6.12 (a) FMR traces of the $\text{Ni}_{80}\text{Fe}_{20}/\text{Fe}$ structure with varying H_{app} for $\theta = 0^\circ$; (b) Experimental 2-D absorption spectra. Results for reference Fe dots (solid line), $\text{Ni}_{80}\text{Fe}_{20}$ antidot (dashed line) and $\text{Ni}_{80}\text{Fe}_{20}$ film (dot-dash line) are also shown. (c) Simulated FMR spectra for $H_{app} = -1000$ Oe. (d) The spatial distributions of spin precession amplitudes for respective modes.

Only one main peak with wider linewidth (compared with the peak B) can be observed when H_{app} is increased to -350 Oe. This observation could be attributed to the fact that the resonance happens in the dot and antidot simultaneously due to the strong magnetostatic coupling between the two FM structures. The higher frequency mode comes out again when the $H_{app} = 350$ Oe because of the formation of vortex ground state in the Fe dots as observed in the static results in Fig. 6.9(c). Interestingly, the FMR resonance frequency for the lower mode is higher than the main mode for $H_{app} = -350$ Oe. When H_{app} is further increased to 1000 Oe, the magnetization of the $\text{Ni}_{80}\text{Fe}_{20}$ / Fe structure is saturated along positive X-direction and the FMR curve is identical to the one for $H_{app} = -1000$ Oe.

Detailed FMR measurements were performed along the field hysteresis loops as shown in the absorption spectra in Fig. 6.12(b). Mode profiles transformation can be clearly observed. We found that the intensity of mode A decreases when the H_{app} is increased and disappears at around $H_{app} = -400$ Oe even though the magnetization of the Fe dots in the $\text{Ni}_{80}\text{Fe}_{20}$ /Fe structure has not changed significantly based on the M-H loop in Fig. 6.9(c). The tilted magnetic configurations near the edge of the Fe dots may be responsible for this observation if we assume that the in-plane demagnetizing field does not change significantly when the magnetization at the edge of dot is slightly tilted. This assumption is reasonable because the accumulated magnetic poles at the boundary of the Fe dot and $\text{Ni}_{80}\text{Fe}_{20}$ antidot are partially canceled due to the very small gap between them. From this argument, it is plausible that resonance frequency of Fe near the edge of the dot decreases because of the decrease of internal field along the magnetization direction when the spin direction is tilted. Another possible reason may be due to the enhanced spin precession amplitude in $\text{Ni}_{80}\text{Fe}_{20}$ at lower H_{app} . The precessions of Fe dots and $\text{Ni}_{80}\text{Fe}_{20}$ antidot near the boundary will be similar because of the stronger dynamic interaction between the two FM structures^[128]. This implies that, the

resonance frequency of the spins in the Fe dots (near the edge) has been dragged to lower frequency by the adjacent Ni₈₀Fe₂₀ antidot. The larger linewidth of the lower frequency peak for $H_{app} = -350$ Oe also suggests the coupling between the two FM structures as shown in Fig. 6.12(a) due to the smaller damping factor (α) of Fe.

We have plotted on the same figure for direct comparison, the measured experimental FMR resonance frequencies of the reference Fe dots and Ni₈₀Fe₂₀ antidot array in solid and dash line, respectively. At saturation state, frequencies of both the Fe and Ni₈₀Fe₂₀ peaks in the Ni₈₀Fe₂₀/Fe structure are higher than the reference Fe dots and Ni₈₀Fe₂₀ antidot array, respectively. For the Fe dots in the Ni₈₀Fe₂₀/Fe structure, the neutralization of the magnetic poles at the boundary reduces the demagnetizing field along the X-axis and increases the internal field, which in turn pushes the resonance peak to a higher frequency. The internal field in Ni₈₀Fe₂₀ is also increased because the direction of total demagnetizing field in the Ni₈₀Fe₂₀ antidot array is reversed by the embedded Fe dots^[60]. Interestingly, the resonance frequency of Ni₈₀Fe₂₀ in the Ni₈₀Fe₂₀/Fe structure gradually decreases and becomes lower than that of reference Ni₈₀Fe₂₀ antidot array when H_{app} is in a range of -400 Oe to -150 Oe. This may also be attributed to the significant modification of internal field in the Ni₈₀Fe₂₀/Fe structure. The X-component of the internal field in the whole Ni₈₀Fe₂₀/Fe structures will be similar to that of a continuous film, which is shown as dash-dot line in Fig. 6.12(b). When H_{app} is further decreased, the stray field of Fe dots is significantly reduced in the X-Y plane due to the formation of the vortex core. A faint Ni₈₀Fe₂₀ mode (indicated by the dashed arrow) can be observed at remanence with a similar resonance frequency compare to that of reference Ni₈₀Fe₂₀ antidot. When a reverse field is applied, the vortex cores shift to one side and the switched region of the Fe dot may be attributed to the origin of the weak high frequency mode for $H_{app} = 350$ Oe. The resonance frequency of the Ni₈₀Fe₂₀ antidot array in the

Ni₈₀Fe₂₀/Fe structure is higher than that of reference Ni₈₀Fe₂₀ antidot array due to the stray field of the switched Fe dots. All of the above analyses are consistent with the M-H loop shown in Fig. 6.9(c).

To further understand the origin of the resonance modes, we performed quantitative analysis of the dynamic responses on the Ni₈₀Fe₂₀/Fe structure as shown in Fig. 6.12(c) for $H_{app} = -1000$ Oe. There is a good agreement between the experimental results and the simulations for the main peaks in the resonance curve. The resonance mode A in Fig. 6.12(a) however, splits to a group of small peaks at around 14 GHz in the simulated FMR curve. The difference between the experimental results and dynamic micromagnetic simulations is reasonable because only a limited number of unit cells with periodic boundaries have been considered in the simulation. The assumption that the roughness is uniform across the entire sample may influence the simulation results. A weak mode C is also observed at lower frequency. Shown in Fig. 6.12(d) are simulated mode profiles, corresponding to the frequencies for the three (groups of) peaks observed in the simulated FMR curve. Clearly, the large spin precession amplitude in the Fe dots is the source of resonance mode A, while mode B originates from the resonance of Ni₈₀Fe₂₀ antidot area. Due to dynamic interactions, partial Ni₈₀Fe₂₀ or Fe area is also coupled with the other component for these frequencies. The resonance mode C originates mainly from the edge of the Fe dots. Similar to resonance mode A and B, the small Ni₈₀Fe₂₀ area between two nearest Fe dots is also involved.

In order to investigate the effects of magnetic anisotropy on the dynamic behavior of the matrix structure, we have performed FMR measurements as a function of H_{app} orientation θ when the structure is in a saturation state ($H_{app} = -1000$ Oe) as shown in Fig. 6.13(a). We found that the lowest edge mode disappears when $\theta \neq 0^\circ$. This may due to the fact that the edge mode merges with the Ni₈₀Fe₂₀ antidot mode when the field configuration is changed. We found that the two main modes shift to lower frequency and the intensity of

the mode originating from the $\text{Ni}_{80}\text{Fe}_{20}$ antidot is markedly sensitive to θ .

Shown in Fig. 6.13(b) are the FMR absorption spectra as a function of θ in the range from -45° to 45° . We observed clear mode transformation which agrees with the results shown in Fig. 6.13(a). To understand the transformation of resonance area of the modes, we performed dynamic simulation for $\theta = -45^\circ$ with $H_{app} = -1000$ Oe as shown in Fig. 6.13(c). The corresponding simulated mode profiles are shown in Fig. 6.13(d). Again, there is a good agreement between the experimental and simulated results for the two main peaks and amplitudes. The lower frequency mode still comes from the $\text{Ni}_{80}\text{Fe}_{20}$ antidot but the resonance area decreased compared with the second panel of Fig. 6.12(d) leading to a decrease in absorption for the $\text{Ni}_{80}\text{Fe}_{20}$ mode.

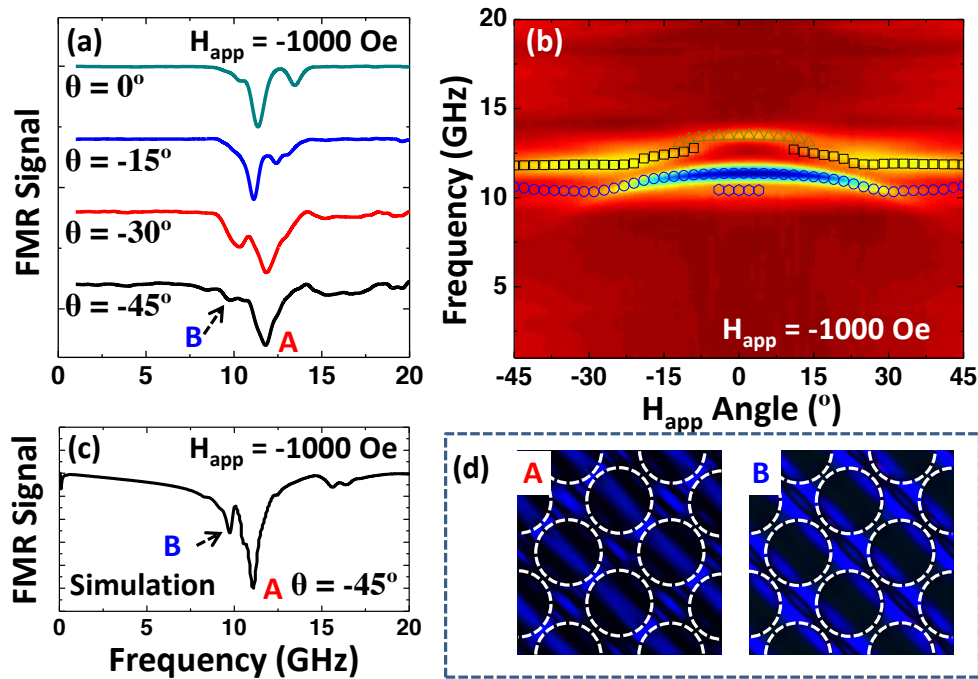


Fig. 6.13(a) FMR traces of the $\text{Ni}_{80}\text{Fe}_{20}/\text{Fe}$ structure with varying θ for $H_{app} = -1000$ Oe. (b) Experimental 2-D angular dependence absorption spectra. (c) Simulated FMR spectra for $\theta = -45^\circ$. (d) The spatial distributions of spin precession amplitudes for respective modes.

6.3.4 Magnetoresistance Behaviors

6.3.4.1 Angular Dependence

We have also investigated the MR behaviors of the $\text{Ni}_{80}\text{Fe}_{20}/\text{Fe}$ structure. In a ferromagnetic material, the AMR effect is determined by the angle between the current density and direction of magnetization given by:

$$R(H) = R_{\perp} + (R_{\parallel} - R_{\perp}) \cos^2 \theta \quad (6.1)$$

where θ is the angle between current density and magnetization. Since the AMR output depends on two physical terms, namely current density and magnetization, it is important to first establish the current density distribution in order to understand the MR behaviors.

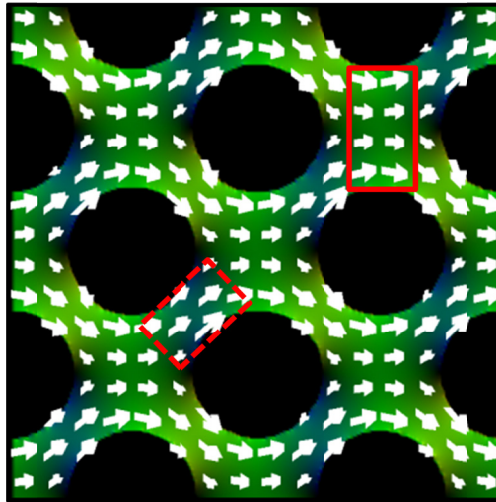


Fig. 6.14 3-D current density distribution of the $\text{Ni}_{80}\text{Fe}_{20}$ antidot obtained from LLG simulation at $H_{app} = -10$ kOe.

Shown in Fig. 6.14 is the 3-D current density distribution obtained from LLG simulation for the $\text{Ni}_{80}\text{Fe}_{20}$ antidot with $d=430$ nm. The arrows signify the direction of current flow at each location while the length of the arrows indicates the magnitude of current density. The current tends to follow the circumference of holes in the antidot (in the solid rectangular region, the current mainly points along $\theta = 0^\circ$, while in the dashed region, it is forced

along the $\theta = 45^\circ$ direction relative to X-axis). The current density of the dashed region is slightly larger than the solid region based on the current continuity law. We have also analyzed the current density distribution in the $\text{Ni}_{80}\text{Fe}_{20}/\text{Fe}$ structure and observed similar results because no current is flowing through the Fe dots due to the small gap seen in the SEM inset of Fig. 6.11(e).

Shown in Fig. 6.15(a) is the measured longitudinal MR (LMR, field applied along $\theta = 0^\circ$) response for a 25 nm thick $\text{Ni}_{80}\text{Fe}_{20}$ antidot with applied field swept ascendingly from negative saturation to positive saturation. A full loop LMR curve is shown as an inset in Fig. 6.15(a). As expected the two loops are symmetric and therefore we will focus only on the ascending half loop in our discussion below. As H_{app} is swept from negative to positive saturation, we observed a clear resistance maximum at around zero field followed by a sharp MR dip corresponding to the magnetic switching of the $\text{Ni}_{80}\text{Fe}_{20}$ antidot. The field value for the dip is in agreement with the switching field in the experimental M-H loop (Fig. 6.11(b)).

We have performed numerical calculation based on the simulated 3-D current density distribution and magnetization states which we obtained from the LLG simulator. The AMR was calculated using the method described by Wang et al.^[165], by averaging the resistivity of all the cells at a given field value. The average resistivity was given by:

$$\rho_{AMR}(H) = \frac{\sum_i [(m_i \cdot j_i)^2]}{n} \quad (6.2)$$

where m_i , j_i , and n represent the moment of cell i , the current density of cell i and the total number of cells respectively. The calculated magnetoresistance was then normalized to zero field resistivity and plotted as a function of the applied field.

Shown in Figs. 6.15(b) and (c) are the simulated LMR curve and representative magnetization states for different applied fields. There is a good

qualitative agreement between the simulated and experimental MR curves. Clearly, the monotonic increase of resistance with reduced negative field arises mainly from magnetization relaxation towards the current density direction (states a_1 to a_3), leading to a MR maximum around the zero field, while the subsequent dip in the MR (state a_4) is related to magnetic switching of the $\text{Ni}_{80}\text{Fe}_{20}$ antidot. Further increase in H_{app} along the positive direction results in alignment of magnetic moment of the $\text{Ni}_{80}\text{Fe}_{20}$ antidot along the field direction. This results in a deviation of the magnetization orientation with respect to the current density and hence a reduction in MR (states a_5 to a_6).

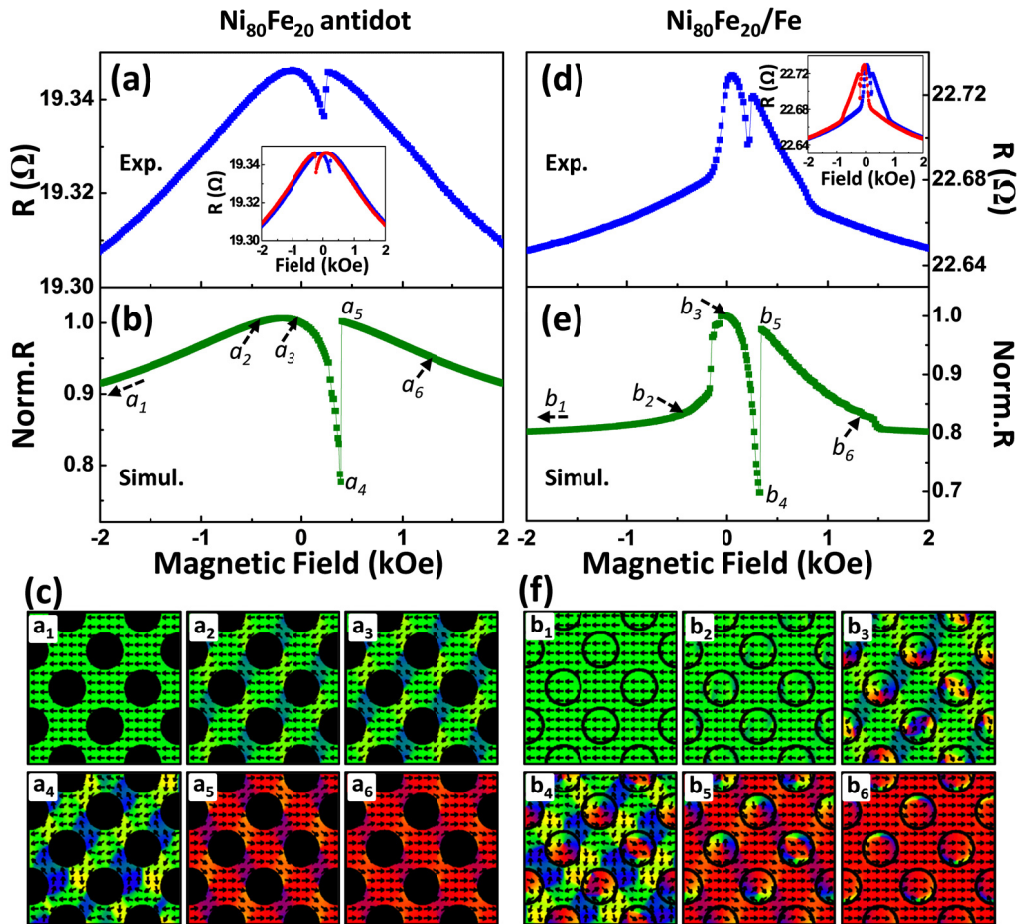


Fig. 6.15 (a) Experimental; (b) simulated longitudinal MR curves; and (c) simulated magnetization states at various applied fields for the $\text{Ni}_{80}\text{Fe}_{20}$ antidot with $d=430$ nm. The corresponding results for the $\text{Ni}_{80}\text{Fe}_{20}/\text{Fe}$ structure are shown in (d)-(f) respectively.

Shown in Fig. 6.15(d) is the measured LMR response of the $\text{Ni}_{80}\text{Fe}_{20}/\text{Fe}$ structure for $d = 430$ nm (the full MR loop is shown as an inset). Interestingly, the MR response is markedly different when compared with Fig. 6.15(a). The absolute value of the resistance of the two structures are of the same order as expected due to the fact that the Fe dots are not exchange coupled with the $\text{Ni}_{80}\text{Fe}_{20}$ antidot and therefore the measured resistance value is from the $\text{Ni}_{80}\text{Fe}_{20}$ antidot in the matrix; however, the significant difference in the detailed features in the MR curves can be attributed to the stray field from the Fe dots modifying the magnetic ground states of the $\text{Ni}_{80}\text{Fe}_{20}$ antidot regions due to the strong magnetostatic coupling.

We have also simulated the LMR curve of the $\text{Ni}_{80}\text{Fe}_{20}/\text{Fe}$ structure, as shown in Fig. 6.15(e). Again, there is good qualitative agreement between the experimental and simulated results. The corresponding magnetic ground states are shown in Fig. 6.15(f) as a direct comparison with the ground states of $\text{Ni}_{80}\text{Fe}_{20}$ antidot without the Fe dots in Fig 6.15(c). It can be clearly seen that the presence of Fe dots in close proximity with the $\text{Ni}_{80}\text{Fe}_{20}$ antidot significantly alters the magnetic ground states hence the MR response. In the $\text{Ni}_{80}\text{Fe}_{20}$ antidot without the Fe dots, the magnetic state at position a_2 shows that the spins are aligned along the circumference of holes in the antidot due to strong demagnetizing effects. The magnetic state at position b_2 corresponding to the $\text{Ni}_{80}\text{Fe}_{20}/\text{Fe}$ structure is closer to the geometry of a continuous film (b_2) which stays in quasi-saturation state above the nucleation field of the Fe dots. This consequently results in a much smaller magnetization change and hence the smaller MR slope (b_1 to b_2 in Fig. 6.15(e)) as H_{app} is reduced from negative saturation when compared with the $\text{Ni}_{80}\text{Fe}_{20}$ antidot (a_1 to a_2 in Fig. 6.15(b)).

While the $\text{Ni}_{80}\text{Fe}_{20}/\text{Fe}$ structure has a magnetic configuration very close to one of a continuous film in b_2 , formation of the vortex core in the Fe dots destroys the uniform magnetic configuration due to the vanishing stray field

and the magnetic state (b_3) resembles that of $\text{Ni}_{80}\text{Fe}_{20}$ antidot (a_3). At $H_{app}=0$, the relative contribution of the Fe dots to the overall MR response of $\text{Ni}_{80}\text{Fe}_{20}$ antidot is significantly reduced, leading to a sharp increase in the MR. When the applied field is further increased, the $\text{Ni}_{80}\text{Fe}_{20}$ antidot switches irreversibly, resulting in a sharp dip in the MR curve corresponding to state b_4 in agreement with the switching behavior in Fig. 6.15(b). Subsequently, the propagation of the vortex core in the Fe dots results in a monotonic decrease in the MR curve corresponding to the transition from states b_5 to b_6 in Fig. 6.15(e) due to the strong magnetostatic coupling. As H_{app} is increased further, the vortex core is annihilated.

We then investigate the effect of applied field orientation (θ) on the transport properties of the structures. Shown in Figs. 6.16(a-d) are the representative MR curves for $\text{Ni}_{80}\text{Fe}_{20}$ antidot with $d = 430$ nm as a function of θ . For $\theta \leq 30^\circ$ as shown in Figs. 6.16(a-b), the shapes and features of the MR curves resemble that of $\theta = 0^\circ$ shown in Fig. 6.15(a), suggesting that the same magnetization reversal mechanism is responsible for the MR behavior. However, for $\theta = 45^\circ$, the shape of the MR curve is markedly different due to the lattice arrangement of the $\text{Ni}_{80}\text{Fe}_{20}$ antidot as can be seen from the SEM image (the right inset). The corresponding M-H loop is shown as left inset. The M-H loop displays a two-step switching related to the magnetization reversal of regions α (marked on the SEM inset) at lower field and region β at higher field respectively due to differences in the demagnetizing fields. Shown in Fig. 6.16(d) is the MR curve for $\theta = 90^\circ$. This loop can easily be explained using similar argument for explaining Fig. 6.15(a) due to the AMR effect.

Shown in Figs. 6.16(e-h) are the corresponding MR curves for the $\text{Ni}_{80}\text{Fe}_{20}/\text{Fe}$ structure. Again, for $\theta \leq 30^\circ$ as shown in Figs. 6.16(e-f), the shapes and features of the MR curves resemble that of $\theta = 0^\circ$ shown in Fig. 6.15(d), suggesting that the same mechanism is responsible for the MR behavior. For $\theta = 45^\circ$ (Fig. 6.16(g)), the dip in the MR curve corresponding

to the switching of the $\text{Ni}_{80}\text{Fe}_{20}$ antidot disappears, suggesting a continuous rotation of magnetization of the $\text{Ni}_{80}\text{Fe}_{20}$ antidot and the Fe dots due to the strong magnetostatic coupling. The MR curve for $\theta = 90^\circ$ shown in Fig. 6.16(h) can be readily explained based on the AMR effects as discussed in Fig. 6.15(d).

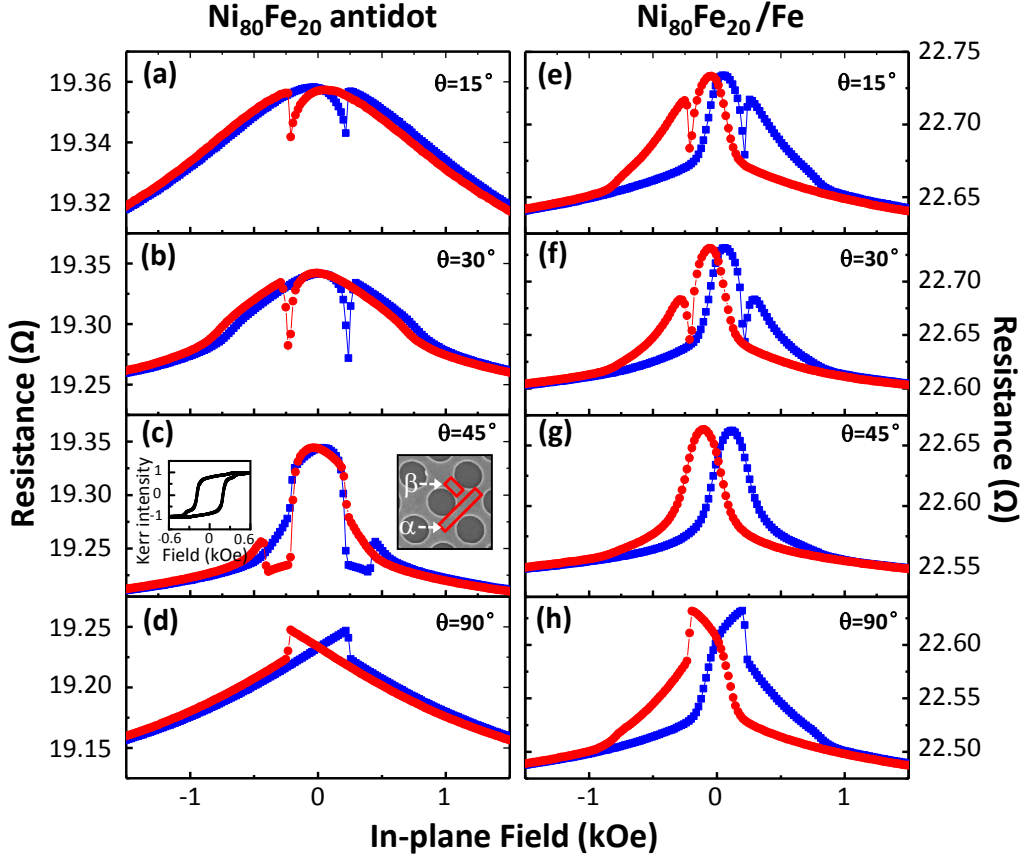


Fig. 6.16 MR responses as a function of θ for (a-d) $\text{Ni}_{80}\text{Fe}_{20}$ antidot; and (e-h) $\text{Ni}_{80}\text{Fe}_{20}/\text{Fe}$ structure with $d=430$ nm. The measured M-H loop of $\text{Ni}_{80}\text{Fe}_{20}$ antidot at $\theta=45^\circ$ is shown as an inset in (c).

6.3.4.2 Temperature Dependence

We have also investigated the effects of temperature on the MR behaviors. Shown in Figs. 6.17(a) and 6.17(b) are the representative LMR curves on the $\text{Ni}_{80}\text{Fe}_{20}$ antidot and the $\text{Ni}_{80}\text{Fe}_{20}/\text{Fe}$ structure taken at $T = 150$ K and $T = 4.2$ K respectively. We have defined H_{sw} corresponding to the switching field at which the $\text{Ni}_{80}\text{Fe}_{20}$ antidot reverses irreversibly in Fig.

6.17(a) to characterize the temperature dependence. As expected, the H_{sw} is increased at low T for both structures, as indicated by the dashed arrows. Fig. 6.17(c) summarizes the temperature dependence of the H_{sw} for both structures. We clearly see that for all T values the $\text{Ni}_{80}\text{Fe}_{20}$ antidot matrix in the $\text{Ni}_{80}\text{Fe}_{20}/\text{Fe}$ structure switches at lower values of H_{sw} with respect to the $\text{Ni}_{80}\text{Fe}_{20}$ antidot array without the Fe dots. This observation can be explained by the fact that the stray field from the Fe dots lowers the switching field of the $\text{Ni}_{80}\text{Fe}_{20}$ antidot regions in the $\text{Ni}_{80}\text{Fe}_{20}/\text{Fe}$ structure due to the strong magnetostatic coupling.

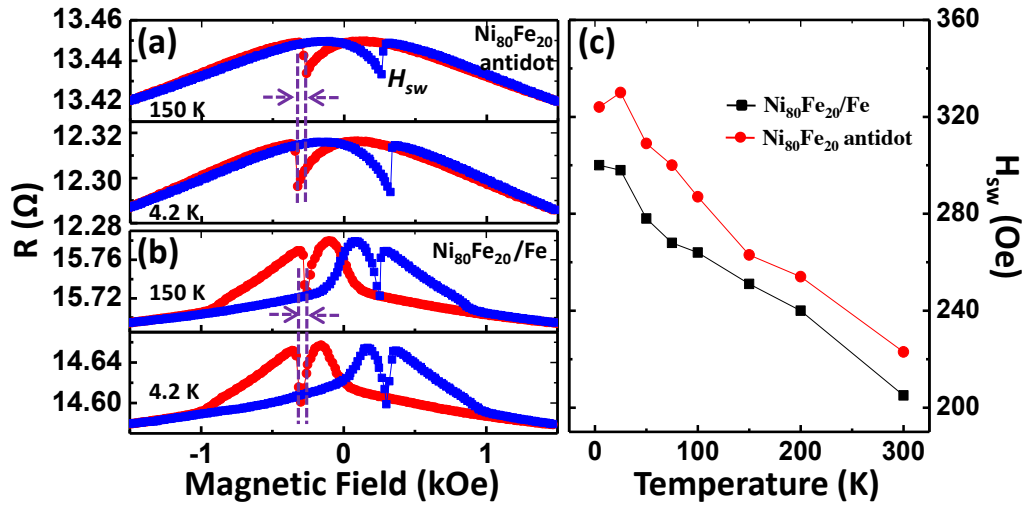


Fig. 6.17 LMR responses as a function of temperature T for (a) $\text{Ni}_{80}\text{Fe}_{20}$ antidot and (b) the $\text{Ni}_{80}\text{Fe}_{20}/\text{Fe}$ structure with $d=430$ nm. The extracted H_{sw} (defined in (a)) as a function of T for the two structures are shown in (c).

6.3.4.3 Effects of Antidot Diameter

The effects of antidot diameter d on the MR behaviors of the $\text{Ni}_{80}\text{Fe}_{20}/\text{Fe}$ structure have also been studied. Shown in Fig. 6.18(a) are the measured LMR curves of the $\text{Ni}_{80}\text{Fe}_{20}/\text{Fe}$ structure as a function of d . The shapes of the MR curves and detailed features are similar, suggesting that similar magnetization reversal mechanism is involved in the switching process. Here, we have identified two contributions to the MR response i.e. from vortex core

formation of Fe dots and magnetic switching of $\text{Ni}_{80}\text{Fe}_{20}$ antidot (marked in Fig. 6.18(a) as P_1 and P_2 respectively). For $d = 300$ nm, the resistance at point P_1 is lower than that for P_2 . However, as d is increased to 430 nm and 550 nm, the situation is reversed (the resistance for P_1 is higher than that for P_2), suggesting that the larger Fe dots play a more important role in determining the MR behaviors of the $\text{Ni}_{80}\text{Fe}_{20}/\text{Fe}$ structure. This diameter dependent MR behavior is well reproduced in the simulated MR curves, as shown in Fig. 6.18(b).

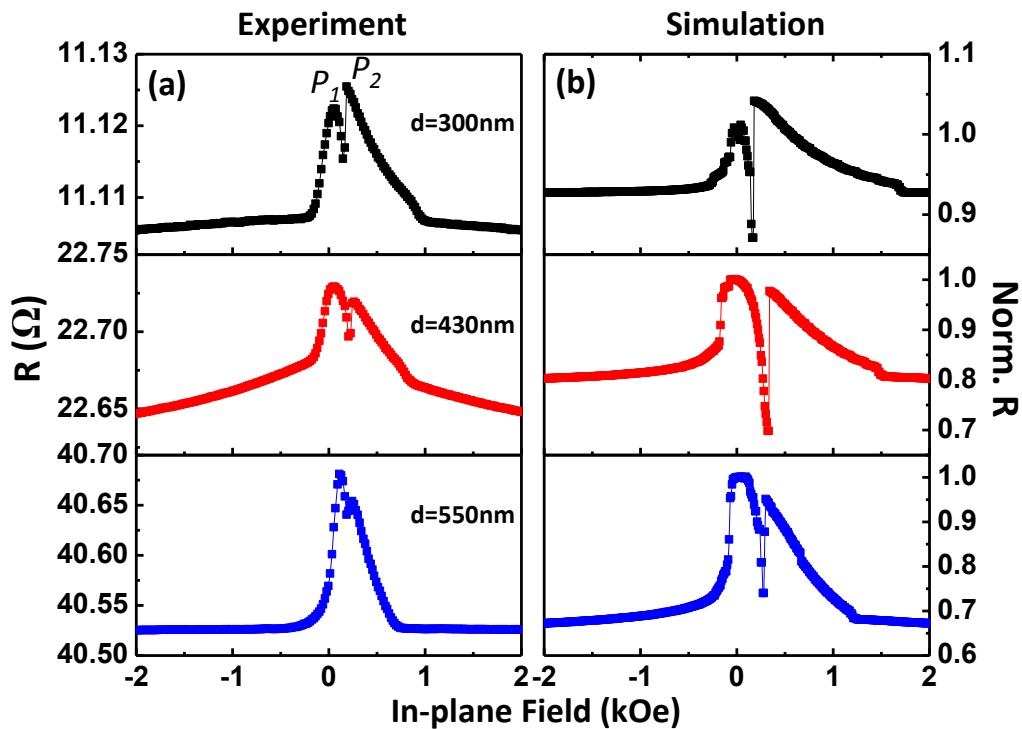


Fig. 6.18 (a) Experimental; and (b) Simulated LMR curves for the $\text{Ni}_{80}\text{Fe}_{20}/\text{Fe}$ structure as a function of the antidot diameter d .

6.4 Summary

In this chapter, a systematic investigation of magnetization reversal mechanism and dynamic behaviors of bi-component 2-D MCs including modulated $\text{Ni}_{80}\text{Fe}_{20}$ film and Fe filled $\text{Ni}_{80}\text{Fe}_{20}$ antidot structures is presented. The modulated $\text{Ni}_{80}\text{Fe}_{20}$ film consists of continuous $\text{Ni}_{80}\text{Fe}_{20}$ film on top of periodic 2-D arrays of perpendicularly magnetized Co/Pd dots (or in-plane

magnetized $\text{Ni}_{80}\text{Fe}_{20}$ dots). It was observed that the presence of bottom dot arrays significantly modifies the static and dynamic behaviors of the top $\text{Ni}_{80}\text{Fe}_{20}$ film when compared with the reference $\text{Ni}_{80}\text{Fe}_{20}$ film without the dot array underneath. Created by bottom dots, the periodic perturbations of internal fields in the neighbor regions of the continuous $\text{Ni}_{80}\text{Fe}_{20}$ film can be additionally controlled by magnetic field. The hysteresis loops and FMR mode profiles of the modulated film structures depend significantly on the film thickness.

In the Fe filled $\text{Ni}_{80}\text{Fe}_{20}$ antidot structures, the “holes” of the $\text{Ni}_{80}\text{Fe}_{20}$ antidot are filled with another ferromagnetic material Fe. It was shown that the stray field of the Fe dots significantly modifies the magnetization reversal, the FMR responses and the MR behaviors of the host $\text{Ni}_{80}\text{Fe}_{20}$ antidot, despite the fact that the Fe dots are not in direct contact with the $\text{Ni}_{80}\text{Fe}_{20}$ antidot. The effects of applied field orientation, temperature and antidot diameter on the magnetic behaviors of the Fe filled $\text{Ni}_{80}\text{Fe}_{20}$ antidot structures are also investigated.

Chapter 7

Conclusion and Outlook

7.1 Overview

This thesis provides a detailed insight into the magnetization reversal process, magneto-transport properties and dynamic behaviors of Co/Pd multilayer based nanostructures and 2-D MCs. The key achievements of this work are:

- (a) Successful fabrication of perpendicularly magnetized Co/Pd multilayer based nanostructures (including nanodots, antidot, nanorings and nanowires) over a large area using deep ultraviolet lithography at 248 nm exposure wavelength.
- (b) Systematic investigation of magnetization reversal and MR behaviors of the Co/Pd multilayer based nanostructures as a function of their geometrical parameters.
- (c) A comprehensive study of the effects of interlayer coupling on the magnetization reversal and MR behaviors of $[\text{Co/Pd}]_4/\text{Au}/[\text{Co/Pd}]_2$ NWs.
- (d) Development of novel processes for fabricating high quality bi-component 2-D MCs and characterization of their static and dynamic behaviors.

7.2 Summary of Results

To obtain the above mentioned results, various high quality nanostructures were fabricated and different characterization techniques were used to probe the static and dynamic behaviors, while micromagnetic simulations were performed to better understand the experimental observations. This section summarizes the main results presented in this thesis.

In the first part of the thesis, magnetization reversal of circular Co/Pd nanomagnets including nanodots, antidot and nanorings were investigated. The switching field of the Co/Pd dots on top of the pillars is significantly dependent on both the bi-layer repeat n and the pillar diameter d , while the Co/Pd antidot in the trench area shows no clear dependence on the two parameters. As the Co/Pd dots are densely arranged in a cluster, magnetostatic interactions largely affect their switching behaviors. In addition, by applying a suitable clock-field cycle, the Co/Pd two-dot cluster can perform logical ‘NOT’ operation. Subsequently, the effects of interlayer and inter-ring dipolar coupling on the magnetization reversal process were studied using $[\text{Co/Pd}]_4/\text{Au}(t_{\text{Au}})/[\text{Co/Pd}]_2$ pseudo-spin-valve (PSV) nanorings by modifying t_{Au} and the ring edge-to-edge spacing s respectively.

The second part of the thesis focuses on the magnetization reversal and MR behaviors of $[\text{Co/Pd}]_n$ NWs as a function of bi-layer the repeat n and temperature T . A linear non-saturating MR response was observed in the multilayer NWs up to a maximum field as large as 40 kOe. This is attributed to magnon magnetoresistance (MMR) effect resulting from spin wave damping at high field. The MMR effect was found to be strongly dependent on both n and T . The switching field of the $[\text{Co/Pd}]_n$ NWs shows a greater temperature dependence with smaller n . Furthermore, by adding a Cu buffer layer below the Co/Pd NWs, the switching field can be greatly enhanced due to the combination of increased mean grain size and film roughness.

Thereafter, the effects of interlayer coupling of $[\text{Co/Pd}]_4/\text{Au}(t_{\text{Au}})/[\text{Co/Pd}]_2$ PSV NWs were further investigated as a function of t_{Au} and T . We observed that for continuous film deposited under the same condition, the interlayer coupling is almost independent of both t_{Au} and T . However, the interlayer coupling of the PSV NWs is much larger and markedly sensitive to the two parameters due to stray field interactions. At low T , the competition between the interlayer coupling and switching field difference among the soft and hard

Co/Pd stacks determines the overall magnetization reversal process and MR behavior of the PSV NWs. Interlayer coupling can also be manipulated effectively by adding a Co or Pd insertion layer which changes the effective spacer layer thickness of the PSV NWs. At 3 nm Pd insertion layer thickness, a transition between GMR and MMR (and possibly AMR, DWR) domination in the overall MR effects was observed in the PSVs due to temperature induced switching field crossover between the soft and hard Co/Pd stacks. It was further shown that either ferromagnetic or antiferromagnetic type of coupling can be achieved in the $[\text{Co/Pd}]_4/\text{Co/Ru}(t_{Ru})/[\text{Co/Pd}]_2$ PSVs with a Ru spacer layer. The above investigation on MR behavior and tunable interlayer coupling in Co/Pd NWs might find its application in future MRAM design.

The last part of the thesis investigates the static and dynamic behaviors of dot modulated $\text{Ni}_{80}\text{Fe}_{20}$ film and Fe filled $\text{Ni}_{80}\text{Fe}_{20}$ antidot structures. In the dot modulated $\text{Ni}_{80}\text{Fe}_{20}$ film, the presence of Co/Pd dot arrays (or $\text{Ni}_{80}\text{Fe}_{20}$ dots with in-plane anisotropy) underneath the $\text{Ni}_{80}\text{Fe}_{20}$ continuous film create periodic perturbation of internal fields in the $\text{Ni}_{80}\text{Fe}_{20}$ film, which significantly modifies the magnetization reversal process and FMR mode profiles of the $\text{Ni}_{80}\text{Fe}_{20}$ film when compared with the reference $\text{Ni}_{80}\text{Fe}_{20}$ film without the dot array underneath. The Fe filled $\text{Ni}_{80}\text{Fe}_{20}$ antidot nanostructures were fabricated using a self-aligned deposition technique followed by a double-stage lift-off process. Although the Fe dots are not in direct contact with the $\text{Ni}_{80}\text{Fe}_{20}$ antidot, their stray fields significantly modify the magnetic ground states which subsequently affect the magnetization reversal, the FMR responses and the MR behaviors of the host $\text{Ni}_{80}\text{Fe}_{20}$ antidot. The application of these works is two-fold. Firstly, the self-aligned deposition technique simplifies the fabrication process of bi-component MCs as compared with the conventional multi-level lithography process^[59, 61]. Secondly, the experimental study on bi-component MCs might benefit those who work in MCs and magnonic devices.

7.3 Future Work

In this thesis, various promising findings related to Co/Pd multilayer based nanostructures have been reported. There are still several promising avenues which can be further explored. One such area is the investigation of dynamic properties of the perpendicularly magnetized Co/Pd nanostructures using a polar FMR spectroscopy i.e. by applying an external field perpendicular to the plane of the sample.

Another interesting area of research is to fabricate a modulated Co/Pd film by depositing Co/Pd dots on top of a continuous Co/Pd film. This modulated Co/Pd film represents a new type of magnonic crystal with perpendicular magnetic anisotropy. Similar to the modulated $\text{Ni}_{80}\text{Fe}_{20}$ film presented in this thesis, the top Co/Pd dots will create periodic perturbations of internal fields in the neighboring regions of the continuous Co/Pd film. This perturbation may cause a drastic modification in the static and dynamic properties of the bottom continuous Co/Pd film. The perturbation strength can be additionally controlled by adding a Pd spacer layer in between the Co/Pd continuous film and dots.

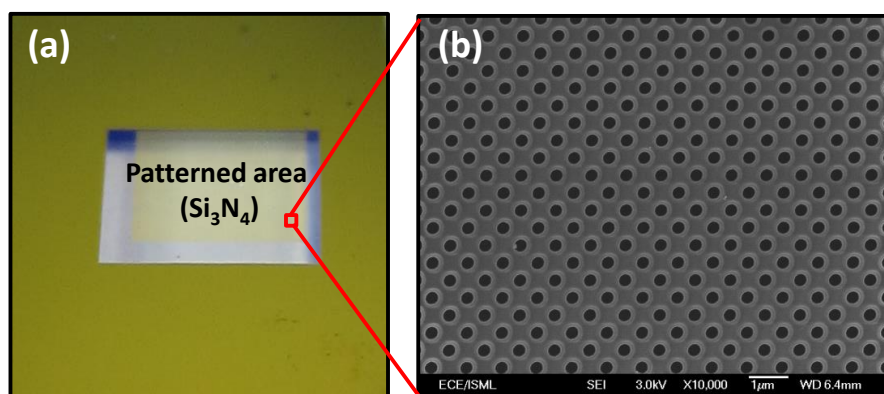


Fig. 7.1 (a) Optical photo; and (b) SEM micrograph of a Si_3N_4 membrane mask.

The modulated Co/Pd film can be fabricated using Si_3N_4 membrane masks. The membrane is a Si chip with patterned nanostructures in the central

Si_3N_4 area. Shown in Fig. 7.1(a) and (b) are an optical photo of the membrane and an enlarged SEM micrograph of the patterned area respectively. The masks allow the large area ($4 \text{ mm} \times 4 \text{ mm}$) fabrication of uniform nanostructures.

Shown in Fig. 7.2 is a typical fabrication process flow for fabricating the modulated Co/Pd film structure. After the Si substrate cleaning, a continuous $[\text{Co}/\text{Pd}]_2$ film is firstly deposited on the sample using DC magnetron sputtering. The sample is then covered by a Si_3N_4 membrane mask containing a patterned dots array. The following deposition of $[\text{Co}/\text{Pd}]_4$ film results in a periodic array of $[\text{Co}/\text{Pd}]_4$ dots on top of $[\text{Co}/\text{Pd}]_2$ continuous film. The schematics of the final nanostructure and its corresponding atomic force micrograph are shown in Fig. 7.2(d). This method is promising because it simplifies the fabrication process of high quality Co/Pd based MCs. And since no photoresist is used, the interface of the Co/Pd multilayer is clean.

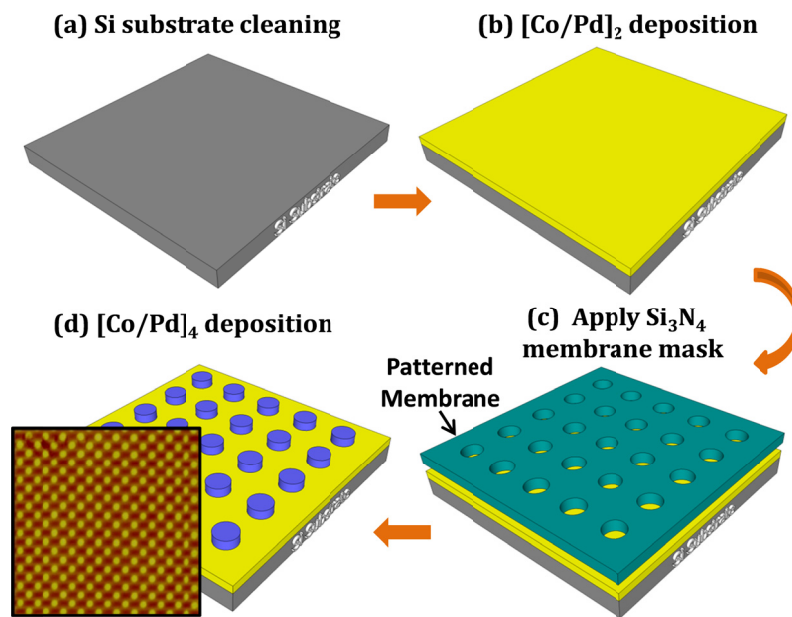


Fig. 7.2 Schematics of fabrication process flow for the modulated Co/Pd film.

References

- [1] B. D. Terris, and T. Thomson, *J. Phys. D: Appl. Phys.*, **38**, R199 (2005).
- [2] B. Terris, T. Thomson, and G. Hu, *Microsyst. Technol.*, **13**, 189 (2007).
- [3] A. O. Adeyeye, and N. Singh, *J. Phys. D: Appl. Phys.*, **41**, 153001 (2008).
- [4] R. P. Cowburn, *J. Phys. D: Appl. Phys.*, **33**, R1 (2000).
- [5] G. Dumpich, B. Leven, and M. Brands, *physica status solidi (a)*, **201**, 3237 (2004).
- [6] A. O. Adeyeye, G. Lauhoff, J. A. C. Bland, C. Daboo, D. G. Hasko, and H. Ahmed, *Appl. Phys. Lett.*, **70**, 1046 (1997).
- [7] S. Neusser, and D. Grundler, *Adv. Mater.*, **21**, 2927 (2009).
- [8] V. V. Kruglyak, S. O. Demokritov, and D. Grundler, *J. Phys. D: Appl. Phys.*, **43**, 264001 (2010).
- [9] R. P. Cowburn, D. K. Koltsov, A. O. Adeyeye, M. E. Welland, and D. M. Tricker, *Phys. Rev. Lett.*, **83**, 1042 (1999).
- [10] S. Jain, Ph.D. Thesis title "Magnetotransport and magneto-optical properties of ferromagnetic nanostructures" from National University of Singapore (2009).
- [11] D. A. Allwood, G. Xiong, C. C. Faulkner, D. Atkinson, D. Petit, and R. P. Cowburn, *Science*, **309**, 1688 (2005).
- [12] J. Jaworowicz, N. Vernier, J. Ferré, A. Maziewski, D. Stanescu, D. Ravelosona, A. S. Jacqueline, C. Chappert, B. Rodmacq, and B. Dieny, *Nanotechnol.*, **20**, 215401 (2009).
- [13] X. C. Zhu, and J. G. Zhu, *IEEE Trans. Magn.*, **39**, 2854 (2003).
- [14] J. G. Zhu, *Proceedings of the IEEE*, **96**, 1786 (2008).
- [15] N. Thiyagarajah, H. W. Joo, and S. Bae, *Appl. Phys. Lett.*, **95**, 232513 (2009).

References

- [16] R. Sbiaa, H. Meng, and S. N. Piramanayagam, *Phys. Status Solidi Rapid Res. Lett.*, **5**, 413 (2011).
- [17] H. Meng, and J. P. Wang, *Appl. Phys. Lett.*, **88**, 172506 (2006).
- [18] J. H. Park, M. T. Moneck, C. Park, and J. G. Zhu, *J. Appl. Phys.*, **105**, 07D129 (2009).
- [19] R. Law, R. Sbiaa, T. Liew, and T. C. Chong, *J. Appl. Phys.*, **105**, 103911 (2009).
- [20] D. Litvinov, V. Parekh, C. E. D. Smith, J. O. Rantschler, and P. Ruchhoeft, *IEEE Trans. Nanotechnol.*, **7**, 463 (2008).
- [21] C. E. V. Parekh, P. Ruchhoeft, S. Khizroev, and D. Litvinov, *J. Appl. Phys.*, **103**, 063904 (2008).
- [22] T. Koda, H. Awano, H. Hieda, K. Naito, A. Kikitsu, T. Matsumoto, K. Nakamura, and T. Nishida, *J. Appl. Phys.*, **103**, 07C502 (2008).
- [23] F. S. Ma, H. S. Lim, Z. K. Wang, S. N. Piramanayagam, S. C. Ng, and M. H. Kuok, *Appl. Phys. Lett.*, **98**, 153107 (2011).
- [24] G. Hu, T. Thomson, M. Albrecht, M. E. Best, B. D. Terris, C. T. Rettner, S. Raoux, G. M. McClelland, and M. W. Hart, *J. Appl. Phys.*, **95**, 7013 (2004).
- [25] R. Dittrich, G. Hu, T. Schrefl, T. Thomson, D. Suess, B. D. Terris, and J. Fidler, *J. Appl. Phys.*, **97**, 10J705 (2005).
- [26] T. Thomson, G. Hu, and B. D. Terris, *Phys. Rev. Lett.*, **96**, 257204 (2006).
- [27] G. P. Lin, P. C. Kuo, K. T. Huang, C. L. Shen, T. L. Tsai, Y. H. Lin, and M. S. Wu, *Thin Solid Films*, **518**, 2167 (2010).
- [28] D. Navas, F. Ilievski, and C. A. Ross, *J. Appl. Phys.*, **105**, 113921 (2009).
- [29] M. T. Rahman, N. N. Shams, and C.-H. Lai, *Nanotechnol.*, **19**, 325302 (2008).
- [30] M. T. Rahman, N. N. Shams, C. H. Lai, J. Fidler, and D. Suess, *Phys. Rev. B.*, **81**, 014418 (2010).

References

- [31] S. N. Piramanayagam, M. Ranjbar, H. K. Tan, W. C. A. Poh, R. Sbiaa, and T. C. Chong, *J. Appl. Phys.*, **111**, 07B916 (2012).
- [32] X. M. Liu, S. Jain, and A. O. Adeyeye, *IEEE. Trans. Magn.*, **47**, 2628 (2011).
- [33] B. Leven, and et al., *Europhys. Lett.*, **70**, 803 (2005).
- [34] C. Hassel, M. Brands, F. Y. Lo, A. D. Wieck, and G. Dumpich, *Phys. Rev. Lett.*, **97**, 226805 (2006).
- [35] S.-B. Choe, *phys. stat. sol. (c)* **4**, 4 (2007).
- [36] L. Vila, L. Piraux, J. M. George, and G. Faini, *Appl. Phys. Lett.*, **80**, 3805 (2002).
- [37] V. D. Nguyen, C. Naylor, L. Vila, A. Marty, P. Laczkowski, C. Beigne, L. Notin, Z. Ishaque, and J. P. Attane, *Appl. Phys. Lett.*, **99**, 262504 (2011).
- [38] M. Brands, and G. Dumpich, *J. Appl. Phys.*, **98**, 014309 (2005).
- [39] Y. Lu, R. A. Altman, A. Marley, S. A. Rishton, P. L. Trouilloud, G. Xiao, W. J. Gallagher, and S. S. P. Parkin, *Appl. Phys. Lett.*, **70**, 2610 (1997).
- [40] I. Tudosa, J. A. Katine, S. Mangin, and E. E. Fullerton, *Appl. Phys. Lett.*, **96**, 212504 (2010).
- [41] S. S. P. Parkin, and D. Mauri, *Phys. Rev. B.*, **44**, 7131 (1991).
- [42] S. S. P. Parkin, N. More, and K. P. Roche, *Phys. Rev. Lett.*, **64**, 2304 (1990).
- [43] T. J. Hayward, J. Llandro, R. B. Balsod, J. A. C. Bland, D. Morecroft, F. J. Castano, and C. A. Ross, *Phys. Rev. B.*, **74**, 134405 (2006).
- [44] T. Kimura, Y. Itagaki, F. Wakaya, and K. Gamo, *Appl. Phys. Lett.*, **78**, 4007 (2001).
- [45] Z. Y. Liu, F. Zhang, N. Li, B. Xu, D. L. Yu, J. L. He, and Y. J. Tian, *J. Appl. Phys.*, **104**, 113903 (2008).
- [46] K. M. Dobrich, M. Wietstruk, J. E. Prieto, F. Heigl, O. Krupin, K. Starke, and G. Kaindl, *Phys. Rev. Lett.*, **100**, 227203 (2008).

References

- [47] P. Pouloupoulos, U. Bovensiepen, M. Farle, and K. Baberschke, *Phys. Rev. B.*, **57**, R14036 (1998).
- [48] N. Thiyagarajah, and S. Bae, *J. Appl. Phys.*, **104**, 113906 (2008).
- [49] N. Thiyagarajah, S. Bae, H. W. Joo, Y. C. Han, and J. Kim, *Appl. Phys. Lett.*, **92**, 062504 (2008).
- [50] P. Ho, G. C. Han, G. M. Chow, and J. S. Chen, *Appl. Phys. Lett.*, **98**, 252503 (2011).
- [51] J. Moritz, F. Garcia, J. C. Toussaint, B. Dieny, and J. P. Nozières, *Europhys. Lett.*, **65**, 123 (2004).
- [52] S. Mangin, D. Ravelosona, J. A. Katine, M. J. Carey, B. D. Terris, and E. E. Fullerton, *Nat. Mater.*, **5**, 210 (2006).
- [53] A. V. Chumak, V. S. Tiberkevich, A. D. Karenowska, A. A. Serga, J. F. Gregg, A. N. Slavin, and B. Hillebrands, *Nat. Comms.*, **1**, 141 (2010).
- [54] K. Alexander, B. Mingqiang, and L. W. Kang, *J. Phys. D: Appl. Phys.*, **43**, 264005 (2010).
- [55] G. Gubbiotti, S. Tacchi, M. Madami, G. Carlotti, A. O. Adeyeye, and M. Kostylev, *J. Phys. D: Appl. Phys.*, **43**, 264003 (2010).
- [56] S. Neusser, G. Duerr, H. G. Bauer, S. Tacchi, M. Madami, G. Woltersdorf, G. Gubbiotti, C. H. Back, and D. Grundler, *Phys. Rev. Lett.*, **105**, 067208 (2010).
- [57] M. Kostylev, G. Gubbiotti, G. Carlotti, G. Socino, S. Tacchi, C. Wang, N. Singh, A. O. Adeyeye, and R. L. Stamps, *J. Appl. Phys.*, **103**, 07C507 (2008).
- [58] J. O. Vasseur, L. Dobrzynski, B. Djafari-Rouhani, and H. Puszkarski, *Phys. Rev. B.*, **54**, 1043 (1996).
- [59] A. O. Adeyeye, S. Jain, and Y. Ren, *IEEE. Trans. Magn.*, **47**, 1639 (2011).
- [60] G. Duerr, M. Madami, S. Neusser, S. Tacchi, G. Gubbiotti, G. Carlotti, and D. Grundler, *Appl. Phys. Lett.*, **99**, 202502 (2011).
- [61] Z. K. Wang, V. L. Zhang, H. S. Lim, S. C. Ng, M. H. Kuok, S. Jain,

References

- and A. O. Adeyeye, *Appl. Phys. Lett.*, **94**, 083112 (2009).
- [62] P. F. Carcia, A. D. Meinhaldt, and A. Suna, *Appl. Phys. Lett.*, **47**, 178 (1985).
- [63] F. J. A. d. Broeder, H. C. Donkersloot, H. J. G. Draaisma, and W. J. M. d. Jonge, *J. Appl. Phys.*, **61**, 4317 (1987).
- [64] H. J. G. Draaisma, W. J. M. de Jonge, and F. J. A. den Broeder, *J. Magn. Magn. Mater.*, **66**, 351 (1987).
- [65] S. Hashimoto, Y. Ochiai, and K. Aso, *J. Appl. Phys.*, **66**, 4909 (1989).
- [66] D.-s. Wang, R. Wu, and A. J. Freeman, *Phys. Rev. B.*, **48**, 15886 (1993).
- [67] D. Weller, Y. Wu, J. Stohr, M. G. Samant, B. D. Hermsmeier, and C. Chappert, *Phys. Rev. B.*, **49**, 12888 (1994).
- [68] Y.-S. Kim, and S.-C. Shin, *J. Appl. Phys.*, **76**, 6087 (1994).
- [69] K. Kyuno, J. G. Ha, R. Yamamoto, and S. Asano, *Phys. Rev. B.*, **54**, 1092 (1996).
- [70] P. M. L. Néel, *Le Journal De Physique Et Le Radium*, **15**, 15 (1954).
- [71] Y. Liu, Z. S. Shan, and D. J. Sellmyer, *J. Appl. Phys.*, **81**, 5061 (1997).
- [72] M. Tekielak, P. Mazalski, A. Maziewski, R. Schafer, J. McCord, B. Szymanski, M. Urbaniak, and F. Stobiecki, *IEEE. Trans. Magn.*, **44**, 2850 (2008).
- [73] M. Sawada, K. Hayashi, and A. Kakizaki, *Surf. Rev. Lett.*, **9**, 865 (2002).
- [74] W. Kuch, A. Dittschar, M. Salvietti, M. T. Lin, M. Zharnikov, C. M. Schneider, J. Camarero, J. J. de Miguel, R. Miranda, and J. Kirschner, *Phys. Rev. B.*, **57**, 5340 (1998).
- [75] F. Huang, M. T. Kief, G. J. Mankey, and R. F. Willis, *Phys. Rev. B.*, **49**, 3962 (1994).
- [76] M. B. A. Jalil, J. Guo, and S. G. Tan, *Physica B: Condensed Matter*, **404**, 1305 (2009).
- [77] K. Kyuno, J. G. Ha, R. Yamamoto, and S. Asano, *Solid. State.*
-

References

- Commun.*, **98**, 327 (1996).
- [78] H. Nemoto, H. Nakagawa, and Y. Hosoe, *IEEE. Trans. Magn.*, **39**, 2714 (2003).
- [79] D. G. Stinson, and S.-C. Shin, *J. Appl. Phys.*, **67**, 4459 (1990).
- [80] N. Thiyagarajah, Ph.D. Thesis title "Physical and magnetic properties of [Co/Pd] based spinvalves with perpendicular anisotropy towards spintronic device applications" from National University of Singapore (2011).
- [81] A. S. H. Rozatian, CHMarrows, T. PAHase, and B. K. Tanner, *J. Phys.: Condens. Matter* **17**, 12 (2005).
- [82] B. Hu, N. Amos, Y. Tian, J. Butler, D. Litvinov, and S. Khizroev, *J. Appl. Phys.*, **109**, 4 (2011).
- [83] G. Hu, and T. Thomson, *IEEE. Trans. Magn.*, **41**, 3589 (2005).
- [84] W. Thomson, *Proc. Roy. Soc.*, **8**, 546 (1857).
- [85] T. R. McGuire, and R. I. Potter, *IEEE Trans. Magn.*, **11**, 1018 (1975).
- [86] M. N. Baibich, J. M. Broto, A. Fert, F. N. Van Dau, F. Petroff, P. Etienne, G. Creuzet, A. Friederich, and J. Chazelas, *Phys. Rev. Lett.*, **61**, 2472 (1988).
- [87] G. Binasch, P. Grunberg, F. Saurenbach, and W. Zinn, *Phys. Rev. B.*, **39**, 4828 (1989).
- [88] R. E. Camley, and J. Barnas, *Phys. Rev. Lett.*, **63**, 664 (1989).
- [89] J. Barnas, A. Fuss, R. E. Camley, P. Grunberg, and W. Zinn, *Phys. Rev. B.*, **42**, 8110 (1990).
- [90] F. Bloch, *Z. Physik*, **61**, 206 (1930).
- [91] V. D. Nguyen, L. Vila, P. Laczkowski, A. Marty, T. Faivre, and J. P. Attane, *Phys. Rev. Lett.*, **107**, 136605 (2011).
- [92] B. Raquet, M. Viret, E. Sondergard, O. Cespedes, and R. Mamy, *Phys. Rev. B.*, **66**, 024433 (2002).
- [93] B. Raquet, M. Viret, P. Warin, E. Sondergard, and R. Mamy, *Physica B: Condensed Matter*, **294**, 102 (2001).
-

References

- [94] A. P. Mihai, Attan, eacute, J. P., A. Marty, P. Warin, and Y. Samson, *Phys. Rev. B.*, **77**, 060401 (2008).
- [95] M. V. Costache, G. Bridoux, I. Neumann, and S. O. Valenzuela, *Nat. Mater.*, **11**, 199 (2012).
- [96] P. W. T. Pong, C. L. Dennis, A. Castillo, A. Chen, and W. F. Egelhoff, *J. Appl. Phys.*, **103**, 07A902 (2008).
- [97] L. E. Nistor, B. Rodmacq, S. Auffret, A. Schuhl, M. Chshiev, and B. Dieny, *Phys. Rev. B.*, **81**, 220407 (2010).
- [98] L. Thomas, M. G. Samant, and S. S. P. Parkin, *Phys. Rev. Lett.*, **84**, 1816 (2000).
- [99] V. Baltz, A. Marty, B. Rodmacq, and B. Dieny, *Phys. Rev. B.*, **75**, 014406 (2007).
- [100] Y. Ren, A. O. Adeyeye, C. Nam, and C. A. Ross, *IEEE Trans. Magn.*, **46**, 1906 (2010).
- [101] D. d. Tang, and Y. J. Lee, *Magnetic Memory*, Cambridge University Press (2009).
- [102] P. Bruno, and C. Chappert, *Phys. Rev. Lett.*, **67**, 1602 (1991).
- [103] L. Néel, and C. R. Hebd., *Seances Acad. Sci.*, **255**, 1676 (1962).
- [104] M. Albrecht, G. Hu, A. Moser, and O. Hellwig, *J. Appl. Phys.*, **97**, 103910 (2005).
- [105] Y. Fu, W. Pei, J. Yuan, T. Wang, T. Hasegawa, T. Washiya, H. Saito, and S. Ishio, *Appl. Phys. Lett.*, **91**, 152505 (2007).
- [106] A. Baruth, L. Yuan, J. D. Burton, K. Janicka, E. Y. Tsymbal, S. H. Liou, and S. Adenwalla, *Appl. Phys. Lett.*, **89**, 202505 (2006).
- [107] S. Wiebel, J. P. Jamet, N. Vernier, A. Mougín, J. Ferre, V. Baltz, B. Rodmacq, and B. Dieny, *Appl. Phys. Lett.*, **86**, 142502 (2005).
- [108] T. Hauet, uuml, C. M. nther, B. Pfau, M. E. Schabes, J. U. Thiele, R. L. Rick, P. Fischer, S. Eisebitt, and O. Hellwig, *Phys. Rev. B.*, **77**, 184421 (2008).
- [109] S. Park, N. M. Nguyen, C. Burrowes, E. E. Fullerton, C. Chappert, L.

References

- Prejebeanu, F. Garcia-Sanchez, and D. Ravelosona, *Appl. Phys. Lett.*, **98**, 232512 (2011).
- [110] P. J. Metaxas, P. J. Zermatten, J. P. Jamet, J. Ferre, G. Gaudin, B. Rodmacq, A. Schuhl, and R. L. Stamps, *Appl. Phys. Lett.*, **94**, 132504 (2009).
- [111] L. Landau, and E. Lifshitz, *Physik. Z. Sowjetunion*, **8**, 153 (1935).
- [112] T. L. Gilbert, *Phys. Rev.*, **100**, 1243 (1955).
- [113] J. H. E. Griffiths, *Nature*, **158**, 670 (1946).
- [114] C. Kittel, *Phys. Rev.*, **73**, 155 (1948).
- [115] G. Gubbiotti, S. Tacchi, G. Carlotti, P. Vavassori, N. Singh, S. Goolaup, A. O. Adeyeye, A. Stashkevich, and M. Kostylev, *Phys. Rev. B.*, **72**, 224413 (2005).
- [116] A. V. Chumak, A. A. Serga, S. Wolff, B. Hillebrands, and M. P. Kostylev, *Appl. Phys. Lett.*, **94**, 172511 (2009).
- [117] N. Singh, Ph.D. Thesis title "Applications of deep UV lithography in magnetic nanostructures" from National University of Singapore (2008).
- [118] N. Singh, S. Goolaup, and A. O. Adeyeye, *Nanotechnol.*, **15**, 1539 (2004).
- [119] P. F. Fewster, *Rep. Prog. Phys.*, **59**, 1339 (1996).
- [120] P. C. Yashar, and W. D. Sproul, *Vacuum*, **55**, 179 (1999).
- [121] Q. Yang, and L. R. Zhao, *Surf. Coat. Tech.*, **200**, 1709 (2005).
- [122] Y. C. Liang, T. B. Wu, H. Y. Lee, and H. J. Liu, *Thin Solid Films*, **469**, 500 (2004).
- [123] L. G. Parratt, *Phys. Rev.*, **95**, 359 (1954).
- [124] B. Cappella, and G. Dietler, *Surf. Sci. Rep.*, **34**, 1 (1999).
- [125] S. Goolaup, Ph.D. Thesis title "Patterned ferromagnetic meso and nano structures" from National University of Singapore (2007).
- [126] Z. Q. Qiu, and S. D. Bader, *J. Magn. Magn. Mater.*, **200**, 665 (1999).
- [127] W. S. Kim, M. Aderholz, and W. Kleemann, *Meas. Sci. Technol.*, **4**, 7

References

- (1993).
- [128] J. Ding, M. Kostylev, and A. O. Adeyeye, *Phys. Rev. B.*, **84**, 054425 (2011).
- [129] R. Sbiaa, Z. Bilin, M. Ranjbar, H. K. Tan, S. J. Wong, S. N. Piramanayagam, and T. C. Chong, *J. Appl. Phys.*, **107**, 103901 (2010).
- [130] R. Sbiaa, C. Z. Hua, S. N. Piramanayagam, R. Law, K. O. Aung, and N. Thiagarajah, *J. Appl. Phys.*, **106**, 023906 (2009).
- [131] K. Janicka, J. D. Burton, and E. Y. Tsymbal, *J. Appl. Phys.*, **101**, 113921 (2007).
- [132] R. Sbiaa, Z. Bilin, M. Ranjbar, H. K. Tan, S. J. Wong, S. N. Piramanayagam, and T. C. Chong, *J. Appl. Phys.*, **107**, 103901 (2010).
- [133] D. X. Chen, J. A. Brug, and R. B. Goldfarb, *IEEE. Trans. Magn.*, **27**, 3601 (1991).
- [134] G. Hu, and T. Thomson, *J. Appl. Phys.*, **97**, 10J702 (2005).
- [135] R. L. Stamps, and R. E. Camley, *Phys. Rev. B.*, **60**, 11694 (1999).
- [136] L. F. Zhang, C. Xu, P. M. Hui, and Y. Q. Ma, *J. Appl. Phys.*, **97**, 103912 (2005).
- [137] E. Mengotti, L. J. Heyderman, R. Fraile, A. Guez, A. Bisig, L. Le Guyader, F. Nolting, and H. B. Braun, *Phys. Rev. B.*, **78**, 144402 (2008).
- [138] E. Mengotti, L. J. Heyderman, A. Bisig, A. F. Rodriguez, L. Le Guyader, F. Nolting, and H. B. Braun, *J. Appl. Phys.*, **105**, 113113 (2009).
- [139] T. Aign, P. Meyer, S. Lemerle, J. P. Jamet, Ferr, eacute, J., V. Mathet, C. Chappert, J. Gierak, C. Vieu, F. Rousseaux, H. Launois, and H. Bernas, *Phys. Rev. Lett.*, **81**, 5656 (1998).
- [140] Y. Ren, X. M. Liu, N. Singh, and A. O. Adeyeye, *IEEE. Trans. Magn.*, **49**, 3620 (2013).
- [141] J. K. n. Moser, V. Kunej, H.-F. Pernau, E. Scheer, and M. Albrecht, *J. Appl. Phys.*, **107**, 09C506 (2010).

References

- [142] S. A. Boye, P. Lazor, and R. Ahuja, *J. Appl. Phys.*, **97**, 083902 (2005).
- [143] C. H. Marrows, and B. C. Dalton, *Phys. Rev. Lett.*, **92**, 097206 (2004).
- [144] Uuml, U. diger, J. Yu, L. Thomas, S. S. P. Parkin, and A. D. Kent, *Phys. Rev. B.*, **59**, 11914 (1999).
- [145] A. D. Kent, and et al., *J. Phys.: Condens. Matter*, **13**, R461 (2001).
- [146] I. Kato, S. Takei, X. X. Liu, and A. Morisako, *IEEE. Trans. Magn.*, **42**, 2366 (2006).
- [147] J. M. Shaw, H. T. Nembach, T. J. Silva, S. E. Russek, R. Geiss, C. Jones, N. Clark, T. Leo, and D. J. Smith, *Phys. Rev. B.*, **80**, 184419 (2009).
- [148] J. Kanak, M. Czapkiewicz, T. Stobieckf, M. Kachel, I. Sveklo, A. Maziewski, and S. van Dijken, *Phys. Stat. Sol.*, **204**, 3950 (2007).
- [149] S. K. Wong, B. H. Chia, K. Srinivasan, R. Law, E. L. Tan, H. K. Tan, R. Sbiaa, and S. N. Piramanayagam, *J. Appl. Phys.*, **106**, 093904 (2009).
- [150] G. Herzer, *IEEE. Trans. Magn.*, **26**, 1397 (1990).
- [151] J. M. Shaw, M. Olsen, J. W. Lau, M. L. Schneider, T. J. Silva, O. Hellwig, E. Dobisz, and B. D. Terris, *Phys. Rev. B.*, **82**, 144437 (2010).
- [152] C.-H. Lai, C. J. Chen, and T. S. Chin, *J. Appl. Phys.*, **89**, 6928 (2001).
- [153] H. Yuasa, M. Hara, and H. Fukuzawa, *Appl. Phys. Lett.*, **92**, 262509 (2008).
- [154] J. Norpoth, and et al., *J. Phys. D: Appl. Phys.*, **41**, 025001 (2008).
- [155] R. Engel-Herbert, and T. Hesjedal, *J. Appl. Phys.*, **97**, 074504 (2005).
- [156] J. W. Knepper, and F. Y. Yang, *Phys. Rev. B.*, **71**, 224403 (2005).
- [157] S. M. Mohseni, R. K. Dumas, Y. Fang, J. W. Lau, S. R. Sani, J. Persson, and J. Akerman, *Phys. Rev. B.*, **84**, 174432 (2011).
- [158] G. Feng, H. C. Wu, J. F. Feng, and J. M. D. Coey, *Appl. Phys. Lett.*, **99**, 042502 (2011).
- [159] F. Zhang, F. S. Wen, L. Li, N. Wang, Y. F. Lu, Z. Y. Liu, B. Xu, D. L. Yu, J. L. He, and Y. J. Tian, *Thin Solid Films*, **519**, 1980 (2011).
- [160] M. R. Scheinfein, *LLG Micromagnetics Simulator*, software for

References

- micromagnetic simulations. "<http://llgmicro.home.mindspring.com/>" (1997).
- [161] J. P. Park, P. Eames, D. M. Engebretson, J. Berezovsky, and P. A. Crowell, *Phys. Rev. Lett.*, **89**, 277201 (2002).
- [162] M. Buess, R. Hollinger, T. Haug, K. Perzlmaier, U. Krey, D. Pescia, M. R. Scheinfein, D. Weiss, and C. H. Back, *Phys. Rev. Lett.*, **93**, 077207 (2004).
- [163] R. D. McMichael, and M. D. Stiles, *J. Appl. Phys.*, **97**, 10J901 (2005).
- [164] K. Zakeri, J. Lindner, I. Barsukov, R. Meckenstock, M. Farle, U. von Horsten, H. Wende, W. Keune, J. Rucker, S. S. Kalarickal, K. Lenz, W. Kuch, K. Baberschke, and Z. Frait, *Phys. Rev. B.*, **76**, 104416 (2007).
- [165] C. C. Wang, A. O. Adeyeye, N. Singh, Y. S. Huang, and Y. H. Wu, *Phys. Rev. B.*, **72**, 174426 (2005).
- [166] G. N. Kakazei, P. E. Wigen, K. Y. Guslienko, R. W. Chantrell, N. A. Lesnik, V. Metlushko, H. Shima, K. Fukamichi, Y. Otani, and V. Novosad, *J. Appl. Phys.*, **93**, 8418 (2003).
- [167] X. M. Liu, J. Ding, and A. O. Adeyeye, *Appl. Phys. Lett.*, **100**, 242411 (2012).
- [168] Y. S. Huang, A. O. Adeyeye, and N. Singh, *J. Phys.: Condens. Matter*, **17**, 3931 (2005).
- [169] S. Neusser, B. Botters, and D. Grundler, *Phys. Rev. B.*, **78**, 054406 (2008).

List of Publications

Journal Publications

- [1] “Magnonic crystals composed of Ni₈₀Fe₂₀ film on top of Ni₈₀Fe₂₀ two-dimensional dot array”, X. M. Liu, J. Ding, G.N. Kakazei, and A.O. Adeyeye, *Appl. Phys. Lett.* **103**, 062401 (2013).
- [2] “Magnetoresistance Behavior of Bi-component Antidot Nanostructures”, X. M. Liu, J. Ding, N. Singh, M. Kostylev, and A. O. Adeyeye, *Europhys. Lett.* **103** 67002 (2013).
- [3] “Magnetization dynamics and reversal mechanism of Fe filled Ni₈₀Fe₂₀ antidot nanostructures”, X. M. Liu, J. Ding, and A. O. Adeyeye, *Appl. Phys. Lett.* **100**, 242411 (2012).
- [4] “Magnetization reversal and magnetoresistance behavior of perpendicularly magnetized [Co/Pd]₄/Au/[Co/Pd]₂ nanowires”, X. M. Liu, P. Ho, J. S. Chen, and A. O. Adeyeye, *J. Appl. Phys.* **112**, 073902 (2012).
- [5] “Magnetic Properties of Perpendicularly Magnetized [Co/Pd]/Au/[Co/Pd] Pseudo-Spin-Valve Nanoring Structures”, X. M. Liu, S. Jain, and A. O. Adeyeye, *IEEE Trans. Magn.* **47**, 2628 (2011).
- [6] “Influence of magnetostatic interaction on the magnetization reversal of patterned Co/Pd multilayers nanorings”, Y. Ren, X. M. Liu, N. Singh, and A. O. Adeyeye, *IEEE Trans. Magn.* **49**, 3620 (2013).
- [7] “Synthesis of silicon oxide nanowires and nanotubes with cobalt-palladium or palladium catalysts”, R. Esterina, X. M. Liu, C. A. Ross, A. O. Adeyeye, and W. K. Choi, *J. Appl. Phys.* **112**, 024312 (2012).

Conference Proceedings

- [1] “Interlayer Coupling and Magnetoresistance Behaviors of [Co/Pd]₄/Co/Ru/[Co/Pd]₂ Pseudo-spin-valve Multilayers”, X. M. Liu, J. Ding, G. N. Kakazei and A. O. Adeyeye, *58th Magnetism and Magnetic Materials Conference*, Denver, Colorado, USA, November 4-8, 2013 (Accepted).
- [2] “Magnonic crystals made from Permalloy film on top of 2-D dot array”, X. M. Liu, J. Ding, G. N. Kakazei and A. O. Adeyeye, *58th Magnetism and Magnetic Materials Conference*, Denver, Colorado, USA, November 4-8, 2013 (Accepted).
- [3] “Static and Dynamic Behaviors of Fe Filled Ni₈₀Fe₂₀ Antidot Nanostructures”, X. M. Liu, J. Ding and A. O. Adeyeye, *12th Joint MMM/Intermag Conference*, Chicago, Illinois, USA, January 14–18, 2013.
- [4] “Magnetic and Transport Properties of Perpendicularly Magnetized Co/Pd Nano-wires”, X. M. Liu and A. O. Adeyeye, presented at *56th Magnetism and Magnetic Materials Conference*, Scottsdale, Arizona, USA, October 30th – November 3rd, 2011.
- [5] “Magnetic and Transport Properties of [Co/Pd]₄/Au/[Co/Pd]₂ Pseudo-spin-valve Nano-wires”, X. M. Liu and A. O. Adeyeye, presented at *56th Magnetism and Magnetic Materials Conference*, Scottsdale, Arizona, USA, October 30th – November 3rd, 2011.
- [6] “Magnetic properties of perpendicularly magnetized [Co/Pd]/Au/[Co/Pd] pseudo-spin-valve nanoring structures”, X. M. Liu, S. Jain and A. O. Adeyeye, presented at *IEEE International Magnetism Conference (Intermag 2011)*, Taipei, April 25-29, 2011.
- [7] “Magnetic Behaviors of Perpendicularly Magnetized Co/Pd nanopillars”, X. M. Liu, Y. Ren and A. O. Adeyeye, presented at *55th Magnetism and Magnetic Materials Conference*, Atlanta, Georgia, USA, November 14-18, 2010.